PolyPublie
Polytechnique Montréal

POLYTECHNIQUE MONTRÉAL
UNIVERSITÉ D'INGÉNIERIE

Titre: Title:	Numerical Seismic Assessment of a Deep and Narrow Tabular Mine
Auteur: Author:	Maciej Armatys
Date:	2023
Type:	Mémoire ou thèse / Dissertation or Thesis
Référence: Citation:	Armatys, M. (2023). Numerical Seismic Assessment of a Deep and Narrow Tabular Mine [Thèse de doctorat, Polytechnique Montréal]. PolyPublie. https://publications.polymtl.ca/55113/

Document en libre accès dans PolyPublie
Open Access document in PolyPublie

URL de PolyPublie: PolyPublie URL:	https://publications.polymtl.ca/55113/
Directeurs de recherche: Advisors:	Richard Simon
Programme: Program:	Génie minéral

Ce fichier a été téléchargé à partir de PolyPublie, le dépôt institutionnel de Polytechnique Montréal
This file has been downloaded from PolyPublie, the institutional repository of Polytechnique Montréal

https://publications.polymtl.ca

POLYTECHNIQUE MONTRÉAL

affiliée à l'Université de Montréal

Numerical seismic assessment of a deep and narrow tabular mine

MACIEJ ARMATYS

Département des génies civil, géologique et des mines

Thèse présentée en vue de l'obtention du diplôme de *Philosophiæ Doctor*

Génie Minéral

Août 2023

© Maciej Armatys, 2023.

POLYTECHNIQUE MONTRÉAL

affiliée à l'Université de Montréal

Cette thèse intitulée :

Numerical seismic assessment of a deep and narrow tabular mine

présenté par **Maciej ARMATYS**

en vue de l'obtention du diplôme de *Philosophiæ Doctor*

a été dûment acceptée par le jury d'examen constitué de :

Li LI, président
Richard SIMON, membre et directeur de recherche
Antoine JACQUEY, membre
Jonathan AUBERTIN, membre externe

DEDICATION

This work is dedicated to my parents.

ACKNOWLEDGEMENTS

First, I would like to thank my thesis advisor, Professor Richard Simon, for providing me with guidance and encouragement during my research and leading me to complete my research.

Second, I need to recognize the impact joining Hecla has had on my career and their openness to allow their employees to pursue higher education, such as in my case. The company truly values education/knowledge, which in return attracts exceptional engineers, geologists, and operators, creating a setting for discussion and exchange. During this thesis, I had the pleasure of working with brilliant individuals at the Lucky Friday mine and at the Hecla corporate office, notably Dr. Mark Board (VP-Hecla Mining, Corp.), Jim Meyers (Senior Geologist, Corp.), Terry DeVoe (Chief Geologist, LF), Steve Achord (Senior Mine Technician, LF), all of whom have retired now, and Bob Golden (Chief Geotech., LF), Wes Johnson (Chief Engineer, Corp.), Matt Blattman (Director Tech. Services, Corp.) and Chris Neville (VP-General Manager, LF), in current roles/positions. Thank you all for your technical discussions, impromptu moral support, and (*mainly directed at Mark*) allowing me to stumble with my modelling, results and reasoning while gently nudging me back to first principles of rock mechanics. My gratitude is also extended to Hecla's upper management for keeping confidence that I could accomplish this feat, notably Phil, with his kind words of encouragement whenever we spoke.

Third, I also need to acknowledge the generosity of ACG for providing me with a student license of their seismic software (*free of charge*) — mXrap seismic suite; many thanks to Dr. Yves Potvin, Dr. Johan Wesseloo, and Paul Harris, as well as their incredible support staff. Many thanks are also extended to Dr. Terry Wiles from MAP3D for his attentive support, given my numerous inquiries during the BEM setup stage.

In closing, this work wouldn't have been at all possible without the care and patience of my wife, Thu (*I will forever be grateful to you*), and my two sons, Nathan and Thomas, who have significantly grown during the course of this endeavour (*may this adventure inspire you)*.

RÉSUMÉ

Les mines tabulaires étroites en roche dure révèlent souvent le potentiel de génération de la sismicité induite par le minage en profondeur. Les ruptures de roche fortement déformées et les glissements de failles produisent ces réponses déséquilibrées. Une fois initiées, les opérations souterraines sont soumises à des événements sismiques quotidiens, qui peuvent conduire à de violentes éjections de roches aux abords des excavations. Ce phénomène de sous-ensemble se classifie comme coup de terrain. Pendant plusieurs décennies, des recherches approfondies ont jailli des mines les plus profondes du monde pour soulager les opérations de ce fardeau néfaste. Malheureusement, les mines en Australie, Canada, Chili, Chine, Suède, Afrique du Sud et aux États-Unis continuent de signaler des pertes et de lourdes compensations économiques. Au fur et à mesure que les gisements de minerai proches de la surface s'éteignent, les mines souterraines entament leurs lourdes descentes dans la masse rocheuse avec des contraintes in-situ gonflantes. Pour gérer efficacement le risque sismique, les mines modernes exploitent des systèmes de surveillance sismique locaux, capturant la réponse sismique par rapport à l'exploitation minière. En analysant ces modèles sismiques, le mécanisme de la source sismique peut être extrait, ce qui conduit à une meilleure conception technique. Cette thèse analyse le catalogue sismique, en portant une attention particulière aux événements notables supérieurs à +0,5 M_w, enregistrés depuis le début de l'exploitation du gisement Gold Hunter à la mine Lucky Friday. Les principaux paramètres sismologiques (magnitude, temps, localisation) ont été liés aux paramètres opérationnels (aménagement de la mine, séquence, tonnage) pour deux périodes minières initiales entre 1997–2016. Le mécanisme de source primaire du Gold Hunter indique un comportement de glissement de faille. Plus tard, les concepts du *Energy Release Rate* (ERR) et le *Excess Shear Stress* (ESS) ont été utilisés pour évaluer plus en détail le mécanisme de la source sismique. Le ERR a permis de complémenter le tableau de conception sismique empirique, indiquant que la réponse sismique globale du Gold Hunter est comparable à celle observée dans les mines tabulaires profondes d'Afrique du Sud. L'ESS a permis de développer une masse rocheuse synthétique pour confirmer davantage l'environnement de glissement de faille, en utilisant le catalogue sismique pour contraindre les propriétés de friction des structures. Enfin, deux périodes de minage subséquentes ont été validées entre 2017–2021. Il a été observé que ces périodes produisaient une réponse sismique différente (inférieure) à une plus grande profondeur d'exploitation. Des analyses de détails ont indiqué que les conditions d'exploitation ultérieures ont

suffisamment changé, ce qui a eu un impact sur la réponse sismique à la mine. Ces facteurs se relient au taux d'extraction et à un changement important dans la méthode d'extraction, passant d'une coupe-et-remblai à une nouvelle technique intitulée *Underhand Closed Bench*. Alors que la mine entre dans sa descente pour atteindre sa profondeur d'exploitation ultime à 2,9 km, ces méthodes de planification développées permettront à l'ingénierie de fournir des prévisions supplémentaires sur les risques sismiques.

Mots-clés : Coupe-et-remblai, exploitation minière en profondeur, glissement de faille, mine Lucky Friday, mine tabulaire en roche dure, sismicité induite, *Underhand Closed Bench*.

ABSTRACT

Narrow tabular hardrock mines often uncover the potential for generating mine-induced seismicity at depth. High-strained rock failures and fault-slips yield these unbalanced kinetic responses. Once initiated, the underground operations are subjected to daily seismic outbursts, which can lead to violent rock ejections around the excavation boundaries. This subset phenomenon classifies rockbursting. During several decades, extensive research surged from the deepest mines in the world to relieve operations of this adverse burden. Unfortunately, mines in Australia, Canada, Chile, China, Sweden, South Africa, and the United States continue to report casualties and heavy economic offsets. As near-surface ore deposits extinguish, underground mines endure their lumbering descents into the rockmass through swelling in-situ stresses. Modern mines operate local seismic monitoring systems to effectively manage seismic risk, capturing the seismic response with respect to mining. By analyzing these seismic patterns, the seismic source mechanism can be extracted, which leads to better engineering design. This dissertation analyses the seismic catalogue, focusing on notable events greater than +0.5 M_w, recorded since mining was initiated in the Gold Hunter deposit at the Lucky Friday mine. The primary seismological parameters (magnitude, time, location) were linked with operational settings (mine layout, sequence, tonnage) for two initial mining periods between 1997 and 2016. The Gold Hunter's primary source parameter indicates fault-slip behaviour. Later, numerical concepts of the Energy Release Rate and the Excess Shear Stress were used to further assess the seismic source mechanism. The ERR results were integrated into the empirical seismic design chart, where the Gold Hunter's overall seismic response compares to that observed in deep tabular South African mines. The ESS allowed the development of a synthetic rockmass to further confirm the fault-slip environment, utilizing the seismic catalog to constrain the frictional properties of structures. Finally, two additional subsequent mining periods were investigated between 2017 and 2021. It was observed that these periods produced a different (lesser) seismic response at greater mining depth. Further analyses indicated that the subsequent mining conditions have sufficiently changed, impacting the seismic response at the mine. These factors include the mining rate and the effects of introducing a new mining method, transitioning from underhand cut-&-fill to a novel underhand closed bench technique. As the mine enters its descent to reach the 2.9 km mining depth, these developed planning methods will allow engineers to provide additional seismic hazard forecasts.

Keywords: Cut-and-fill, deep mining, fault-slip, Lucky Friday mine, mine-induced seismicity, tabular deposit, tabular hardrock mine, Underhand Closed Bench.

TABLE OF CONTENTS

DEDICATION III

ACKNOWLEDGEMENTS IV

RÉSUMÉ V

ABSTRACT VII

Table OF CONTENTS ix

LIST OF TABLES XIII

LIST OF FIGURES XIV

LIST OF SYMBOLS AND ABBREVIATIONS XXIII

LIST OF APPENDICES XXVI

CHAPTER 1 INTRODUCTION 1

1.1 Problem Statement 1

1.2 Engineering Methods for Seismic Control 3

1.3 Evolution of Seismicity with Mining Depth 5

1.4 Developing a Deterministic Approach to Forecast Seismicity 7

1.5 Summary of Thesis Content 10

CHAPTER 2 LITERATURE REVIEW 12

2.1 Mine-Induced Seismicity 12

2.1.1 Definition of Rockburst & Seismicity 12

2.1.2 A Brief Overview of the Severity of Mine-Induced Seismicity 13

2.1.3 Factors Affecting Mine Seismicity and Rockbursts 17

2.1.4 Rockbursts & Seismic Classifications 18

2.2 Seismic Source Mechanisms 21

2.2.1 Failure of Rock 21

2.2.2 Rockmass Response to Tabular Mining....40
2.3 Assessment of Mine Seismicity....50
2.3.1 Rock Mechanics Approach....50
2.3.2 Seismological Approach....62
2.3.3 Numerical Modelling Approach....70
CHAPTER 3 SEISMICITY AT THE LUCKY FRIDAY MINE....81
3.1 Mining, Geological & Geomechanical Setting....81
3.1.1 Mining Context....81
3.1.2 Geology & Relevant Structures....85
3.1.3 Mechanical Properties of Rock....89
3.2 Seismic Review....102
3.2.1 Seismic Response at the Lucky Friday Mine....102
3.2.2 Local Seismic System Employed at the Mine....104
3.2.3 Seismic Response to Mining....107
3.2.4 Mining Factors Affecting the Seismic Output....118
3.3 Chapter Summary....123
CHAPTER 4 NUMERICAL ASSESSMENT OF THE SEISMIC CATALOG....125
4.1 BEM Setup....125
4.2 Grid-Based Analysis (BEM-DD)....130
4.2.1 Closure Calibration Procedure & Assessment....130
4.2.2 Stress Analysis in Abutments....134
4.2.3 ERR Analysis (BEM-DD)....139
4.3 Block-Based Analysis (BEM-FF)....161
4.3.1 ESS Analysis (BEM-FF)....162

4.3.2 ESS_S Analysis of Recorded Seismic Events (2013–2016) 166
4.3.3 ESS Analysis of DFN 171
4.4 Chapter Summary 183
CHAPTER 5 FORECASTING MINE-INDUCED SEISMICITY 185
5.1 Deepening Mine Conditions in the Gold Hunter Deposit 185
5.2 Validation of Developed Seismic Design Chart 186
5.2.1 Back Analysis of Subsequent Mining Periods 187
5.2.2 Discussion on the Effects of Mining Conditions 189
5.3 Mechanisms Affecting Seismic Response 199
5.3.1 Investigating the Mechanism of Seismic Control in UCB 199
5.3.2 Seismic Release Mechanism in Pillars 212
5.4 Forecasting Seismicity as Mining Progresses 215
5.4.1 Tracking Magnitude-Time-Location 215
5.4.2 Procedures & Applications 218
5.4.3 Discussion on Forecasting Seismic Energy Release 221
5.5 Chapter Summary 223
CHAPTER 6 CONCLUSION, CONTRIBUTIONS AND RECOMMENDATIONS 226
6.1 Summary & Limitations 226
6.1.1 Seismicity at the Lucky Friday Mine (Chapter 3) 227
6.1.2 Numerical Assessment of the Seismic Catalog (Chapter 4) 231
6.1.3 Assessing the Seismic Source Mechanism (Chapter 5) 236
6.2 Contributions 239
6.3 Recommendations for future work 241
REFERENCES 243

APPENDICES 263

LIST OF TABLES

Table 1.1: Thesis objectives 8

Table 2.1: Suggested rockburst type based on seismic source (Ortlepp, 1992) 19

Table 2.2: General advantages and disadvantages of numerical codes (Hoek et al., 1991; Simon, 1999) 71

Table 3.1: Mechanical properties of intact rock at Gold Hunter 90

Table 3.2: Mechanical properties of confined rock at Gold Hunter 90

Table 3.3: Mine-wide stress field estimates assumed for the Gold Hunter 91

Table 4.1: Displacement history points (at the center of a DD element) with respect to the nearest closure instrument (in metric coordinates) 131

Table 4.2: Summary of seismic efficiency (η%) per stope for the entire period, 2013–2016 157

Table 5.1: The largest events recorded in Pillars and mining abutments per mining period 189

Table 5.2: Comparison of forecast to recorded seismic energy release in 15 Stope 219

LIST OF FIGURES

Figure 1.1: Relationship between the largest mining dimension and the maximum recorded magnitude event at the GH, LF and SM (compared with results reported in McGarr et al., 2002 & Wesseloo, 2018). 7

Figure 1.2: Venn diagram for evaluating the Seismic Potential (SP) 10

Figure 2.1: Worldwide survey of seismically active mines (n = 279) (Wilson et al., 2017) 13

Figure 2.2: Recorded seismic response (dots) while advancing a single stope on a reef, where (a) shows the plan view, and (b) shows a section view looking east (Legge & Spottiswoode, 1987)..... 14

Figure 2.3: Increase in rockburst damage observed at the steel-set reef drive in the Champion Reef Mine of the Kolar fields, India (Fairhurst, 1990, after Caw, 1956)..... 16

Figure 2.4: Schematic diagram of six seismic mechanisms (Horner & Hasegawa, 1978) 20

Figure 2.5: Schematic representation of Griffith's model of (a) crack propagating in a rod under constant tensile strength, and (b) the associated energy distribution (Scholz, 2019)..... 23

Figure 2.6: Schematic representation of Obreimoff's mode for (a) mica cleaving, and (b) the associated energy distribution (Scholtz, 2019) 23

Figure 2.7: Four stages of crack progression under compressive test, where stage (**i**) crack closure, (**ii**) elastic region, (**iii**) stable crack growth, and (**iv**) unstable crack growth (after Martin & Christiansson, 2009)..... 25

Figure 2.8: Mohr-Coulomb's failure criterion (a) shear planes, and (b) strength envelope 26

Figure 2.9: Theoretical stress-strain curves for stable and unstable conditions assuming constant loading machine stiffness (Cook, 1965a)..... 28

Figure 2.10: Schematic of a complete load-displacement curve of a brittle rock sample obtained by load cycling (Goodman, 1989)..... 29

Figure 2.11: Schematic constitutive stress-strain response of hardrock under increased confinement, showing brittle-ductile transition (Goodman, 1989)..... 30

Figure 2.12: Schematic direct-shear model with associative static shear-stress and shear-displacement responses 31

Figure 2.13: Shear-normal stress behaviour for a wide variety of rocks (Byerlee, 1978) 32

Figure 2.14: Three main surface-asperity interactions (a) plowing, (b) dilation, and (c) asperity shear (after Jaeger et al., 2009, from Scholz, 2019).....33

Figure 2.15: Shear and normal stiffness associations within (a) normal-closure relation, and (b) shear-displacement.....35

Figure 2.16: Spring-block model (a) analogue representation, (b) high-stiffness loading response (stable response), and (c) low-stiffness loading (kinematic) response (Rice, 1984).....36

Figure 2.17: Scheme of experimental frictional response to a sudden e-fold (~2.7) increase in velocity following a decrease in sliding velocity (Scholz, 1998) 39

Figure 2.18: Schematic of an advancing reef face illustrating three distinct rock zones (a) fractured, (b) yielding, and (c) sustained (Cook, 1965a) 40

Figure 2.19: Component of released energy for circular excavation in varying mining-step amounts (Salamon, 1983).....43

Figure 2.20: Four mechanisms of pillar-bursts in tabular mines (a) crushing, (b) shearing, (c) punching, and (d) simultaneous shear (Lenhardtl & Hagan, 1989) 45

Figure 2.21: Partitioning of energy during shear slip for transitional peak to residual friction values (Jordan, 2000) 46

Figure 2.22: Magnitude-slip relationship relative to stress drop (Zoback & Gorelick, 2012).....48

Figure 2.23: Factors contributing to frictional shear strengthening (Hencher & Richards, 1989)49

Figure 2.24: Fault surface displaying a jog and a step, with respect to slip vector (Scholz, 2019) 50

Figure 2.25: Seismic source mechanism interpreted from a mining environment (Hudyma & al., 2003).....51

Figure 2.26: Rockburst potential and seismic event occurrences with regards to ERR (COMRO, 1988).....54

Figure 2.27: Schematic of an advancing reef front in a faulted environment (Ryder, 1987) 56

Figure 2.28: Shear-Normal stress relation representing static to dynamic transition through a stress drop (Ryder, 1987) 57

Figure 2.29: Shear-displacement constitutive model with associative static stress drop and ride (Ryder, 1987) 58

Figure 2.30: Active shear stress and shear strength (static/dynamic) along a conceptual fault trace (Ryder, 1987) 59

Figure 2.31: Analytical ESS lobes for a typical advancing tabular stope (Ryder, 1987).....60

Figure 2.32: Velocity seismogram of a seismic event and the associated S-wave displacement spectrum density plot (McGarr, 1984) 65

Figure 2.33: Simulated fault slip events ahead of a tabular mining front (Board, 1994).....76

Figure 2.34: Frequency-magnitude response of simulated vs recorded (Board, 1994) 76

Figure 2.35: Flaws integration and failure logic according to various rockmass populating methods (a) Salamon, (b) Linkov, and (c) Malovichko-Basson (Malovichko & Basson, 2014).....77

Figure 3.1: Geographical location of the Lucky Friday mine relative to Idaho state (USA).....82

Figure 3.2: Isometric view of the GH (30-Vein) and the LF historical workings, looking ~North/East 83

Figure 3.3: Longitudinal of GH 30-Vein and Intermediate-Veins (shaded), view is due North. As-built geometry 2021 year-end.....84

Figure 3.4: Section view showing the ramp and slot access into the underhand stope.....85

Figure 3.5: Local geology of the Star and Lucky Friday mine in the Coeur D'Alene mining district.....86

Figure 3.6: Geological cross-section of the Lucky Friday mine, highlighting the LF and the GH deposits.....87

Figure 3.7: Digitized mapped joint sets in the GH expansion area.....89

Figure 3.8: Hoek-Brown rockmass failure envelopes for vein and wall rock.....91

Figure 3.9: Rosette plot showing the frequency of σ_{h1} direction inferred from overcore measurements and observable breakouts at the Lucky Friday mine (Whyatt et al., 1995)....92

Figure 3.10: BEM DD construction of 30-Vein for 2016 year-end, section through 15S (17,661E).....94

Figure 3.11: Normal stresses and closures computed across the 30-Vein (section 17,661E).....96

Figure 3.12: Principal and minor (a–b) stresses and (c–d) vector trajectories (section 17661E) .96

Figure 3.13: Underhand cut-&-fill heading showing rock yielding via tensile fracturing which occurs in the floor of the previous cut (photo courtesy of Dr. Board) 97

Figure 3.14: Normal closure computed along the extracted portions of 30-Vein.....98

Figure 3.15: In-stope closure measurement locations, green markers (Raffaldi et al., 2019).....99

Figure 3.16: In-stope normal displacement measured in (a) 11S, and (b) 15S (Seymour et al., 2017).....100

Figure 3.17: In-situ CPB loading in (a) 11S, and (b) 15S (Seymour et al., 2017).....101

Figure 3.18: Overview of fault-slip classifications at the LF (Whyatt et al., 1996) 103

Figure 3.19: Magnitude-Time relationship per mining periods (a) 2013–2016, (b) 2017–2019, and (c) 2020–2021.....105

Figure 3.20: Stope volume filters applied in the Gold-Hunter.....107

Figure 3.21: Gutenberg Richter Magnitude Frequency plot in Gold Hunter, 2013–2016.....108

Figure 3.22: Gutenberg-Richter Magnitude-Frequency in 30-Vein stopes (a-b), 2013–2016....109

Figure 3.23: Magnitude-Time chart in Gold-Hunter, 2013–2016.....110

Figure 3.24: Magnitude distribution in the GH per production period, 2013–2016 111

Figure 3.25: Magnitude-Time charts per 30-Vein stope, 2013–2016 112

Figure 3.26: Magnitude distribution per 30-Vein stope, 2013–2016.....113

Figure 3.27: Notable seismic events ($\geq +0.5$ M_w) locations projected on to the GH, the view is looking north, 2013–2016 114

Figure 3.28: Probable fault-slips and pillar events, the view is from the footwall looking southwest towards the F3 and F4 faults, 2013–2016 115

Figure 3.29: Frequency distribution of relative distance between notable events and active mining for (a) 50 m, and (b) 10 m bin widths 116

Figure 3.30: Spatial distribution of notable events next to active mining for plots equivalent to (a) a longitudinal view (x-z plane), (b) a cross-section view (y-z- plane), and (c) a plan view (x-y plane) 117

Figure 3.31: Annual seismic-production rate in terms of tons mined in the Gold Hunter 119

Figure 3.32: Annual seismic-production rate in terms of radiated seismic energy in the Gold Hunter deposit 120

Figure 3.33: Total radiated energy release per ton mined as observed in tabular mines 121

Figure 3.34: Total energy release per area mined as observed in tabular mines 122

Figure 3.35: Lag time study between end of shift blasts and event trigger, 2013–2016 123

Figure 4.1: Longitudinal view of the grid-based model (DD elements), reconstructing the main 30-Vein of the Gold-Hunter deposit. The view is looking North 128

Figure 4.2: Longitudinal view of the block-based model (FF elements), reconstructing the main 30-Vein of the Gold-Hunter deposit. The view is looking North 129

Figure 4.3: Best-fit (E = 29.4 GPa) normal displacement curves in (a) 11S, and (b) 15S 132

Figure 4.4: Normal displacements (δn) on 30-Vein for year-end geometries (a) 2011, and (b) 2016 133

Figure 4.5: Normal stresses (σ_n) in lower abutments & in remnant pillars for year-end geometries (a) 2011, and (b) 2016 135

Figure 4.6: Normal stress modeled in abutment under 12 Stope (17,055E) for 2016 year-end geometry 137

Figure 4.7: Evolution of normal stress modeled in the 5,700 Pillar for year end geometries (a) 2011 with pillar height ~62 m, and (b) 2016 with pillar height ~25 m 138

Figure 4.8: Grid-based modelling flow chart of ERR 141

Figure 4.9: Annual extraction sequences with spatial relation to events ≥ +0.7 Mw projected onto the 30-Vein, 2007–2011 (inset arrows indicate the mining directions) 143

Figure 4.10: Average ERR per total annual extraction period in GH for 1997–2011 144

Figure 4.11: Average annual ERR per longwall in Gold Hunter (a–e) between 2007 and 2011 145

Figure 4.12: Average annual seismic efficiency (η%) computed in Gold Hunter, 1997–2011 ..147

Figure 4.13: Annual extraction sequences with spatial relation to events ≥ +1 M_w projected onto the 30-Vein, 2013–2016 (inset arrows indicate mining directions) 148

Figure 4.14: Average ERR per annual production for (a) total mine, and (b) per stope..... 149

Figure 4.15: Average annual ERR per stope with associated events ≥ +1 M_w projected onto the 30-Vein for (a-d) 2013–2016, respectively 151

Figure 4.16: Computed ERR per DD-element from monthly increments grouped by annual production with associated events ≥ +1 M_w projected onto 30-Vein for (a-d) 2013–2016 .152

Figure 4.17: Computed Wk [MJ] per DD-element from monthly increments grouped per annual production with associated events ≥ +1 M_w projected onto 30-Vein for (a-d) 2013–2016 .155

Figure 4.18: Average annual seismic efficiency (η%) computed for Gold Hunter, 2013–2016 157

Figure 4.19: Seismic efficiency comparison between GH and SA energy-magnitude scaling relationship 159

Figure 4.20: Seismic response in GH (a–c) compared to SA practice 160

Figure 4.21: The block-based (FF-element) geometries with the S1, F3, and F4 faults..... 163

Figure 4.22: Block-based model flow chart for investigating CEV_S 166

Figure 4.23: Mohr-Coulomb slip strength criterion sensitivity analysis (a-b)..... 167

Figure 4.24: The Es/Ep in GH for events (a) ≥ +1 M_w & (b) ≥ +2 M_w, 2013–2016..... 169

Figure 4.25: Slip potential on F3 and F4 with recorded notable events within 12 m from the structures, 2013–2016 170

Figure 4.26: Slip potential on S1 with recorded notable events within 12 m from the structure where (a) shows no slip at φ_s = 25°, and (b) slip initiation regions for φ_s reduced from 15–25° 171

Figure 4.27: Persistent in-stope fracture set visible on the South rib in 15 Stope (JRC ~2)..... 172

Figure 4.28: Typical structural layout in the GH vicinity (DeVoe & Meyers, 2017) 173

Figure 4.29: Slip radius to moment magnitude relationship given a static stress drop 174

Figure 4.30: Histogram of adjusted fracture sizes (2Ls) 174

Figure 4.31: DFN catalog of mapped related structures showing fracture size ≥ 30 m 175

Figure 4.32: Cross-section through 15 Stope showing CEV_S (in red) and ESS_S (in blue) where (a) compares simulated with recorded seismic events, and (b) identifies fracture sets prone to initiate slip. The view is looking due West 177

Figure 4.33: Modelling flow chart for $ESS_{S(FFS)}$ 178

Figure 4.34: Rerun analysis on cross-section through 15S showing FFS results for CEV_S (in red) and ESS_S (in blue) where (a) compares simulated with recorded events, and (b) identifies favourable fracture sets prone to initiate slip. The view is looking due West 179

Figure 4.35: Isometric view of (a) simulated, and (b) recorded notable events..... 181

Figure 4.36: Comparison between simulated fault slips on FFS with relation to recorded seismicity for varying static friction angles (20°, 25° & 30°). The view is looking West.. 182

Figure 4.37: Recorded vs simulated GRMF response in GH for (a) varying dynamic friction angle, and (b) varying slip lengths 183

Figure 5.1: Resource and reserve estimate in the GH (Hecla, 2022) 185

Figure 5.2: Mining on 30-Vein with projected large seismic events (> +1 M_w) for (a) 2017–2019, and (b) 2020–2021 187

Figure 5.3: ERR forecast comparison with those recorded during subsequent mining 188

Figure 5.4: The normalized annual occurrence of seismic events by mining period in GH..... 189

Figure 5.5: Normalized tons per year for each mining period in GH 190

Figure 5.6: The Underhand Close Benching (UCB) mining method (Hecla, 2022).....191

Figure 5.7: Energy release forecast by production year in GH.....192

Figure 5.8: Energy release per tons forecast by production year in GH.....192

Figure 5.9: Gutenberg-Richter Magnitude Frequency plot per mining period in GH.....193

Figure 5.10: The lag time between blasting and large seismic events in 15 Stope.....194

Figure 5.11: Seismic occurrence of notable events, 2020–2021.....195

Figure 5.12: Annual production tonnage taken from lower 30-Vein stopes (12S, 15S & 16S) .196

Figure 5.13: Cumulative seismic energy release recorded in lower 30-Vein stopes, comparing the last year of LFUL mining (2016) with one complete year of UCB (2021).....197

Figure 5.14: Distribution of the annual seismic energy release in active 30-Vein stopes, comparing the last year of LFUL mining (2016) with one complete year of UCB (2021) .198

Figure 5.15: Omori chart for energy release captured in 48h following UCB blasts (n=31).....199

Figure 5.16: Modelling flow chart for ESS_D analysis.....201

Figure 5.17: Modeled UCB geometry utilizing the block-based (FF-element) BEM in 15S.....204

Figure 5.18: Cross section through 15S showing the (a) major (red) and minor (blue) principal stress vectors induced after extracting the UCB geometry, and (b) construct of slipped structures.....205

Figure 5.19: Cross section through 15S showing the simulated UCB events for (a) slip initiation, and (b) slip extent.....206

Figure 5.20: Cross section through 15S showing the simulated fault slip events vs recorded notable seismic response of UCB projected onto the section.....207

Figure 5.21: Cross section through 15 Stope showing simulated seismic response for (a) LFUL, and (b) UCB.....209

Figure 5.22: Stress path of a near stope fault slip triggered by LFUL, and induced by UCB....210

Figure 5.23: Slip radii obtained from the ESG seismic system, 2016 and 2021.....210

Figure 5.24: Concept of near stope fault slip response for (a) LFUL, and (b) UCB method.....212

Figure 5.25: Triggered pillar events from the UCB analysis 213

Figure 5.26: Concept of fault slip response in proximity of pillar where (a) presents a stable structure, while (b) shows the structure to have triggered due to increased mining depth ..214

Figure 5.27: Cumulative seismic energy release as a function of advancing the cuts in 15S, mining period set between July 2020 and December 2021 217

Figure 5.28: Seismic energy – seismic moment relationship in 15S, 2020–2021 218

Figure 5.29: Flow chart of the Energy Buildup procedure 219

Figure 5.30: Conceptual tracking of energy build-up for Gold Hunter 220

Figure 5.31: GRMF for the GH between 2016-11-11 and 2021-12-31 221

Figure 6.1: Change in potential energy (ΔW_t) over the mined-out 30-Vein, resulting from extraction in (a) 14S exclusive, and (b) multiple stopes 229

Figure 6.2: Change in potential energy (ΔW_t) over the mined-out 30-Vein, resulting from exclusively extracting the bottom 30-vein stopes 230

Figure 6.3: Schemes for reducing stress in the mined-out block (a) elastic rockmass assumption, (b) constant cap (crushing) stress assumption, (c) consecutive strength weakening (yielding) assumptions (Spottiswoode et al., 2008) 232

Figure 6.4: Range of half-closures (closure divided by 2) of the stope as a function of distance from the panel midspan, assuming various rockmass properties and fill assumptions (Whyatt et al., 1992) 233

Figure 6.5: Preliminary direct-shear results on core from 7500L, in argillites: (a) single stage result at highest normal stress, (b) surface structure condition pre-test, (c) static and residual strength estimates 235

LIST OF SYMBOLS AND ABBREVIATIONS

The list of most prominent symbols and abbreviations used in the thesis in alphabetical order, along with their meanings.

11S	11 Stope of the Gold Hunter deposit
14S	14 Stope of the Gold Hunter deposit
15S	15 Stope of the Gold Hunter deposit
16S	16 Stope of the Gold Hunter deposit
30-Vein	Main production vein in the Gold Hunter deposit
b-value	Slope of the GRFM plot
BEM	Boundary Element Method
CLR	Carbon Leader Reef
CEV	Coulomb ESS vector (Ryder, 1988)
DFN	Discrete Fracture Network
DD	Displacement Discontinuity element
ERR	Energy Release Rate
ESS	Excess Shear Stress
ESS_d	Excess Shear Stress computed from the dynamic friction angle (i.e., slip potential)
ESS_s	Excess Shear Stress computed from the static friction angle (i.e., slip initiation)
FF	Fictitious Force element
FS	Fracture Set
FFS	Favourable Fracture Set
GH	Gold Hunter deposit (at the Lucky Friday mine)
GRMF	Gutenberg Richter Magnitude Frequency plot
JRC	Joint Roughness Coefficient

LF	Lucky Friday mine
LFUL	Lucky Friday Underhand Longwall (i.e., underhand cut-&-fill mining method)
M	Magnitude (unspecified)
MTL	Magnitude-Time-Location
U_c	Stored strain energy in the rockmass
U_m	Stored strain energy in the mining block
UCB	Underhand Closed Bench
VCR	Ventersdorp Contact Reef
W_k	Kinetic energy release (specified when modelled, in J)
W_r	Energy release
W_s	Work done in deforming the support
W_t	Change in potential energy
C	Cohesion [Pa]
$\delta_{post\text{-}mining}$	Effective displacement resulting from mining [m]
δ_n	Normal displacement [m]
δ_s	Shear displacement [m]
$\Delta\tau$	Static stress-drop from static to dynamic strengths [Pa] ($\Delta\tau = \tau_s - \tau_d$)
$\Delta\hat{\tau}$	Peak stress-drop from active to dynamic strengths [Pa] ($\Delta\hat{\tau} = \tau_a - \tau_d$)
E	Young Modulus [Pa]
E_s	Seismic energy as recorded by the seismic system [J]
ε_1, ε_2, ε_3	Principal (major, intermediate, minor) strain [m/m]
F_f	Frictional force [N]
L_s	Slip radius [m]
l	half-span of stope along [m]

λ	exponent coefficient
K	Stiffness [N/m]
M_L	Richter magnitude [1]
M_n	Nuttli magnitude [1]
M_o	Seismic moment [N-m]
M_w	Moment magnitude [1]
N	Normal force [N]
p_n	Pre-mining (virgin) stress state [Pa]
φ	Friction angle [°]
φ_s	Static friction angle [°]
φ_d	Dynamic friction angle [°]
σ_1, σ_2, σ_3	Principal (major, intermediate, minor) stresses [Pa]
σ_n	Normal stress [Pa]
$\sigma_{pre\text{-}mining}$	Pre-mining stress across the mining element [Pa]
τ	Shear stress or strength [Pa]
τ_a	Active shear stress [Pa]
τ_e	ESS leading to slip potential [Pa] ($\tau_e = \tau_a - \tau_d$), equivalent to ESS_d
$\hat{\tau}_e$	ESS leading to slip initiation [Pa] ($\hat{\tau}_e = \tau_a - \tau_s$), equivalent to ESS_s
τ_s	Resistive static shear stress or strength [Pa]
τ_d	Residual dynamic shear stress or strength [Pa]
UCS	Uniaxial Compressive Strength [Pa]
υ	Poison ratio [1]
x	distance along the span (x-axis) taken from the stope center [m]

LIST OF APPENDICES

Appendix A — ERR verification for a horizontal reff in an infinite elastic medium.....263

Appendix B — MAP3D V68 input parameters 269

Appendix C — Young's modulus calibration.....270

CHAPTER 1 INTRODUCTION

1.1 Problem Statement

Deep hardrock narrow vein mines exhibit the potential to become seismically active under certain conditions. As operations extract the ore body, the relieved stresses residing inside the mined block transfer into the remaining abutments. Excessive stresses in the rockmass lead to dynamic failures, releasing transient seismic waves which are experienced locally as ground vibrations, acoustic emissions, or rock displacements (i.e., rockbursts). For a producing mine, these manifestations correspond to mine-induced seismicity (Mendecki, 2013). Mine seismicity compares to naturally occurring crustal earthquakes as both groups produce similar waveforms (Cook, 1963b; McGarr, 1971; Scholz, 2019). For this reason, seismic systems have integrated the mining industry as early as the 1940s in North America (Blake & Hedley, 2003). This integration complemented the emerging rock mechanic discipline of stresses and displacements (Ortlepp & Cook, 1964; Salamon, 1963; Salmon 1964a–c). Modern seismic monitoring systems allow the mine to track seismic occurrences in real time, providing *instant* estimates of magnitude, time, and location.

Extraction drives seismic occurrences (Blake & Hedley, 2003), where the events are colloquially referred to as bumps, bursts, pops, quakes, shocks, or tremors at a mine. The Richter magnitude scale (M_L) is a common size measure used within the industry, along with the Nuttli magnitude (M_n) and the moment magnitude (M_w) (Cai & Kaiser, 2018). The recorded magnitudes at a mine vary from low-intensity micro-seismic events (-2 M_L) to large-intensity macro events (+5 M_L) (Gibowicz, 2009). The next integer magnitude increase releases ~32 times more energy than its previous magnitude. A literature survey indicates that the largest recorded mine-induced event was a +6.1 M_L fault-slip at the Bachatsky open pit coal mine in Kuzbass (Russia) in 2013 (Emanov et al., 2014). For underground operations, the largest recorded event measured at +5.6 M_L in 1989 was attributed to an abrupt sequential pillar failure in the potash mining district of southern Germany (Knoll, 1990). A recent mine survey observed an increase in occurrences of larger events (≥ +3 Mn) across Canadian underground operations (Ollila, 2021).

The source of seismic energy is generally agreed to be produced by unstable failure processes in a highly strained volume of rock or along geological planes (Linkov, 1992). Unstable energy

transfers arise during post-yielding of the failing material, where a stiffness contrast with the loading system produces energy surpluses that dissipate through kinetic energy release instead of further crushing the material (Salamon, 1993). In contrast, a fault presents the potential for generating a stress drop when the critical shear strength has been reached along the structure (Ryder, 1987). Certain high-strained rockmass or unfavourably orientated faults can succumb to these unbalanced processes. Once initiated, seismically active mines endure daily energy outbursts (Hedley, 1992).

Amongst the diverse mining activities, underground operations exhibit the highest seismic risk due to the proximity of seismic occurrence with active development or production headings (e.g., Hedley & Blake, 2003). Seismic events can generate sudden high-velocity rock ejections in the most vulnerable excavation boundaries — this phenomenon corresponds to rockbursting. However, there is no direct correlation between the amount of damage an excavation can sustain with respect to the size of an event (Hedley, 1992). Although empirical trends support increased damage count for large-magnitude occurrences (Hudyma, 2008; Morissette, 2015), the intensity of damage varies across the upper magnitude range (Hudyma et al., 2017). The distance from the hypocentre (the focus) to the mining infrastructure appears crucial in generating rockbursts (Ortlepp, 1984). Transient seismic waves attenuate (lose energy) as they travel through the medium (Mendecki, 2013). However, the transition mechanism which transforms seismic source energy into damage is poorly understood (Ortlepp, 2005). Therefore, rockbursts are classified as unforeseeable, damaging, violent releases of kinetic energy stored within the rockmass (e.g., Hedley 1992; Ortlepp, 2001; Cai & Kaiser, 2018).

The South African mines in the Witwatersrand basin have suffered greatly from rockbursting in the last century (Durrheim, 2010). In 2005, a +5.3 M_L mine-induced event shocked the Klerksdrop goldfield in South Africa, fatally injuring two workers and severely disrupting the nearby town of Stilfontein, causing minor injuries to the inhabitants (Durrheim et al., 2011). The repercussions extended past the managerial estate as the mine went into liquidation, affecting communities as ~6,500 miners lost their jobs (Durrheim et al., 2006). Throughout India's mining history, rockbursts have been occurring in the Kolar gold fields as early as 1902 and persevered throughout the district as mines reached record-breaking depths of 3 km below the surface (Murthy & Gupta, 1983). Mining in the district ceased in 2001, yet seismic events persisted for several years after the mine closure (Adhikari, 2007). Currently, in China, rockbursts in deep

hardrock mines present the most important industrial hazard, where 13,000 incidents have led to 16,000 casualties between 2001 and 2007 (Zhou et al., 2012). First World countries also continue to report fatalities related to mine seismicity (e.g., Potvin & Wesseloo, 2013).

During the last six decades, extensive research emerged from the deepest mines in the world to help alleviate this operational seismic hazard (Ortlepp, 2005). Unfortunately, mines in Australia, Canada, Chile, China, Eastern & Northern Europe, South Africa, and the United States continue to report increasing seismic occurrences as the average mining depth continues to deepen in search of economic ore. The impact rockbursts may have on mining operations translates to fatalities and the loss of equipment, infrastructure, or access to active production areas. The echo of a devastating rockburst commonly forces the mine to retreat into temporary or prolonged shutdowns (Potvin, 2009). Many engineering assessments and redesigns are performed to recover mine health and safety. Consequently, the affected mining operation increases its operational costs, which compromises the overall mining viability in the long term (Cai, 2013). Although global mine fatality rates between 2001 and 2010 seem to be steadily declining, casualties related to rockbursts account for 20 to 30% of the total mine fatalities (Vogt, 2011).

1.2 Engineering Methods for Seismic Control

In practice, seismically active mines have developed different methods to alleviate seismic hazards. Mining engineers commonly apply (at least one of) the following strategies:

1. Strategic mine design and planning.
2. Active ground control procedures.
3. Passive seismic monitoring.

Strategic mine design processes often rely on numerical modelling software to help minimize the seismic energy release for proposed mine layouts. Two modelling approaches are generally used to evaluate these effects: (***i***) the *extraction method* computes the energy generated by specific extraction sequences, and (***ii***) the *combined method* correlates simulated seismicity with recorded events. The Energy Release Rate (Cook et al., 1966), the Excess Shear Stress (Ryder, 1987), and the Rockburst Hazard Index (Esterhuizen, 1997) fall under the *extraction method* for design. The Local Energy Release Density (Wiles, 1998), the modelled Groundwork (Beck, 2000), and the Salamon-Linkov synthetic rockmass method (Malovichko & Basson, 2014) represent the *combined method* for design. Overall, strategic mine design methods allow

engineers to manage stress migrations in abutments (such as pillars or mining fronts) and assist in selecting the adequate mining sequence which limits the seismic energy release. These models can be further joined with structural geological information to help identify seismically active faults. To fully exploit these numerical approaches, the mine must have a good understanding of the primary seismic source mechanism. Successful designs significantly increase mine safety and decrease (unplanned) production interruptions.

Active ground control procedures rely on intentionally yielding (fracturing) the rockmass to shed high stresses into the abutment — this changes the stress state in the affected area. Two general methods attempt to reduce mine-induced stresses: by (***i***) preconditioning or destress blasting of development drifts and pillars, and (***ii***) fluid injections of geological discontinuities. The first approach relies on strategically placing down-the-hole explosives to fracture the rockmass before it has reached its critical strength state. This is achieved by sufficiently fracturing the rockmass (termed preconditioning) or successfully fragmenting the rockmass (termed destressing). In both cases, the affected area sheds stresses while dissipating energy along new fracture surfaces (e.g., Blake et al., 1998). These new fractures reduce the overall stiffness of the targeted volume. Practical considerations need to be evaluated before attempting rockmass destressing (Andrieux, 2005; Zhou et al., 2020). Practice also suggests that preconditioning a highly confined pillar dislodges mated discontinuities rather than generating blast-induced fractures (Board & Fairhurst, 1983). The second approach employs the injection of high-pressure fluid into known fault intercepts to stimulate slip at a predetermined time (when workers are out of the stopes). The injected fluid reduces the clamping (normal) stress acting on the structure, allowing the active shear to reach the Coulomb slip criteria and triggering a seismic release. Practice suggests that fluid injection is strenuous as the fault topography is seldom understood (Board et al., 1992). Additional practical considerations need to be evaluated before attempting hydraulic stimulation (Schmidt, 2018). Ground support systems can also be employed to provide additional coverage against seismicity, such as installing dynamically rated bolts (e.g., d-bolt from Normet, mdx-bolt from Sandvik) with deformable mesh (e.g., chain link mesh, rockstop mesh from Epiroc). Dynamic reinforcement provides a higher load-to-strain rating than its quasi-static counterpart, while the mesh performs work by absorbing rockmass bulking during rockbursts. In practice, seismically active mines tend to increase the dynamic demand of ground support proportionally to the seismic output, as was observed at Vale's Creighton, Copper Cliff

and Coleman mines (Morissette, 2015). Successful ground-yielding bolts combined with adequate dynamic support systems significantly reduce daily exposures to seismic hazards at mine sites.

Passive seismic monitoring protocols scrutinize the daily seismic outputs recorded by the local seismic array. Techniques derived from crustal seismology enable mine engineers to identify hazardous seismic patterns around mining sectors (Mendecki, 2013). This method allows for continuous monitoring of the rockmass and enables to infer seismic source mechanisms. Several practical passive retreat protocols have been developed in South African mines (e.g., Mendecki, 1993), as well as re-entry protocols into active seismic headings (RASIM, 2022). The passive monitoring method depends on high-quality data, which requires reliable seismic system upkeep through annual maintenance and relies on capital-intensive sensor array expansions.

1.3 Evolution of Seismicity with Mining Depth

Several mining factors impact mine-induced seismicity, which can be broadly grouped into three categories (Hudyma, 2004), namely: (***i***) geological, (***ii***) geomechanical, and (***iii***) operational. **Geological** factors include rock units (formations) and surface characteristics of structures. **Geomechanical** factors account for the magnitude and orientation of in-situ stresses with the rockmass strength characteristics (elastic & friction response, strength and post-yield behaviour). **Operational** factors encompass the mining method, layout, and sequence, as well as the extraction rate. Other considerations include mining depth, mining width, total extraction length, and the persistence, surface planarity and offsets of discontinuities (Salamon, 1993). The magnitude of observed stope closure has also been linked with seismic occurrence (Jager & Ryder, 1999). All these factors amplify the seismic output at a mine, individually or collectively. Consequently, no fail-safe mining procedure stops seismicity (Hedley, 1992).

As global mineral extraction rates steadily increase, underground mines will continue to deepen their mining horizons through gradually increasing ground stresses. During the transition from medium mining depth (typically set at 1 km) to deep mining conditions (> 2.25 km), South African practice (COMRO, 1988) dictates that induced seismicity increases proportionally with mining depth in tabular orebodies. Strikingly, the turn of the century has seen a growth in (active) deep mines in other countries like Canada and the United States (Mining Technology,

2019). In addition, many deep mines have proven and probable ore reserves below their current mining depths. Such is the case at the Lucky Friday (LF) mine, where the present mining depth in the Gold Hunter deposit (GH) has reached the 6500 mine level, resting at ~2.29 km below the ground surface. The recently completed #4 Shaft project has been developed to reach ~2.92 km depth, securing access to the deeper production levels while potentially extending the mine life by 20–30 years (Hecla, 2022; Sturgis et al., 2017). As the mining industry prospects to develop stoping operations to depths below 2.7 km, these ultra-deep operations will pose new challenges in ventilation, material handling, health and safety, rock stress, and risk management (UDMN, 2019). Regarding the latter, ground control practices continue to evolve steadily, yet the opposing nature of rockbursting and seismicity might eventually limit operations' incentive to mine deeper (Ortlepp, 2005).

Therefore, seismically active mines, such as the Lucky Friday, are continuously subjected to the following question:

How will the seismic hazard evolve as the mining front deepens?

The effects of mining depth govern many cited factors contributing to increases in seismicity (Jager & Ryder, 1999). The rockmass response to mining changes visibly with depth as stress fracturing and stope convergence increase at the working face. The mining scale is another effective compounding measure of seismic intensity. Empirical data collected at various mining operations suggests a correlation between the largest mining dimension and the maximum recorded magnitude (Figure 1.1). Note that the enlarged markers represent mining operations. For underground operations, the spatial dimensions can vary between 4.5 m (equivalent to the height of a standard development drift) to ~27 km in strike length (an extensive tabular mine operation), with resulting magnitudes ranging between -2 M_L and +5 M_L. Hecla's Lucky Friday mine (LF & GH) and the Star mine (SM) were inserted into the figure for reference. Unfortunately, this empirical relationship does not provide insight into the event type, time of occurrence, or event location and how the GH will evolve as mining deepens.

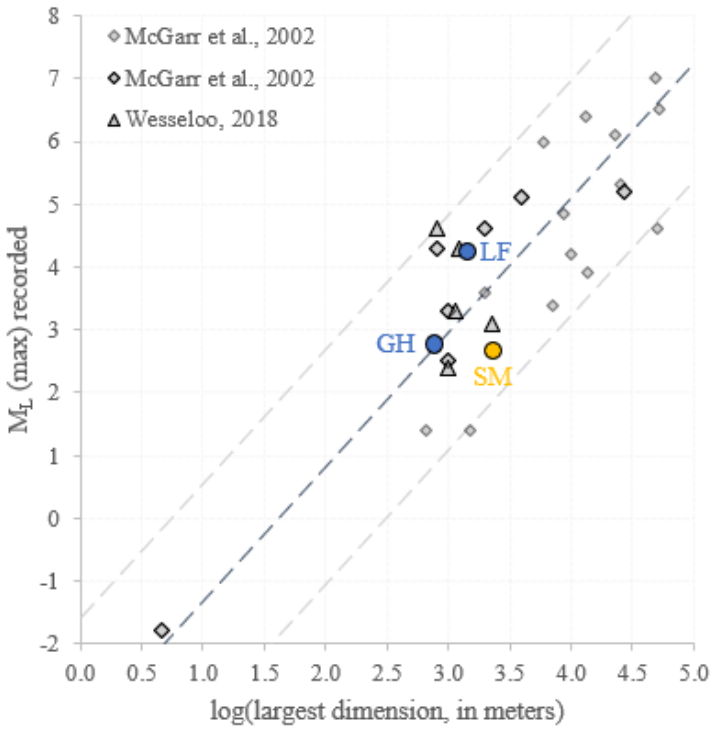


Figure 1.1: Relationship between the largest mining dimension and the maximum recorded magnitude event at the GH, LF and SM (compared with results reported in McGarr et al., 2002 & Wesseloo, 2018).

1.4 Developing a Deterministic Approach to Forecast Seismicity

In this thesis, a new approach to numerically forecast mine-induced seismicity, derived from mine-wide seismic and production records, was developed to assist engineers in stope and mine design. The approach assumes that the (stochastic) seismic variability output by the rockmass is due to the (deterministic) effect of induced stresses and displacements acting on the preferential seismic source release. By zoning the production (stoping) areas into discrete adjoined volumes, available seismological processes based on the magnitude-time-location relationship with mining provide insight into the primary source mechanism. Then, simple elastic numerical methods simulate the rockmass response (i.e., stresses and displacements) to geometrical changes (extraction layouts and tonnages). Finally, the stochastic nature of the seismic response (e.g., Gutenberg-Richter Frequency Magnitude relation) was used to calibrate the numerical input parameters as well as bound the numerical results, providing techniques to quickly evaluate probable seismicity for different mine layouts and extraction sequences. The generated outputs

are seismic energy (E_s), seismic moment (M_o) and moment magnitude (M_w), analogous to those recorded by a digitizing seismic system. Time dependence through rockmass creep was ignored.

In this pursuit, a mine-wide case study was made at the tabular Gold-Hunter (GH) deposit of the Lucky Friday (LF) mine, owned and operated by Hecla Limited since 1964. Mine-induced seismicity constitutes an inherent rock mechanic challenge at the mine, which has persisted since the 1960s. Seismicity was first recorded in the LF deposit after mining progressed into the deeper, harder quarzitic rock of the brittle upper Revett Formation. In the late 1990s, the mine was ramping down production in the LF sector due to increased large seismic occurrences. Therefore, efforts turned toward the GH deposit in 1997, where the top of the continuous narrow-vein orebody rests ~1.6 km below the surface in the ductile Wallace and St-Regis formations, with mining proceeding by overhand/underhand cut-and-fill. Seismicity finally emerged from the GH in late 2007 and continued since. Until 2021-year end, over 195 large seismic events (> +1.5 M_w) have been recorded within the GH at an average mining rate of ~800 ore tons per day. As the mine embarks on another 20+ years production plan, increasing the mining depth from ~2.3 km to ~2.9 km below the surface, practical processes to forecast seismic risk need to be developed. The GH case study presents a unique opportunity to assess a mine-wide seismic response of a tabular hardrock deposit by analyzing its behaviour since mining began.

The objectives for this thesis are explicitly listed in Table 1.1.

Table 1.1: Thesis objectives

Global objective:	Create a practical numerical process to evaluate the seismic response of the Gold Hunter deposit as mining progresses, where the output is directly relatable to those produced by a digitizing seismic system.
Secondary objectives:	Use established seismological concepts to identify, quantify, and classify the primary seismic source mechanism.
	Correlate elastic numerical rockmass responses (stresses & displacements) with operational and seismic records, which calibrate and constrain the analyses.
	Test the validity of the design processes for subsequent mining periods, which were affected by a reduction in the mining rate and a significant change in the mining method.

First, the primary cause of seismic activity in the GH was investigated using established seismological concepts. Notable events (≥ +0.5 Mw) from 2013 to 2016 were analyzed based on their magnitude, time, and location. This mining period was chosen because of reliable seismic records following a mine-wide upgrade to a digital monitoring system in 2013. The analysis outcome indicated fault-slip as the source of the seismic activity.

Second, to numerically analyze the impact of production in the GH, a three-dimensional elastic Boundary Element Method (BEM) code was utilized to calculate the stresses and displacements imposed by geometrical layout changes from 1997 to 2016. The input properties for the rockmass (Young's modulus & Poisson's ratio) were incrementally reduced from laboratory values until a reasonable match was obtained with measured in-stope wall-to-wall closure records performed by NIOSH (National Institute of Safety and Health) before initiating this study. The Energy Release Rate (ERR) concept, as proposed by Cook *et al.* (1966), was integrated into the numerical code at the mine-scale level. The ERR was computed on annual extraction increments, where the results were linked with seismic records (1997–2011 & 2013–2016) and compared with South African practice to obtain an empirical design chart for the Gold Hunter. The Excess Shear Stress (ESS) concept was adapted to assess the notable events recorded between 2013 and 2016, where stresses (resulting from annual extraction) were mapped onto the event coordinates and tested for slip initiation (confirming slip on >50% of the events). Subsequently, a numerical slip assessment scheme was established for known fault orientations subjected to changing mine layouts. This was achieved by calibrating the frictional properties of discontinuities in a Discrete Fracture Network, developed by Itasca from detailed field mapping in the GH, by correlating a synthetic GRMF plot with the recorded GRMF. This numerical scheme increased confidence in the fault-slip analysis and evaluated the seismic potential for the mine layout.

Finally, two subsequent mining periods (2017–2019 & 2020–2021) were validated against the empirical design chart. These periods were observed to have produced less seismicity due to likely operational changes. The unspecified DFN ESS analysis was used to shed some light on the seismic response where a specific mine geometry was run under variable extraction rates (simulating a change in mining method) with the seismic outputs (E_s, M_o, M_w, including location) compared with actual events on the vein. This analysis showed that simulated seismicity was reasonably well forecasted.

The Venn diagram illustrates how the different seismic disciplines overlap in this study (*Figure 1.2*). The study progresses from determining the seismic source to validating the seismic simulations to constraining the numerical results. The middle intersect highlights the seismic potential, achieved by combining all relevant domains of mine-induced seismicity. Therefore, although this study focuses on understanding the seismic response in the GH through extensive case studies, the methodologies developed herein are transferable to other tabular hardrock, narrow mines and allow to probe the mining environment for fault-slip.

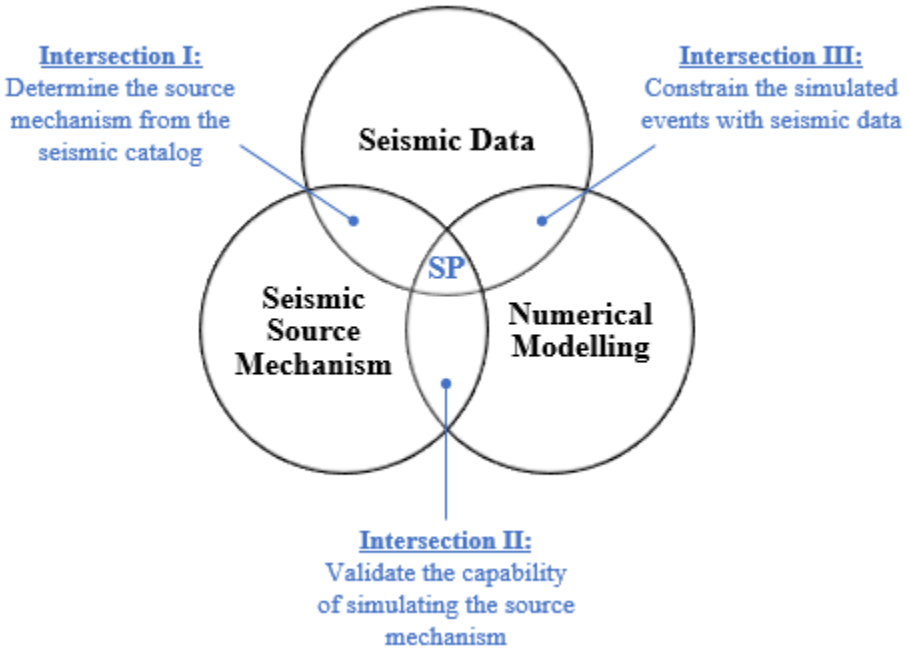


Figure 1.2: Venn diagram for evaluating the Seismic Potential (SP)

1.5 Summary of Thesis Content

The main chapters in this thesis are briefly described below:

CHAPTER 1 — defines the context, objectives, and methods developed throughout this research for assessing seismic risk for deepening mine settings.

CHAPTER 2 — provides the literature background necessary to understand the impact of mine-induced seismicity, investigates the procedures for determining seismic source mechanisms, and validates the state-of-the-art in numerical assessments of rockmass-seismic response.

CHAPTER 3 — introduces the seismicity at the Lucky Friday mine, specifically in the Gold Hunter deposit, where the mine, geological, and geomechanical settings are presented along with the complete seismic history and a general overview of relevant case studies (i.e., lag-time study, stope closure measurements, and backfill performance studies). Preliminary numerical stress and closure analyses developed for this thesis are also presented.

CHAPTER 4 — establishes the core connections between seismic source mechanisms, numerical modelling, and recorded seismicity. This chapter presents the assessment strategies of current data for mining periods (1997–2011 & 2013–2016). Procedures for numerical stope closure calibrations are laid out. The energy release rate and excess shear stress analysis are performed and correlated with seismicity to quantify the current mining state. Empirical seismic design charts are derived.

CHAPTER 5 — demonstrates the application of the model to deepening mine settings where both the design charts and the numerical model are tested at deeper mine conditions for two subsequent mining periods (2017–2019 & 2020–2021). A case study is made for a new mining method (Underhand Closed Benching - UCB), which changed (favourably) the seismic response of the rockmass. The models developed in the previous section were used to shed light on the seismic control offered by UCB.

CHAPTER 6 — presents an independent discussion section where the ensemble of the thesis work is critiqued and validated. Model boundaries with their limitations are discussed, and the major findings are highlighted with recommendations for further research.

CHAPTER 2 LITERATURE REVIEW

2.1 Mine-Induced Seismicity

2.1.1 Definition of Rockburst & Seismicity

Throughout literature, the term *rockburst* is often used interchangeably with that of *seismicity*. However, both terms refer to distinct conditions leading to distinct operational hazards (Coates, 1965; Cook et al., 1978; Ortlepp, 1984; Müller, 1991; Whyatt et al., 2002; Gibowicz, 2009). This misperception is primarily due to the variability of mine-induced seismicity, which is physically manifested by (underground and surface occurrences of) strong ground motion, spalling, buckling, crushing and airblasts. In addition, most rockbursts are classified by their seismic source mechanism and magnitude release (Ortlepp, 1992), which adds to the confusion.

Rockbursts produce sudden high-velocity rock projections around mine openings, which can reach (theoretical) velocities above 10 m/s (Ortlepp, 1993; McGarr, 1997). There is no apparent correlation between the amount of damage and the magnitude of an event (Hedley, 1992; Scheepers, 2022). The proximity of the event's hypocentre to the mining infrastructure plays a greater part in generating rockbursts (Ortlepp, 1984). These damaging events form only a small subset (1–10%) of the large events count within a seismic catalog (Salamon, 1993). The mechanism for transitioning from the seismic source to the rockburst is still unclear (Ortlepp, 1992; Cai & Kaiser, 2018). Consequently, rockbursting is amongst the most adverse, misunderstood phenomena that seismically active mines must manage. Therefore, rockbursts are commonly described as unforeseeable, damaging, and violent manifestations (Cook et al., 1966; Hedley, 1992; Blake & Hedley, 2003). On the other hand, seismic events result from unstable failure processes taking place in the rockmass, which releases seismic energy as transient strain waves (COMRO, 1988). Seismic monitoring systems record these waves (Hedley, 1992).

Therefore, ***seismicity*** results from mechanical processes following unstable rock failure through strain, slip, or mixed types, which release stored energy into the rockmass. A ***rockburst*** is the consequence of *seismicity* (i.e., seismic waves), which has the potential to lead to observable (often dynamic) rock movement around mine openings. These definitions are assumed throughout the thesis.

2.1.2 A Brief Overview of the Severity of Mine-Induced Seismicity

The source for mine seismicity appears to be anthropic (Kisslinger, 1976; Simpson, 1986; Wilson et al., 2017). It is not certain when the first mine-induced seismic event occurred, but the earliest documented case of rockburst was in the British Derbyshire lead ore mine in 1738 (Bukowska, 2006). However, there are written accounts of major seismic activity occurring at the Altenberg tin mine in Germany as early as 1640 (Ortlepp, 1984). This suggests that mine-induced seismicity may have been underreported before the 1900s due to the lack of knowledge or technology needed for monitoring, with the first documented cases emerging from South Africa and India. Throughout the last century, the accounts of mine-induced seismicity have become more reliable as government agencies that monitor naturally occurring earthquakes have started to distinguish events related to mining. By supplementing accounts from the literature, Wilson & al. (2017) have compiled 279 confirmed cases across six continents, with Asia presenting the most occurrences, followed by Europe and North America (*Figure 2.1*).

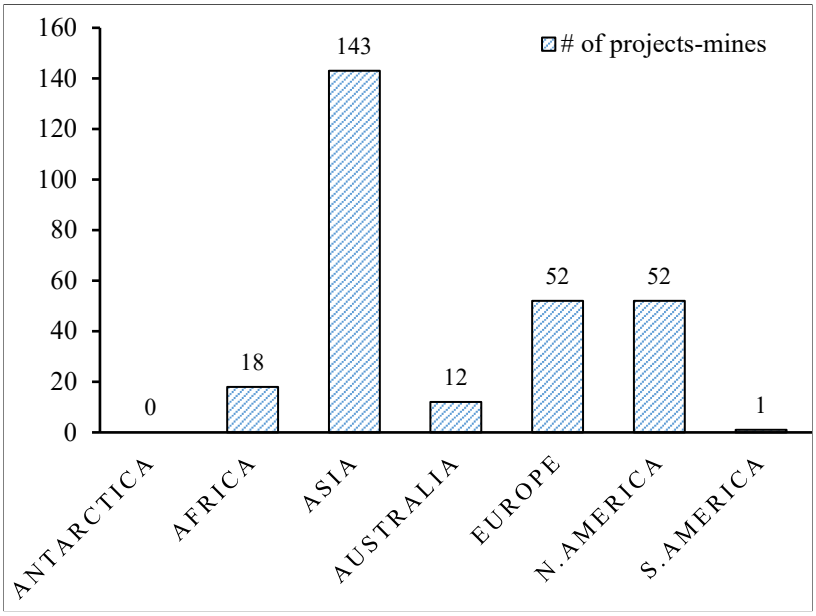


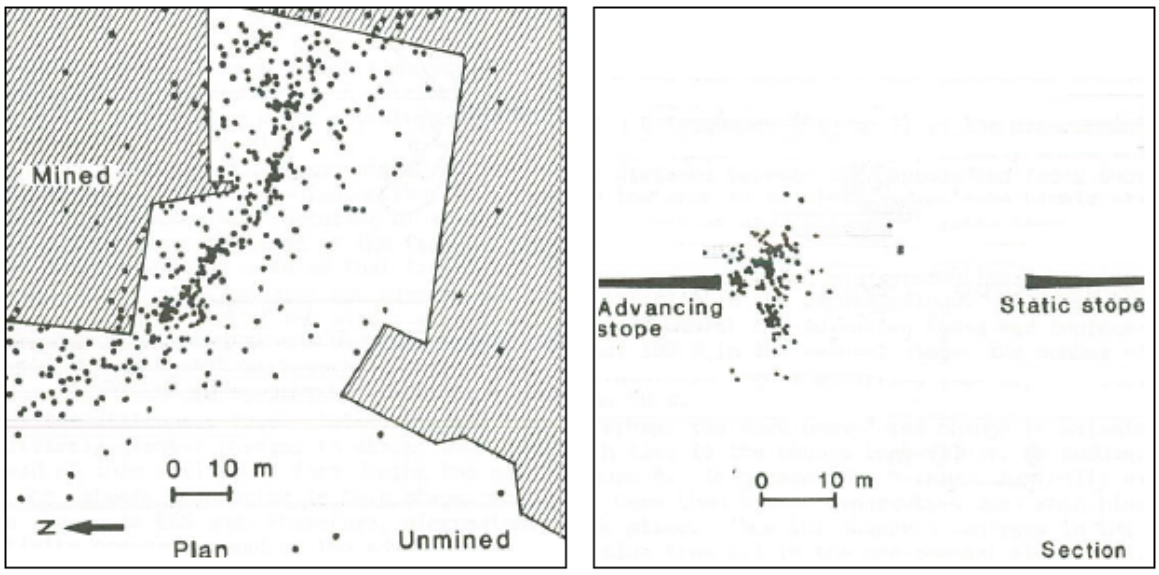
Figure 2.1: Worldwide survey of seismically active mines (n = 279) (Wilson et al., 2017)

2.1.2.1 South Africa — the Witwatersrand Basin

The South African gold mines in the Witwatersrand Basin have suffered greatly from rockbursting for over 100 years (Durrheim, 2010). The reef deposits host several thin tabular underground mines, which have collaboratively extracted a substantial area of the earth's crust.

At peak production during the 1970s, approximately 28 km^2 of tabular orebody was extracted annually from the ground (Ortlepp, 2005). This created extensive flat lateral voids in the quarzitic strata (Cook, 1976). To this day, South African mines represent the most extracted areas in the deepest mines in the world, with depths breaching 4 km below the surface (i.e., the Mponeng mine from Harmony Gold).

In the Witwatersrand Basin, the first documented seismic event dates to 1908, having initiated the first ever rockburst committee (Ophirton Earth Tremors Committee), where the crushing of remnant pillars was recognized as the primary source leading to a mine collapse. In 1939, the first seismographs were installed on the surface and quickly established the relationship between mining activity and seismic occurrences (Gane et al.,1946). This relationship appeared similar throughout the Basin (e.g., Cook, 1963a; McGarr et al., 1975; Spottiswoode, 1984). A close spatial relationship between seismicity and mining activity emerged, such as those illustrated by Legge & Spottiswoode (1987), where seismic activity occurs around the active (leading) mining front (*Figure 2.2*). The vertical extent of seismic influence can also vary significantly between 400 to 2,300 m from the mining front (Lawrence, 1984).



(a) (b)

Figure 2.2: Recorded seismic response (dots) while advancing a single stope on a reef, where (a) shows the plan view, and (b) shows a section view looking east (Legge & Spottiswoode, 1987)

The global mine fatality rates in the South African Mining Industry seem to be steadily improving for the period 2001–2010, with casualties due to rockbursting maintained at 20–30%

of all mine-related fatalities (Vogt, 2011). For 2010–2020, the Minerals Council is reporting a steady rate in the number of fatal rockburst accidents. However, the lack of improvement raises the concern for renewed research efforts and the advancement of technology (Scheepers, 2022).

2.1.2.2 India — Historical Kolar Gold Fields

In India, rockbursts have been occurring in the historical gold mines of the Kolar Gold Fields in the state of Karnataka and persevered through mining in the district as mines were reaching record-breaking depths of ≥ 3 km below the surface. The earliest rockburst record, at only ~290 m below the surface, dates to 1898 in the Ooegaum mine (Murthy & Gupta, 1983). Rockbursts were often classified as *airblasts* or *quakes* to classify them by their intensity and their damage extent (Murthy & Gupta, 1983). It wasn't until after the installation of a seismic system (around 1968) that the rockburst term was notably attributed to damaging events. At the Kolar Gold Fields mines, rockbursting events account for large-scale fatalities, surface damage, loss of shafts and secondary infrastructure, as well as the loss of valuable ore reserves (Murthy & Gupta, 1983). As the orebody is subvertical, with varying widths between 1 and 6 m, mining was performed longwall to some varying degree. Single major rockbursting accounts mention damage on multiple levels with great lateral and vertical extent on several mining levels, known as area-bursts (Miller, 1967). The typical damage succumbed to mine drives following rockbursts is illustrated explicitly in *Figure 2.3*.

The rockbursting temporal pattern suggests the potential for mild bursting every 58 days, while those of major intensity occur every 246 days (Murthy & Gupta, 1983). Seismic frequency analysis indicated momentary seismic clusters (swarms of 20–200 events of low magnitude) in a small volume (~150 m average radius) associated with a characteristic drop in seismic activity prior to a rockbursting event (Krishnamurthy & Shringarputale, 1990). The occurrence of damaging area bursts was generally attributed to a cluster series of 20 to 200 smaller magnitude events in proximity to mine working triggered by a single seismic event ≥ +3 M_L (Karekal et al., 2005). Seismicity was also located in the shallow porting of the Kolar Gold Fields (Subbaramu et al., 1985). The mines have been marked by major rockbursting events in 1952, 1956, 1960, 1962, 1963, 1966, 1971, 1972, 1983 and 1985, with the largest rockburst following a +5 M_L seismic event (Guha, 2013). Mining in the district has ceased since 2001, yet seismic events are still being recorded on the surface, most noticeably during rainfall (Adhikari, 2007).

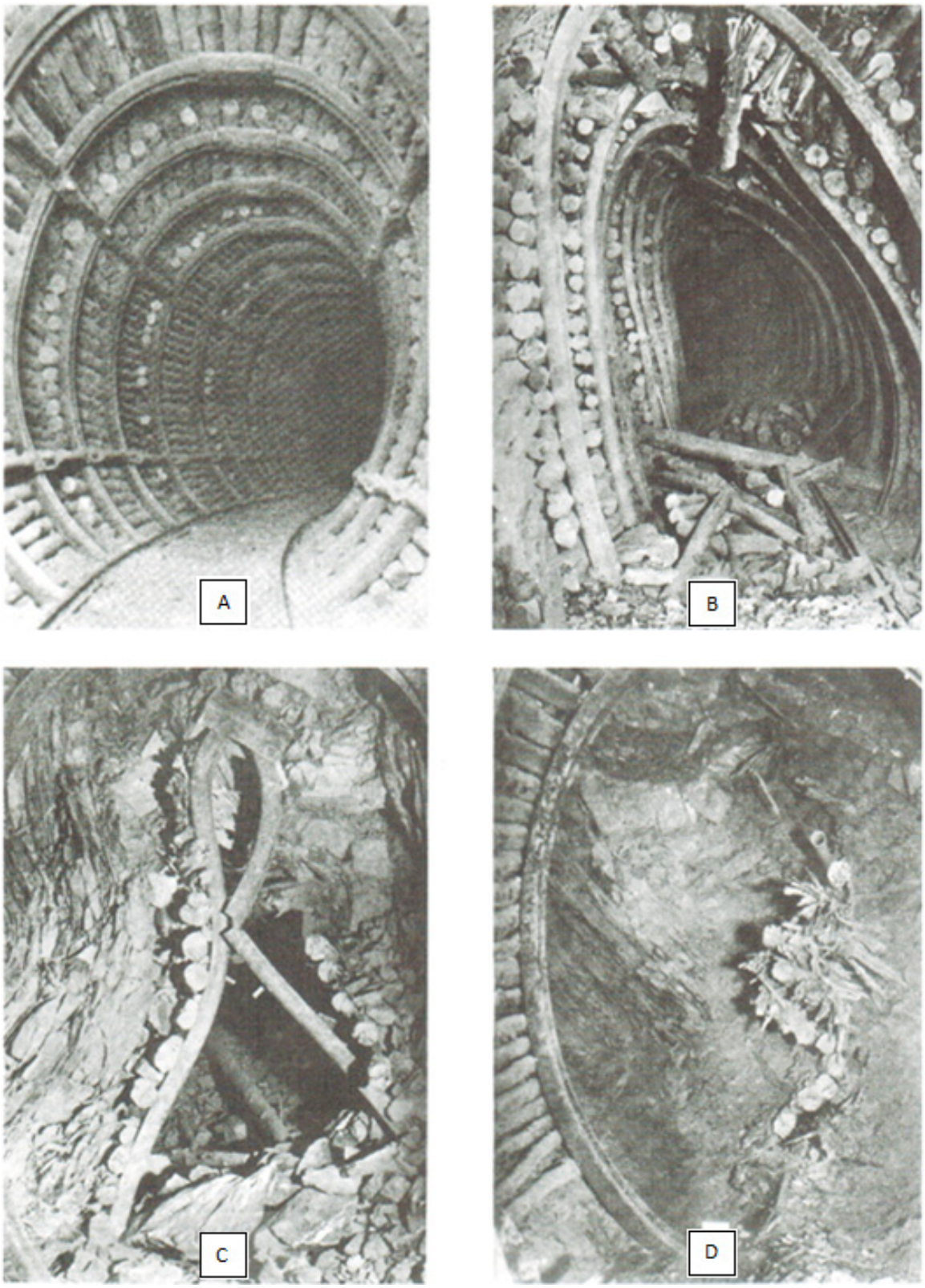


Figure 2.3: Increase in rockburst damage observed at the steel-set reef drive in the Champion Reef Mine of the Kolar fields, India (Fairhurst, 1990, after Caw, 1956)

2.1.2.3 Canada — Underground Hardrock Mines

The historical Kirkland Lake mines had a notorious history of bursting incidents, which made them the most prone to such accidents in North America (comparable to the Coeur d'Alene mining district). The largest recorded event in Canadian history, which measured +4.4Mn, occurred at the Lake Shore mine in 1939. Although rockbursting resulted in over 40 casualties in that mining district by the turn of the century, practical research has helped soften the rockburst-related fatalities trend since 1940 (Blake & Hedley, 2003). Since the 1990s, the research generated in collaboration with the Canadian mining industry has produced several practical guidelines for improving safety in seismically active mines (i.e., Hedley, 1992; Kaiser et al., 1996; Cai & Kaiser, 2018).

Recently, Ollila (2021) compiled mine-related events for Canadian operations between 1985-2021, utilizing data gathered from Earthquake Canada. Ollila noticed that the last decade (2011–2021) saw the average release of events ≥ +3 Mn increase to 8.7 events per year when compared to the historical average of 3.2 of the previous decades (1985–2011). LaRonde (Agnico Eagle), Kidd Creek (Glencore) and Creighton (Vale) accounted for about 50% of the registered large events in the catalog. These mines correspond to the three deepest operations in Canada and reside amongst the top ten deepest in the world (Mining Technology, 2019). Hudyma *et al.* (2017) identified 25 seismically active mines across Ontario (18 out of 26) and Quebec (7 out of 10) in 2016. This data indicated that 70% of active hardrock underground mines in eastern Canada rely on seismic monitoring.

2.1.3 Factors Affecting Mine Seismicity and Rockbursts

Several factors influence the degree of seismic release in a mine environment, such as mining depth and geometry, extraction ratio, and mining rate (Gibowicz & Kijko, 1994). In addition, inherited geological conditions such as rock stress, rock strength, and frictional properties of discontinuities, along with their occurrence in space, have also been linked with increased seismic occurrences (COMRO, 1988). These factors are grouped into operational or geological-geomechanical characteristics. Mining takes place within the rockmass which holds these parameters, forcing an effect on the seismic response. Although seismicity may appear similar within a mining district, the seismic intensity varies within the district mines (Blake & Hedley,

2003). Therefore, there does not appear to be a single explicit parameter that unfailingly reduces the severity of seismicity other than ceasing mining itself (Gibowicz, 2009).

Looking at practice, the Lapa Mine (owned by Agnico Eagle) is a narrow-vein deposit that hasn't experienced significant seismic activity, unlike its seismically active neighbouring mines, LaRonde (also owned by Agnico Eagle) and Westwood (owned by IAMGOLD). The three mines are located along the Cadillac-Larder Lake fault zone in the Abitibi region, Québec, and employ the long-hole mining method. This behaviour hints at the possible impact variation in geology has on seismic release.

Mine seismicity displays a stochastic appearance due to these complex interactions with the mining layout. This makes prediction (if possible) a statistical problem rather than a deterministic foreseeable outcome (Salamon, 1983). However, if seismic failure is limited to volumetric strain and fault-slip, a practical forecasting procedure can be achieved by coupling operational with geological parameters. Unfortunately, many of the geological parameters will need to be estimated.

On the other hand, rockbursts damage relates to mining factors such as excavation profiles, drift stand-up time, support type, installation quality and the weakening of support through mine cycles. Many authors have extensively studied these factors (e.g., Kaiser & Cai, 2012; Stacey, 2012; Morissette et al., 2017). Additionally, the direction of the excavation with regard to the inherent geological foliation is observed to have an impact on damage from seismicity (Turcotte, 2014). The magnitude of seismicity does not necessarily correlate with damage (McGarr, 1981); however, Kaiser *et al.* (1996) have identified the Peak Particle Velocity (PPV) generated during the event to contribute to the source of damage. Rockburst severity is mainly influenced by the mining practices employed and is considered a unique field of study that focuses on the excavation's ability to absorb kinematic energy. This is different from seismicity, which deals with the causes of seismic activity. Hence, rockbursts depend primarily on the dynamic loading of the mine (Tannant et al., 1995).

2.1.4 Rockbursts & Seismic Classifications

Engineers have an inherent trait of classifying phenomena to aid in their comprehension. Several empirical classifications for rockbursts and seismicity have been developed in the last decades.

Their underlying seismic source mechanism usually categorizes rockbursts. Hasegawa *et al.* (1989) suggest likely seismic sources observed in practice (*Figure 2.4*). Half of these six possible rockbursts result from volumetric strain (including relaxation) or from double-couple shear-type events. Hedley (1992) also proposed to classify rockbursts based on their seismic source mechanism: (***i***) strain-bursts, (***ii***) fault-slips, and (***iii***) pillar-bursts. ***Strain-bursts*** tend to correlate with induced volumetric failure in proximity to the mining front, with the rockburst showing small fragmentation. ***Fault-slips*** can either be induced or triggered events on discontinuities, with the rockburst resulting in larger fragmentation. ***Pillar-bursts*** present a unique environment due to the complex stress distribution inside the core, impacted by the width-to-height ratio, resulting in an expulsion of mixed fragmentation.

Ortlepp (1992) identified five rockburst types with their inferred seismic source mechanisms, possible wave characteristics and specified their magnitude ranges, see Table 2.1.

Table 2.1: Suggested rockburst type based on seismic source (Ortlepp, 1992)

Rockburst Type	**Postulated Source Mechanism**	**First Motion from Seismic Records**	**Richter Magnitude M_L**
Strain-bursting	Superficial spalling with violent ejection of fragments	Usually undetected, could be implosive	-0.2 – 0.0
Buckling	Outward expulsion of large slabs pre-existing parallel to surface of opening	Probably implosive	0.0 – +1.5
Pillar or face crush	Sudden collapse of stope pillar, or violent expulsion of large volume of rock from tabular stope face or tunnel face	Possibly complex, implosive and shear	+1.0 – +2.5
Shear rupture	Violent propagation of shear fracture through intact rockmass	Double-couple shear	+2.0 – +3.5
Fault-slip	Sudden movement along existing fault	Double-couple shear	+2.5 – +5.0

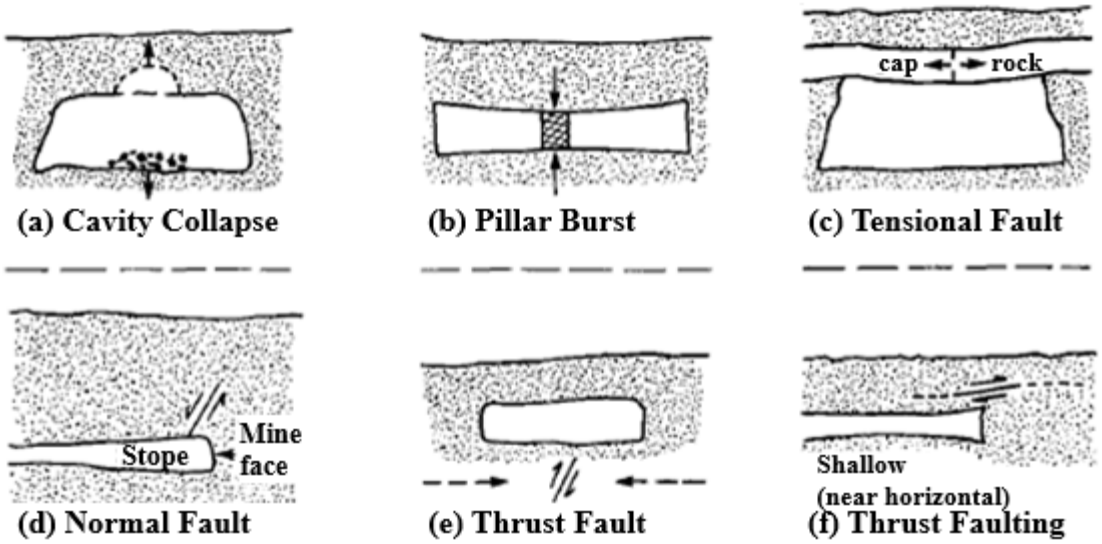


Figure 2.4: Schematic diagram of six seismic mechanisms (Horner & Hasegawa, 1978)

These rockburst classifications infer a seismic source but have a limited understanding of rockmass failure in the absence of damage. They were derived from observable damage case studies. In practice, the seismic source is often classified on magnitude.

A seismic event classification relates to the spatial-temporal relation between events and the mining front (McGarr et al., 1975; Stiller et al., 1983). In general, the effects mining has on seismic occurrence are subdivided into two broad types (Gibowicz & Kijko, 1994): (***i***) induced, and (***ii***) triggered responses. ***Induced*** seismic events result from a direct impact caused by a production blast or a large stress change induced in the rockmass, producing *instant* low–medium magnitude releases. These events are located in proximity to the active mining front (< 100 m). The number of induced seismic events is affected by the mining scale, discontinuity characteristics (spacing, count, orientation) and the mining rate. ***Triggered*** seismicity results from the global mining impact where compounded changes of incremental stresses eventually disrupt the volumetric or fault equilibrium, producing a *latent* upper magnitude release. These events locate generally outside the mining front (> 100 m). In addition, triggered events tend to be independent of mining activities such as blast-time. This characteristic greatly increases the seismic risk since the time-frequency responses appear erratic and difficult to plan against (Hudyma, 2010). Unfortunately, this seismic grouping remains empirical as it only infers the seismic source mechanism.

2.2 Seismic Source Mechanisms

This survey defines the *seismic source mechanism* as the mechanical process that enables the release of strain energy (seismic waves) within the rockmass. Mining subjects the rock boundary to continuous and dynamic stress changes, allowing for closure and the release of energy during extraction (Cook & al., 1966; Salamon, 1984). This process can lead to stable (crushing, fracturing or heating) or unstable rockmass failure processes (explosive, implosive or slip), resulting in mine-induced seismicity (Cook, 1965b; Salamon, 1983; Brady, 1990). Based on the volumetric strain theory, seismicity arises from non-linearity in the material response to loading and post-peak stiffness contrasts during failure (Cook, 1965a; Linkov, 1992). Based on contact-slip discontinuity theory, seismicity arises from slip on pre-existing faults in response to stress changes (Ryder, 1987; Salamon, 1993). These instabilities are similar to a certain extent as they release strain energy from some volume of stressed rock (Ortlepp, 1984). As will be seen, the mechanical instabilities arise from distinct physical processes. Understanding the seismic source mechanism provides insight into potential damage mechanisms of rockbursts (Ortlepp, 1997), which are explored in this section. First, the rock behaviour under various laboratory conditions for intact and discontinuous rock is presented. Second, the energy balance theory is described as derived from South African research (Cook et al., 1966; later refined by Salamon, 1984) as well as fault slip release (Ryder, 1987 & 1988).

2.2.1 Failure of Rock

2.2.1.1 Strength & Deformation Characteristic of Intact Rock

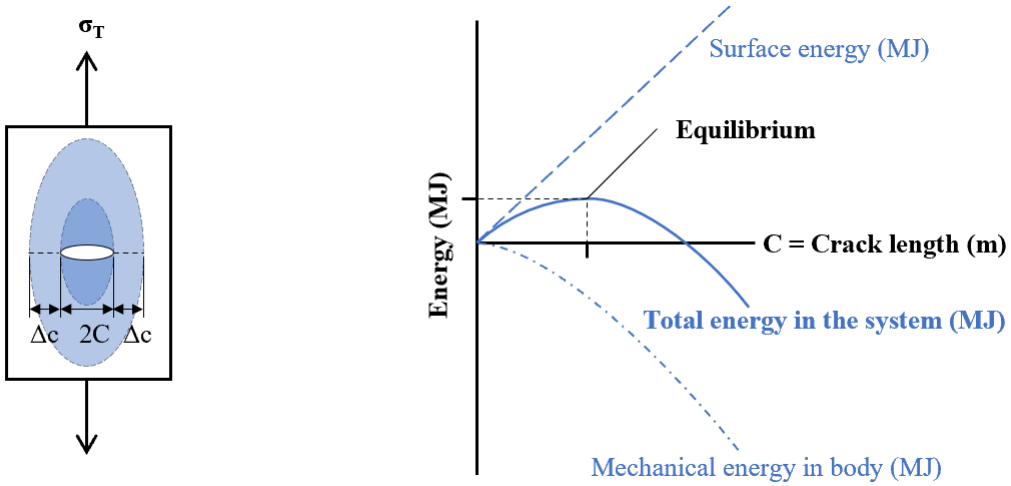
2.2.1.1.1 A Mechanistic Approach

On a microscopic scale, rock material constitutes an amalgam of various solid grains of minerals fastened together by intermolecular bonds. The strength of rock, as a material taken on an atomistic level, is attributed to the quality of these bonds, which can be weak or strong. For a laboratory-scaled rock sample, if enough bonds fail along a preferential plane or orientation, separating the specimen in at least two pieces, the sample is considered broken, although some residual strength can still be mobilized by frictional forces on the plane of failure. In reality, the measured peak strength observed in rock is several orders of magnitude lower than the theoretical

interatomic cohesive strength of the *pure* material (Fairhurst, 2004). This discrepancy brought about by the atomic theory of matter was first treated by Griffith in his theory of brittle fractures (1921; 1924). Griffith (1921) postulated that the weaker strength observed in isotropic solids was due to the existence of inherent sub-microscopic flaws (i.e., open ellipsoidal cracks), which lowered the materials' strength by 10 or 20 times when compared to the inter-atomic cohesive stress. As the material is mechanically loaded, the flaws produce amplified stress concentrations at their tips, which allows a crack to expand across the element while lowering the material's mechanical energy (this is Griffith's energy balance for crack propagation). The rupture mechanism, therefore, involves two key processes (Fairhurst, 2004): (**i**) a stress condition (or available mechanical energy in the solid), and (**ii**) an energy condition (the required energy to create new fracture surfaces). In addition to the intrinsic material properties, the strength of rock specimens reflects the variation (in orientation, density and length) of these dislocations within the fabric of the solid (Hoek & Bieniawski, 1965).

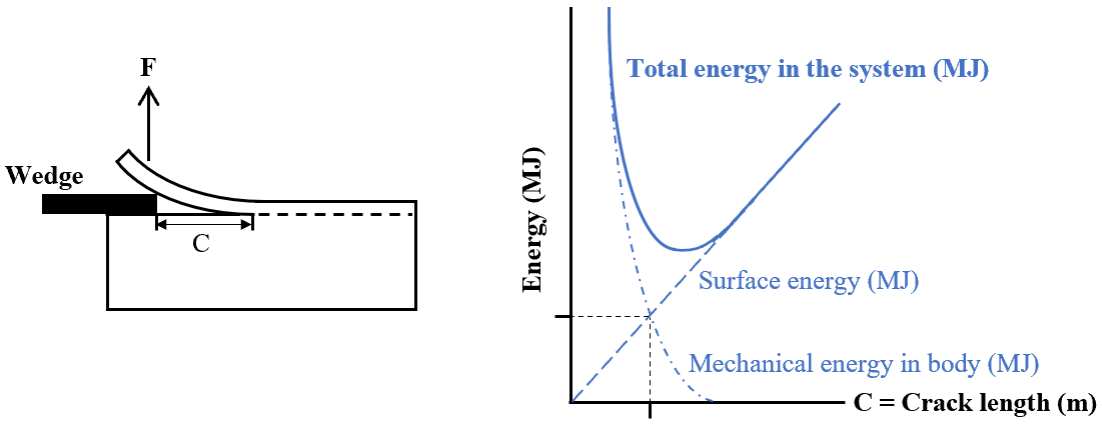
For a single flaw in an elastic glass rod subjected to uniform extensional stress, Griffith (1921) demonstrated the possibility that a minimal constant extension force could break the superior resistive atomic bonds (*Figure 2.5*). By applying Inglis's (1913) analytical solution in an elastic medium for stress concentrations around an elliptical hole (Fairhurst, 2004), Griffith determined that enough tensile stress (σ_t) develops at the tip of the flaw to generate new fracture surfaces. The magnitude of the stress concentration arises solely from the geometry of the ellipsoidal flaw (e.g., the ratio of the crack length, 2C, to the radius of curvature at the tip) and not by its actual area. These stresses increase as the crack length increases. To propagate a fissure, Griffith (1921) postulated that energy must be supplied to rupture enough atomic bonds to coalesce into distinct surfaces within the material (forming two distinct surfaces), representing the surface energy. Under Griffith's boundary conditions, where the tensile force is constant while the displacement is not (allowing for mechanical work), mechanical energy decreases as surface energy increases during crack extension. Griffith's (1921) model for crack propagation in a rod suggests that a maximum stress level exists at the equilibrium between these two opposing energies. Upon reaching this equilibrium (or critical crack length), the crack will propagate instantly without additional load, failing the sample (Fairhurst, 2004). See Scholtz (2019) for additional details.

In contrast, by assuming a boundary condition of constant displacement and not one of constant stress, Obreimoff (1930) achieved stable crack propagation in mica cleaving experiments (*Figure 2.6*). Therefore, the loading system controls the specimen's rupture response rather than its ability to store energy (Scholz, 2019). The loading condition can be arranged to be stiffer than that of the sample, allowing for stable crack growth.



(a) (b)

Figure 2.5: Schematic representation of Griffith's model of (a) crack propagating in a rod under constant tensile strength, and (b) the associated energy distribution (Scholz, 2019)



(a) (b)

Figure 2.6: Schematic representation of Obreimoff's mode for (a) mica cleaving, and (b) the associated energy distribution (Scholtz, 2019)

Subsequently, Griffith (1924) extended his theory of brittle fracture to include a biaxial compression stress field, in which he suggested that the ratio of 8:1 (uniaxial compressive to tensile strength) leads to unstable failure. This does not agree with laboratory measurements, which report greater uniaxial strength for rock specimens (e.g., Brace, 1964; Hoek & Bieniawski, 1965). By assuming that the elliptical crack would not close, and that unstable failure would arise after reaching equilibrium, Griffith misrepresented the theorem of minimum potential energy (Fairhurst, 2004). Griffith inadvertently predicted tensile rock fracture initiation at about 40–60% of the compressive strength under low confinement (Hoek & Bieniawski, 1965). An elliptical crack under compression differs in process since the crack does not rupture along its plane but rather develops a tensile crack close to its tip, propagating along the principal stress direction irrespective of flaw orientation (Hoek & Bieniawski, 1965). Confinement provided by the principal minor stress plays a critical role in tensile crack propagation and length. In the range of ($\sigma_3/\sigma_1 \geq 0.2$), tensile propagation suppresses completely (Hoek & Martin, 2014). In addition, when compression progresses, the closure of the elliptical crack incurs an additional shearing mechanism. Hence, tensile fissures on flaws and shearing on grain bonds are the two mechanisms that lead a rock sample to its peak compressive strength. Therefore, the actual mode of rock failure in uniaxial compression is in shear or in tension (Jaeger et al., 2009), not in compression itself (compressional rupture does not actually exist in welded rock — Fairhurst, 2004). For rocks, these inherent Griffith flaws constitute the material matrix. Dislocation around the microscopic contacting grain boundaries is analogous to shear of macroscopic discontinuities (Paterson & Wong, 2005).

Other than the basic elastic material properties (Poisson's ratio & Young's modulus), the strength of a rock specimen results from the variation (in orientation, density and length) of these dislocations within its fabric (Hoek & Martin, 2014). During uniaxial and triaxial compressive testing of rock, slip on these flaws causes a deviation from the linear elastic material response and induces (most often) microseismicity at the lab scale.

Martin & Simmons (1992) recorded a significant amount of acoustic emission during compressional testing of Lac du Bonnet granite and correlated them to crack initiation processes within the specimen (*Figure 2.7*). Acoustic emissions (AE) emerge at ~40–60% of the peak strength and increase at ~70–90% of the peak strength, where unstable crack growth leads the sample toward failure. Many authors have related AE to microseismicity at the mine scale (e.g.,

Hardy, 2003). In mines, microseismicity (M < 0.0) indicates fracturing or stress transfers within the rockmass and not necessarily hazardous conditions such as those imposed by notable seismic events (M ≥ +0.5) (McMahon, 1988). For a hardrock rockmass (ignoring creep), failure cannot arise in the stable crack grown. It is upon reaching peak strength that unstable conditions arise within the specimen, which leads to violent-dynamic ruptures in brittle samples. This peak strength behaviour provided the first insight into the relationship between the strain energy release and the failure mechanism of rock (Cook, 1965a). The post-peak response will be discussed later.

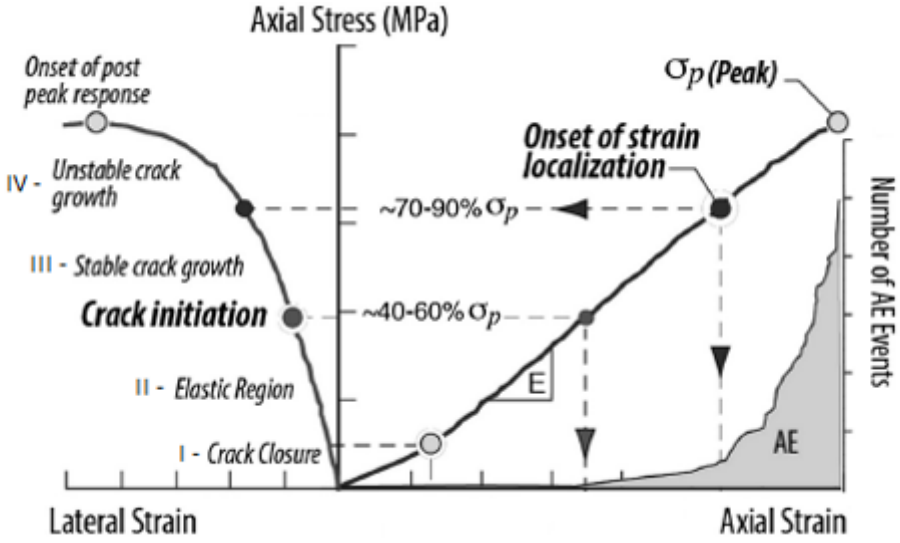


*Figure 2.7: Four stages of crack progression under compressive test, where stage **(i)** crack closure, **(ii)** elastic region, **(iii)** stable crack growth, and **(iv)** unstable crack growth (after Martin & Christiansson, 2009)*

2.2.1.1.2 Failure Criterion Approach

Rock is a frictional-cohesive material that develops shear resistance with increased biaxial stress loading (Drescher & Fairhurst, 1987). At a constant normal stress state (σ_n), the shear strength (τ) remains at peak strength but increases with applied confinement (σ_3). This characteristic contributes to greater strength of rock in compression than in tension. In its simplest form, shear strength of rock follows a linear Mohr-Coulomb strength criterion derived from cohesionless soils by adding a *cohesive* (C) component (Scholz, 2019).

$$\tau = C + \sigma_n \cdot \tan(\varphi) \qquad 2.1$$

where: τ = shear resistance along the rupture plane [Pa]

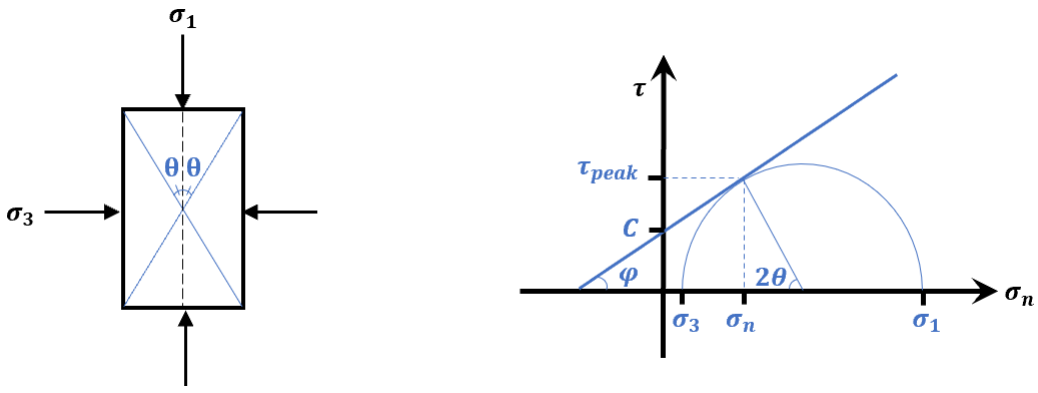
C = cohesion [Pa]

σ_n = normal stress [Pa]

φ = friction angle [°]

As a rock sample is loaded to failure in a biaxial stress field (with σ_1 increasing), two (theoretical) conjugate shear failure planes appear, and the relationship between stress and failure orientation is characterized by the failure envelope (*Figure 2.8*). The Mohr circle illustrates the material's stress condition leading to failure as it touches the linear rupture envelope at peak shear strength. The acute failure angle (θ), taken between the conjugate failure plane and the direction of applied principal stress, relates to the angle of friction (φ), an intrinsic material property of rock:

$$\theta = {}^{\pi}/_{4} - {}^{\varphi}/_{2} \qquad 2.2$$



(a) (b)

Figure 2.8: Mohr-Coulomb's failure criterion (a) shear planes, and (b) strength envelope

To estimate the laboratory rock strengths to that of the rockmass, the most common method used within the mining industry employs the Hoek-Brown failure criterion (Hoek & Brown, 1980). For intact rock, the Hoek-Brown criterion (preferentially) organizes laboratory results in the σ_1-σ_3 space rather than the τ-σ_n as in the Mohr-Coulomb. Although the Hoek-Brown criterion is non-linear, the cohesion (C) and the friction angle (φ) can be readily computed for equivalent linear Mohr-Coulomb inputs at a specified confinement range (Hoek & Brown, 2019). By providing infield rockmass classification estimates through the Geological Strength Index (GSI — Hoek et

al., 2013), laboratory strength envelopes are reduced to estimate rockmass strength through procedures developed in the Hoek-Brown criterion (Hoek & al., 2002; Hoek & Brown, 2018).

2.2.1.1.3 Stiffness Contrast

Cook (1965a) provided perspective on dynamic instability in rock, challenging the belief that the total strain energy accumulated in a rock volume was the sole source for instability. Cook suggested that the stiffness contrast between the rock sample and the loading system stiffness plays a crucial role in the post-peak strain energy release. When applied stresses act on a body and deform it, the work done is stored within the body in the form of elastic strain energy (Budavari, 1983). For a perfectly elastic material (assuming a continuum medium), the stored strain energy (U_m) takes the following form:

$$U_m = \frac{1}{2}(\sigma_1\varepsilon_1 + \sigma_2\varepsilon_2 + \sigma_3\varepsilon_3) \tag{2.3}$$

$$U_m = \frac{1}{2E}\left(\sigma_1{}^2 + \sigma_2{}^2 + \sigma_3{}^2 - 2v(\sigma_1\sigma_2 + \sigma_2\sigma_3 + \sigma_3\sigma_1)\right) \tag{2.4}$$

where: U_m = stored strain energy per unit volume [J/m^3]
σ_1, σ_2, σ_3 = principal stresses [Pa]
ε_1, ε_2, ε_3 = principal strains [m/m]
E = Young's modulus [Pa]
υ = Poisson's ratio [1]

During standard laboratory testing, a hydraulic or mechanical press loads a rock sample, producing the stress-strain (or load-displacement) constitutive material response. As the material passes the peak strength, the stability in post-peak depends on the ratio between the rock stiffness (K_r) and the loading system stiffness (K_m), see *Figure 2.9*. Ductile rock of lower stiffness ($K_{(r-d)} \leq K_m$) will dissipate fracture energy (W_f) during unloading, observed as (stable) plastic deformation such as crushing. When brittle rock is stiffer than the loading machine ($K_{(r-b)} \geq K_m$), it fails catastrophically soon after reaching the peak strength because the unloading process cannot be absorbed by the specimen, ultimately producing (violent) kinetic energy release (W_k).

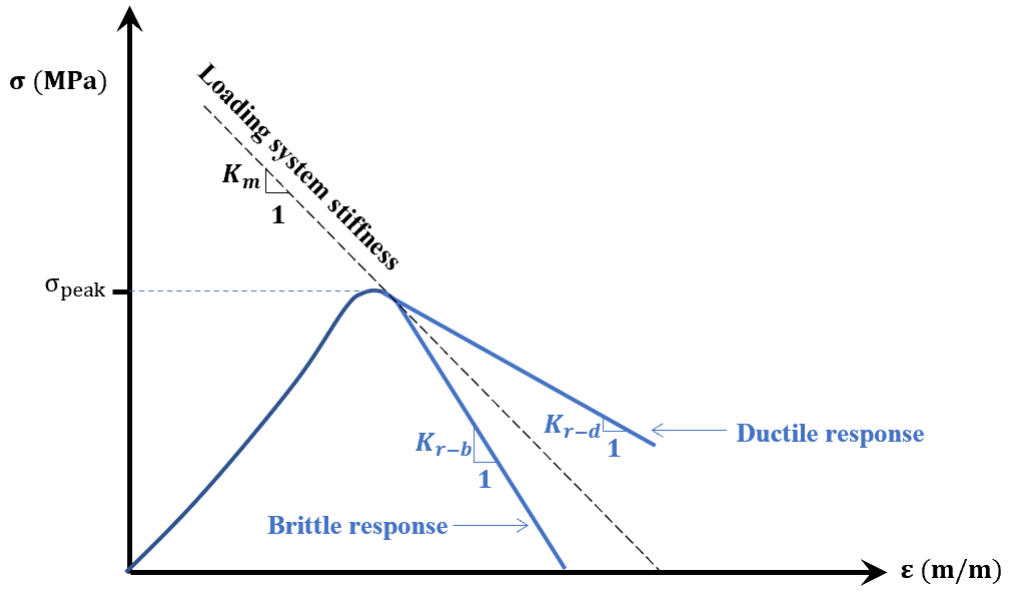


Figure 2.9: Theoretical stress-strain curves for stable and unstable conditions assuming constant loading machine stiffness (Cook, 1965a)

Therefore, Cook (1965a) postulated the following criteria for post-peak response:

$$\left.\frac{\partial\sigma}{\partial\varepsilon}\right|_{K_m} < 1 \quad \therefore \ produces\ a\ stable\ crushing\ process \tag{2.5}$$

$$\left.\frac{\partial\sigma}{\partial\varepsilon}\right|_{K_m} > 1 \ \therefore \ produces\ an\ unstable\ crushing\ process \tag{2.6}$$

To reiterate, dynamic instability arises when the loading system stiffness is unable to control the post-peak fracturing (or crushing) process. Additional energy is supplied to the sample, which leads to kinetic energy release (violently shattering the specimen).

2.2.1.1.4 Post-Peak Behaviour

To understand the constitutive behaviour of rock, the complete stress-strain curve needs to be expressed (Fairhurst & Cook, 1966). As we discussed earlier, loading systems with low stiffness have limited potential to surpass the peak strength, even for ductile rocks. Many other (physical and mechanical) factors control the post-peak response of rock, such as the specimen width and height-width ratio, as well as the loading frame and loading-displacement rates (just to name a few). However, applying servo-controlled processes during sample loading, by quickly switching between loading-unloading states based on displacement rates allows one to determine

the complete stress-strain curve of brittle rock from moderately stiff testing machines. (*Figure 2.10*). As seen in the figure, the post-peak side of the complete stress-strain curve was determined. A series of hysteresis loops were created during the unloading-loading cycle, successfully controlling the onset of yielding. Without servo-control, the sample would have likely failed under normal loading conditions.

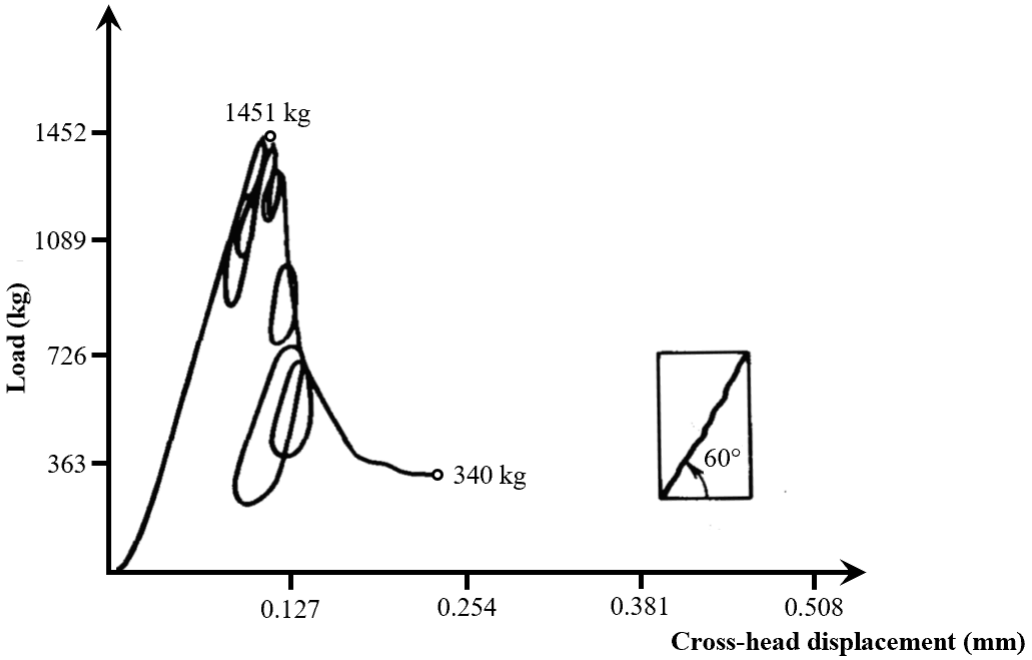


Figure 2.10: Schematic of a complete load-displacement curve of a brittle rock sample obtained by load cycling (Goodman, 1989)

The post-peak response was observed to transition in rock from a brittle to a ductile response under increasing confinement states (*Figure 2.11*). The stress-strain failure envelope displays an increase in axial strain and a decrease in dilatancy with an increase in confinement (from p_1 to p_4). As the confinement pressure on the rock specimen rises above $\sigma_3/\sigma_1 = 0.2$, the tensile crack fissures (spalling) subside (at p_2), allowing the sample to mobilize and strengthen through frictional shearing of mineral grains (Byerlee, 1968; Goodman, 1989). The discrete single-failure plane in the rock sample (p_2 to p_3) slowly develops into a conjugate series of inclined parallel fissures across the entire surface of the specimen. Due to an increased load at peak strength because of the higher confinement state, subsequent surface and internal shearing mechanism consumes all the additional energy, and no further strengthening is apparent (this is the peak ductile plateau at p_4). Therefore, rock specimens subjected to increasing confinement allow

strain-hardening mechanisms to develop at post-peak, resulting in progressive plastic deformation of the sample as grains undergo cataclastic flow (Wawersik & Fairhurst, 1970). Although, in practice, the transitional confinement stress varies between rock types by several orders of magnitude, from ~20 MPa for shale to ~100 MPa for sandstone (Goodman, 1989). Metamorphic and siliceous igneous rocks (quartzite or granite) remain brittle for confining pressures above 1,000 MPa (Paterson & Wong, 2005).

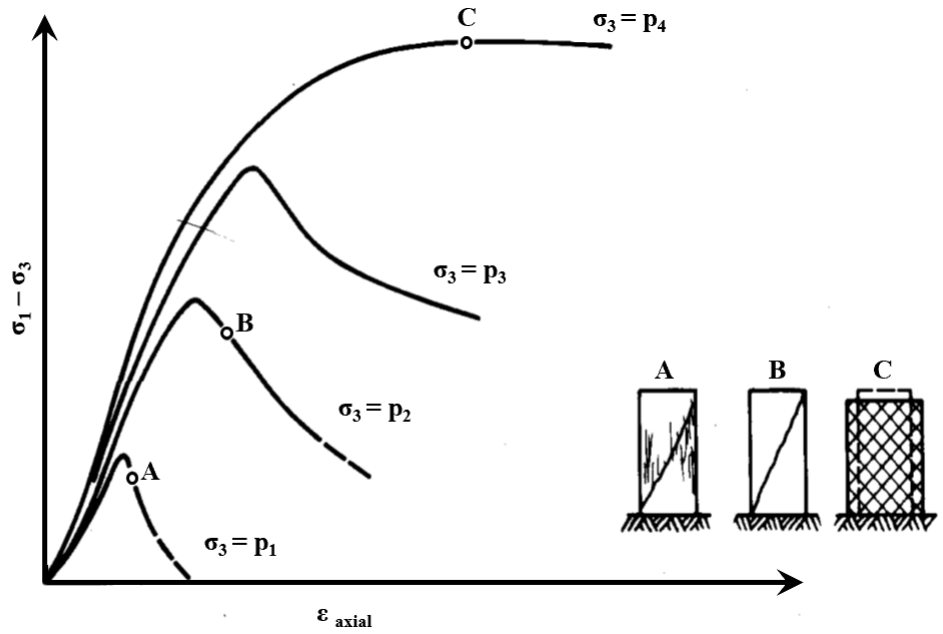


Figure 2.11: Schematic constitutive stress-strain response of hardrock under increased confinement, showing brittle-ductile transition (Goodman, 1989)

The post-peak behaviour of rock depends on the stiffness of the loading system, the sample energy consumption processes, and the overall applied confinement state. No official standard exists for obtaining the post-peak curve at the laboratory scale.

2.2.1.2 Shear Behaviour of Discontinuities

At the laboratory scale, the shear strength of discontinuities has been shown to behave in accordance with Amonton's friction laws, where the surface characteristic plays a critical part in resisting movement. Many authors have investigated rock friction at the laboratory scale in detail (Byerlee & Wyss, 1979; Goodman, 1989; Scholz, 2019). Some of the most critical aspects are presented herein with a focus on the difference between the static and dynamic shear strengths, which establishes the mechanical basis of seismic slip response.

2.2.1.2.1 Basic Frictional Properties

The direct-shear test is the most common method to estimate the shear strength of a discontinuity, where two separate rock pieces align parallel in the direction of the applied shear under constant normal stress. Schematic shear-stress and shear-displacement responses are illustrated in *Figure 2.12*. With the bottom of the sample secured, the shear-stress progressively develops within the sample until the static (initial) friction yields, mobilizing the top piece. The static shear stress (τ_s) is proportional to the normal stress (σ_n) before the slip onset (δ_s) without any cohesion (i.e., Amonton's second law of friction). The coefficient of static friction (μ_s) controls the shear-normal stress relationship up until that point (i.e., before the static bond between the contacting surface is broken). Thereafter, the shear-displacement response (ride) is characterized by the constitutive behaviour of the discontinuity, past its peak shear strength, where it follows a *shear-hardening* or *shear-weakening* slip motion process.

The Mohr-Coulomb static frictional strength criterion is expressed as follows:

$$\tau_s = \sigma_n \cdot tan(\varphi_s) \qquad 2.7$$

where: τ_s = static shear-strength [Pa]

σ_n = normal stress [Pa]

φ_s = static angle of friction [°] with $\mu_s = \tan(\varphi_s)$

μ_s = coefficient of static friction [1]

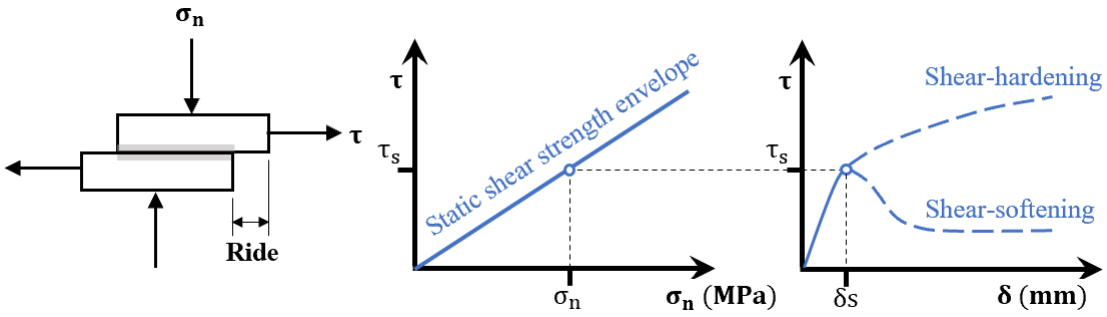


Figure 2.12: Schematic direct-shear model with associative static shear-stress and shear-displacement responses

In direct-shear experiments conducted on various types of discontinuities, a bilinear peak strength envelope is observed, where low normal stresses are not enough to produce cohesion, and the static friction coefficient is related to asperity profiles (Patton, 1966; Jaeger, 1971). When sliding

under low normal confinement, the specimen experiences dilation as the contacting pieces travel over each other on the steepest asperity incline. As the normal stress increases, dilation is suppressed, promoting the shearing of asperities that produce a cohesive response.

Rock discontinuities that occur naturally present contact characteristics and possible infill. A great body of literature attempts to empirically relate the peak static strength, observed at the laboratory scale, as a unified fault characteristic. These static models are as follows (to name a few):

1. Geometrical asperity model (Newland & Allely, 1957; Patton, 1966; Ladanyi & Archambault, 1970; Davis & Salt, 1986; Saeb,1990).
2. Surface roughness model (Barton, 1973; Barton & Choubey, 1977; Lee et al., 2006).
3. Infilling material type model (Ladanyi & Archambault, 1977; Papaliangas et al., 1993; Indraratna & al., 2008).

Byerlee (1978) compiled the frictional strength for ground surfaces of various rocks and found the shape of the envelope to be (also) bimodal, independent of lithology and temperature (*Figure 2.13*). Notable exceptions to this law are clay minerals and sheet silicates (Lockner, 1995).

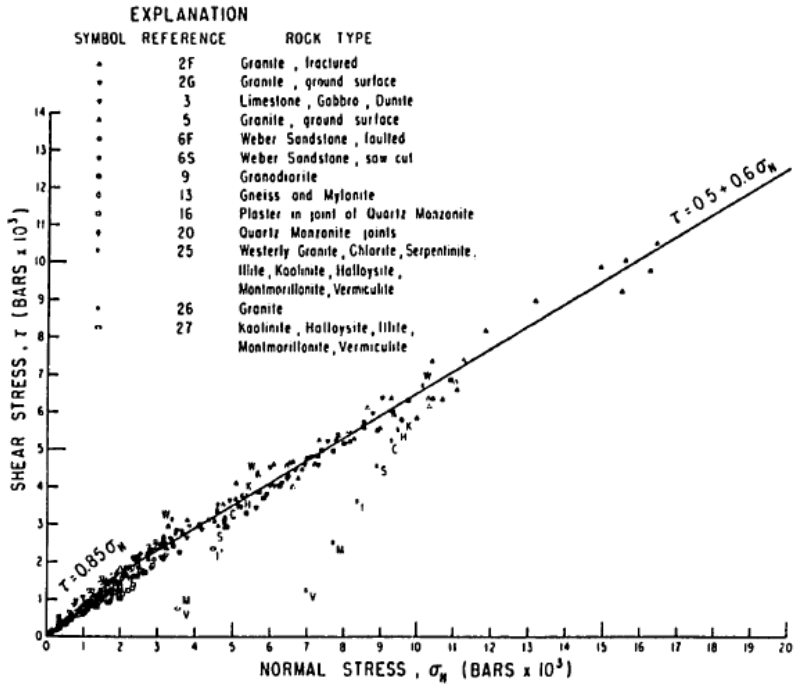


Figure 2.13: Shear-normal stress behaviour for a wide variety of rocks (Byerlee, 1978)

Many authors advocate that Byerlee's Law correlates well with most frictional fault responses (Lockner, 1995; Jaeger et al., 2009; Scholz, 2019). Byerlee's Law follows a relationship describing the shear strength with respect to confining pressures (Byerlee, 1978):

$$\tau_s = 0.85 \cdot \sigma_n \quad 2.8$$

when $\sigma_n \leq 200$ MPa, and

$$\tau_s = 50 + 0.60 \cdot \sigma_n \quad 2.9$$

at higher clamping stresses up to 1,700 MPa.

Based on Byerlee's Law, the typical values for the static friction coefficient (μ_s) range between ~0.60 and 0.85, corresponding to a static friction angle (φ_s) of 30–40°.

Jaeger *et al.* (2009) provided key mechanisms to deform surface asperities (*Figure 2.14*). Contrasting fault stiffness can cause plowing, while low normal loads can cause dilation or ride. At high normal loads, where dilation of contact surfaces is restrained, asperity deformation relates to shearing through a strong spot. The first mechanism represents possible slip-hardening behaviour, while the other two can be pure slip-weakening or mixed behaviours. Byerlee (1967) suggested that brittle fracture of asperity was the underlying mechanism while observing the frictional behaviour of granitic rock. As will be seen later, the slip-weakening constitutive model is the key component in evaluating kinetic energy release (Salamon, 1974; Rice, 1984; Ryder, 1987).



(a) (b) (c)

Figure 2.14: Three main surface-asperity interactions (a) plowing, (b) dilation, and (c) asperity shear (after Jaeger et al., 2009, from Scholz, 2019)

After the initial frictional condition on the contacting surfaces has ruptured, shear resistance will converge to a dynamic steady-state motion (τ_d). Scholz (2019) has associated slip-hardening ($\tau_s \leq \tau_d$) to smooth contacting surfaces, whereas slip-weakening ($\tau_s \geq \tau_d$) has been linked to rough

fractures. *Slip-hardening* requires an increase in shear stress to upkeep motion. S*lip-weakening* allows movement under a lower shear stress and is dictated by friction. The acting shear strength converges towards the dynamic frictional behaviour (in a stable or kinematic manner) through decreases in the coefficient of friction:

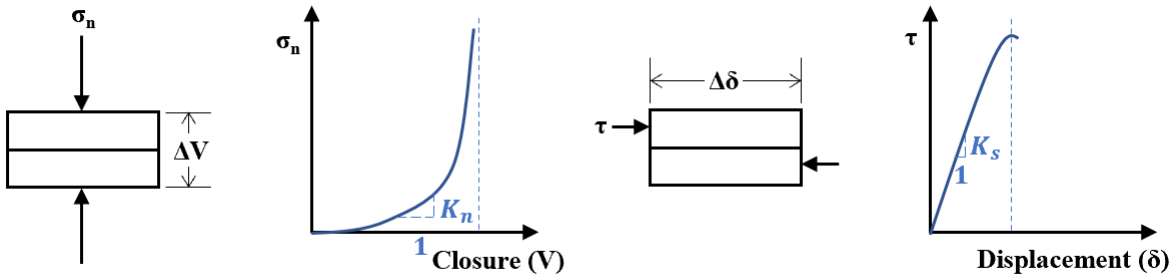
$$\tau_d = \sigma_n \cdot tan(\varphi_d) \qquad 2.10$$

where: τ_d = dynamic residual shear-strength [Pa]
φ_d = dynamic angle of friction [°] with $\mu_d = tan(\varphi_d)$
μ_d = coefficient of dynamic friction [1]

The dynamic friction coefficient varies between ~0.47 and 0.6, which relates to a dynamic friction angle of 25–30° (Scholz, 2019). In practice, the dynamic friction angle (or coefficient) is often regarded as 90% of its static condition (Salamon, 1993). The static stress drop ($\Delta\tau$), resulting from the difference between the static and the dynamic shear strength envelopes, is a critical parameter in developing seismic moment (as will be seen later).

The normal and shear stiffnesses of contacting rock surfaces contribute to characterizing a discontinuity (*Figure 2.15*). Normal stiffness is the ratio of the normal stress (σ_n) to observed closure (ΔV) during a direct-shear test. It characterizes the deformation of the fault where the maximum normal closure (asymptote) is closely related to the intact uniaxial compressive strength of the rock. This parameter describes the infill material as well as the dilation of unmated fault contacts. Shear tests under constant normal stiffness (allowing for adjusted confining stress) present different constitutive behaviour as ride is no longer possible (Goodman, 1989). Shear stiffness is the ratio of shear-strength (τ_s) to shear-displacement ($\Delta\delta$) before the onset of static slip. This parameter accounts for the elastic portion of the shear-displacement constitutive behaviour. These stiffness properties are employed in numerical codes, such as finite difference (FLAC) or discrete element (UDEC) methods, as they describe contact logic between blocks, which allows to calculate the deformation and stress evolution along the fault. They also allow for boundary element codes (MAP3D) to specify deformability of infill fault material, determining closure (perpendicular displacement) and ride (shear displacement).

Hence, the fixed values for stiffness and frictional shear properties obtained from laboratory experiments commonly characterize faults, wherein they might significantly vary, to some extent, from normal stresses or boundary conditions.



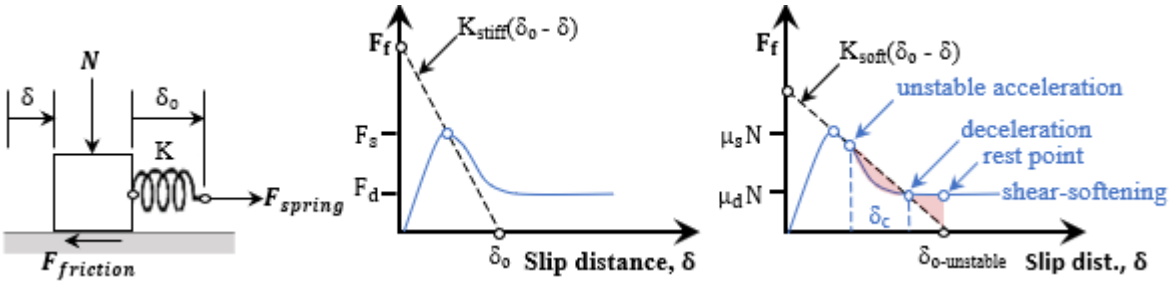
(a) (b)

Figure 2.15: Shear and normal stiffness associations within (a) normal-closure relation, and (b) shear-displacement

2.2.1.2.2 Spring-Block Model

The classic spring-block model describes the kinetic motion of discontinuities where a block rests on a plane, subjected to a normal load (N), where a stiff spring applies a shear force (F) on the block (*Figure 2.16*). Also known as the spring-slider, this model was developed by geophysical and seismological communities (Rice, 1984). In this experiment, the block is allowed to slip completely and repeatedly as opposed to the direct-shear test, which restricts the top piece from mobilizing past the stationary base. When the static friction breaks, the block will move a certain distance, and the contacting surfaces will unload along the loading system provided by the spring. Hence, the resultant block motion produces stable or kinematic slip, controlled by the stiffness ratio of the post-peak slip weakening frictional response to that of the spring. A stable sliding motion arises when the slope of the post-peak frictional response is lower than that of the loading system (similar to eq. 2.5), where the released energy converts mainly into frictional heat. In contrast, an unstable sliding motion arises when the loading system stiffness is lower than that of the block's post-peak frictional response (similar to eq. 2.6), where the block slips in a sudden, dynamic manner. The released kinetic energy is summed above the areas of the post-peak slip response and the intersecting loading system at peak shear strength (Rice, 1984; Ryder, 1987; Salamon, 1993). Rabinowicz (1951) noted the existence of a critical distance (δ_c) for transitioning between the two coefficient of friction states. Past that distance, the slider decelerates due to frictional resistance being greater than that of the spring force. The block will arrest at a distance where the area of deceleration is equal to the area of unstable acceleration. As

can be observed, both instabilities resulted from slip-weakening frictional responses ($\mu_s \geq \mu_d$), but dissipated energy differently.



(a) (b) (c)

Figure 2.16: Spring-block model (a) analogue representation, (b) high-stiffness loading response (stable response), and (c) low-stiffness loading (kinematic) response (Rice, 1984)

Jaeger *et al.* (2009) solved the analytical equations for dynamic slip motion for a force-mass-spring system. Assuming constant velocity of the end of the spring with no damping, an instant stress drop occurs between μ_s and μ_d at the slip onset. The equations of motion simplify to (Scholz, 2019):

$$\delta(t) = \Delta\mu \cdot \frac{N}{K} \cdot (1 - cos\, kt) \quad 2.11$$

$$\dot{\delta}(t) = v = \Delta\mu \cdot \frac{N}{\sqrt{Km}} \cdot (sin\, kt) \quad 2.12$$

$$\ddot{\delta}(t) = a = \Delta\mu \cdot \frac{N}{K} \cdot (cos\, kt) \quad 2.13$$

$$\Delta\mu = (\mu_s - \mu_d) \quad 2.14$$

$$k = \sqrt{K/m} \quad 2.15$$

where: $\Delta\mu$ = friction coefficient drop [1]
K = spring stiffness [N/m]
N = normal force [N]
m = mass of the block [kg]
k = force parameter [N]

The slip duration (t_r), expressed in seconds, represents the time for the block to come to rest:

$$t_r = 2\pi \cdot \sqrt{m/K} \quad 2.16$$

and, the total slip displacement ($\Delta\delta$), expressed in meters, is:

$$\Delta\delta = 2 \cdot \Delta\mu \cdot \frac{N}{K} \quad 2.17$$

As noted by Hedley (1992), the total kinetic (or seismic) energy (W_k) released during sliding can be computed from:

$$W_k = \frac{N^2\pi}{2Kk} \cdot (\mu_s - \mu_d)^2 \quad 2.18$$

These solutions suggest that the block mass and the spring stiffness control the slip duration process, not the frictional properties. A stress drop is necessary to measure dissipated seismic energy, although the stiffness of the system plays a critical role in the amount of kinematic energy released (Hedley, 1992). A more complex analysis of seismic energy release can be encountered when assuming a transition between the static and the dynamic friction properties.

Analytical slip-weakening (or displacement-weakening) friction models attempt to describe potentially complex constitutive fault responses. They were established to reproduce varying laboratory discontinuity behaviours (in the hope of attaining a general *Law*). Many slip-weakening solutions were developed to account for:

1. Transitional (instant or non-linear) response of static to dynamic friction condition, μ_s-μ_d (e.g., Bizzarri, 2011; Hart et al., 1988; Tinti et al.,2009).
2. Alternating slip-hardening and slip-weakening conditions (e.g., Ohnaka & Yamashita, 1989; Ohnaka, 1993).
3. Gouge and infill presence (e.g., Chambon et al., 2006).

These analytical constitutive equations arose by setting a critical displacement distance (δ_c), which constrains the transition between static to dynamic friction. The characterized slip-softening response displays scale dependencies due to geometrical surface irregularities, which produce naturally varying slip distances (Ohnaka, 2003). Additionally, displacement-weakening laws inherently neglect time and rate effects, impeding their ability to allow the residual shear-stress to regain progressively its static strength without resetting the friction level after the induced slip occurred (Rice, 1984).

A true stick-slip model (as described by Scholz, 2019) must have a mechanism that will permit the system to regain its initial frictional strength following slip, allowing for repetitive motion to occur. Essentially, a period of rest follows the fault-slip, associated with no motion, where the discontinuity regains (heals) to its static value. This repetitive nature is called regular stick-slip (Scholz, 2019). Discontinuities heal from the increase in contact area through asperity creep (Rabinowicz, 1951; Dieterich & Kilgore, 1994) and from interfacial chemical bonds (Beeler et al., 1994). Experimental studies found that static friction of contacting surfaces recovers logarithmically with time under constant hold (Rabinowicz, 1958).

Brace & Byerlee (1966) were the first to suggest that regular stick-slip, as observed in rock discontinuity shear tests, is the mechanism of earthquakes where pre-existing faults undergo intermittent slip while remaining stable between tremors. It is due to the prominence of stability, and not strength, which makes earthquakes recurrent stick-slip phenomena (Scholz, 2019).

Continuously-yielding joint models attempt to reconstruct a fault's ability to re-strengthen after having mobilized in order to relate to the stick-slip mechanism suggested for earthquake mechanics (Brace & Byerlee, 1966). This model considers a continual reduction of joint friction properties (from static to dynamic) through cumulative increments of plastic shear deformation, which is dependent on the normal stress along various portions of discontinuity length. Dilation and load reversal effects are taken into consideration during the displacement weakening model development based on joint rock laboratory testing (Hart et al., 1988). This allows for numerous cycles of stick-slip motion (Cundall & Lemos, 1990). Consequently, the displacement-weakening concept depends on readjusting the discontinuities normal and shear stiffness, ultimately relating shear-displacement with normal-closure. Due to complexity, discontinuum codes best investigate Cundall & Lemos's (1990) formulation of joint response. Velocity is indirectly calculated when the code explicitly relies on the laws of motion. Making them simpler than the rate/state-variable laws (which will be seen subsequently). The continuously-yield model appears to be more reliable for evolving mine settings (Lemos, 1987; Ng et al., 1993), where mine stiffness evolves with extraction.

Velocity models (or rate- and state-dependent laws) take into consideration the effects of time and velocity in order to best approximate the frictional aging process (allowing to regain static frictional strength after slip). Dieterich (1972) and Scholz *et al.* (1972) demonstrated that these

components have a prominent outcome on rock friction properties. Ruina (1983) generalized the velocity concept by showing that velocity-weakening systems, where μ_d decreases logarithmically as the sliding velocity increases, will exhibit an increasing oscillation and reach a state of regular stick-slip. In contrast, a velocity-hardening system will quickly dampen unstable motion upon slip and eventually reach a state of stable slip (Scholz, 1998). Many versions of rate/state-variable constitutive laws have been proposed (e.g., Dieterich 1992; Kato & Tullis, 2003; Kato & al., 2007). These rate/state-dependent laws are considered the most complete constitutive characteristic of discontinuity behaviour (Okubo, 1989) and include the most prominent features of slip-weakening (Bizzarri et al., 2001). However, there appears to be no universal friction law that can successfully describe all experimental data (Kato & Tullis, 2003). According to Beeler *et al.* (1994), the version in best agreement is the Dieterich-Ruina or slowness-law (*Figure 2.17*). A sudden increase in shear velocity produces an instant increase in friction (known as the frictional jump), followed by a frictional decay along a critical slip distance, undershooting the steady-state friction. A sudden drop in shear velocity produces an instant loss of friction, regaining slowly to steady-state. The rate/state frictional law captures the mathematical evolution of the friction coefficient with changing velocity. Although this law (along with its numerous variations) primarily appears in geophysical studies (Bizzarri et al., 2001).

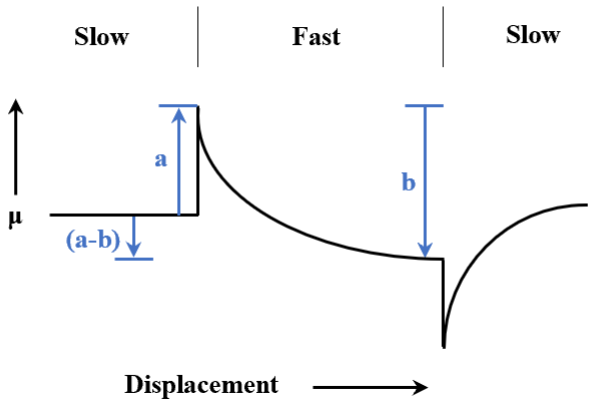


Figure 2.17: Scheme of experimental frictional response to a sudden e-fold (~2.7) increase in velocity following a decrease in sliding velocity (Scholz, 1998)

There are many factors contributing to the variation of frictional properties of discontinuities. In a mine environment, where in-situ stresses and loading systems are constantly evolving, these complex formulations might be more challenging to implement and interpret. Recently, Sainoki

(2014) and Sainoki *et al.* (2017) attempted this endeavour at the mine setting with good success. As a reminder to keep things simple, Scholz states:

It remains an open question, however, to what extent these details, worked out in idealized laboratory conditions, apply to the natural faults, or conversely, to what extent observations of natural phenomena will allow their confirmation. (Scholz, 2002, p.97)

2.2.2 Rockmass Response to Tabular Mining

The rockmass accounts for intact rock and discontinuities, and hosts the mining activities. Mining induces energy exchanges between the extracted rock and the resulting boundary profile. Stress transfers occur if the removed rock hasn't completely crushed out. Hence, the vicinity of narrow tabular abutments often displays a zone of transitional state between (a) crushed or fractured, (b) failed and (c) intact rock material (*Figure 2.18*). These zones correspond to the material's constitutive strength response to high stresses at the mining front (i.e., as illustrated by the contrast between the elastic and theoretical stresses in the remaining abutment). The transitional failed rock section in the post-peak region (b) represents the seismogenic zone. Slip on discontinuities can occur outside this zone, in proximity or away from active mining. In this section we will define the seismic energy for volumetric and contact conditions with focus on tabular deposits.

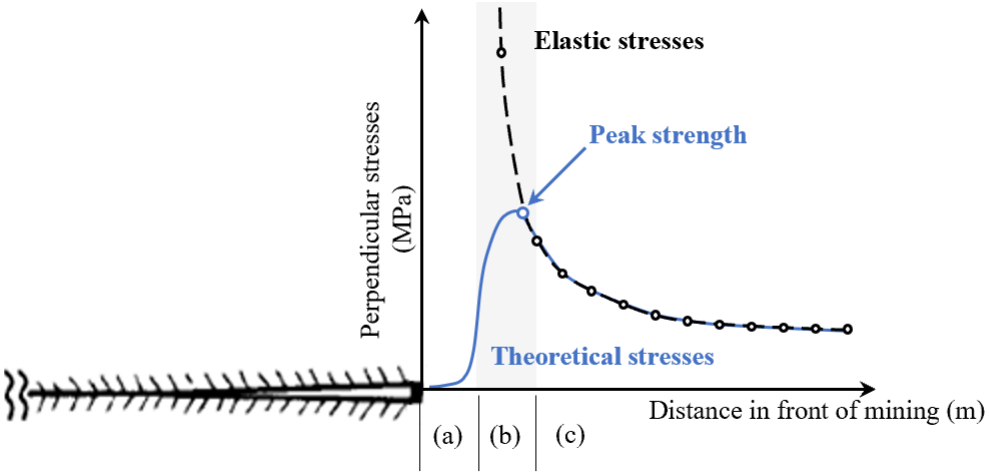


Figure 2.18: Schematic of an advancing reef face illustrating three distinct rock zones (a) fractured, (b) yielding, and (c) sustained (Cook, 1965a)

2.2.2.1 Energy Balance in Tabular Mining

Cook (1963a) noted that stored strain energy accumulated in a volume of rock is not the only source of seismic energy release, as the event locations presented a pattern that scattered rather than concentrate on the immediate mining front. Cook noted a variation in potential energy (closure) in the surrounding rockmass of hardrock tabular mines in South Africa. This led to the energy balance concept where the overall change in the energy state of the rock medium must be redistributed or dissipated since a quantity of energy becomes available after extraction. By applying conservation of energy, Cook *et al.* (1966) first presented the energy balance equations which were later refined by Salamon (1974; 1984). Salamon's annotations are considered throughout this review. Hence, the general energy conservation established for an idealized case is as follows (Salamon, 1984):

$$W_t + U_m = U_c + W_r \tag{2.19}$$

where: W_t = potential energy change resulting from the rockmass moving inward, toward the excavation, observed as gravity-induced settlement (for a horizontal seem) and convergence (for a vertical seem)

U_m = stored energy that was in the rock removed by excavation

U_c = increase in stored strain energy in the rock surrounding the excavation due to stress transfers and concentration

W_r = energy released

Thus, the primary energy source due to mining is the sum of the potential energy (W_t) and that of the stored strain energy (U_m). A great portion of the source energy stores back in the rockmass as strain energy (U_c) while an amount of residual energy gets *lost* in the system (W_r) by dissipating the energy stored in the excavated rock (U_m), through kinetic energy release (W_k) and deforming ground support (W_s). When suddenly extracting a rock volume (by blasting), the removal of stored strain energy (U_m) produces vibrations (oscillations) of the excavation boundary, inducing potential seismic energy release (W_k). Contemporary waveform monitoring systems record these seismic waves (Hedley, 1992). Equilibrium reaches through damping of the rockmass vibrations, usually accompanied by slight inelasticity, and the throw of excavated-broken rock into the excavation. The amount of energy absorbed by the support (W_s) is the work done deforming the local ground support and compressing the backfill (Salamon, 1974). Most often, the amount of absorbed energy by the support (W_s) is small and can be ignored in the balance equation (Hedley,

1992). Additionally, it must be reiterated that this is an elastic analysis, energy dissipated through plastic deformations of the rockmass is ignored for simplicity. Nonetheless, one could imagine that this dissipated energy can be substantial for ductile type rock, inadvertently reducing the seismic energy output. It is important to note that the energy from explosives used for extraction is also ignored. Blast energy is believed not as large a contributor since much of the energy goes into breaking and ejecting the mined block. With these assumptions in place, the released energy term (W_r) gives:

$$W_r = U_m + W_k \tag{2.20}$$

Hence, by rearranging the energy equation 2.20 in 2.19:

$$W_k = W_t - U_C \tag{2.21}$$

Salamon (1974) performed analytical verification of the impact of extraction size on the U_m (stored) and W_k (kinetic) constituents of the energy release parameter. When mining takes place in very small quasi-static steps (Δ) equivalent to rotor head extraction, the stored strain energy (ΔU_m) composes the entirety of the energy release (ΔW_r), nulling the kinetic energy release (ΔW_k) component:

$$\Delta W_r = \Delta U_m \tag{2.22}$$

$$\Delta W_k = 0 \tag{2.23}$$

The change in potential energy (ΔW_t) is the driving force behind all the other components. Reducing this parameter allows for the entire portion to transfer to the rockmass (ΔU_c) potentially reducing the seismic energy output (ΔW_k) for the mining step.

$$\Delta W_t = \Delta U_c \tag{2.24}$$

The energy released (W_r) will be limited to the available strain energy (U_m) dissipated through stable processes.

As the excavation step increases, the seismic efficiency (W_k / W_r) also increases and becomes larger than the stored strain efficiency (U_m / W_r). Salamon (1983) presented an analytical case example, under a hydrostatic stress field, for a tunnel achieving a final profile through varying numbers of mining steps (*Figure 2.19*). Salamon calculated that when a tunnel instantly increases to its ultimate radius (by blasting), ~60% of the released energy is kinetic (W_k / W_r) as

opposed to ~40% dissipated through stable processes (U_m / W_r). By gradually reducing the excavated volume, Salamon demonstrated that the seismic efficiency decreases progressively until reaching an absolute stored strain efficiency. Hedley (1992) extended this analysis by comparing mining sequences in which the total seismic efficiency was ~90% for long-hole settings as opposed to 72% for cut-and-fill. In addition, by incrementally extracting the last cut-and-fill stope in 3 cuts, he reduced the seismic efficiency for that method to ~60%. In practice, this is somewhat contradictory as some cut-and-fill mines still experience severe seismicity (Hedley, 1992), as is the case for the Lucky-Friday mine. Hedley (1992) states that to achieve zero seismic efficiency (i.e., $W_k = 0$) the extraction method must be equivalent to tunnel boring.

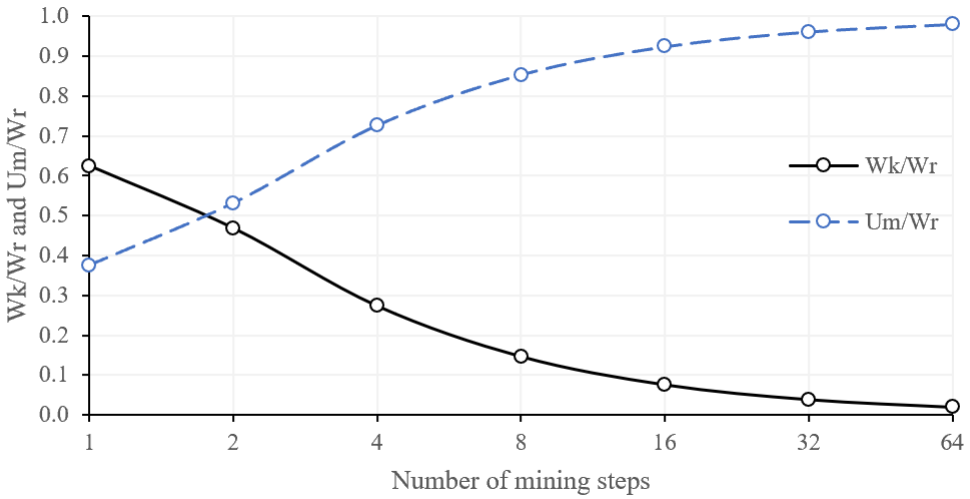


Figure 2.19: Component of released energy for circular excavation in varying mining-step amounts (Salamon, 1983)

Based on this theory, seismic energy release would immediately follow mine extraction. In practice this is not the case, Gibowicz (1990) classified seismicity with respect to blasting to be either triggered (delayed) or induced (instant). From deep hardrock mines in northern Idaho, Swanson and Sines (1992) observed that ~60% of seismic events, as well as ~75% of rockbursts, occurred 45 minutes after mine blasts. Heal *et al.* (2005), at the Laronde mine, found that ~65% of the total seismic events released after 1-hour from blast-initiation, accounting for ~70% of the cumulated seismic energy, while ~90% accumulated by the 14th hour. The strain seismic source mechanism changes the longer the lag-time between a blast and an occurrence (Hedley, 1992).

2.2.2.2 Strain-Bursting

Strain-bursting events in mines occur in proximity of mine openings, where stress concentrations exceed the rock strength (Cook, 1965a). Strength failure commonly relates to the materials constitutive response after surpassing the peak strength. Kinetic energy releases due to contrasting stiffness between the material post-peak characteristic and the local mine stiffness (Cook, 1965a). Additional contributions include sudden deconfinement, reducing a rock volume to a biaxial or uniaxial stress state. At that point, instant seismic release of stored strain energy occurs if the previous loads were superior to that of the rock's uniaxial compression strength (Hedley, 1992). Mine stiffness evolves with mining (Starfield & Fairhurst, 1968), potentially seismically activating *softer* rock types as the mine stiffness slope transitions above the materials unloading curve (the mine losses stiffness). Contact between contrasting geological stiffness is another mechanism for strain-bursting (Hedley, 1992), as stress conditions can differ in the contrasting materials' contact boundaries. Significantly higher stresses will be incurred in the stiffest material assuming that both convey to the same strain displacement (e.g., Kalenchuk et al., 2017). Upon excavating such events, damage should be observed in the brittle material as the softer one will allow for deformation.

Some authors present a specific distance for strain-bursting to occur such as < 100 m from active mining (Gibowicz & Kijko, 1994). Numerical analysis can be used to define a more accurate radius. If severe fractures appear in an otherwise competent mining front (Ryder & Jager, 2002), a possible fracture zone exists where the immediate mining block has low strain energy (low seismic probability) and rises rapidly only a couple metres ahead of the face (higher seismic probability). This has the potential to produce rock ejections from distant strain-bursting source events (Kaiser et al., 1996).

2.2.2.3 Pillar-Bursting

Pillar-burst events in mines result from loading induced by boundary closure as mining progresses. Their basic failure mechanism relates to the load-displacement stiffness contrast, where unstable failure results if the pillar stiffness is larger than that provided by the confinement of the regional rockmass (Hedley, 1992). The pillar designs allow for temporary (crush) or permanent (regional) support pillars. The crush pillars are designed for stable failure, while the regional pillars are expected to remain intact for the duration of mining. Numerous tabular mines

report dynamic pillar-bursts for both designs (Spottiswoode & Drummond, 2014; Kgarume et al., 2009).

Hasegawa *et al.* (1989) observed crushing as the main mechanism leading to rockburst damage. From observations made in South African mines, Lenhardt & Hagan (1989) have proposed three additional mechanisms associated to pillar burting (*Figure 2.20*). Pillar shears induced by offsetting perpendicular wall-to-wall closure axis, where the floor translates in the opposite direction than that of the roof, have been observed to produce wing type shears at the mining front. The punching mechanism has been reported for squat pillars (width / height >> 10) when the core increases in strength and punches through weaker rockmass similarly to the Prandtl foundation effect (Jager & Ryder, 1999). Pillars often display mixed-failure modes. Hudyma & al. (1994) noted that the source mechanism of sill-pillar stopes at Brunswick Mine revealed a combination of close-range volumetric bursts (microseismicity) and fault-slip events (macro-seismicity) occurring ~200 m away from active mining. The mechanical pillar failure descriptions increases in complexity if unfavourably oriented faults cut through the pillars core.

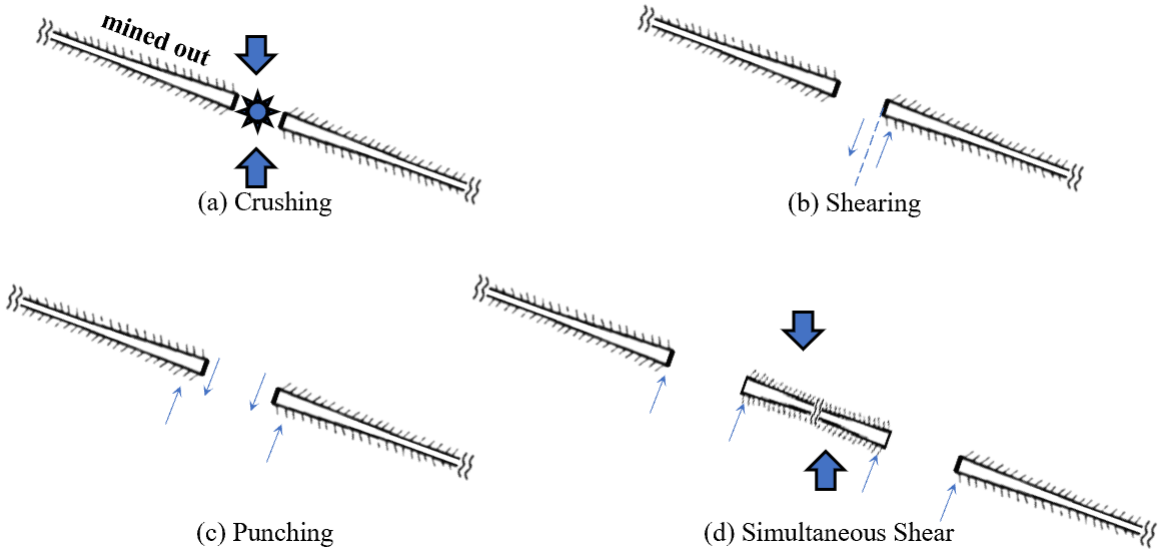


Figure 2.20: Four mechanisms of pillar-bursts in tabular mines (a) crushing, (b) shearing, (c) punching, and (d) simultaneous shear (Lenhardtl & Hagan, 1989)

2.2.2.4 Fault Movement

2.2.2.4.1 Fault-Slip

In mining environments, slip along known discontinuities relate to mechanisms resembling natural earthquakes where very large induced-events (+3 M) often always associate with previously mapped faults (McGarr, 1994; Ortlepp et al., 2001; Richardson & Jordan, 2002). The simplest fault-slip model representing the most accurate slip mechanism is the block-spring analogue (Rice, 1984). The sliding system releases energy through stable or unstable processes. During stable fault sliding, all the released energy (W_r) dissipates in overcoming friction (W_h) with minor oscillations between contacting surfaces. For unstable sliding, a portion of the remaining released energy transformers into kinetic or seismic energy (W_k) trough oscillations, as is similar for both laboratory and natural earthquakes (McGarr, 1994). For this phenomenon to manifest, a static stress drop ($\Delta\tau$) condition needs to be released along the sheared rupture surface ($\mu_s\sigma_n - \mu_d\sigma_n > 0$). For a transitional stress drop, Jordan (2000) postulates that the dissipating friction component (W_h) can be further subdivided in fracture energy ($W_{h\text{-}i}$)) and thermal friction ($W_{h\text{-}ii}$), see *Figure 2.21*. This process would explain the source of energy for secondary fracture growth.

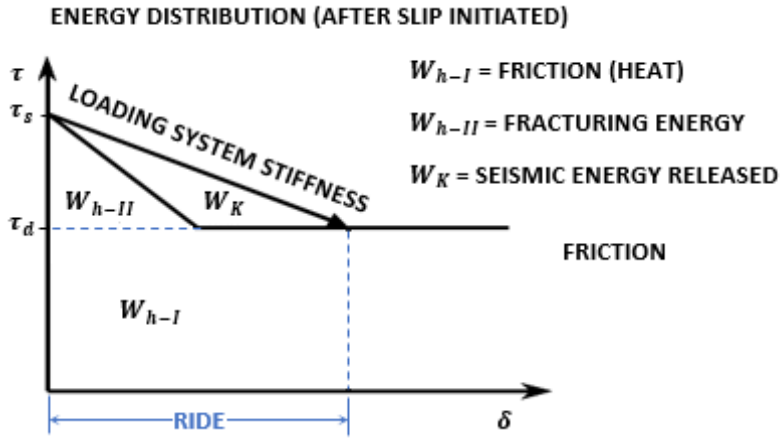


Figure 2.21: Partitioning of energy during shear slip for transitional peak to residual friction values (Jordan, 2000)

Assuming a circular fault area with a slip radius (L_s), a static stress drop ($\Delta\tau$) and constant normal load (σ_n), Salamon (1964c; 1984) proposed the following energy balance distribution for a linearly elastic rockmass:

$$W_k = W_r - W_h \qquad 2.25$$

$$W_r = 0.5 \cdot (\mu_s\sigma_n + \mu_d\sigma_n) \cdot A \cdot \bar{R} \qquad 2.26$$

$$W_h = \mu_d \cdot \sigma_n \cdot A \cdot \bar{R} \quad 2.27$$

$$W_k = 0.5 \cdot \Delta\tau \cdot A \cdot \bar{R} \quad 2.28$$

where: $A = \pi \cdot {L_s}^2$: circular slip area [m^2]

$\bar{R}$ = average ride [m]

$\Delta\tau$ = static stress drop [Pa]

The average ride ($\bar{R}$) along the rupture surface is:

$$\bar{R} = \frac{8 \cdot (1 - v)}{3 \cdot \pi \cdot \left(1 - {}^{v}/_{2}\right) \cdot G} \cdot \Delta\tau \cdot L_s \quad 2.29$$

Furthermore, the seismic moment (M_o), here expressed in [N·m], relates to the following formulation (Salamon, 1993):

$$M_o = \frac{8 \cdot (1 - v)}{3 \cdot \left(1 - {}^{v}/_{2}\right)} \cdot \Delta\tau \cdot {L_s}^3 \quad 2.30$$

The following relationship exists between W_k and M_o, both expressed in [J]:

$$W_k = \frac{\Delta\tau}{2G} \cdot M_o \quad 2.31$$

Based on data from the East Rand Property Mines (ERPM — South Africa), Spottiswoode and McGarr (1975) postulated the following local magnitude (M_L) relationship with energy [MJ]:

$$\log W_k = 1.5\, M_L - 1.2 \quad 2.32$$

$$\log M_o = 1.2\, M_L + 4.7 \quad 2.33$$

Zoback & Gorelick (2012) plotted the relationship on observational data of earthquake between magnitude-slip dependence with **peak** stress drops ranging from 0.1 to 10 MPa (*Figure 2.22*). Fault lengths must range 20–100 m to generate a +1 M, and 700–3,000 m to generate a +4 M event. Conversely, a fracture size of 100 m has the potential to generate events up to +2 M, inferring slip radius to be inversely proportional to stress drop (i.e., shorter faults require a larger stress drop to produce larger events). Unfortunately, mine environments seldom apprehend major fault systems and characteristics at the early stages of the mine life. These are often discovered as mining proceeds over time.

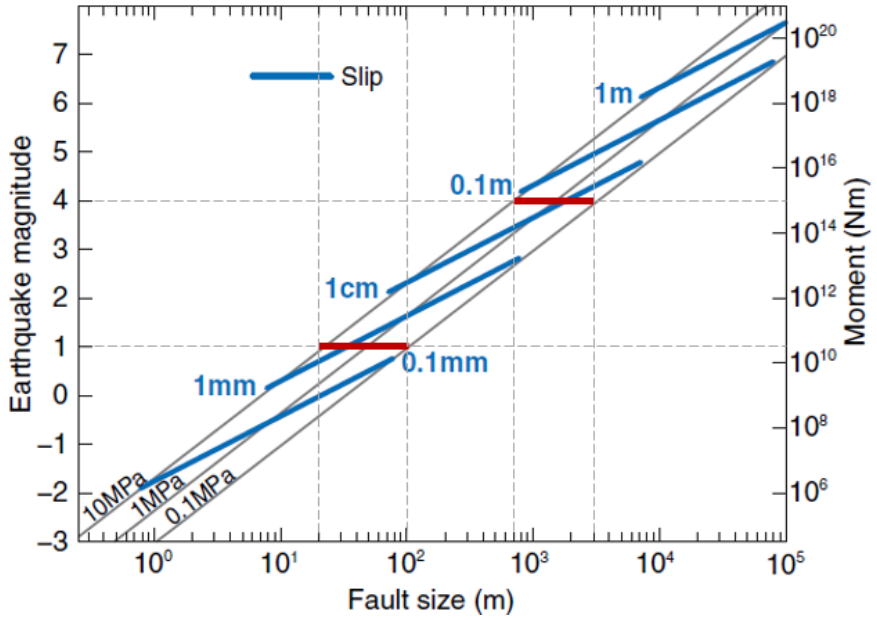


Figure 2.22: Magnitude-slip relationship relative to stress drop (Zoback & Gorelick, 2012)

2.2.2.4.2 Mine Fault Characterization

Unlike the simple spring-block analogue, mine fault surfaces can be much larger than the inferred slip region and present complex topography, geometrical features and associative fracture zones either side of the main fault structure (Wallace & Morris 1986; Ortlepp et al., 2001). For South African gold mines, it has been demonstrated that shear failure primarily occurs on some type of pre-existing fault or shear system (Spottiswoode & McGarr, 1975; McGarr et al., 1979; Richardson & Jordan, 2002). Pre-existing structures experience local and regional unclamping, extraction weakening and stress reorientation (Castro et al., 2009). Ortlepp (2000) discussed the possibility of an evolutionary genesis of micro-slip to macro-slip and the rapid shear propagation through pristine highly stressed intact rock volumes. Sibson (1986) noted that pre-existing micro shears initiate the principal macro slip surface. These mechanisms are proposed to explain the relatively high magnitude events recorded at certain mines.

Many factors contribute to the frictional slip strength of fault surfaces (*Figure 2.23*). The base friction strength of contacting planes significantly increases by interlocking and cohesion (Hencher & Richards, 1989). Fault asperities play a critical role as they act like strong-spots locking slip motion (McGarr et al., 1979). The acquired additional frictional resistance yields to plowing, dilation and asperity shear mechanisms which invoke motion (Jaeger et al., 2009). The

failure of these asperities allow slip to initiation. Trifu & Urbancic (1996) suggested that shearing of asperities can release significant amount of strain energy potentially accounting for aftershocks.

In nature, the topography of faults and fractures have been shown to present fractal (self-similarities) behaviour over a broad band of scale (e.g., Scholz, 2019; Moore et al., 1989; Power et al., 1987). For a bandwidth range of $10^5 – 10^{-5}$ m, Scholz & Aviles (1986) have suggested that asperity distribution on faults follows an inverse power law and roughness scales with spatial wavelength, dependent on the spatial frequency. Hence, roughness occurs on all scales of fracture length. This contributes to the idea that rockmass structures are not continuous smooth planar features, but commonly present offsets and secondary structural branches. As noticed by Lockner & Beeler (2002), this scaling property hinders the ability to correctly extrapolate the constitutive behaviour of faults and little framework exists attempting to address this.

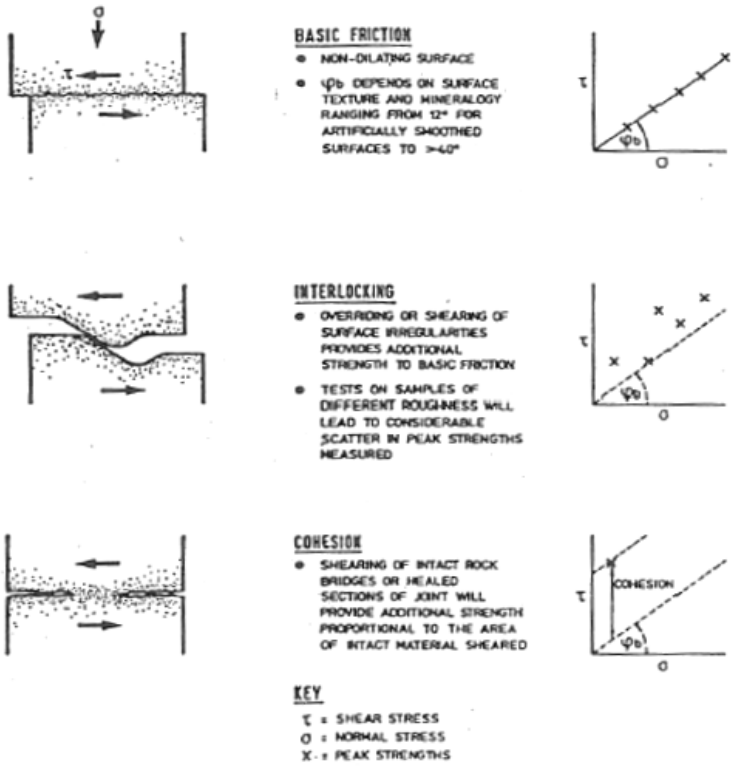


Figure 2.23: Factors contributing to frictional shear strengthening (Hencher & Richards, 1989)

Scholz (2019) has identified jogs and steps as the general form of asperity on a fault surface (*Figure 2.24*). Jogs oriented perpendicular to the slip vector either impede sliding or terminate rupture. In contrast, parallel steps allow unobstructed movement. In addition, offset faults can

harbor rock bridges, acting as strong asperities. Kim et al. (2004) produced a classification scheme for characterizing fault damage by observing where the damage occurs along the fault. *Linked damage* types characterize rock bridging between faults, which mainly consists of extension fractures, rotated blocks and strike-slip duplexes. These bridges affect fault movement.

Geological characterization suggests that surface roughness evolves with increasing slip and faults with relatively small displacements will tend to have rougher surfaces (Sagy et al., 2007). As pointed out by Scholz (2019), surface roughness is most likely anisotropic with a predisposition to its slip history, as the surface tends to be rougher in the direction perpendicular to the dominant slip vector. In mining setting, where stress orientations vary due to extraction (inducing variable slip vectors), asperities could systematically be sheared and regenerated through this mechanism, allowing multiple slip to occur on a single fault plane.

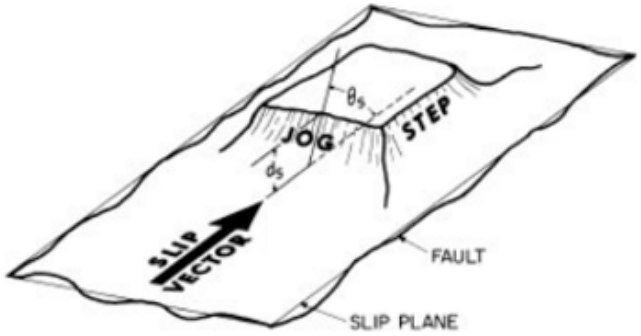


Figure 2.24: Fault surface displaying a jog and a step, with respect to slip vector (Scholz, 2019)

2.3 Assessment of Mine Seismicity

2.3.1 Rock Mechanics Approach

From a rock mechanics perspective, rockburst classifications attempt to correlate observed mine seismicity to a seismic source mechanism as seen in **Section 2.1.4**. These methods lack preventive capabilities as a seismic event needs to have occurred and offer little possibility in forward engineering or predicting seismic hazard. Determining the seismic source mechanism can be complex and challenging since the mining environment needs to be adequately understood (Hudyma, & al. 2003), see *Figure 2.25*. Acknowledging that seismic events are unstable failures

taking place within the rockmass has led to the development of mine layout assessment procedures. The most relevant and earliest applications attempting to relate seismicity with mining activity are the Energy Release Rate (Cook et al., 1966) and the Excess Shear Stress (Ryder, 1987). The ERR makes an overall estimation of seismic potential, while the ESS explains punctual seismic occurrences on geological structures. Since their conceptions, South African practice has routinely employed these approaches (Jager & Ryder, 1999). The following section elaborates these concepts further.

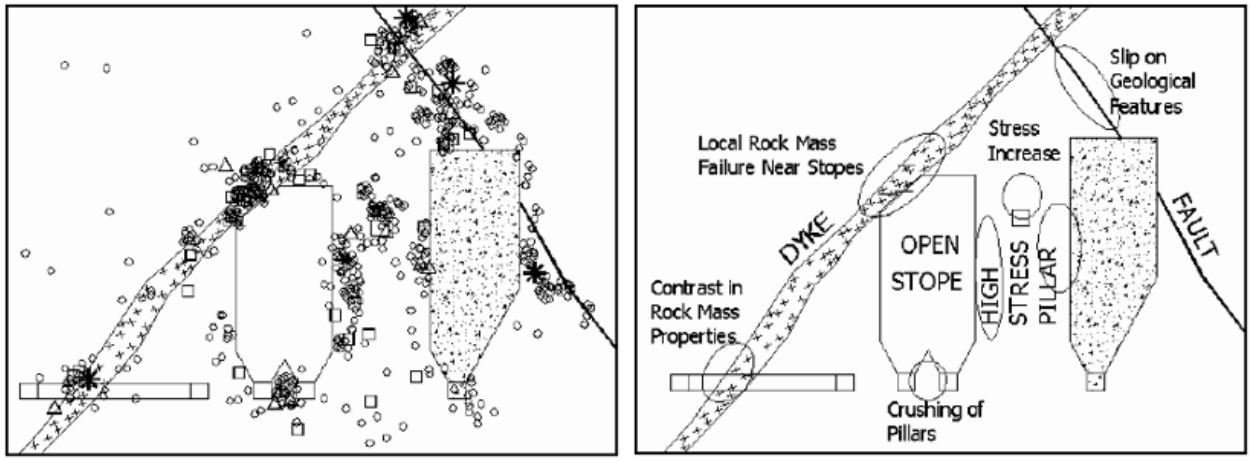


Figure 2.25: Seismic source mechanism interpreted from a mining environment (Hudyma & al., 2003)

2.3.1.1 Energy Release Rate

Cook & al. (1966) developed the Energy Release Rate to address the problem of selecting appropriate design layouts for reef-type tabular mining in rockburst-prone ground. Prior to that, the basic principles of energy release were established for underground excavation (Coates, 1959; Cook, 1963a; Duvall & Stephenson, 1965). Ignoring any contribution from blast energy, the energy available is from stored strain energy (U_m), the energy stored the mined block, and the potential energy (W_t), change resulting from the rockmass converging toward the excavation. Applying the conservation of energy theorem, an elastic continuum allows to ignore plastic dissipations. The formulation further simplifies by ignoring the work term used for deforming support and crushing fill material (W_s). Therefore, the total source energy transfers to stored strain energy in the surrounding rockmass (U_c) and a portion dissipates in the process of enlarging the excavation (W_r) — termed energy release. The released energy accounts for both

non-violent and violent dissipations. The former corresponds to the mined block (U_m) dissipating store strain energy through possible vibration of the rockmass and throw of fractures rock in the excavation. Whereas the latter could be related to the oscillating damping mechanism as the rockmass reaches equilibrium, which can generate seismic energy (W_k) in the process (Hedley, 1992). To reiterate, the seismic energy release (W_k) relates to:

$$W_k = W_t - U_C \tag{2.34}$$

Cook *et al.* (1966) suggest that at least half the work done by the body and external forces (W_t) should associate with the energy release (W_r). Although no clear specification for acquiring the kinetic energy portion was offered, Salamon (1974) derived the analytical proof for an unsupported cavity in an elastic medium and observed agreement with the conjecture:

$$W_r \geq 0.5\, W_t \tag{2.35}$$

Consequently, Cook *et al.* (1966) states that kinetic energy release (W_k) will occur when the amount of released energy (W_r) is greater than the stored strain energy in the mined block (U_m). Hence, the minimal lowest limit of energy release (W_r) becomes (Salamon, 1983):

$$W_r \geq U_m > 0 \tag{2.36}$$

Furthermore, by tracking the amount of available elastic strain energy across a mining element, one can assume that a rockburst will be more likely to occur for higher values as compared to lower ones. These hypotheses give rise to the Energy Release Rate (ERR) where the generalized formulation, applied in numerical codes, is as follows (Cook et al., 1966):

$$ERR = \frac{1}{2} \cdot \sigma_{pre-mining} \cdot \delta_{post-mining} \tag{2.37}$$

where: ERR = energy release rate [MJ·m^{-2}]

$\sigma_{pre-mining}$ = pre-mining stress acting on the element before mining it [MPa]

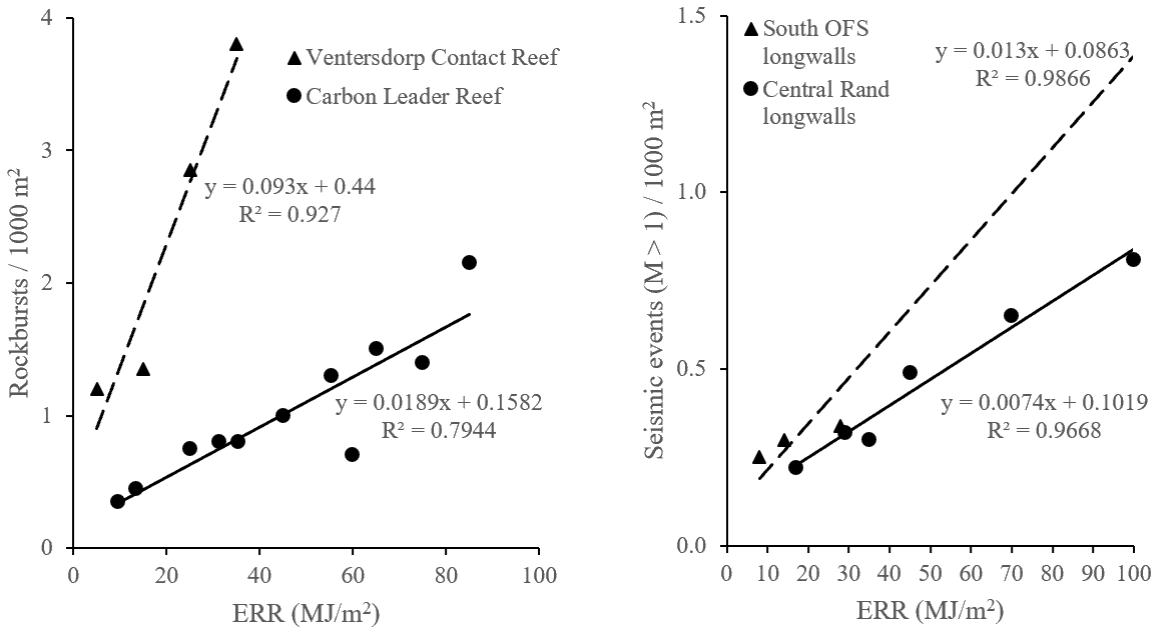
$\delta_{post-mining}$ = displacement resulting from mining the element [m]

Many other variations to compute ERR exist such as the analytical plane strain solution for a slit type excavation (Salamon, 1983) as well as the stress intensity factor borrowed from fracture mechanics (Linkov, 1992; Jager & Ryder 1999). All these computational methods relate to the concept that probability and magnitude of seismicity tend to increase with increased average ERR

values (Jager & Ryder, 1999). Numerical modelling techniques adhere commonly to the above formulation.

The computed ERR value represents a spatial rate for energy release expected for a given mining step. The ERR term implies the amount of work done in excavating a mined block. It is a strain energy density term which evolves as mining progresses. Mining depth and mine geometry influence the ERR value. In addition, this concept does not assess in any way for structural instabilities and assumes elastic conditions. It is important to note that the calculated ERR value is somewhat fictitious since it allows the stresses at the reef extremities to be very large (assuming an elastic behaviour for the material). In practice, the expected volume of rock that is to be mined could have already dissipated part of its store strain energy through plastic crushing or fracturing. The ERR increases in reliability when calibrated to actual in stope wall-to-wall closure measurements.

The increasing ERR rating is usually observed to correlate with increased seismic output. South African practice (COMRO, 1988) has succeeded in empirically calibrating ERR values to rockbursting potential for several of its deep hardrock and narrow tabular mines, *Figure 2.26*. The ERR ≥ 30 is usually associated with a moderate seismic potential, anything above that value has an increased seismic risk (COMRO, 1988). It can be postulated that ERR accounts for the strain-bursting phenomena where mining conditions are relatively uniform (Budavari, 2003). As suggested by Cook (1965b), these events account for volumetric failure relating to brittle failure with rapid load-shedding characteristics. The ERR does not explicitly consider the potential of seismicity on geological structures (Ryder, 1987).



(a) (b)

Figure 2.26: Rockburst potential and seismic event occurrences with regards to ERR (COMRO, 1988)

Since the ERR is an energy density term, when multiplied by the mined area we obtain the strain energy release (W_k) relatable to seismic energy (E_s) output by the seismic monitoring system. The seismic efficiency release (η), ratio E_s / W_k, does not relate these two measurements readily. Reported values of $\eta < 1\%$ have been observed in South African mines (Cook, 1976; Spottiswoode, 1980; Spottiswoode et al., 2008). The ERR does not account for past mined out areas or remnant pillars where seismic activity can still arise (Spottiswood et al., 2000). This analysis is therefore highly zone dependent and procedures for zoning need to be devised. Moreover, the ERR is primarily criticized for not accounting for non-linearity, not accounting for post-failure potential softening (Salamon, 1984; Spottiswoode, 2000; Lachenicht 2001). The ERR value is computed from fictional elastic stress in the advancing abutment. Hedley (1992) has noted that, for plane strain condition (assuming E = 70 GPa & $\upsilon = 0.2$) producing a value of ERR ~50, the elastic stresses can be up to 2,700 MPa in the mining element. South African mines have been observed to generally behave elastically (Jager & Ryder, 1999). Exception is made for the immediate face which cannot withstand high abutment stresses and is most likely yielded to a certain depth (Cook, 1965a). Most of the energy released through mining dissipates

aseismically (> 97%) by crushing, fracturing and heating (Jager & Ryder, 1999). For these reasons, some care needs to be undertaken when assessing for ERR in mining settings (Durrheim et al., 1998).

Nonetheless, the ERR approach does present practical value in comparing quantitatively different mining layouts to each another (e.g., Spottiswoode, 1997). Due to the elastic energy assumption, the total amount of energy released for a given final mining layout will be constant regardless of the sequence (Spottiswood et al., 2000). However, the rate of release within a scenario may be different between sequences. By carefully controlling the ERR output (looking for sequences which gradually releases rather than sudden jumps) allows for a better pillar design, mining layout valuation and extraction sequence assessment. For these reasons, actual South African procedures still rely to some extent on the ERR approach (Spottiswoode et al., 2008; Hofmann, 2012; Scheepers, 2012).

Currently, numerical modelling codes have the capability of constructing complex mine geometry and sequencing, for varying material types. Using BEM (mainly because of superior computing time), two types of ERR assessments are possible: (1) a plane strain slit construct, and (2) a 3-dimensional reef construction, both using DD elements. Similar results have been observed between methods (Budavari, 1983), but the latter offers more accuracy by relating the influence of mine geometry. Complex mine settings do not correlate ERR linearly with seismicity (Milev & Spottiswoode, 1997).

2.3.1.2 Excess Shear Stress

Ryder (1987; 1988) developed the Excess Shear Stress in response to the ERR volumetric assessment inability to explain distant seismic events with higher magnitudes. The natural mining environment has structural features (joints, faults, dykes) which significantly increase the frequency of seismicity (Ryder, 1987), see *Figure 2.27*. Predominance to shear failure, for large mine-induced events (M ~+1 to +4), was verified by many authors (Mendecki, 1993; Gibowicz & Kijko, 1994; Richardson & Jordan, 2002). It is now well established that shear events do occur in mine settings. Alike natural earthquake characteristics, mining fault events exhibit significantly low volume changes with predominance for shear rupture during sliding (Spottiswood, 1984). The dominant feature appears to be the ride movements associated to stress relief (Ryder, 1987). Hence, the ESS is an approach elaborated to account for the likelihood of

seismicity along a pre-defined geological structure. The basic slip mechanism is quantifiable and provides a mean for estimating the violent dynamic response.

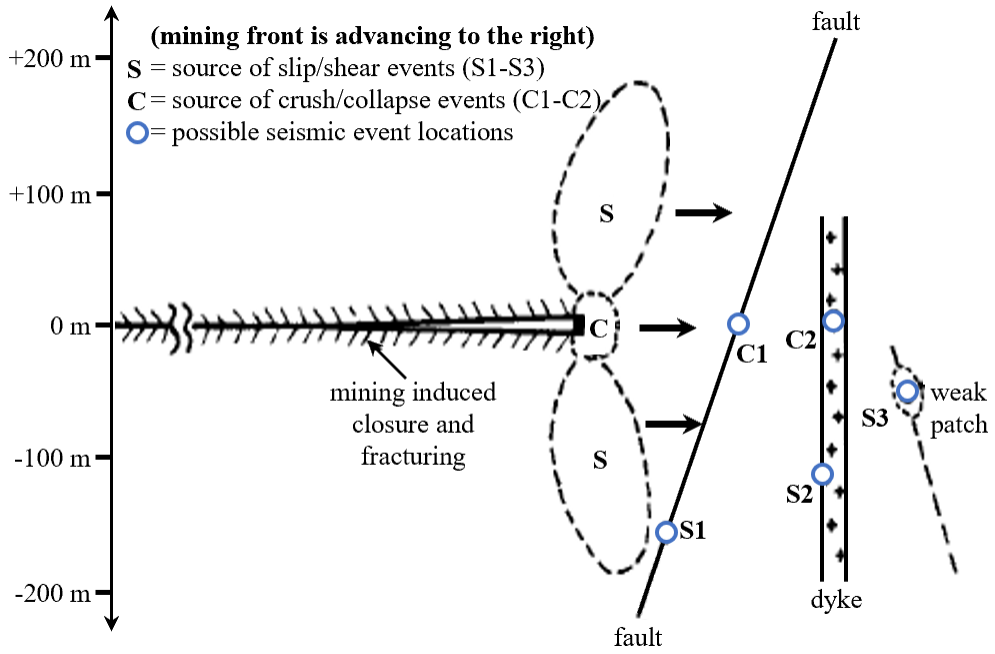


Figure 2.27: Schematic of an advancing reef front in a faulted environment (Ryder, 1987)

Ryder's ESS concept rests on generating a stress drop when a fault mobilises, between the static and the dynamic shear strength envelopes (*Figure 2.28*). At every point across the fault, the static strength (τ_s) component resists the active shear stress (τ_a) which evolves under different confinements states (σ_n) induced by mining; the evolution from the *initial stress state* existing on a fault is depicted on the figure. Once slip **initiates** (i.e., active shear ≥ static shear), the frictional strength drops to the dynamic strength (τ_d), forcing the cohesion to reduce to zero while dropping the friction angle to its residual form. The transition between the frictional strengths describes the static stress drop, assuming to occur under a constant confinement state. The frictional strength envelops are expressed in the Mohr-Coulomb form (eq. 2.1), where cohesion (C) and the static friction angle (φ_s) governs the static strength profile (eq. 2.7), while the dynamic friction angle (φ_d) governs the dynamic strength profile (eq. 2.10).

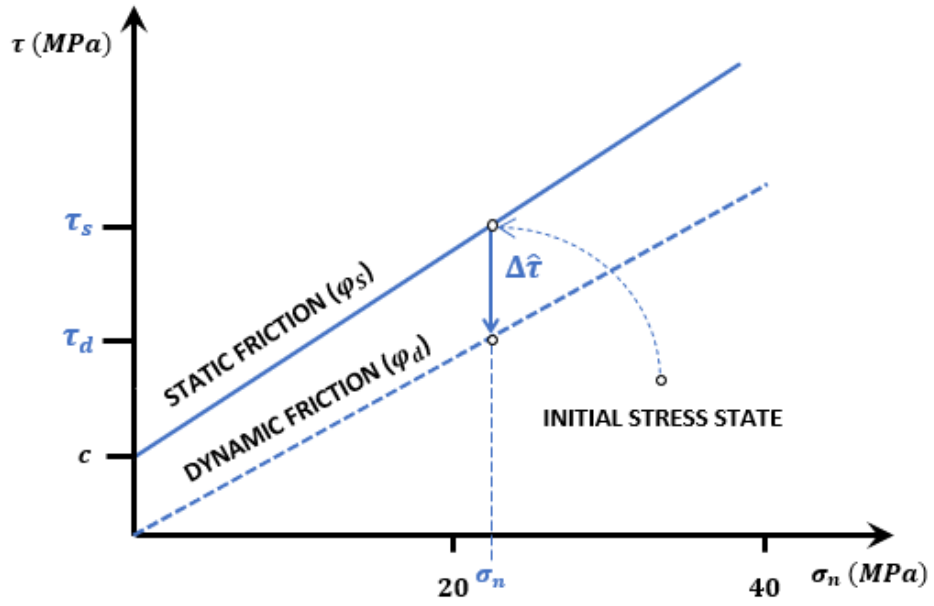


Figure 2.28: Shear-Normal stress relation representing static to dynamic transition through a stress drop (Ryder, 1987)

Therefore, slip **initiates** at a point along a structure when the following conditions is met:

$$\tau_a \geq \tau_s \qquad 2.38$$

Once the fault is mobilized, the confinement stress is conserved and generates a static stress drop ($\Delta\tau$), defined by:

$$\Delta\tau = \tau_s - \tau_d \qquad 2.39$$

Based on seismological observations, Ryder (1987) suggested that the **peak** shear stress drop ($\Delta\hat{\tau}$) value of 5–10 MPa is reasonable for unstable slip on a plane of weakness, while values in the upper range ~20 MPa result from unstable rupture through intact rock. The shear stress drop has a strong correlation with asperity ruptures (McGarr, 1981). The average peak stress drop observed in seismology is suggested to be in the order of 0.1–10 MPa (Spottiswoode & McGarr, 1975; Gibowicz, 1993; Zoback & Gorelick, 2012). Upon reaching the dynamic shear stress condition, the ride stopes by the expenditure of shear stress or halted by some possible intact rock barriers (*Figure 2.29*). Relative shear displacement calculated in South African gold mines present displacement as little as 1–13 mm for small to large seismic events, respectively (Spottiswoode & McGarr, 1975).

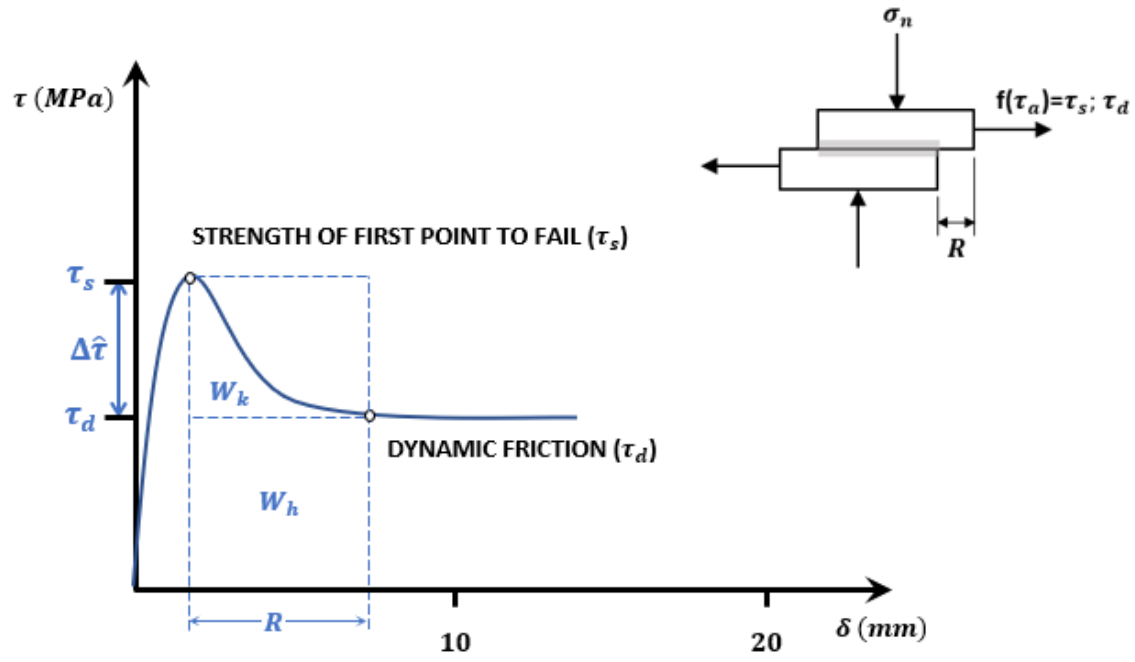


Figure 2.29: Shear-displacement constitutive model with associative static stress drop and ride (Ryder, 1987)

Therefore, Ryder's Excess Shear Stress represents the shear stress necessary to power a shear type seismic event once rupture along a fault initiates:

$$ESS_d = \tau_a - \tau_d \qquad 2.40$$

where: ESS_d = excess shear stress computed from the residual strength [MPa]
τ_a = shear stress acting on the weakness plane [MPa]
τ_d = dynamic (residual) frictional strength of the plane [MPa]

The suffix in the ESS_d refers to the dynamic shear stress component used for the computation.

Ryder provides a practical representation of the static, dynamic and the active shear stresses acting on a discontinuity in a mine setting (*Figure 2.30*). Both strength envelopes vary with the level of confinement according to eq. 2.7 and. 2.10. However, the irregular static strength profile along the fault reflects the erratic effects of asperities and possibly matting contacts along the structure (Ryder, 1988). The dashes line represents the active shear stress acting on the fault, induced by mining. As can be observed, when the active shear reaches a slip **initiation** point along the fault, a rupture instantly propagates along the positive ESS values of the discontinuity, shearing through other asperities until the ESS is sufficiently negative to constrain further movement (Ryder, 1988). This effectively estimates the total slip area. The final rupture length

can overshoot the positive ESS area due to inertial effects by ~20% (Aki & Richards, 1980). However, Ryder's slip condition ignores dilation, which is estimated to reduce ride by ~10% (Ryder, 1987). Therefore, in practice, ESS elastic models simply ignore the dynamic overshoot (Board, 1994).

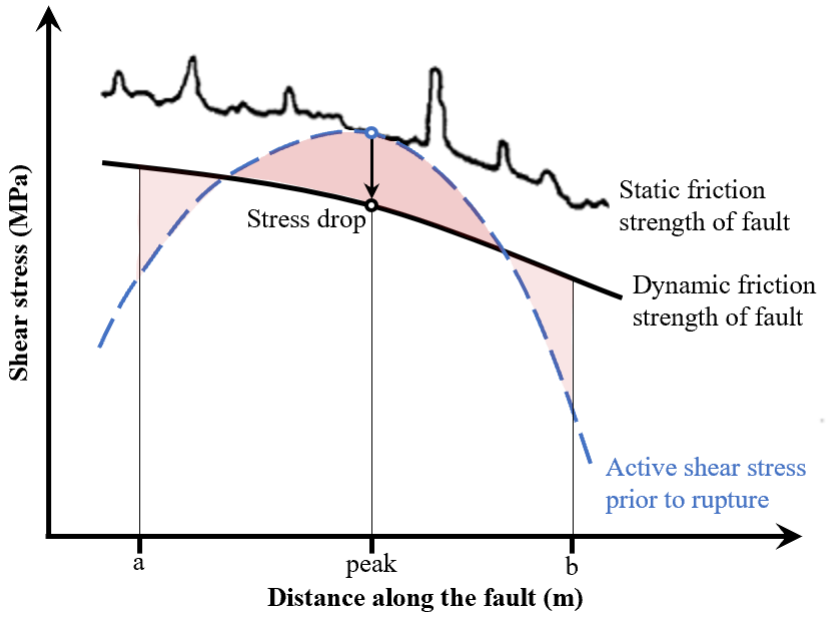


Figure 2.30: Active shear stress and shear strength (static/dynamic) along a conceptual fault trace (Ryder, 1987)

The strength of the ESS analysis lies on its **implicit** ability to estimate seismic source parameters by defining simple fault characteristics such as frictional properties (at min. φ_d), orientation, and length found in a mine setting (*Figure 2.31*). Ryder (1988) related several analytical solutions to estimate magnitude (M_L), peak ride (R), average stress drop ($\Delta\tau_{av.}$) and the final half-rupture length (L_s), including overshoot. These parameters are determined by generating the ESS lobes for a specific fault and by positioning the *physical* fault trace projection onto an ESS lobe representing a specific **peak** shear stress drop ($\Delta\hat{\tau}$) value necessary to induce slip. The slip length (2a) resides inside the positive ESS lobe values. By assuming a ride profile and a source dislocation model, such as the Brune (1970) circular or the Madariaga (1976) rectangular slip, the seismic source parameters can be readily estimated (Ryder, 1988). Consequently, the ESS lobes vary with fault characteristics (notably orientation) where a specific fault may produce only minor seismic outputs for the modelled mine geometry. However, Ryder has proposed a CEV (Coulomb ESS Vector) procedure to assess the maximum ESS potential for unspecified fault

orientations (Ryder, 1988). This procedure is useful for visualising the maximum slip potential near the mining front.

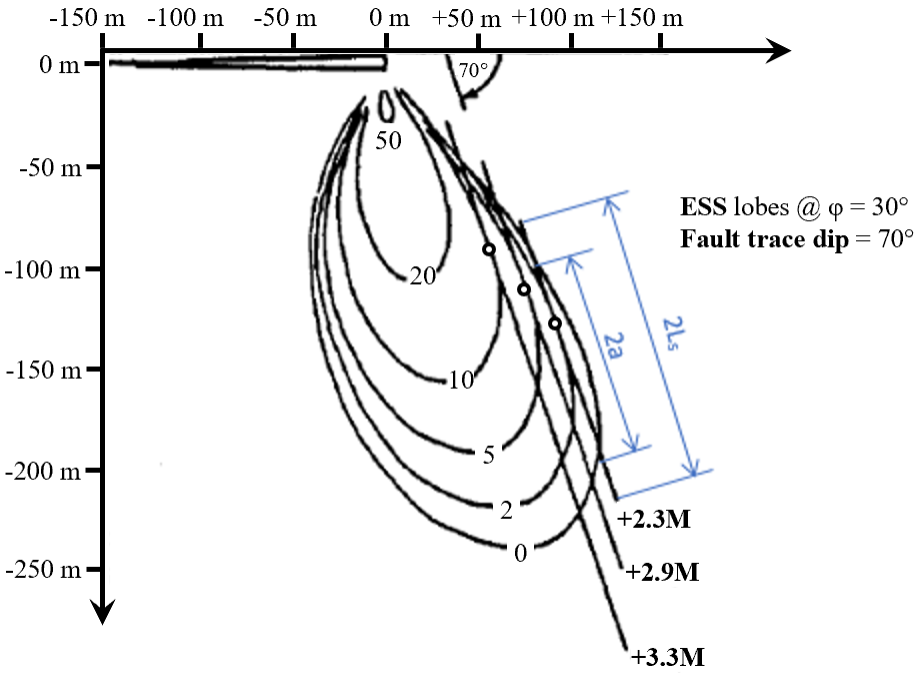


Figure 2.31: Analytical ESS lobes for a typical advancing tabular stope (Ryder, 1987)

Alternatively, for an **explicit** fault assuming circular slip (as done by Salamon, 1984), the seismic moment (M_o) is computed from effective slip parameters. The seismic moment describes the shear magnitude of a double-couple source and M_o is computed through the following formulation (Aki & Richards, 1980):

$$M_o = G \cdot \bar{R} \cdot A \qquad 2.41$$

where: M_o = seismic moment [N·m]

G = shear modulus [Pa]

$\bar{R}$ = average ride [m]

A = area of slip [m^2]

For a circular region, Salamon (1964c) formulated the instant ride dimension (R):

$$R = \frac{4 \cdot (1-\nu) \cdot \Delta\tau}{\pi \cdot \left(1 - \frac{\nu}{2}\right) \cdot G} \cdot \sqrt{{L_s}^2 - r^2} \qquad 2.42$$

where: R = instant ride dimension at a specific location along weakness plane [m]

L_s = slip radius [m]
r = distance along the total slip radius [m]

The average ride ($\bar{R}$), expressed in [m], results by averaging the instant ride over the slip area:

$$\bar{R} = \frac{1}{A}\int \frac{4\cdot(1-v)\cdot\Delta\tau}{\pi\cdot\left(1-\frac{v}{2}\right)\cdot G}\sqrt{{L_s}^2 - r^2}\ dA \qquad 2.43$$

$$\bar{R} = \frac{8\cdot(1-v)}{3\cdot\pi\cdot\left(1-\frac{v}{2}\right)\cdot G}\cdot\Delta\tau\cdot L_s \qquad 2.44$$

recall that total slip area is: $A = \pi\cdot L_s^2$

Therefore, the seismic moment proposed by Salamon (1993) is the following:

$$M_o = \frac{8\cdot(1-v)}{3\cdot\left(1-\frac{v}{2}\right)}\cdot\Delta\tau\cdot {L_s}^3 \qquad 2.45$$

The local magnitude estimates correspond to the subsequent scaling law (Spottiswoode & McGarr, 1975):

$$\log M_O = 1.2\cdot M_L + 4.7 \qquad 2.46$$

The seismic moment formulation depends primarily on the static stress drop and the slip radius. If the slip radius is not long enough, high stress drop conditions won't necessarily produce significantly higher magnitude events.

In practice, the quality of the ESS assessment depends on the in-situ stress conditions (including induced mining stresses), knowledge of the friction properties of discontinuities (C, μ_s & μ_d), slip history (seismic locations) and plane profile (strike, dip & continuity). The ESS provides qualitative insight, such as (Jager & Ryder, 1999):

1. Estimates upper magnitude ranges of seismic events potential near known faults in active or past mining areas.
2. Allows the assessment for regional support such as bracket-pillar design (clamping pillars used to confine faults & dykes).

3. Produces seismic hazard reduction and control on mining sequences by minimizing the ESS lobe extent.

Many authors have effectively applied the ESS concept to mine wide situations (Spottiswoode, 1988; Salamon, 1993; Board, 1994), to explain high magnitude events on known structures (van Aswegen, 2005; Hofmann et al. 2012; Troncoso et al., 2012), and to assist with evaluation and implementation of mine design (Sellers & Coetzer, 2003; Mungur, 2005; Zhang et al., 2011).

Nevertheless, the main limit to the original ESS concept lies on the fact that the **peak** stress-drop ($\Delta\hat{\tau}$) needs to be assumed for the fault to mobilize, which is often unknown. The elastic assumption, used in modelling, can overestimate the lobe area. The ESS lobe technique is ideal for implicit analysis with low structural information, but explicit evaluation is restricted in its forward engineering capabilities. In practice, natural fault topography is not planar and could present jogs and steps as pointed out by Scholz (2019). Subsequently, as noted by Gill and Aubertin (1988), this method ignores the stiffness contrasts between rockmass and discontinuity during the kinetic energy release (W_k). Therefore, the ESS ignores aseismic slip.

2.3.2 Seismological Approach

Volumetric rockmass failure (from crushing or slip) radiates energy in the form of seismic waves (Cook, 1965b). Modern mines employ monitoring to record seismic data from different points inside the rockmass. Digitizing waveform systems record these occurrences through uniaxial/triaxial geophones or accelerometers. The source parameters (seismic event characterization) are derived from these waveforms. Seismological processes rely on back-calculation specific wave pattern with idealised conceptual slip models. The produced source parameters provide insight into potential source mechanisms. This has resulted in a greater understanding of mine-induced seismicity. Seismic events described spatial and temporal kinetic irregularities inside the rockmass (Hedley, 1992). Seismic source parameters often attempt to explain the behaviour and the evolution of rockmass failure (Coulson & Bawden, 2008; Lynch et al., 2005; Zhao et al, 2017).

The two most popular distributors of digitizing seismic-monitoring systems are Engineering Seismology Group (ESG) from Kingston, Ontario (Canada), and Institute of Mine Seismology (IMS) which holds offices in South Africa, Australia and Canada. Seismic systems monitor

seismicity for wall stability in open-pit, cave propagation in block-caving and dynamic rock failure in underground hardrock and softrock mines (including coal). The digitizing system allows to follow cluster trends for passive seismic hazard analysis (Mendecki, 1993). Hudyma *et al.* (2017) compiled 25 seismic systems across Ontario (18 out of 26 operating) and Quebec (7 out of 10 operating) in 2016, illustrating that 70% of active hardrock underground mines in eastern Canada rely on seismic monitoring.

In this section, the computation of source parameters is presented, and a variety of seismological techniques are explored for inferring seismic source. The following content consists of work done by Gibowicz & Kijko (1994), Mendecki (1997) and Hudyma (2010).

2.3.2.1 Seismic Source Parameters

The independent seismic source parameters, derived from waveform analysis, characterize a single seismic event in the following manner:

1. Time of occurrence at the source [date-hour]
2. Location of seismic focus (hypocentre) [cartesian system in mine coordinate]
3. Seismic moment (M_o), in [N·m]
4. Seismic energy (E_s), in [J]
5. Source radius (r_o), in [m]

A seismic event is described by at least four (4) independent source parameters, requiring at minimum the location and the time (Mendecki, 1997). All other seismic source terms (e.g., potency, static stress drop, apparent stress) were derived from these prime parameters.

2.3.2.1.1 Event Time & Location

The event-time occurrence and the associative seismic waveform are meshed together by the acquisition-communication components of the monitoring system. In the ESG configuration, a surface GPS antenna relates atomic-time through fibre-optics directly to the underground equipment. High precision timing is crucial as body waves can travel upwards of 6,000 m/s. In practice, the accuracy of GPS time is well within 40 nanoseconds: an inherent temporal error on location of only ~0.24 mm. Hence, the stitching of time to a waveform is independent of any

theoretical assumptions while relying crucially on the mine's level of investment in fibre optic, equipment compatibility (fibre to acquisition) and regular maintenance (cleaning GPS antenna).

At least 4 sensors need to activate to accurately locate a seismic event inside the rockmass (Cook, 1963b), identifying first-motion of P-wave and S-wave influxes. Since the instruments have known positions, a series of spatial-temporal equations relate all the sensors to a single focus (expressed in the x-y-z mine coordinate system). Severe planarity of the sensor array produces inherent error in location (Cook, 1963b). Unreliable arrival-time from a constant velocity model in a complex geological mine setting also contributes to the inherent location error (Gibowicz, 1990). Waves propagating inside an elastic medium depend on its modulus of rigidity (G). Thus, contrasting geometries (i.e., voids, backfill & lithology changes) present distinct wave modifying behaviours. In practice, a mine usually applies a 1-dimensional velocity model (Hedley, 1992). Mining-induced seismic event typically retain an inherent location error of ~10 m (Gibowicz & Kijko, 1994). Recent survey has confirmed a residual (post-processing) location error less than 10 m for Canadian operating mines (Brown & Hudyma, 2018). However, Collins *et al.* (2016) have demonstrated that 3-dimensional velocity models can improve location accuracy by up to 24 m when compared to a 1-dimensional model.

2.3.2.1.2 Seismic Moment

The seismic moment is the measure of the seismic events strength and relates to the analytical formulation (eq. 2.41) developed by Aki & Richard (1980). Although in seismology, the seismic moment is computed from the displacement spectrum of a waveform converted from the time domain to the frequency domain by the fast Fourier Transform (*Figure 2.32*). The seismic moment (M_o) is expressed by the following equation (Gibowicz et Kijko, 1994):

$$M_{o\,(P;S)} = \frac{4\pi\rho C^3 R|\Omega_o|}{F^c R^c} \qquad 2.47$$

where: $M_{o\,(P;S)}$ = seismic moment component of P- or S-wave [N·m]

ρ = rock density [kg/m^3],

C = P-wave or S-wave velocity [m/s]

R = hypocentre distance to sensor [m]

Ω_o = low-frequency spectral plateau (see *Figure 2.32* for physical representation)

F_c = radiation pattern of the seismic wave

R_c = free-surface amplification factor

Since the seismic wave includes two arrivals, the value of the total seismic moment (M_o) is as follows (Gibowicz, 1990):

$$M_o = 0.5\left(M_{o(p)} + M_{o(s)}\right) \qquad 2.49$$

where: $M_{o(p)}$ = compressional component of seismic moment [N·m or J]

$M_{o(s)}$ = shear component of seismic moment [N·m or J]

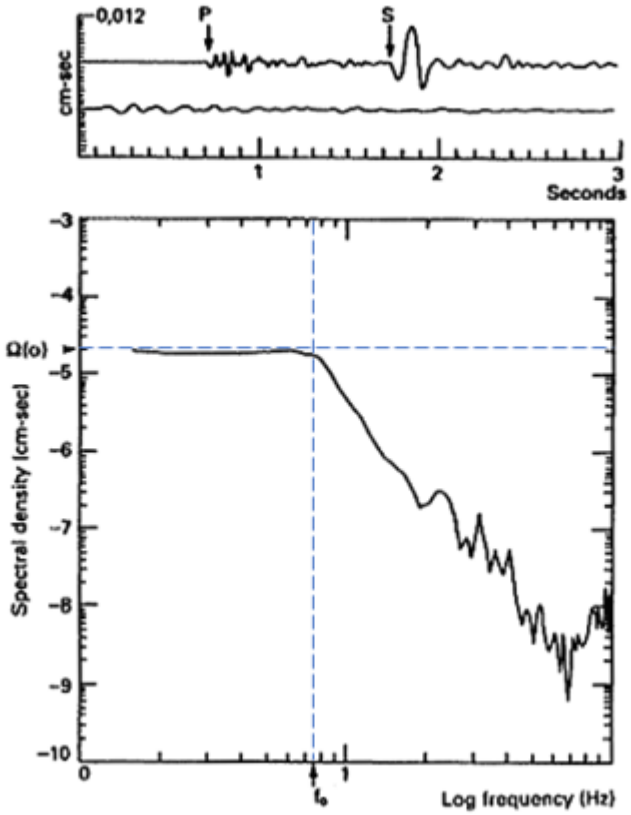


Figure 2.32: Velocity seismogram of a seismic event and the associated S-wave displacement spectrum density plot (McGarr, 1984)

In practice, the seismic moment is felt to be the superior to other source parameters. Since it is independent from the source model, seismic moment provides a robust estimate of the event's strength (Gibowicz et Kijko, 1994).

2.3.2.1.3 Seismic Energy

The seismic energy (E_s), as derived from waveforms, is the measure of radiated kinetic energy. It is proportional to the integral of the squared velocity spectrum in the far field. The seismic energy is relatively small in proportion to the total energy release (Mendecki, 1997). Boatwright & Fletcher (1984) proposed the following seismic energy calculation per wave part:

$$E_{s_{(p,s)}} = 4\pi\rho C \langle F^c \rangle^2 \left(\frac{R}{F^c R^c}\right)^2 \int_0^t v_s^2 \, dt \qquad 2.48$$

where: $E_{s_{(p,s)}}$ = radiated seismic energy component of P- and S-waves [J]

Vs = seismic particle velocity [m/s]

t = duration of the passage of the seismic wave [s]

The integral term is output from the waveform and refers to as the energy flux (J_c). The total radiated seismic energy is as follows (Gibowicz, 1990):

$$E_s = E_{s(p)} + E_{s(s)} \qquad 2.49$$

where: $E_{s(p)}$ = compressional component of seismic energy [J]

$E_{s(s)}$ = shear component of seismic energy [J]

2.3.2.1.4 Source Radius

The source radius (r_o) estimates the slip area produced by a seismic event. This parameter is highly dependent on the source model. The following formulation describes the source radius parameter (Gibowicz, 1990):

$$r_{o\,(P,S)} = \frac{K \cdot C}{2 \cdot \pi \cdot f_o} \qquad 2.50$$

where: K = source model dependent [1]

In mine seismology, the Brune circular shear-dislocation model is used to relate the characteristics of the source to that recorded by the waveform. In an elastic medium, a constant stress drop is assumed over the circular fault, resulting in shear waves propagating orthogonal to the slip surface (Gibowicz 1990; Hedley, 1992; Mendecki, 1997). The Brune model produces K = 2.34 in the previous equation. Although we physically can't measure the entire slip amount of an event, this model has been recognized to overestimate the source dimension (Gibowicz, 1990).

2.3.2.2 Seismic Source Mechanism

In this section, two of the most common seismological methods are presented for investigating seismic source mechanisms from waveform and inferred techniques (Hudyma, 2010). It is not the goal to elaborate the details of these analyses, but rather to give a general feel of these seismology approaches in an effort to identify rockmass failure. Therefore, the main assumptions and limitations of each concept are exposed for a mine setting.

2.3.2.2.1 Waveform Techniques

Fault-plane solution (or first motion analysis) is a graphical representation used in seismology to depict the orientation of faulting or the relative movement of rocks along a fault plane. The first motion of P-wave propagation at different sensor locations is used to determine the orientation and type of faulting that occurred during a seismic event (i.e., normal, thrust or reverse & strike-slip). At the mine scale, the fault-plane solution is used to identify weak geological structures (Urbancic, 1991; Duplancic, 2001) or systematic fracture patterns (Urbancic & Young, 1993).

The Seismic Moment Tensor Inversion (STMI) technique was elaborated in response to the growing evidence of alternative (non-shear) earthquake mechanisms (Gibowicz, 1990). The SMTI goes one step further in describing the rock failure process as compared to the fault-plane solution. A seismic moment tensor is composed of nine couples acting at the focus, derived from the recorded seismic wave data through fitting methods. It provides detailed information about the orientation and magnitude of the forces responsible for generating seismic waves during the event (Aki & Richards, 1980). By decomposing the moment tensor, the failure source can be expended to sudden increase (expansion) or decrease (contraction) in volume. The SMTI allows to gain further insight in the dynamic processes taking place during rockmass failure (Baig & Urbancic, 2010). Jost & Herrmann (1989) outline general technique for moment tensor inversion. A seismic moment tensor decomposes into three components (Gibowicz, 1990):

1. Isotropic (ISO) represents volumetric changes at the source.
2. Double-Couple (DC) represents the shearing mechanism.
3. Compensated Linear Vector Dipole (CLVD) represents compression or tension.

As pointed out by Hudyma (2010), several technical and practical challenges skew the reliability of waveform techniques to confidently decipher source mechanisms:

1. The quality of the recorded waveform, which must be of high resolution.
2. The seismic sensors array must surround the event, which is problematic for mines with infrastructure on the footwall while exhibiting events on the hangingwall.
3. The SMTI analysis requires at least six triggered triaxial geophones, which limits some operations.
4. The STMI requires a hight level of technical oversight with commercial software made limited.

Although both methods regularly appear in seismology studies, there is relatively low success in routine application of mining events due their low radiation quality (Gibowicz et Kijko, 1994; Mendecki, 1997; Hudyma, 2010) and the sheer output of recorded events (mines can produce 100s of seismic events / day). The mining environment generates parasitic noise continuously (e.g., ore-pass, drilling, electrical) which disrupts the quality of the waveform. In consequence, most mine sensor layouts are sub designed. Andersen & Spottiswoode (2001) attempted to corrective the STMI for mine-induced seismicity. Nonetheless, these tasks remain rigorous and usually yield ambiguous results (Gibowicz et Kijko, 1994).

2.3.2.2.2 Inferred Techniques

Inferred techniques use cluster analyses of a *representative* sample size of seismic event in order to characterize the seismic source mechanism through empirical and rule-of-thumb application (Hudyma, 2010). The most comment inferred techniques employed by mines are outlined below (Hudyma, 2010):

1. **Seismic source event location**: Spatial representation of seismic events allows identification of unstable rockmass failures by linking seismic clusters to specific geological structures, mining fronts, pillars, and blast sources (Leslie & Vezina, 2001). The event locations must correlate well within the underground mining environment.
2. **Energy ratio (Es / Ep)**: As observed for earthquakes, the S-wave to P-wave energy ratio of ~ 10 indicates a double-couple source mechanism (Boatwright & Fletcher, 1984). These events are typically associated with fault-slip. Non-shearing seismic source mechanisms present a ratio of S- to P- of 1–3 at the mine scale (Urbancic et al., 1992). This relates to volumetric stress changes, propagation of stress fractures or tensile failures

(Hudyma, 2010). Energy ratios between 3 and 10 represent a mixed failure mode which combines shear and tensile components (Coulson & Bawden, 2008). The energy ratio should scale with increased magnitude occurrences as fault-slip events dominant in that upper range. This is not always the case in practice. Hudyma (2008) noted in a stoping abutment that the energy ratio presents scale independence as low magnitude ($M < 1$) produced a higher cumulative percentage of $Es / Ep > 10$, while greater magnitude ($M > 1$) produced lower energy ratios. Some mines report Es / Ep ratios lower than 10 for 2/3 of their events (Gibowicz et al., 1991; Coulson & Bawden, 2008). In South African gold mines, in the Welkom gold field, evaluation of the Es / Ep ratio for macroseismic events ($M > 1$) inferred slip initiation at $Es / Ep > 1$, while $Es / Ep < 1$ represented pillar or confined dyke ruptures (van Aswegen & Butler, 1993).

3. **Magnitude-Frequency relationship**: The slope of the Gutenberg-Richter Magnitude-Frequency plot, as developed by Gutenberg & Richter (1955), infers the seismic source mechanism. Referred to as the b-value, it is a parameter used to describe the relationship between the number of earthquakes of different magnitudes within a specific region or over a particular period. The b-value quantifies the rate at which the number of earthquakes decreases with increasing magnitude. A higher b-value indicates a steeper slope, meaning that smaller earthquakes are relatively more common compared to larger ones. Some mines present a bimodal (non-linear) distribution over the slope area, resulting in mixed events generated from distinct sources (Gibowicz et Kijko, 1994). Hudyma (2008) noted the importance of zoning during the frequency magnitude analysis. For an isolated fault, he measured a b-value of ~0.5 while the stoping area presented a b-value of ~0.9. It is generally accepted in mines that fault-slip events have relatively low b-value (< 1), while brittle failures due to stress change produce higher b-values (> 1).

4. **Diurnal Analysis**: The lag time between blast-time and temporal occurrences of seismic events can infer the seismic source mechanism. Events closely related to blasts tend to be classified as volumetric strain (induced) events as opposed to remote structural (triggered) events. This interpretation imposes a scale dependence on the magnitude release with blasts. Hudyma (2010) developed procedures for comparing diurnal analyses between different geological zones. In contrast to the challenging waveform analyses, these inferred seismic source techniques allow to quickly investigate the temporal-spatial

variations within a seismic dataset efficiently. However, these techniques inherently rely on adequately zoning enough seismic clusters. Their reliability in inferring the source mechanism rests on grouping similar events. There is no official clustering or zoning procedure for inferred analysis as these composing events depend simultaneously on spatial and temporal distributions (Hudyma, 2010).

Other inferring techniques exist and further attempt to associate seismicity with stress release conditions in the rockmass, such as the Energy-Moment relation (Mendecki, 1997) and the Energy Index method (Mendecki, 1997); stress adjustment evaluation through the Apparent Stress to Time History evaluation (Brown & Hudyma, 2017); and ground deformation analysis by Cumulative Apparent Volume procedures (Minney et al., 1997). Mine seismology progressed in elaborating procedures attempting to correlate seismic parameters with rockmass properties. However, efforts need to be made to improve inherent source location errors. Mendecki (1997) estimated that fewer than 1% of seismic data is utilized to analyze the seismic rockmass response adequately. Potvin & Wesseloo (2013) commented on the current state of mine seismology:

The "Holy Grail" of mine seismicity is the prediction of the time-location-magnitude of large events based on precursors. If this could be achieved, it would allow for the evacuation of the areas at risk in time to avoid exposure of people to rockburst damage. Unfortunately, the current state of knowledge is not even close to achieving this. (Potvin & Wesseloo, 2013, p.379)

This statement also pertains to the field of rock mechanics, where the challenge of forecasting seismicity rests on acquiring reliable input parameters for the rockmass response.

2.3.3 Numerical Modelling Approach

The basic mechanism for inducing seismicity rests on the assumption that unstable failure processes occur inside the rockmass. The energy change brought about by mining contributes to the amount of the seismic release. Energy sources are generated from volumetric closures of the excavation boundary and the available strain energy within the extracted block (Cook, 1965a–b; Cook et al., 1966). At first, electrical resistance analogue constructs computed stresses, displacements and energy changes induced by tabular mine layouts of simple geometries in South Africa (Cook & al., 1966).

The underlying accomplishment of Cook's (and associates') research has been successfully identifying a transition zone between the elastic peak and residual strengths (Linkov, 1992). This allowed seismic mechanism theories to evolve to more complex strain and structural kinematic instabilities (Cook, 1976; Salamon, 1984; Ryder, 1987). Since the 1960s, various codes have been developed to compute elaborate mining layouts and rockmass responses. With improving computational speed, applying numerical methods to rockbursting has been relentlessly attempted. Typical model results present low prediction of seismic failure (on magnitude-time-location), as major events are still being reported today, suggesting that reality does not yet match theory (Wiles et al., 2001). Nonetheless, numerical simulations have been shown to produce reasonable estimates of seismic hazards (e.g., Wiles, 2005). This section will attempt to present the current state in numerical modelling of mine-induced seismicity. A significant body of data has been published on the subject which can be subdivided into four main seismic-modelling applications:

1. Layout modelling assessment.
2. Synthetic mine seismicity.
3. Punctual seismic analysis.
4. Computational learning techniques.

Each application has its own subset of numerical procedures that focus on specific mechanisms related to the physics of failure. Every numerical modelling approach has strengths and limitation as seen in Table 2.2.. Inherently, these characteristics are captured into the seismic forecast schemes.

Table 2.2: General advantages and disadvantages of numerical codes (Hoek et al., 1991; Simon, 1999)

Numerical code	Advantages	Disadvantages
Boundary element method (BEM)	Far-field conditions inherently represented. Only boundaries require discretization.	Coefficient matrix fully populated. Solution time increases exponentially with number of elements used.

Table 2.2: General advantages and disadvantages of numerical codes (Hoek et al., 1991; Simon, 1999) (cont'd)

Numerical code	Advantages	Disadvantages
Finite-element/difference methods (FEM/FED)	Material heterogeneity easily handled. Material and geometric non-linearity handled efficiently with explicit solution techniques. Matrices are banded with implicit solution techniques. Explicit solution techniques are used, less skill is required from user.	Entire volume must be discretized Far-field boundary conditions must be approximated. For linear problems, explicit solutions techniques are slower. Solution time increases exponentially with number of elements used for implicit solution techniques.
Discrete-element method (DEM)	Data structures well suited to model systems with high degree of non-linearity from multiple intersecting joints. Very general constitutive relations may be used with little penalty in terms of computational efforts. Solution time increases only linearly with number of elements used.	Solution time seem much slower than for linear problems. Results can be sensitive to assumed values of modelling parameters.

2.3.3.1 Mine layout assessment

In rockburst-prone ground, mine layouts are often assessed using the numerical ERR or ESS techniques (COMRO, 1988; Jager & Ryder, 1999). Well-designed stoping layouts provide strategic and tactical means for combatting induced seismicity, as described in **Section 2.3.1**. These techniques have been implemented in various elastic BEM codes for routine stope analysis in South African mines (Budavari, 1983). In essence, a grid generator converts the mine layout design to grid elements and stresses are computed on or around these elements.

The ERR criterion allows to assess the energy release rate per element or on the entire extracted layout design. The model is assumed elastic, requiring input parameters for virgin stresses (magnitude & orientation) and the elastic properties of the rockmass (E & υ). At each specific mining step, the pre-mining stress and the post-mining displacement are numerically computed for the centre of each mined element. The individual ERR is computed from these results

(eq. 2.37) and averaged for the entire mining step. The total energy release (ERR multiplied by mined area) is equivalent for both assessments. The mining step is equivalent to the physical area planned to be mined (i.e., the extracted mining steps should match the extraction plan). The average ERR compares to empirical charts for forecasting seismic potential (see *Figure 2.26*). For a specific layout (i.e., a fixed extraction area), all possible mining sequences taking place within the layout boundary will produce the same final energy output (Spottiswoode et al., 2000). This is due to the elastic assumption which ignores plasticity and produces the same amount of convergence at the final layout profile. Consequently, the optimal sequence will result in the smallest energy jumps with high ERR values necessitating remedial actions. Numerous studies for tabular mines (mostly in South African) have been conducted for ERR assessment (Spottiswoode et al., 2008; Hofmann, 2012; Scheepers et al., 2012).

A numerical limitation of the ERR technique arise at the grid size, or the quarter-grid error (Ryder & Napier, 1985). It was observed that ERR was affected by element size where lower ERR values were computed on smaller elements (Spottiswoode et al., 2000). At the mine-wide scale, average ERR must be adequately zoned with their stoping areas. Conceptually, this analysis ignores the seismic potential in final cuts or remnant pillars. As mining progresses, these blocks may continue to produce off-reef seismicity. The elastic assumption produces high fictitious stresses in the mining abutment which quickly increase the ERR output. To counter this effect, Spottiswoode (1997) suggested capping the computational stress at 250 MPa but allow the convergence to take on full effect. This produces lower ERR ratings but hinders its correlation with empirical charts. The energy release component is not a direct expression of recorded seismic energy which has a low radiation efficiency consumed by heating, sliding and crushing (Jager & Ryder, 1999). Studies suggest that ERR correlates with other seismic parameters like magnitude, seismic moment and apparent volume (Spottiswoode et al., 2008). However, it is unsure how ERR derived in North American mines correlates with South African practice (Hedley, 1992).

The ESS criterion gives a quantitative assessment of seismic potential for an effective stope layout. The numerical assessment can be made by using any elastic code. The input parameters are virgin stress and the basic static friction and dynamic friction properties of the structures (C, φ_s & φ_d). The ESS stress lobes can be plotted from the numerical stresses resulting for explicit and implicit fault constructions. For explicit constructs, actual fault dimensions and orientations

can be validated for slip initiation. For the implicit constructs (see *Figure 2.31*), a tangential trace along oriented ESS lobes can suggest critical seismic parameters by selecting a **peak** stress-drop ($\Delta\hat{\tau}$). This technique is particularly useful when there is limited structural information (Salamon, 1993). The ESS modelling technique can account for seismic events as far as >200 m from active mining (Ryder, 1987; 1988). Napier (1987) and Spottiswoode (1997) confirmed the use of the ESS concept as a mine layout tool for South African mines.

The main limitation of the ESS revolves around the uncertainty when selecting the peak stress-drop as physical faults sweeping through the ESS lobes do not necessarily result in immediate trigger. Asperities or rock bridges between offset faults may delay the slip onset. The ESS also ignores the interaction (or stress relief) between faults. As stated by Salamon (1993):

> *The practical disadvantage of the [ESS] method is that, while it identifies regions of potential high seismicity, the relationship between ESS and the mining activities is obscured. (Salamon, 1993, p.298)*

Additional numerical layout concepts have been developed to improve these numerical design analyses. This includes the Generalized Energy Release (GER) and the Volumetric Excess Shear Stress (VESS). The GER (Hildyard et al., 2006) is an extension of the ERR as it includes the strain energy released through fracturing and is suggested to produce more reliable energy release. The potential advantage of the GER is that it outputs the best mining sequence. Unfortunately, not much fellow up has been done on this procedure. The VESS (Spottiswoode, 1990) complements the ESS assessment by constraining the amount of slip with the volumetric seismic moment. This model attempted to consider the three-dimensional rockmass behaviour from a two-dimension model (layout is in plan view), this allowed for slip analysis to be made on offset planes above the mine layout.

The Rockburst Hazard Index (RHI) combined the ERR (which ignores structures), the ESS (often difficult to interpret) and the VESS (relates to a volumetric failed zone) into a single concept (Esterhuizen, 1997). For each mining element along a reef, the RHI is computed by summing the changes in VESS and the moment resulting from the ESS along geological structures and weighted by a factor dependent on the local ERR. The RHI value is scaled from 0 to 2,000 which scales with relative ERR values (ERR ~30 = RHI ~900) and the expected rock front quality (Esterhuizen, 1997).

2.3.3.2 Mine Wide Synthetic Rockmass Modelling

The synthetic rockmass modelling was developed to evaluate slip potential on discontinuities representative of the mining environment. Large mine settings (at the mine scale) can be evaluated by this technique. The induced mining stresses are computed per mining step, mapped onto the faults, and assume a slip criterion. Simulated seismic data can be compared with seismic records. Linkov (2013) identified two main types of synthetic analyses: (**i**) passive (simulates seismicity), and (**ii**) active (employs seismic records for calibration). This technique is independent of model type and can be implemented in a 3-dimensional environment with minimal input parameters (Salamon, 1983).

Salamon (1993) first proposed this methodology for a relatively simple layout where he simulated mine-induced seismicity during reef extraction (Linkov, 2013; 2016). The number and locations of discontinuities were randomly distributed, assuming a uniform probability density function. Salamon utilized the ESS to evaluate slip of the synthetic fracture network, where the Mohr-Coulomb slip condition was evaluated at each of the centroids. If satisfied, slip was assumed over the entire circular surface of the flaw. Salamon successfully rearranged the numerical-seismological assessments into GRMF plots.

Board (1994) expanded on the Salamon concept (utilizing ESS) by testing the synthetic rockmass model at the mine scale with structural parameters estimated from geological mapping and by computing the slip length along the rupture planes. The slip history on faults was ignored by restricting faults from remobilizing after their initial slip. In this manner, only friction controls the fault onset which was first inferred from literature. The concept was applied to a 2-D and 3-D case study at the Lucky Friday mine. Board succeeded in simulating synthetic seismic patterns (*Figure 2.33*) as well as comparing the synthetic GRFM plot with that of the mine (*Figure 2.34*). Board's analysis was observed to correlate well with three of the five slip-type mechanisms identified on major seismic events ($\geq +2.5\ M_L$) at the Lucky Friday Mine (Whyatt, 2000).

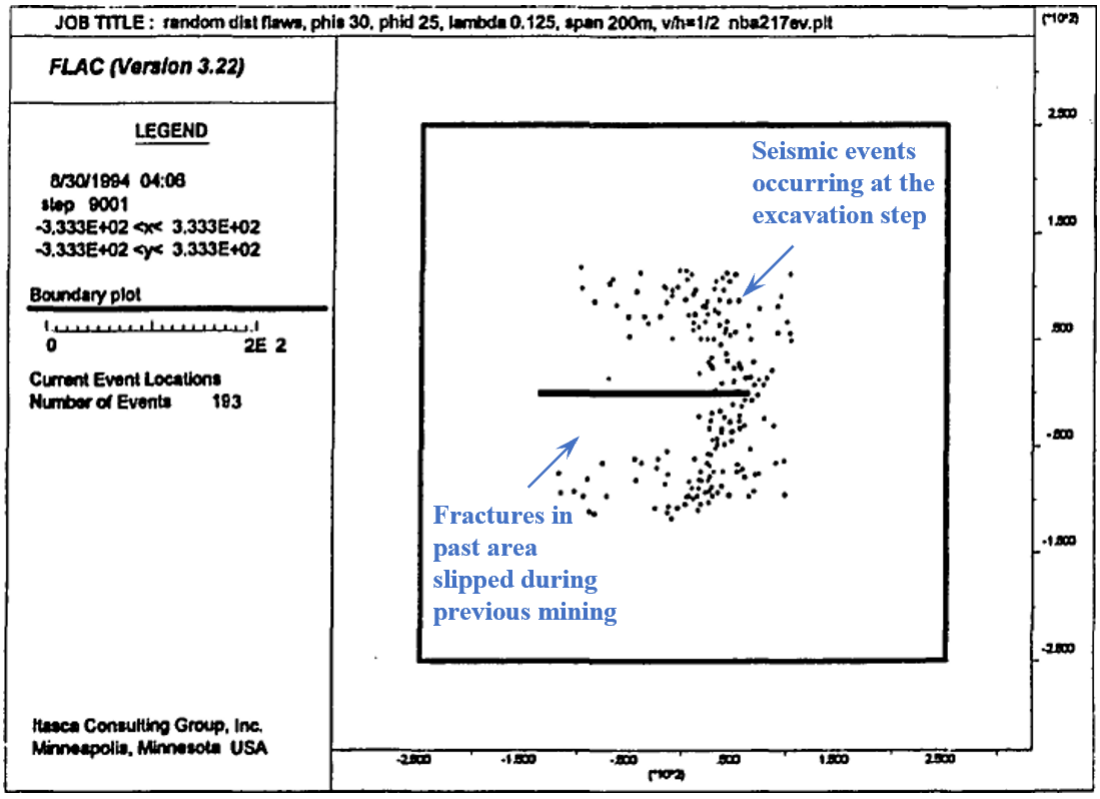


Figure 2.33: Simulated fault slip events ahead of a tabular mining front (Board, 1994)

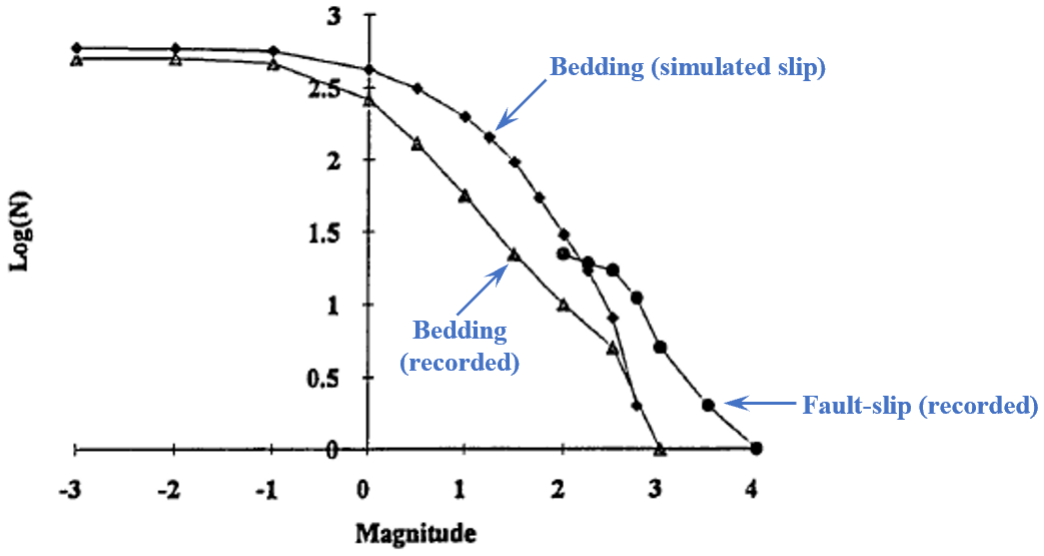
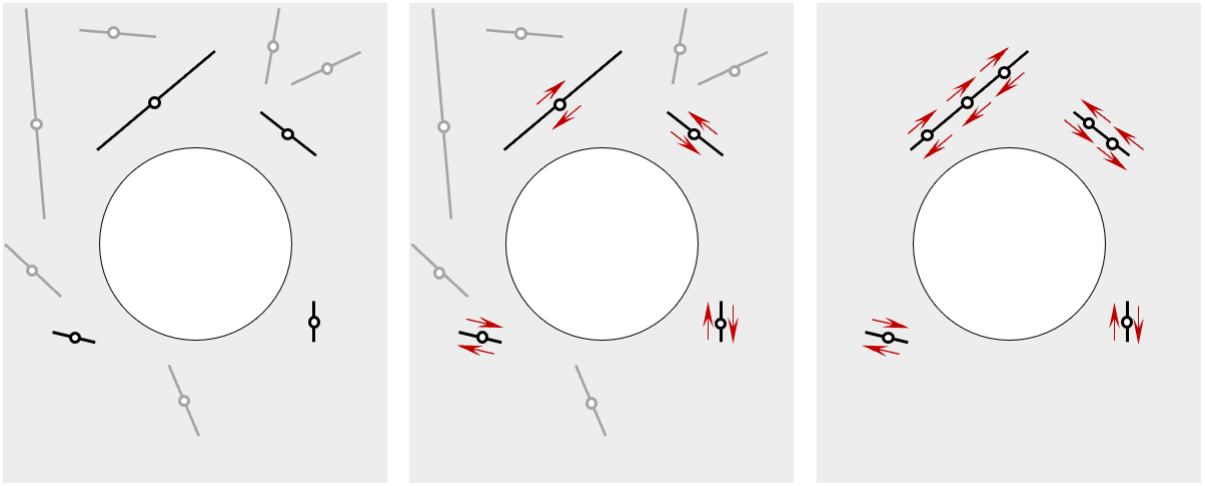


Figure 2.34: Frequency-magnitude response of simulated vs recorded (Board, 1994)

The main draw back for these techniques is they do not account for aseismic slip or any volumetric failure. In this regard, Linkov (2013) adjusted the Salamon (1993) method to

incorporate softening of fractures by incorporating a simple model (termed the Elastic-Softening-Creep) to evaluate seismic and aseismic slip responses. By ignoring tensile failure and creep, Malovichko & Basson (2014) extended the Linkov method by producing an implicit fault generator independent of flaw size, orientation, and location. All three slip models are compared herein (*Figure 2.35*). The Salamon and Linkov (DD) models rely on a synthetic flaw environment where mining stresses are mapped onto the fractures and tested for slip. The Malovichko & Basson (DD) model does not rely on a pre-seeded flaw environment, rather slip is determined by coalescing failed elements into discrete structures. This significantly reduces the amount of input parameters required by synthetic flaw schemes (Malovichko & Basson, 2014). Model grids implicitly assess for volumetric instabilities, although the primary failure assessment presents slip characteristics (intact rock has significantly higher frictional properties than faults). In a further attempt, Linkov *et al.* (2016) evaluated the minimum input parameters to agree with the proposed the Malovichko-Basson method. Additionally, Malovichko (2017) expanded his seismic analysis to compare synthetic seismicity directly to record events. These synthetic flaw techniques have been successfully applied in specific mine studies in Canada, Australia and Russia. Although promising, (to the author's knowledge) not much research into this method has continued since 2017.



(a) (b) (c)

Figure 2.35: Flaws integration and failure logic according to various rockmass populating methods (a) Salamon, (b) Linkov, and (c) Malovichko-Basson (Malovichko & Basson, 2014)

2.3.3.3 Modelling Punctual Seismic Events

Numerical models also apply punctual analyses of seismicity with regards to a specific mine layout or setting. This method attempts to calibrate the numerical results with observed seismicity in order to gain insight on the source mechanism. These techniques are sometimes sensitive to model (code) type.

The stress analysis techniques rely on comparing the deviatoric stress with the spatial-temporal seismicity. By associating seismic events to stress contours induced by mining, this comparison allows to identify seismic initiation stress — comparable to the threshold initiation for AE observed in laboratory. Many studies have conducted this type of analysis (e.g., Castro et al., 2009; Bewick et al., 2009; Morissette et al., 2017).

The numerical assessment of the focal mechanism relies on simulating a mining environment and relating it to the recorded first motions (orientation of the shear plane dislocation). The analysis procedure compares the σ_1 and σ_3 vector orientations with the first-motion spherical (beach ball) representations. As was observed by Lourence *et al.* (1993), orientation of shears does not always agree with the numerical simulation. Malovichko (2013) needed to modify the stress magnitude and orientation to force fit numerical data with the focal results.

Structural fault-slip instabilities identify the mechanism allowing for slip along a known structure plane. These techniques also rely on calibrating the numerical results to observed seismicity. Hofmann *et al.* (2001) successfully identified the unfavourable mining layout responsible for triggering a +3.2 M on a known structure by evaluating regions of increased shear displacement. This methodology utilized an elastic 3-dimensional BEM by adjusting the frictional properties of the fault until the probable condition is met, as was demonstrated in subsequent studies (Hofmann et al., 2013a; Hofmann et al., 2013b, Hofmann et al, 2012). Many authors have attempted this procedure (e.g., Troncoso et al., 2012; Orrego et al., 2013). Wiles (2014) suggested the plastic ride methodology as an extension to the shear-stress fault analysis, allowing for plastic analysis on DD elements in the MAP3D (BEM) software. Dynamic fault slip analysis requires to simulate conditions such as wave propagation and attenuation, ground motion, asperity shear and crack propagation. Sainoki (2014) presented valuable procedures to accomplish these analyses in a mine setting. These techniques rely on dynamic capable models such as FEM or DEM.

Other computational strain energy concepts exist such as the Strain Energy Storage Rate (ESR) (Mitri & al., 1999), the Local Energy Release Density (LERD) (Wiles, 2005), and the Energy Release Speed (Yan et al., 2012). These techniques employ numerical tools for assessing strain energy increases in a volume of rock subjected to mining stresses. The strain energy assessment can be performed elastically, using simple BEM codes, while more complex material responses are executed through FEM or DEM. These techniques attempt to correlate simulated strain energy with seismic energy release. However, their use is punctual to specific mine situations (e.g., diminishing pillar) as they do not rely on critical value onsets like the ERR.

2.3.3.4 Computational Learning Techniques

Up and coming machine learning techniques, reviewed in detail by Zhou *et al.* (2016), calibrate numerical modelling results with recorded seismic and geotechnical information. The biggest problem lies in the input parameters, as rock mechanic data is not always optimal and (most often) obtained from *questionable* sources—as pointed out by Hadjigeorgiou (2012) in the entitled paper: *Where does the data come from?* It is highly unlikely that these programmes will overtake the engineering decision process which strongly relies on the practitioner's experience, knowledge and intuition of the rockmass response. Machine learning models could potentially assist mine planners in decision making—not replace it. Great care is needed when interpretating and integrating any simulated result into an active mine environment.

2.3.3.5 Section Summary

Observations from the literature highlighted that successful approaches for assessing seismic potential need to be simple, repeatable, and applicable to be retained by researchers and, even more, onsite engineers. As was noted by Spottiswoode *et al.* (2002), the VESS (Spottiswoode, 1990) and RHI (Esterhuizen, 1997) approaches were only advocated by their founders and were rapidly overtaken by LERD (Wiles 2005) and other computational programmes that integrated simple hazard procedures. A satisfactory numerical seismic procedure must provide quantitative results, comparable to those output by a seismic system, allowing to forecast seismic activity. The stochastic nature of seismicity hinders any approach's ability to precisely predict an earthquake's magnitude, time and location. In this regard, seismic prediction is even less possible for mining conditions where the act of mining has a direct impact on seismic outcome. However, some daily passive seismic assessments report success in South African gold mines

(van Aswegen, 2005). Only under clear settings can seismicity be *predicted*, where (for example) significant changes in seismic event rate arises before the occurrence of a large event while being distinct from minor events (Spottiswoode, 2010).

Understanding the physical processes of primary source mechanisms is key in reducing seismic risk as mine-operational control measures can be implemented to some extent. From rock mechanics and seismology, the source assessment techniques display distinct underlying limits and disadvantages. Linkov (2013) states that the two primary fields should merge:

We see that the advantage of one tool is the shortcoming of the other. Clearly, their integration serves to cross-fertilization, which preserves their benefits and removes the flaws. (Linkov, 2013, p.198)

Hence, the robust numerical modelling techniques, which are data limited (static), need to integrate seismological rich data (stochastic) provided by seismic monitoring (Linkov, 2013). The basic ingredients for combining these domains are (Spottiswoode, 2001):

1. Both fields need to talk the same language.
2. Identify the type of seismic event without ambiguity.
3. Allow for seismic forecast through forward modelling.

CHAPTER 3 SEISMICITY AT THE LUCKY FRIDAY MINE

3.1 Mining, Geological & Geomechanical Setting

3.1.1 Mining Context

The present-day Lucky Friday crews mine high-grade silver, lead, and zinc on a secondary ore-bearing structure located deep within the Wallace formation of the Coeur D'Alene mining district in northern Idaho, USA (*Figure 3.1*). This sheet-like orebody consists of several stacked sub-vertical mineralized lenses collectively known as the Gold Hunter (GH) vein system. The GH expansion has been mined by Hecla since 1997, relieving production from the primary Lucky Friday deposit in 2002. The captive GH resides ~1.5 km northwest of the historical deposit (*Figure 3.2*). Access between zones is provided by the (top) 4050 Level, the (middle) 4,900L, and the (lower) 5,900L haulage drives at about 1.5 km, 1.8 km and 2.1 km below ground surface, respectively. The 30-Vein is the most economical vein due to its greater continuity and mineralization width.

The prolific vein persists over a strike length of 670 m with a mined vertical extent of 640 m, reaching 6,500L ~2.3 km below the surface. The GH orebody extends significantly beyond the current mining depth, remaining open at 8,000L (~2.7 km below the surface). Current resources extend the mine life for 20+ years (Hecla, 2022).

The minimum mining width on the 30-Vein averages around 3 m but can reach up to 6 m. Secondary sub-parallel, offset veinlets compose the Intermediate-Veins packet, which has shorter vertical and lateral lengths and generally occurs at narrower widths (< 3 m). The tabular vein system strikes ~110° (N80W) and dips at an angle of ~80° south (near vertical). The GH zone produces about +800 ore tons per day (Hecla, 2022), with over 80% of the production occurring on the 30-Vein. The GHs' internal #4 Shaft hoists the ore up to the main lateral connection drifts, linking to the Lucky Friday workings. Haul trucks travel this distance, dumping the ore into the Silver-Shaft chutes leading the way to the surface.

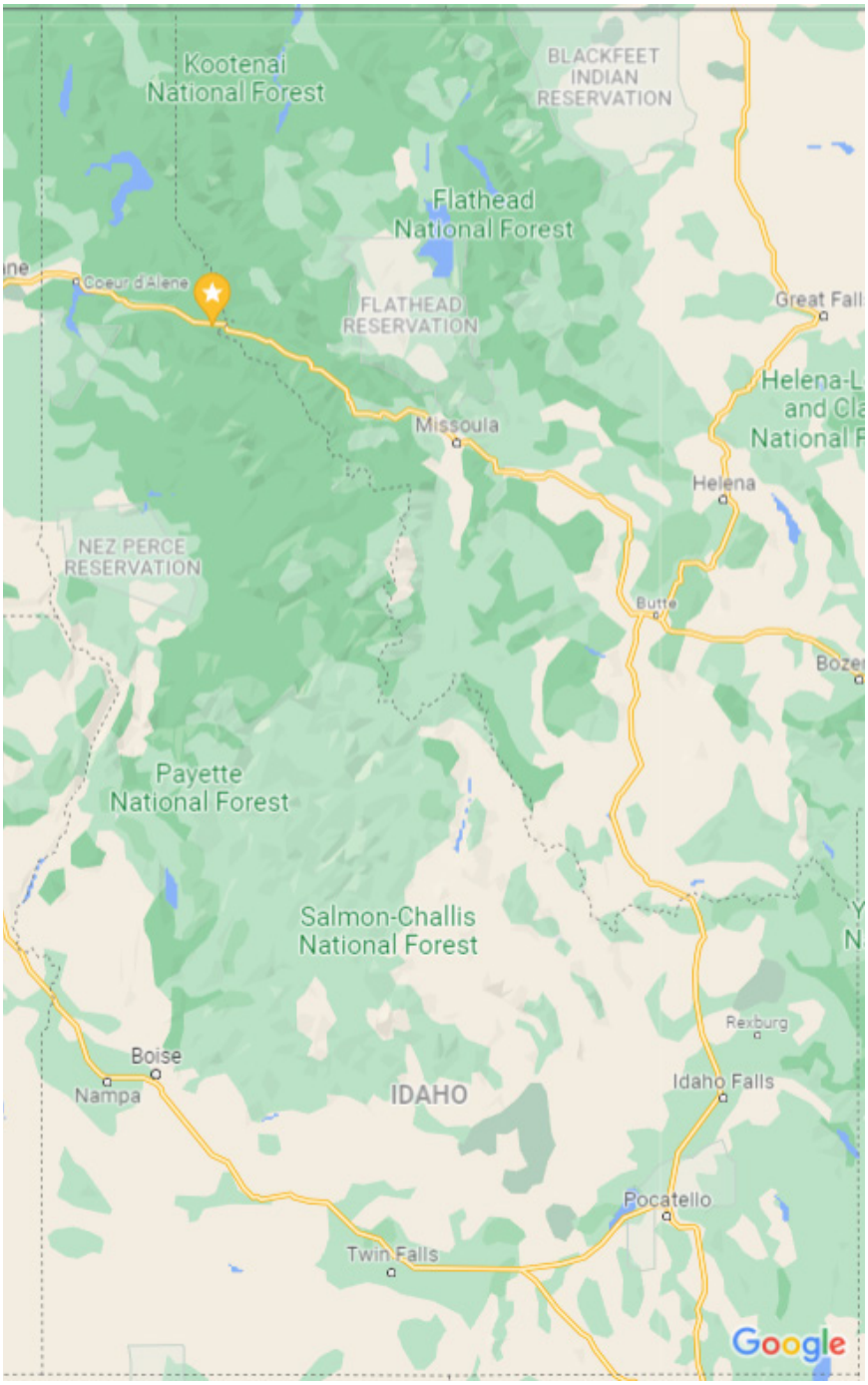


Figure 3.1: Geographical location of the Lucky Friday mine relative to Idaho state (USA)

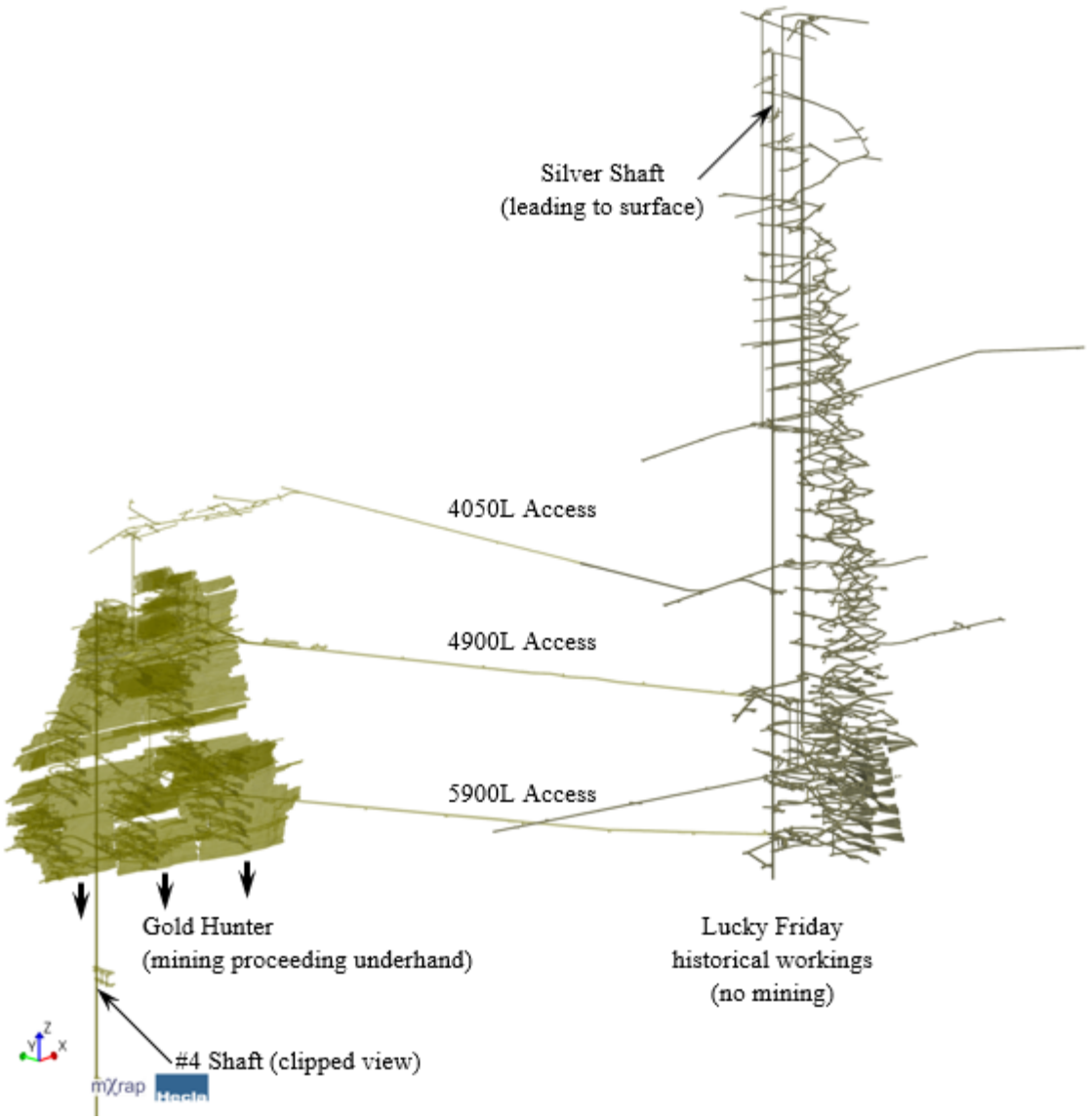


Figure 3.2: Isometric view of the GH (30-Vein) and the LF historical workings, looking ~North/East

Due to the tabular characteristics of the ore deposit (i.e., narrow & continuous), the mine employs cut-and-fill extraction sequences for (occasional) overhand and underhand mining. *Figure 3.3* illustrates the as-built geometry of 30-Vein and the Intermediate-Veins extracted on the GH. To maximize production, the operation mines 2 or 3 stopes on the longwall of the main vein, allowing simultaneous headings along the main vein. The 11S, 12S, 14S, 15S and 16S compose the main production stopes, each having two active faces per cut.

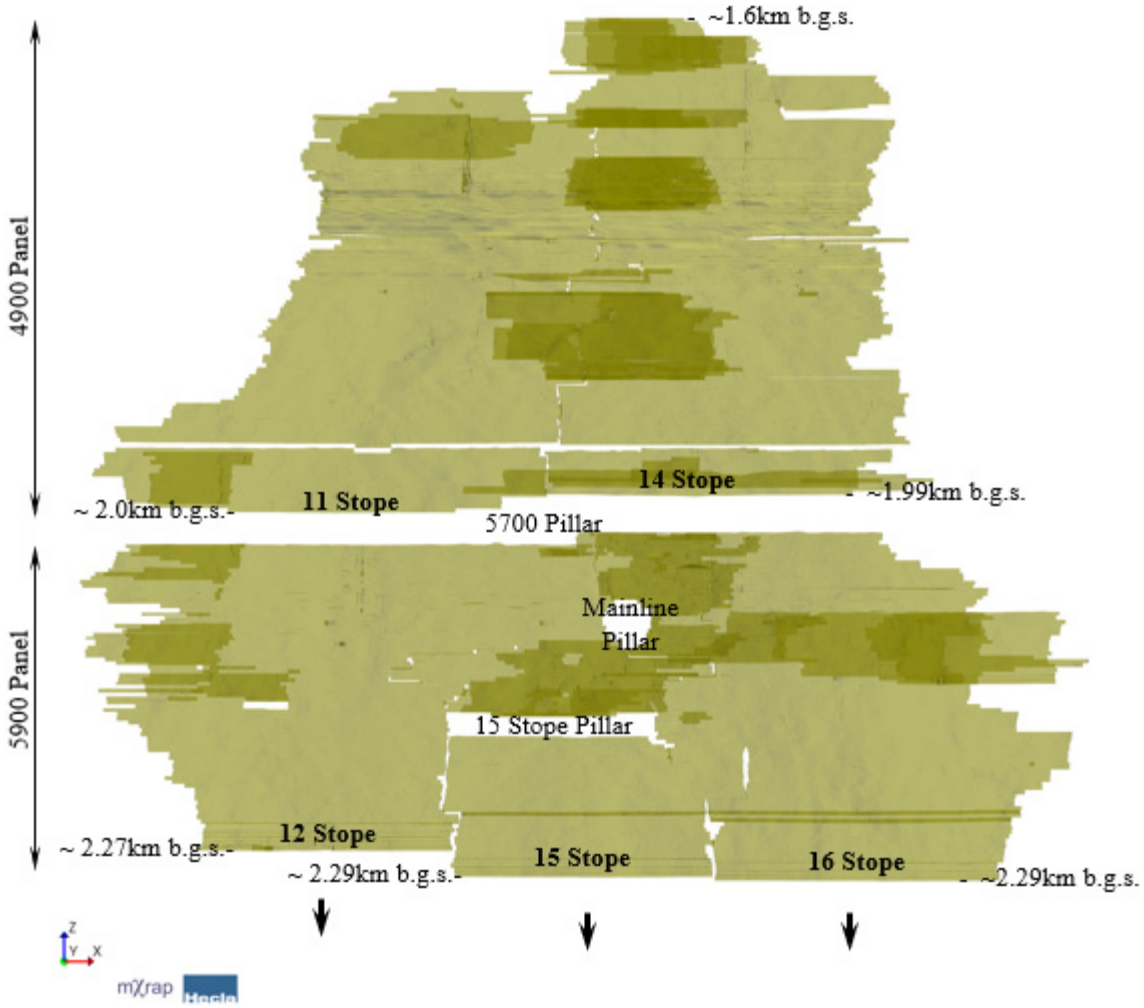


Figure 3.3: Longitudinal of GH 30-Vein and Intermediate-Veins (shaded), view is due North. As-built geometry 2021 year-end

The stope orebody is accessed through a central slot, which off-shots from the main ramp system established on the footwall (north side) of the orebody. The access slot design allows for extracting five (5) consecutive cuts before requiring a new access slot into the vein (*Figure 3.4*). Since the slot is positioned in the center of each stope, crews can mine two active headings per single cut. The typical cut-and-fill dimension is 3 m wide by 3 m high, advanced on 2.4 m horizontal increments, limiting the maximum width to ~6 m. Once stoping reaches the end-of-cut (stope boundary), the mine pours cemented paste backfill and slots underneath the fill to open the subsequent cut, exposing the sill-mat beam above. Underground operations remove about 18.3 vertical meters per production year, equivalent to cycling through one (1) complete cut every two (2) months.

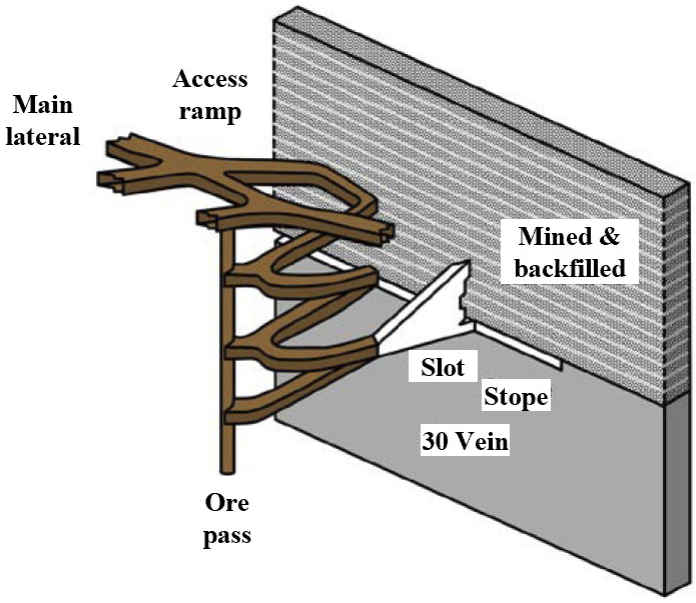


Figure 3.4: Section view showing the ramp and slot access into the underhand stope

Since late 2019, a new narrow-vein underhand long-hole mining method, known as the Underhand Closed Bench (UCB) has been developed and tested at the mine (Board et al., 2023). This novel mining method intends to proactively induce seismicity on structures near the stope using large, down-dip long-hole blasts without a relief sill and will be further described in **Section 5.1**. In 2021, the UCB mining method reached full production on the 30-Vein, accounting for 86% of the total tons mined that year, with a tonnage increase of over 40% when compared to that recorded in 2016 (Hecla, 2022). This operational increase removes about 30.5 equivalent vertical meters of ore in a production year, equivalent to cycling through one (1) complete UCB every three (3) months.

3.1.2 Geology & Relevant Structures

The rocks in the Coeur d'Alene mining district were formed during the Middle Proterozoic (ca. 1.45 Ga to 1.40 Ga), creating the Belt Supergroup series where sediments metamorphosed to quartzites, silts, and argillites (Hobbs et al., 1965). To comprehend the complex folding episodes, the Belt Supergroup quartzite rocks of the district have been subdivided into formations (*Figure 3.5*). At the Lucky Friday mine, the host rocks of the mineralized veins in the LF and GH deposits are the Revett and the Wallace, respectively, with interim occurrences from or into the St-Regis formation (*Figure 3.6*).

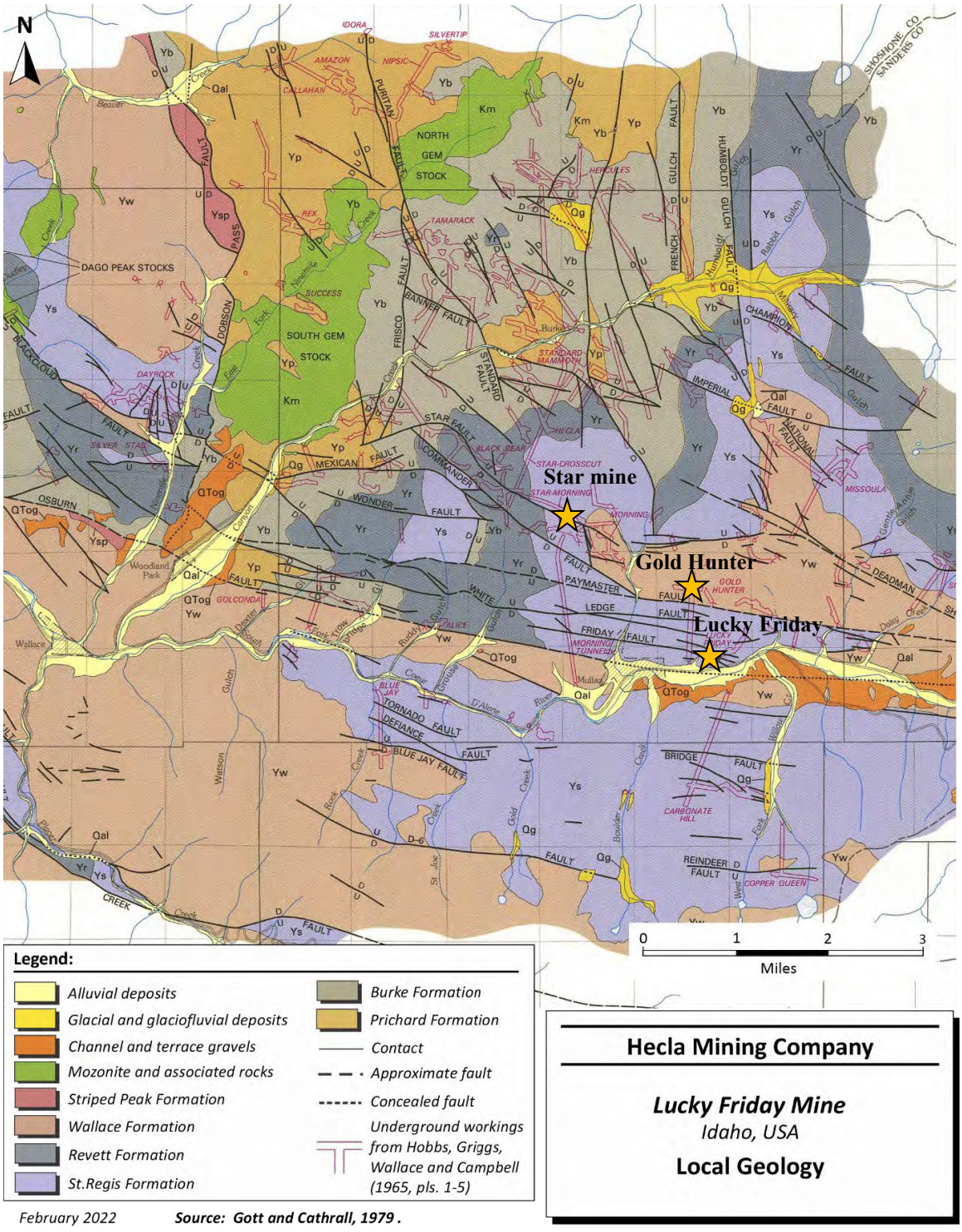


Figure 3.5: Local geology of the Star and Lucky Friday mine in the Coeur D'Alene mining district

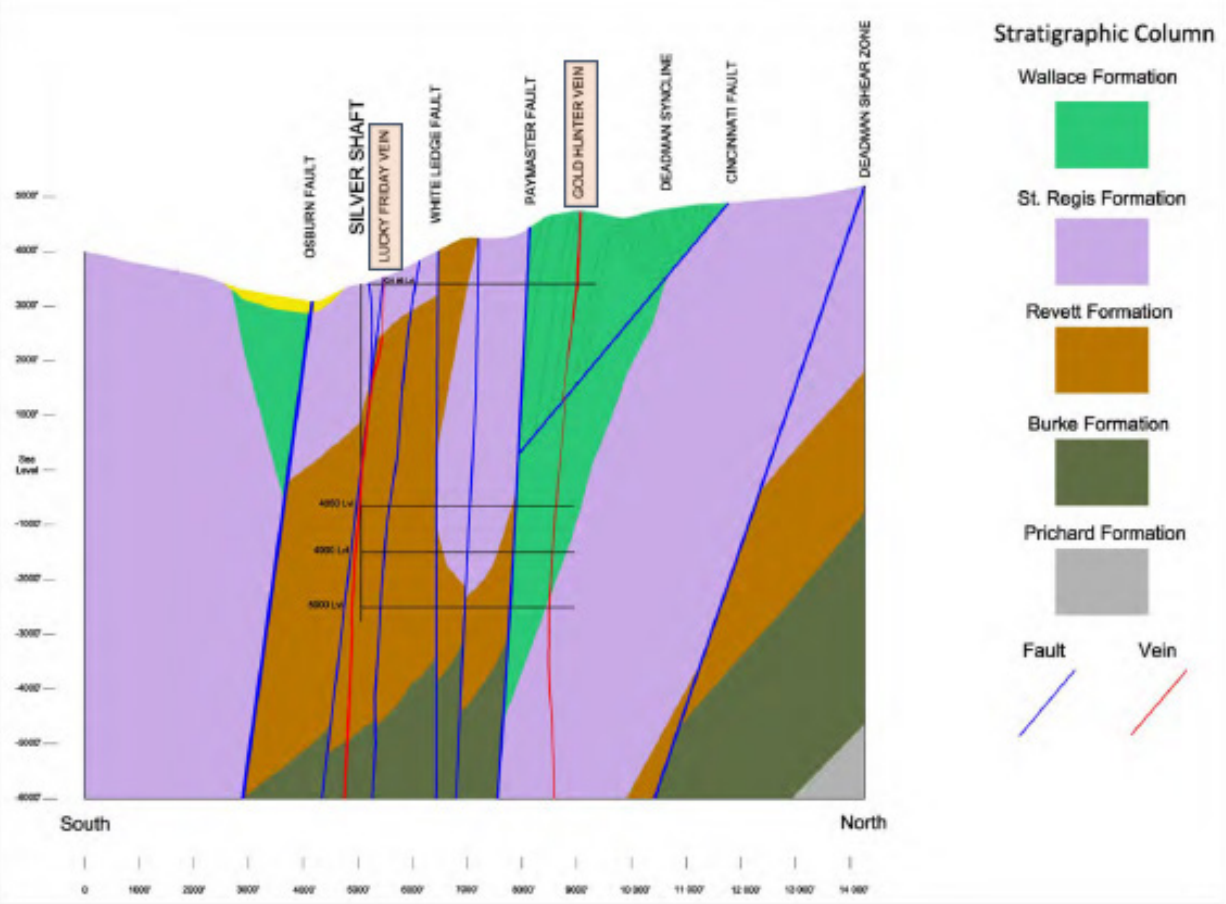


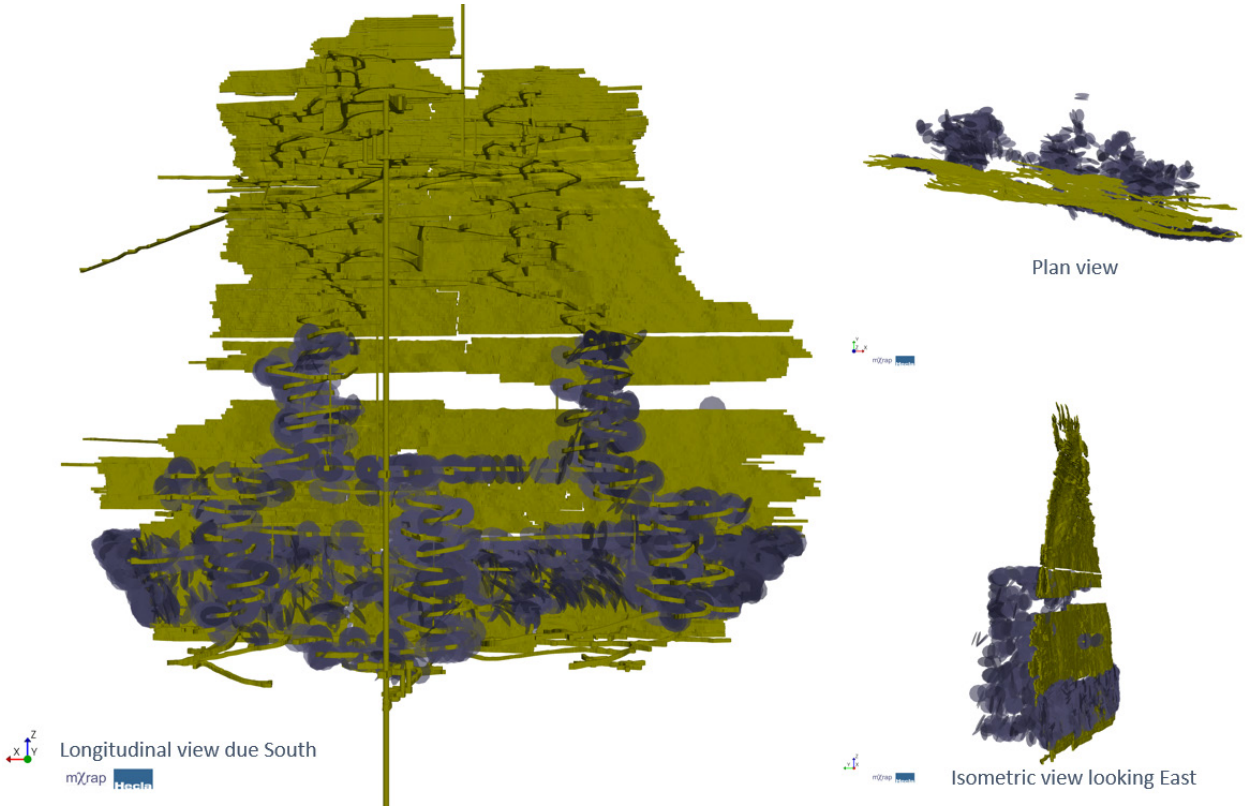
Figure 3.6: Geological cross-section of the Lucky Friday mine, highlighting the LF and the GH deposits

The Revett formation (LF deposit) encompasses most of the stronger quarzitic rock, vertically-bedded (vitreous) quartzite that grades to an argillic-quartzite, characterized by a brittle-type failure response. The Wallace formation (GH deposit) consists of softer rock (with less quartzite), vertically-oriented, thinly-bedded argillites, and argillite alternating with silt caps and local siltites, exhibiting a ductile response. In contrast, the St Regis formation accounts for intermediate rocks where it is reported below the 5,900 Level in the GH. In both portions of the mine, the bedding is roughly parallel to the vein system leading to anisotropic deformation for development headings oriented parallel with the strike of the foliation. Severe ground buckling was encountered during the #4 Shaft construction, forcing a redesign to an elliptical cross-section to complete the project (Sturgis & al., 2017). In practice, the intensity of the anisotropic response (squeezing or buckling) relates to the bedding plane thickness, the degree of surface alteration

and the angle of intercept with the excavation (Armatys, 2012). At the GH, the bedding plane thickness ranges from centimeters to decimeters, representing the main structural feature of the rockmass. Talc or chlorite minerals often coat the slickensided cleavage of structures.

The GH veins consist of gangue and sulfide mineralization. The vein material is predominantly siderite and quartz components with lesser amounts of barite and pyrite. The ore minerals constitute argentiferous galena, sphalerite, and tetrahedrite with minor sulfosalts.

At the mine, major structural features, such as the Paymaster fault, cut the rockmass on a regional scale, separating the two deposits. The GH vein system, which represents the main focus of this study, is further bounded between two sub-parallel east-west striking faults (i.e., the S1 and the Master fault). These secondary faults are near vertical, offset each other by ~91 m, and follow the trace of the 30-Vein for at least 460 m on strike. The Master fault sits on the south rib of 12S and 15S, delineating the hangingwall contact, while the S1 lies inside the footwall to the north. Several conjugated faults and related structures exist within the bounding fault system. Extensive mapping of persistent joints was undertaken in the ramp system between 5,600L and 6,000L (DeVoe & Meyers, 2017) and further supplemented with digitized in-stope fracture sets (Smith, 2021). Over 2,400+ structures were digitized on the footwall and grouped into family sets (*Figure 3.7*). Three (3) clearly defined conjugate sets, with the other designated F-series fault set (FS-2) and the inherent bedding planes (FS-9), emerged from the stereonet analysis to form the rockmass joint sets characterizing the GH zone. Although the minimum discontinuity length mapped was limited to trace lengths greater than 5 m, their continuity is currently unknown. Still, they have been traced up to 100 m when linked on multiple intercepts within the spiral ramp system. In addition, the continuity of these structures through the orebody is unknown due to limited development access into the hangingwall south of the Master fault contact. Traces are suspected to be sufficient in some cases, as certain fracture sets (notably the FS-2 series) have been directly linked to seismic activity at the mine (Seymour et al., 2016), releasing events $> +2\ M_w$. Regarding surface conditions, these fracture sets appear to be narrow and tight with slick surfacing, possibly coated with talcy minerals.



fracture set:	fs-2	fs-3	fs-4	fs-5	fs-6	fs-7	fs-8	fs-9
trend/plunge:	ne/n	ne/s	ne/n	nw/n	nw/s	we/n	we/s	bedding
dip.dir./dip:	347/58	112/55	317/59	067/67	240/71	010/65	194/75	180/60

Figure 3.7: Digitized mapped joint sets in the GH expansion area

3.1.3 Mechanical Properties of Rock

A sensible laboratory testing campaign on rock units taken from the GH wall and ore packages was performed by Agapito & Associates (2011). A total of sixty-two (62) uniaxial compressive strength (UCS) tests and twenty (20) triaxial tests were conducted. Thirty-seven (37) UCS were conducted on wall rocks and twenty-five (25) on vein package rocks. Triaxial confinement tests assumed confining pressures of 3.5, 7, 14, and 21 MPa. Four (4) sets of triaxial tests were conducted on wall rocks (three on footwall rocks & one on hangingwall rocks), with one (1) on the vein-package. Table 3.1 and Table 3.2 summarize the lab-scale results:

Table 3.1: Mechanical properties of intact rock at Gold Hunter

Group	Number of specimens	Mean Poisson's ratio (v) [-]	Mean Modulus of Elasticity (E) [GPa]	Mean uniaxial compressive strength (UCS) [MPa]	UCS min. [MPa]	UCS max. [MPa]	Std dev
Wall rock	45	0.26	33.6	106	26.4	253.1	47.3
Vein rock	17	0.40	48.1	109	12.4	169.7	46.3

Note: the resulting UCS follow a normal distribution with the indicated UCS min & max representing outliers.

Table 3.2: Mechanical properties of confined rock at Gold Hunter

Group	Number of specimens	Confining stress [MPa]	Mean ultimate strength (σ_1) [MPa]	Mean Elastic modulus (E) [GPa]
Wall rock	4	3.5	145	21.0
	4	7	158	19.6
	4	14	159	26.5
	4	21	207	30.1
Vein rock	1	3.5	184	31.4
	1	7	186	31.1
	1	14	240	37.7
	1	21	152	36.3

Ignoring foliation dependencies of intact rocks and attributing a rock quality rating (GSI) of ~60 (equivalent to fair quality rock), the vein rock (assuming lab scale $m_i = 27$) and wall rock (assuming lab scale $m_i = 25$) materials are illustrated at the rockmass scale in the figure below (*Figure 3.8*). As can be observed, both vein and wall rock failure envelopes provide similar strength responses over the confinement range (up to 100 MPa).

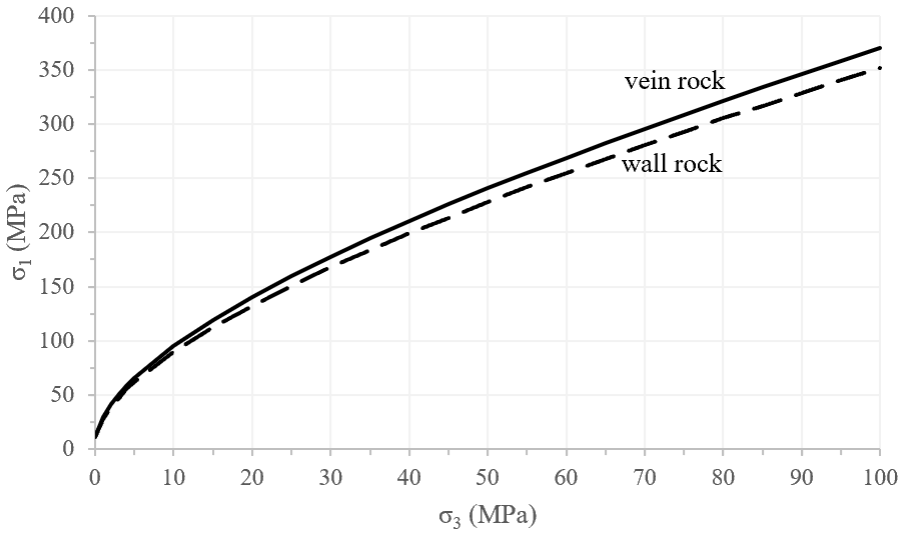


Figure 3.8: Hoek-Brown rockmass failure envelopes for vein and wall rock

3.1.3.1 In-Situ Stress

In-situ stress measurements have been performed at the Lucky Friday mine (Whyatt et al., 1995). Overcore measurement techniques, performed at the 4,250L and 5,300L in the LF sector, have estimated the principal stress (σ_1) to be horizontal. Several in-field observations of breakouts in boreholes, shafts, and raises at the mine have also confirmed this orientation. The maximum stress direction is likely N40°W (*Figure 3.9*). The k stress ratio estimate (σ_h / σ_v) falls between 1.3 and 2.0. These values are within the upper bound of the stress ratios recorded in the Silver Valley (Beus & Chan, 1980; McMahon, 1988). The stress measurements at the nearby Star Mine for the same period indicate a stress ratio of 1.5 (Whyatt et al., 1995). The GH deposit trends west-northwest towards the historic Star mine. The drift conditions at the GH do not support horizontal stresses of 2 times the vertical component. Therefore, the following mine-wide in-situ stress condition is assumed for the GH at the Lucky Friday mine (Table 3.3).

Table 3.3: Mine-wide stress field estimates assumed for the Gold Hunter

Stress Component	Magnitude [MPa/m]	k ratio	Bearing	Plunge
σ_3	0.029	-	vertical	90°
σ_2	0.035	1.2	N 50° E	0°
σ_1	0.044	1.5	N 40° W	0°

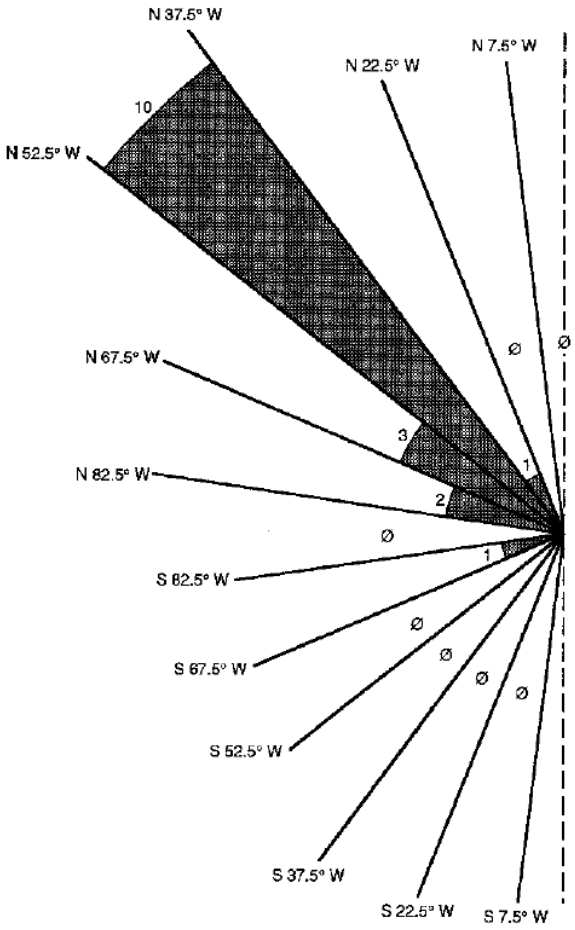


Figure 3.9: Rosette plot showing the frequency of σ_{h1} direction inferred from overcore measurements and observable breakouts at the Lucky Friday mine (Whyatt et al., 1995)

3.1.3.2 Rockmass Response to Mining a Tabular Deposit

The rockmass response to the extraction of tabular orebodies behaves similarly to that of an expending penny-shaped crack (or a planar slit) in a homogeneous elastic medium (Jaeger et al., 2009). As the crack length increases, the host medium succumbs to stress intensification at the crack tip, with volumetric convergence taking place in the back areas of the opening, forcing wall-to-wall closure. Therefore, mining extensive portions of thin tabular deposits is characterized by large, induced stresses and displacements. Analytical solutions exist for computing stresses ahead of the mining front and the convergence distribution along a mined-out horizontal stope span (Salamon, 1968).

$$\sigma_n = \frac{p_n \cdot x}{\sqrt{z^2 - l^2}} \qquad 3.1$$

where: σ_n = perpendicular stress into the abutment [MPa]

p_n = pre-mining stress perpendicular to the orebody [MPa]

x = distance along the span (z-axis) taken from the stope center [m]

l = half span of stope [m]

with: $x \geq l$

$$\delta_n = \frac{4 \cdot (1 - \nu^2)}{E} \cdot p_n \cdot \sqrt{l^2 - x^2} \qquad 3.2$$

where: δ_n = in stope perpendicular wall-to-wall closure [m]

E = Young's modulus of rockmass [MPa]

υ = Poison ratio [1]

with: $-l \leq x \leq l$

BEM codes, which are based on the Displacement Discontinuity (DD) method, are designed to readily perform these computations (Jager & Ryder, 1999). The physical representation of eq. 3.1–3.2 on a tabular orebody are illustrated in Appendix A.

To understand the stress state in the Gold Hunter, numerical assessments of stresses and the closures perpendicular to the 30-Vein are investigated below. However, the complete detail of the DD BEM setup constructed for this thesis is formally given in **Section 4.1**. The DD element mesh was reconstructed for the 2016 year-end mining geometry (*Figure 3.10*). The cross-section taken through 15 Stope on 17,661E (in mine coordinates) was used for querying the numerical results.

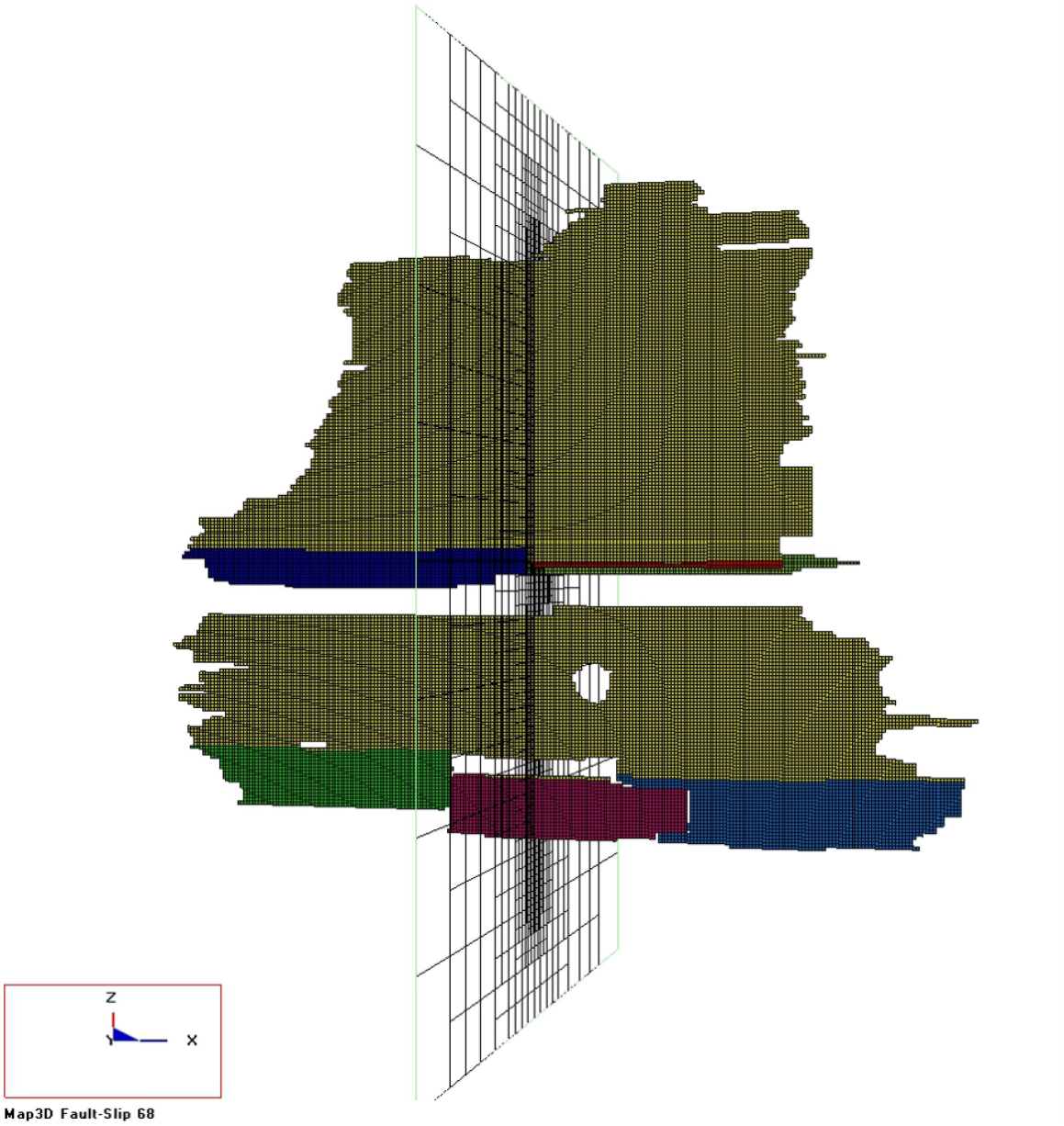
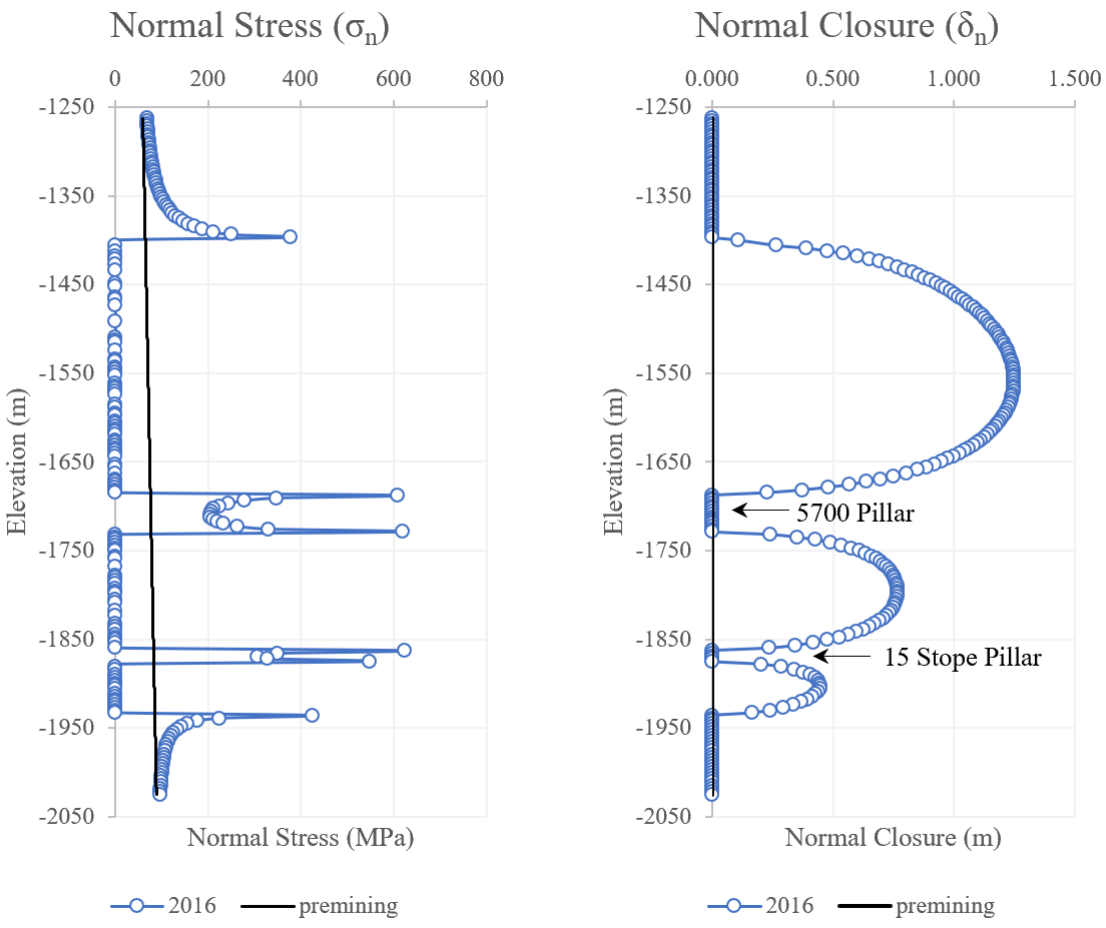


Figure 3.10: BEM DD construction of 30-Vein for 2016 year-end, section through 15S (17,661E)

The model has computed the normal stresses (σ_n) and closures (δ_n), with the results presented herein.

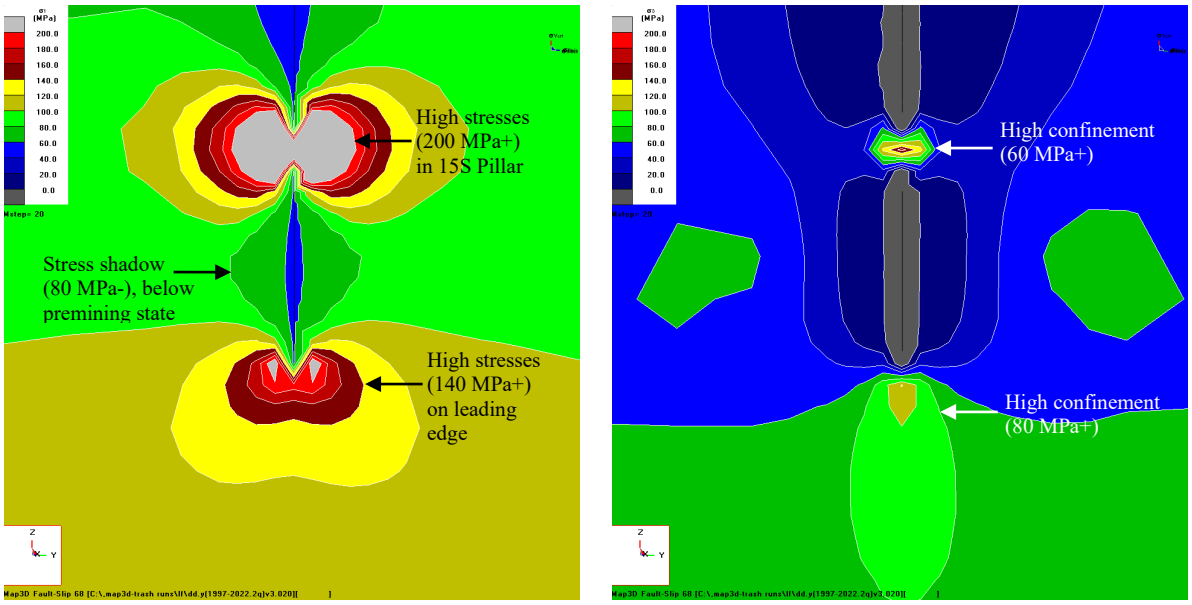
Figure 3.11 shows the variability of the perpendicular stresses and closures across the 30-Vein, into lower abutment of 15S as well as within the two remnant pillar configurations (15S Pillar & 5,700 Pillar). For comparison, the pre-mining stress and closure (taken perpendicular to the vein), were provided as a reference. To further the stress analysis, the stress trajectories of the

principal and minimum stresses are also provided (*Figure 3.12*). It is observed that stresses concentrate at the leading-edge abutment while being relieved behind the mined-out area (analogous to a penny shaped crack as observed by Griffith). In the rockmass abutment, these stresses quickly decay but stay above the pre-mining state for considerable distances into the floor rock. In practice, the rockmass forming the immediate abutment of the mining front yields at these high stresses, producing a zone of damaged material (i.e., post-peak response). At the GH, the process zone is observed regularly in the active cut-and-fill headings (*Figure 3.13*). The horizontal tensile fractures seen at the mining face are not naturally occurring but are induced by mining stresses. The stress-induced fractures follow the principal stress trajectories as they arch under the stope floor in the previous cut (causing spalling due to low confinement). Based on field observations, the yield zone for cut-and-fill is estimated at ~3 m below the floor of the cut (full face height).

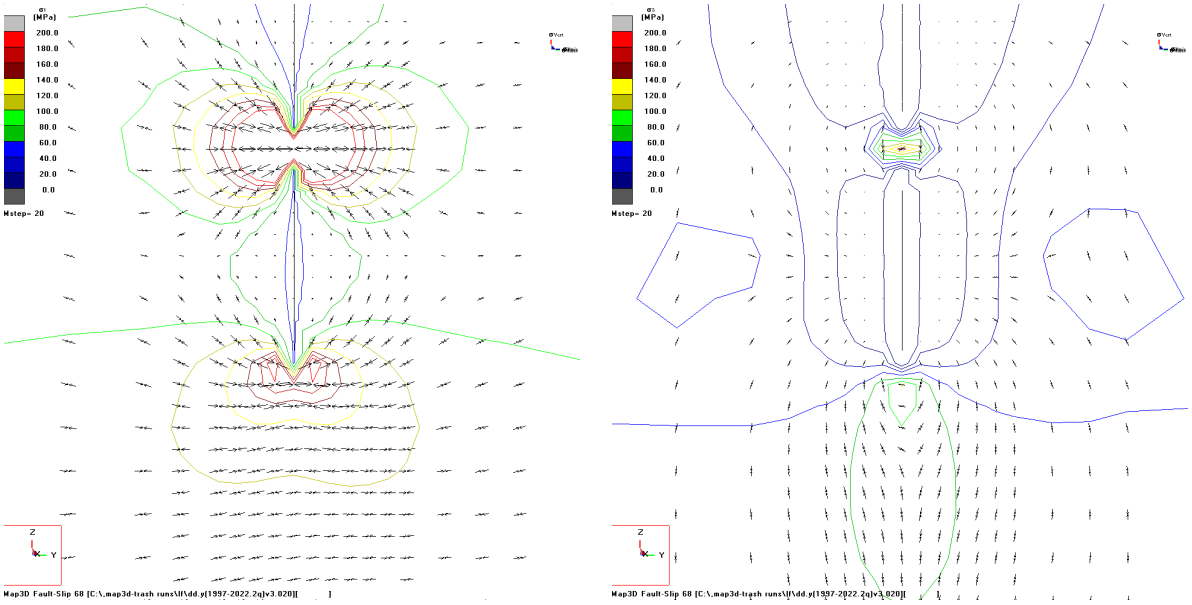


(a) (b)

Figure 3.11: Normal stresses and closures computed across the 30-Vein (section 17,661E)



(a) (b)



(c) (d)

Figure 3.12: Principal and minor (a–b) stresses and (c–d) vector trajectories (section 17661E)



Figure 3.13: Underhand cut-&-fill heading showing rock yielding via tensile fracturing which occurs in the floor of the previous cut (photo courtesy of Dr. Board)

Normal closures have been computed by the elastic boundary model in 15 Stope (*Figure 3.11*(b)). *Figure 3.14* shows the variability of the simulated in-stope wall-to-wall closure across entire vein. As observed in both figures, remnant pillars hinder the maximum closures in each panel. Since the upper panel is extracted completely (without leaving any pillars), the maximum absolute closure was recorded in the 4,900 mining panel rather than in the deepest parts of the mine. Conversely, the maximum closure on that panel appears at its center.

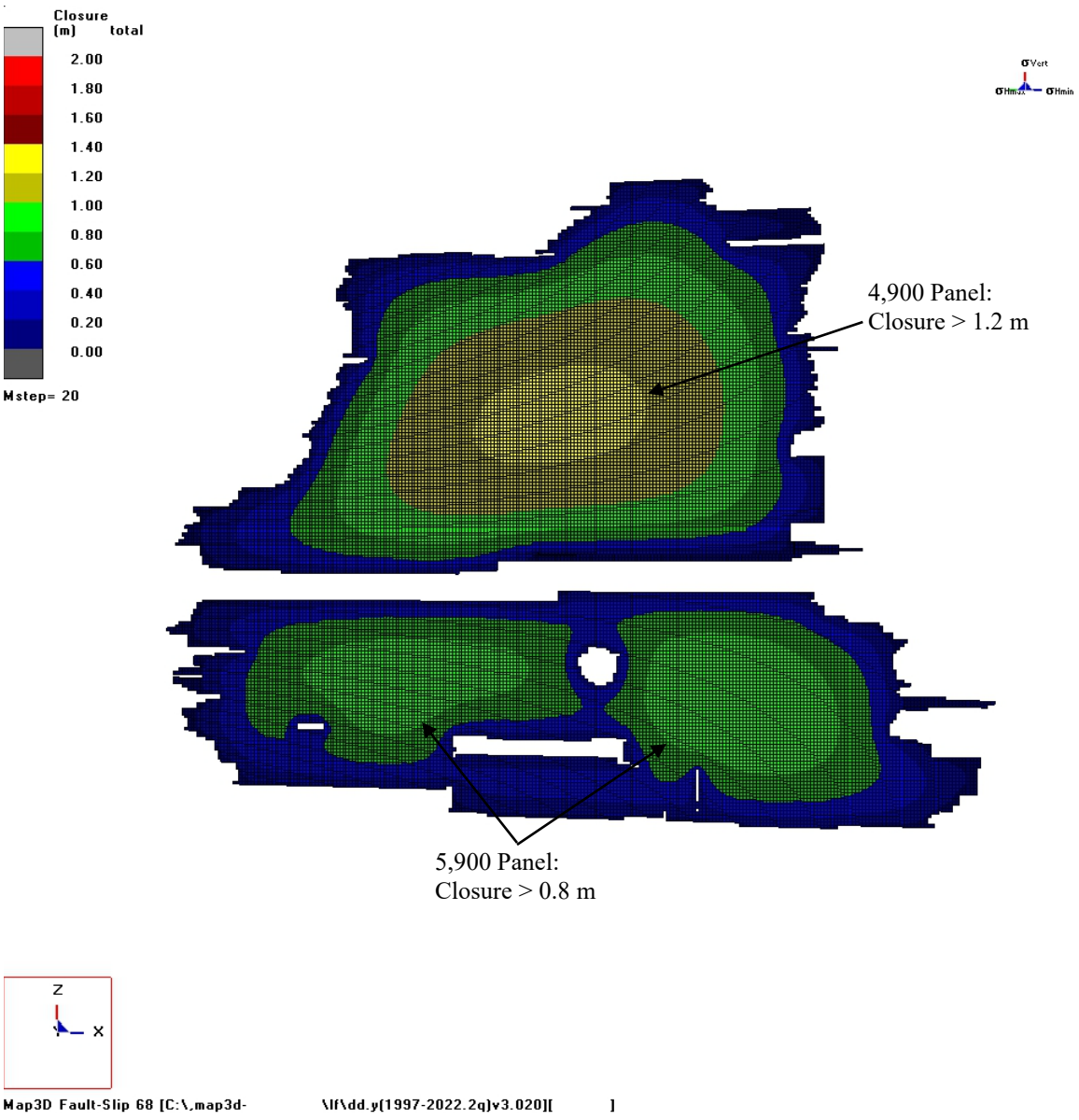


Figure 3.14: Normal closure computed along the extracted portions of 30-Vein

Malan (2011) pointed out that tabular mines continue to induce closure as the mining front progresses away from the measuring station. This progressive convergence has also been previously observed at the Lucky Friday mine (Williams et al., 1992) and most recently measured in the GH sector by Seymour *et al.* (2017) and Raffaldi *et al.* (2019). For the GH, the NIOSH group fabricated custom in-stope wall-to-wall closure instruments designed for contraction due to underhand extraction on the 30-Vein. Each convergence station consisted of extensometers, potentiometers, and earth-pressure cells designed to withstand significant closure. The linear transducers, composing the closure instruments anchored perpendicular to the stope walls, had a

maximum measurable displacement range of 63.5 cm, a resolution of ±0.01%, and an accuracy of ±0.20% full scale (Seymour, 2023). These instruments were installed in-stope (on sections), cast into the backfill pour. Once the backfill cured, the subsequent underhand cut was incrementally developed until its planned completion. As mining advanced below the instruments, closure measurements were captured in the above cut. These instruments have successfully recorded in-stope wall displacement profiles in 555-11-05 cut (11S), above the 5,700 Pillar, and in a deeper-seated area of the mine in 635-15-02 cut (15S), below 15S Pillar. *Figure 3.15* illustrates the approximate locations of the convergence stations in reference to the 30-Vein construct. The relative vertical distance between the instruments is ~227 m.

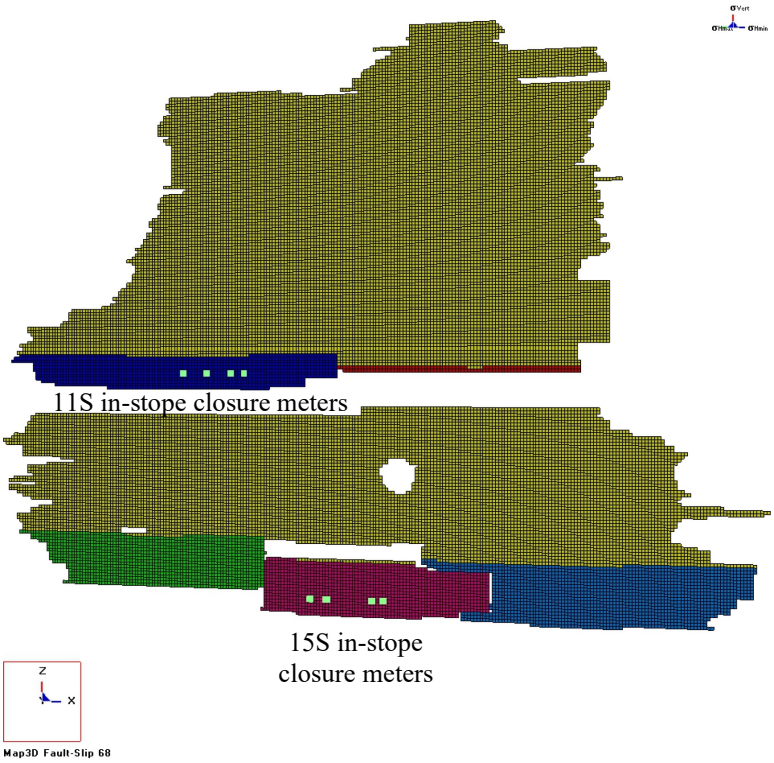
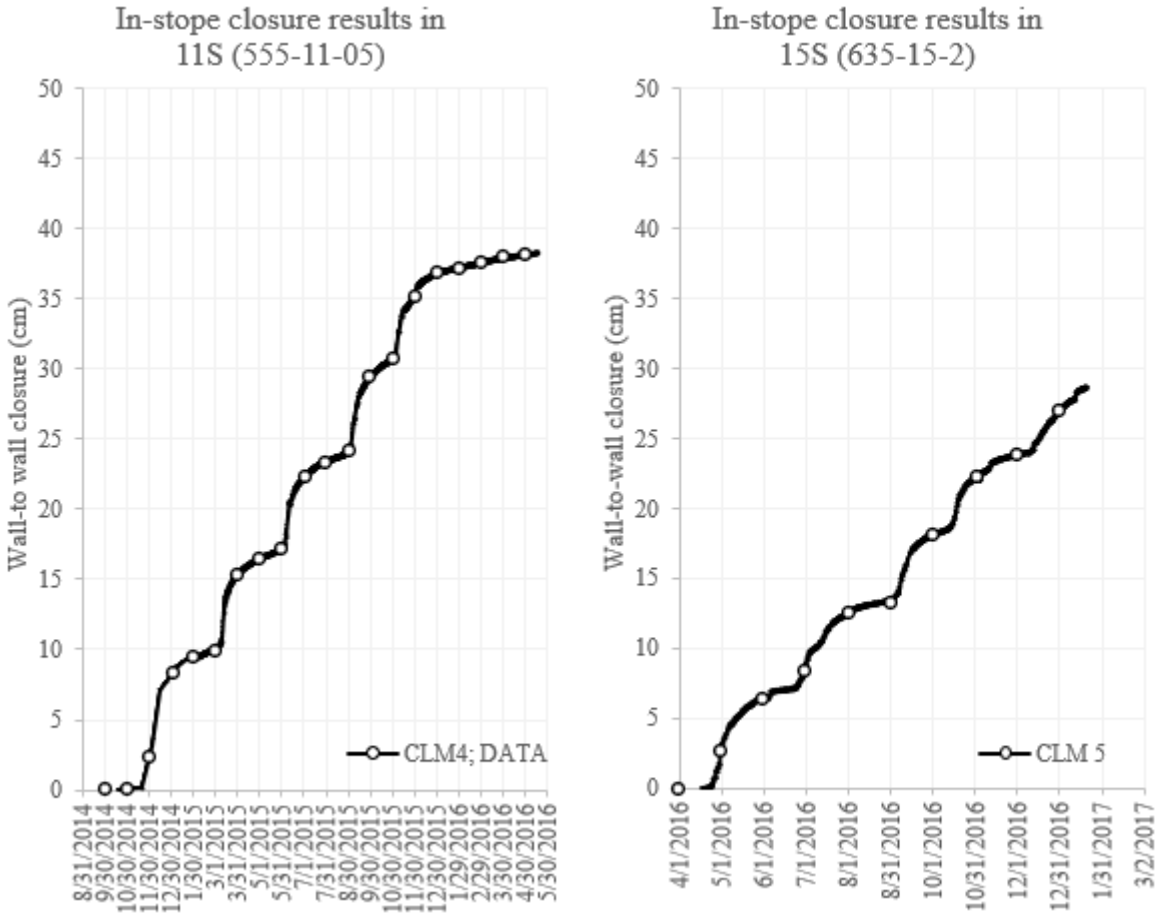


Figure 3.15: In-stope closure measurement locations, green markers (Raffaldi et al., 2019)

The in-stope wall-to-wall closure have been successfully recorded for up mining up to five (5) consecutive underhand cuts in both stopes (*Figure 3.16*). The closure measurements exhibit a *stair-stepped* characteristic often reported in deep narrow South African mines (Malan & Napier, 2021). The convergence rate accelerates as the mining front passes below the measuring station, progressively decelerating to a steady state rate as mining progresses away from said station. At the GH, the backfilled cut experiences about ~7.5 cm of relative in-stope closure as the

underhand cut is mined to completion (Seymour et al., 2017). The cycle is repeated with each subsequent cut extraction but induces less relative displacement as the instruments recess further away from the mining front. Although the results present similar characteristics, the maximum recorded closure in 11S is larger than in 15S (~38 cm versus ~28 cm). Likely, 15S Pillar hinders convergence in 15S while 11S undergoes higher stresses due to the converging mining panels, as previously discussed (*Figure 3.11*).

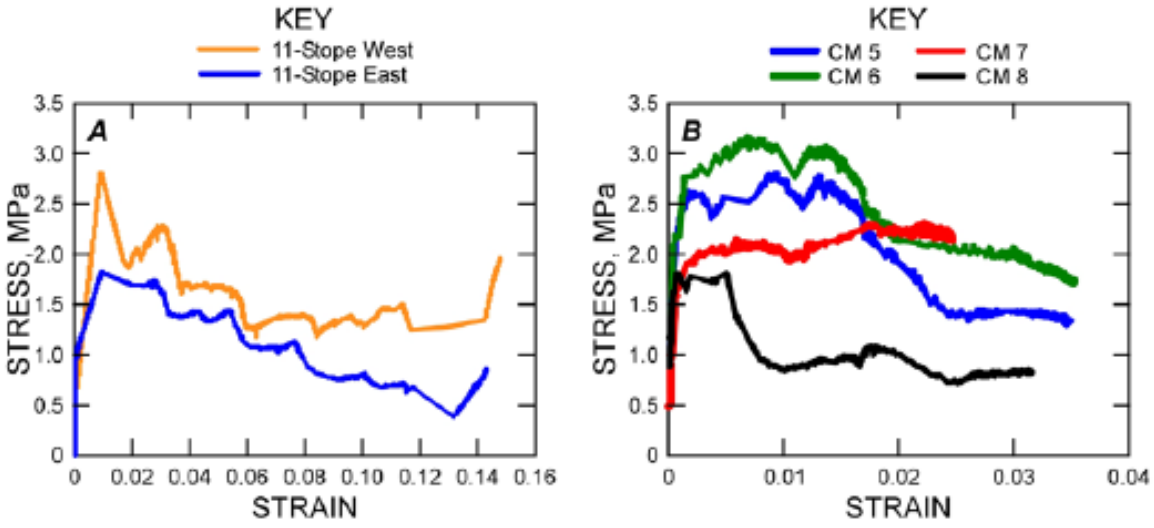


(a) (b)

Figure 3.16: In-stope normal displacement measured in (a) 11S, and (b) 15S (Seymour et al., 2017)

In addition, earth pressure cells (EPC) inside the backfill have captured the loading characteristics of the cement paste backfill (*Figure 3.17*). The in-situ stress-strain data indicates that the average peak strength of the backfill occurs between 0.5 and 1.0% strain, consistent with

laboratory results at peak of ~2.4 MPa (Seymour et al., 2016). Therefore, the backfill is loaded to peak strength at only ~2.25 cm of convergence for a stope width of 3 m (0.75% strain), crushing as soon as the first underhand cut exposes the sill mat. The backfill strength falls quickly to residual strength of ~1.5 MPa. Infield data shows that even after five (5) consecutive underhand cuts the backfill hasn't regained loading capabilities. For this to arise, complete compaction of the voids inside the fill needs to occur where the fill load-deformation response is often modeled as a double-yielding non-linear hyperbolic material (Ryder & Jager, 2002). Assuming a void ratio of ~50% in the GH backfill (which includes pores inside the fill and the unfilled gap up at the back), ~1.5 m of closure has to occur on the cut before the backfill starts to load up again. As previously presented (*Figure 3.14*), the maximum closure magnitudes would most likely appear near the center of the 4,900L mining panel. Although underhand operations depend on CPB, the backfill is less relevant for numerical simulation at the LF mine.



(a) (b)

Figure 3.17: In-situ CPB loading in (a) 11S, and (b) 15S (Seymour et al., 2017)

Mine-induced seismicity is the physical manifestation of all these processes at the Lucky Friday mine. Their location, size, and occurrence are addressed in the subsequent section.

3.2 Seismic Review

Mining-induced seismicity in the Coeur d'Alene district was first reported in the early 1900s. It wasn't until the late 1940s that rockbursts (the physical consequence of mine seismicity) became a severe operational hazard in the district. Amongst the local mining operations, the Lucky Friday is regarded as the most seismically active mine in the district, and possibly in North America, in terms of energy released per ton of ore mined (Jenkins et al., 1990).

3.2.1 Seismic Response at the Lucky Friday Mine

At the historical Lucky Friday deposit (mined between 1942 and 2002), the largest episodes of mine-induced seismicity were observed below the 5,100L while mining the Lower Revett formation (at ~1.36 km depth). This formation is generally characterized as *sandier*, having a higher composition of vitreous quartzite with an overall increased blockiness (Mauk et al., 2002). The higher vitreous quartzite content in this formation was attributed to the increase in seismicity (Blake & Hedley, 2003), potentially also driven by a higher stress k-value (~2) as measured previously in the Revett. Silicified altered rock around quartz vein have been observed to respond in a brittle fashion resulting in strain bursts (Whyatt et al., 2002). Typically, these strain-burst type events release at a much smaller magnitude ($< +1.5\ M_L$) but occur near the headings, projecting rock fragments. Past studies have shown that less than 10% of the LF ramp development was affected by strain bursting, but compounded strain-bursts have damaged as much as 100 tons of rock in the ramps (Whyatt & White, 1998).

The Lucky Friday vein system was mined using the traditional overhand cut-and-fill method until 1986, when the mine converted to the underhand cut-and-fill (termed the Lucky Friday Underhand Longwall — LFUL). The need for this transition arose from the inherent problem of creating sill pillars as mining progresses upward to a neighboring panel. Board & Fairhurst (1983) reported that several district pillar bursts occurred when the sill pillar was reduced to ~18–20 m, peaking in seismic release at ~12–15 m. Similar observations have also been confirmed at the Galena mine (Blake, 1972). The rapid increase in stress concentration within the pillar often resulted in large pillarburst events with magnitudes up to $+2\ M_L$.

Whyatt *et al.* (1996) studied the seismic response of 39 events greater than $+2.5\ M_L$ between 1989 and 1994 at the Lucky Friday (*Figure 3.18*). The largest seismic event recorded during that

period was a single +4.1 M_L confirmed on the North Control Fault. They found that the mine experienced a seismic event of +2.5 M_L on the average of once every eight (8) weeks, with all events (except for two) associated with fault-slip mechanism. The slip was attributed to either the south-dipping bedding planes (+2.4 to +3.3 M_L), the central shear zone (+2.5 to +3.0 M_L), the South Control Fault (+2.5 to +3.0 M_L), the Vein (+2.4 to +3.7 M_L) or the North Control Fault (+2.5 to +4.1 M_L). Board (1994) demonstrated through numerical modelling of the LF that the bedding planes can release up to ~3 M, while slip along the regional faults can easily reproduce events of 3 M or greater. The seismicity (modeled & recorded) occurring on the bedding planes in advance of the stope appeared bounded to the footwall. This asymmetric response constitutes a significant difference between the distribution of seismicity around stopes at the Lucky Friday and that of deep South African gold reefs (White & Whyatt, 1999; Joughin & Jager, 1983).

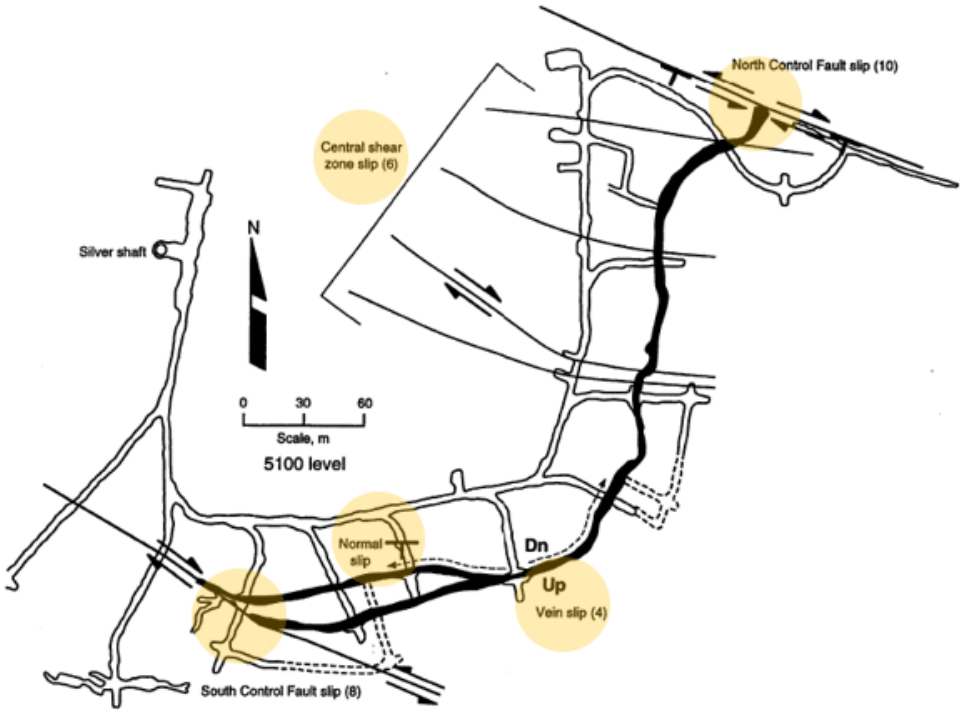


Figure 3.18: Overview of fault-slip classifications at the LF (Whyatt et al., 1996)

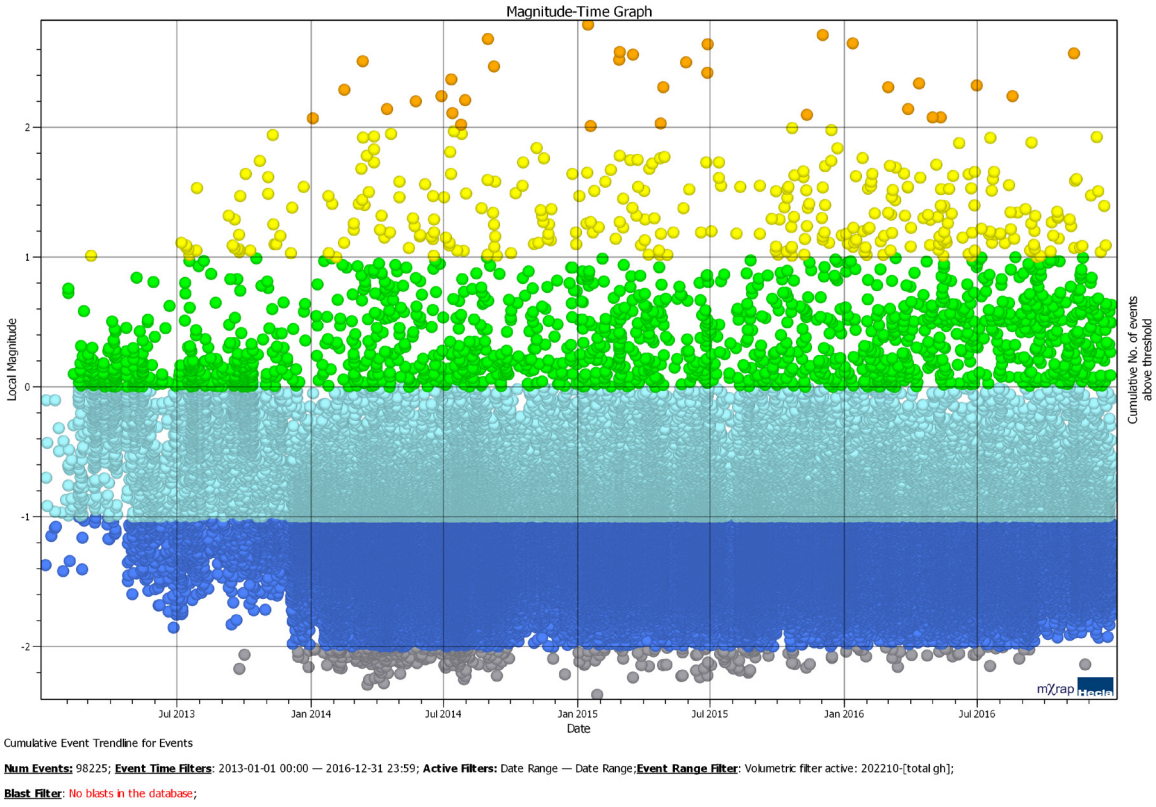
For the mining period between 1988 and 1995, ~90% of all seismic events were recorded near the active stopes, while the remaining 10% originated outside of the zone on known major structures. These distal fault-slips accounted for ~90% of the net seismic energy release at the mine for that period (White & Whyatt, 1999).

3.2.2 Local Seismic System Employed at the Mine

The Lucky Friday mine operates a microseismic system manufactured by Engineering Seismology Group Canada (ESG). The seismic system was commissioned in the Gold Hunter in early 2013. The GH seismic array contains seventeen (17) uniaxial and three (3) triaxial 15Hz geophone sensors, which provide dedicated coverage of the 5,700 Pillar and the bottom 30-Vein stopes and levels. These sensors rest inside the footwall of the 30-Vein, offset by ~100 m from the vein. The inherent event source location error within the array is estimated to be ~12.2 m radius in active mine sectors (ESG, 2016). The Hyperion Network Acquisition Software (HNAS) continuously records and digitizes the waveform in real-time. The sensor indicates a seismic event when the signal amplitude exceeds their pre-set threshold (i.e., the threshold triggering method) or when the short-term to long-term average energy ratio increases past a specific limit (i.e., the STA/LTA ratio triggering method). At least four (4) geophones need to be hit by a seismic wave to trigger a confirmed event. The recorded seismic event stores instantly in the mine's seismic database. It is subsequently processed for source parameters by the Hyperion Seismic Software (HSS), which provides the location (in Euclidean space), time of occurrence, slip radius, seismic moment and seismic energy (derived from the Brune slip models), and correlates the source parameters to an event magnitude (M_w). Due to the potential saturation of the incoming waveform signals (on amplitude or frequency) as often associated with large incoming seismic events, a single strong-ground motion sensor (4.5 Hz) triax-geophones ensure secondary seismic source acquisition. The SGM rests in the far-field of the source, at the top station of the #2 Shaft, recessed into the mountain. Integral event detection and registering procedures are verified and recalibrated annually by ESG, enabling to record events as low as -2 M_w. The combination of the sensor types and the array configuration with adequate triggering procedures offers the mine effective monitoring of seismicity well over +3 M_w for the current mining depth (~6,500L).

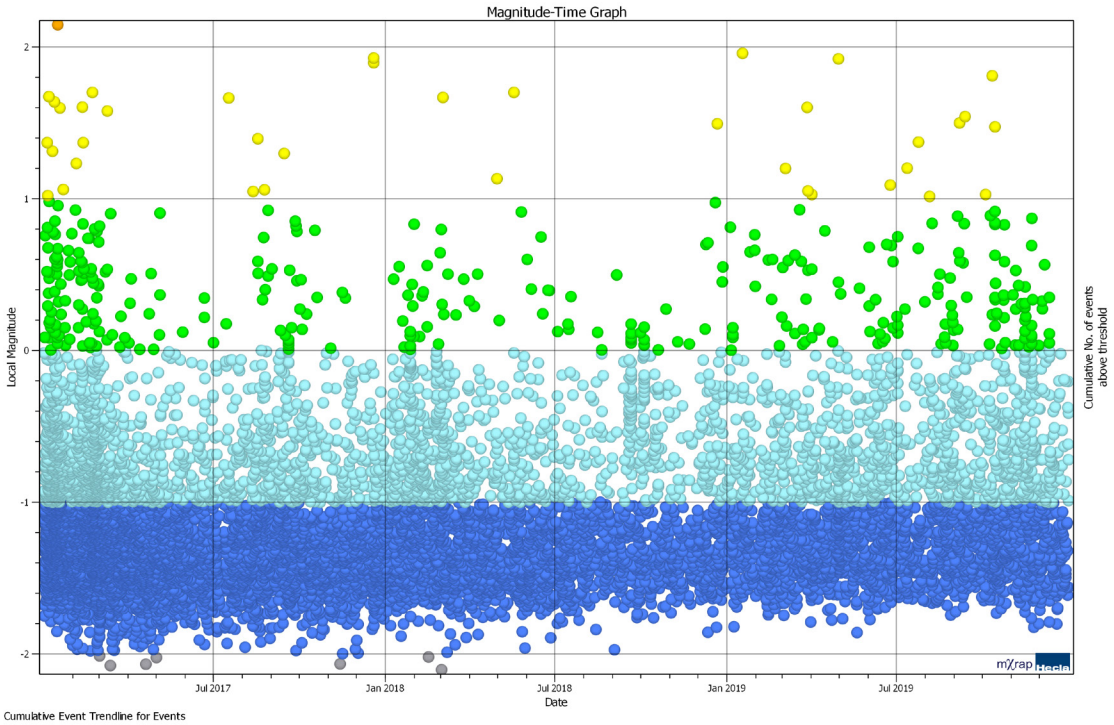
The mine utilizes ESG's advanced auto-processing services (since 2016), where P- and S-picks are manually reassigned to all triggered events by the supplier. This has significantly reduced the source error of smaller events. The Lucky Friday geotechnical staff manually reprocesses all notable events ($\geq$ +0.5 M_w) where the picks are revised to improve event location to active mining. This practice has been performed since the commissioning of the seismic system.

As a result of routine maintenance and the rigor presented by the on-site staff in keeping the system online, the continuity of the event catalog demonstrates the system's reliability, or health, with no significant downtime (> than a week) in data acquisition since 2013 (*Figure 3.19*). Since commissioning the seismic system up to 2016 year-end, roughly 100,000 events have been recorded while mining the GH, and about 25,000 additional events extend the seismic catalog past the 2021 year-end production. To perform seismic analysis per mining area, the following stope volume filters were delineated to group mine-induced seismicity with stope activity (*Figure 3.20*). These volumetric shapes were defined to cover the entire stope geometry and extend at least 100 m into the vertical abutments without overlapping into adjacent stoping areas. The final areas were projected at least several hundred meters into and out of the plane. These volume filters are used throughout the thesis.

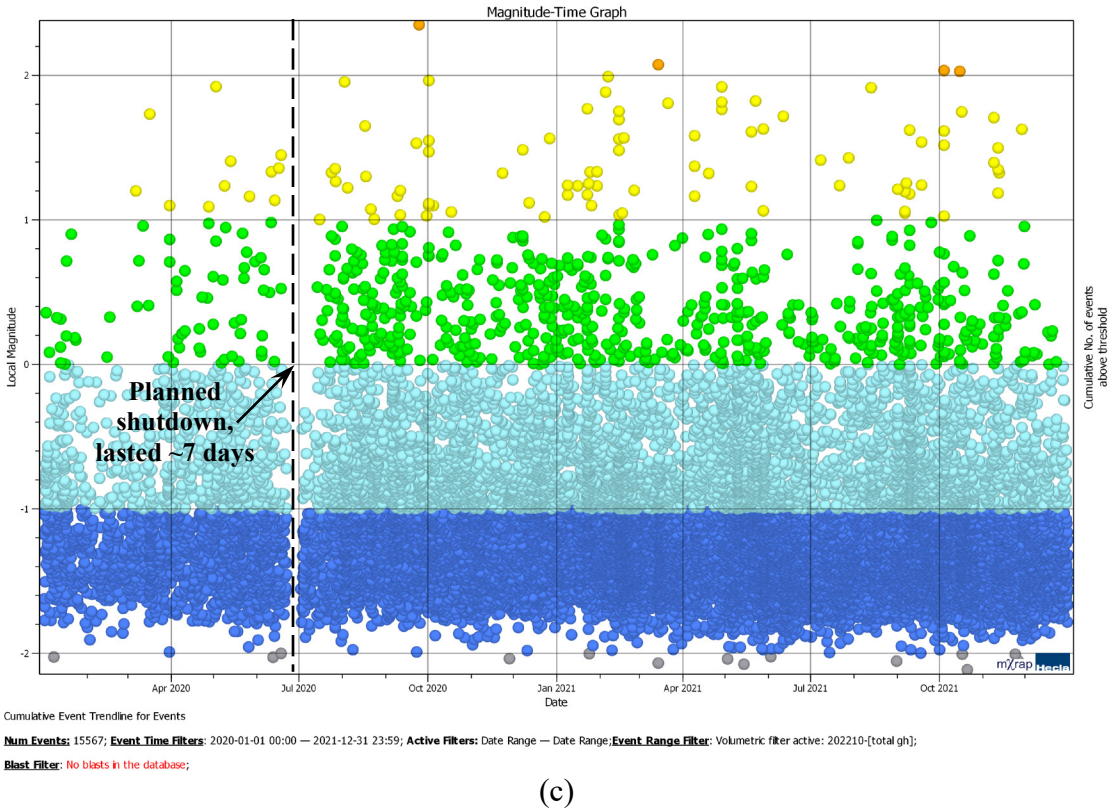


(a)

Figure 3.19: Magnitude-Time relationship per mining periods (a) 2013–2016, (b) 2017–2019, and (c) 2020–2021



(b)



(c)

Figure 3.19: Magnitude-Time relationship per mining periods (a) 2013–2016, (b) 2017–2019, and (c) 2020–2021 (cont'd)

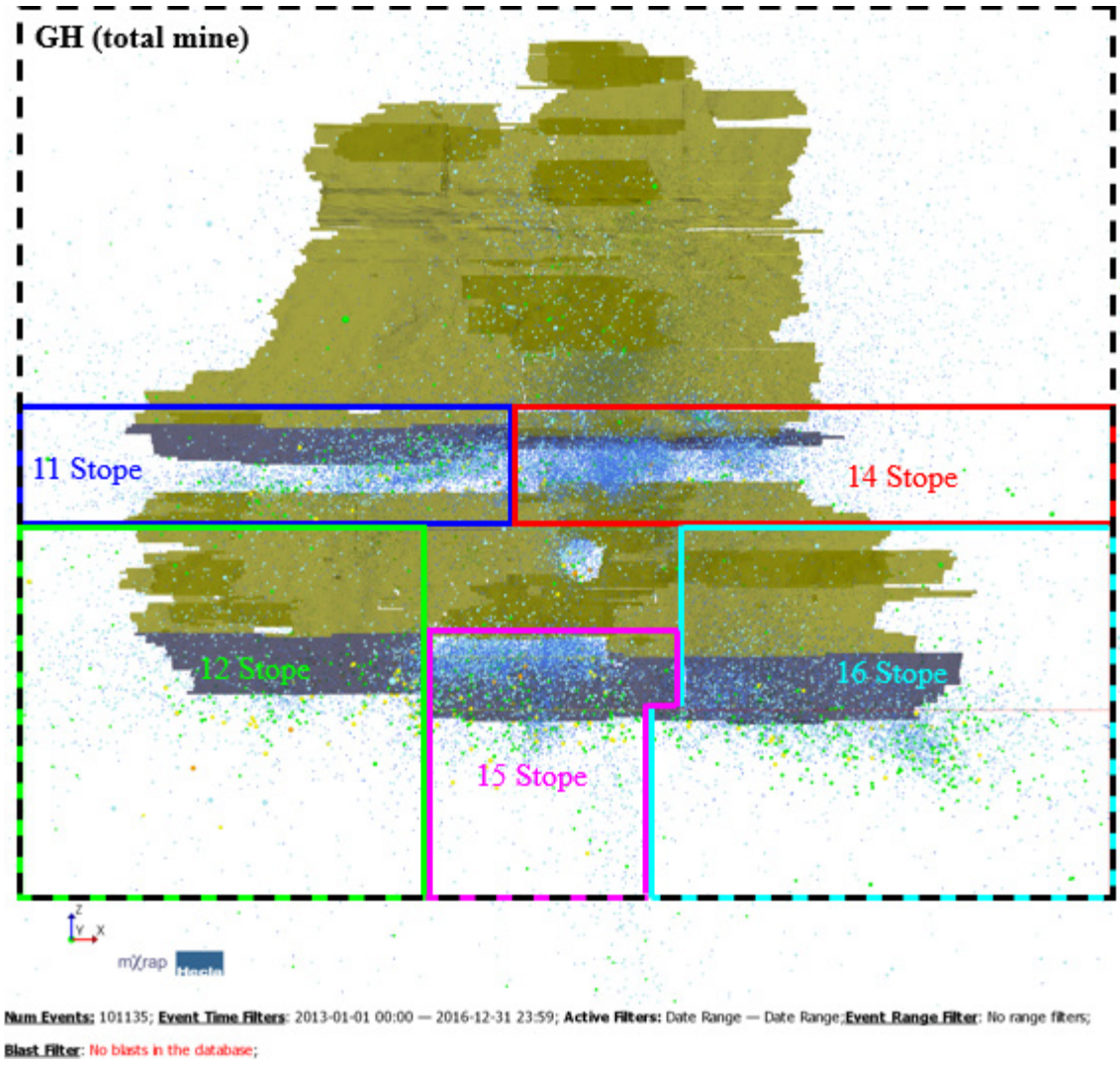


Figure 3.20: Stope volume filters applied in the Gold-Hunter

3.2.3 Seismic Response to Mining

This section covers the magnitude, time, and location relationship of events with respect to mining on the 30-Vein, for the period 2013–2016. The Gold Hunter seismic catalog, for that period, includes 787 events $\geq +0.5$ M_w, 125 events $\geq +1.5$ M_w, and 11 events $\geq +2.5$ M_w. The largest recorded event was a +2.79 M_w, occurring in the 5,700 Pillar under 11 Stope.

3.2.3.1 Event-Magnitude Relation to Mining

The relationship between mine-induced seismicity and magnitudes is well-established in the literature (Gibowicz, 2009). It is generally agreed that mine seismicity shares several similarities

with crustal, naturally occurring earthquakes (McGarr, 1971). Therefore, the increase in magnitude output depends on a magnitude-frequency relationship, the Gutenberg-Richter Magnitude-Frequency law (Gutenberg & Richter, 1955). Earthquake research shows that the b-value (slope of the GRMF plot) range falls between 0.7 and 1.5, suggesting that 5 to 32 events need to be released before triggering the next integer magnitude increase, respectively. For the Gold Hunter deposit, the relationship between magnitude-frequency of occurrence indicated a b-value of 0.9 for 2013–2016 (*Figure 3.21*). Projecting the slope line can indicate the maximum event release (Mendecki, 2013). This plot includes pillar geometries. Hence, the total mine has a maximum seismic potential of around +3.5 M_w.

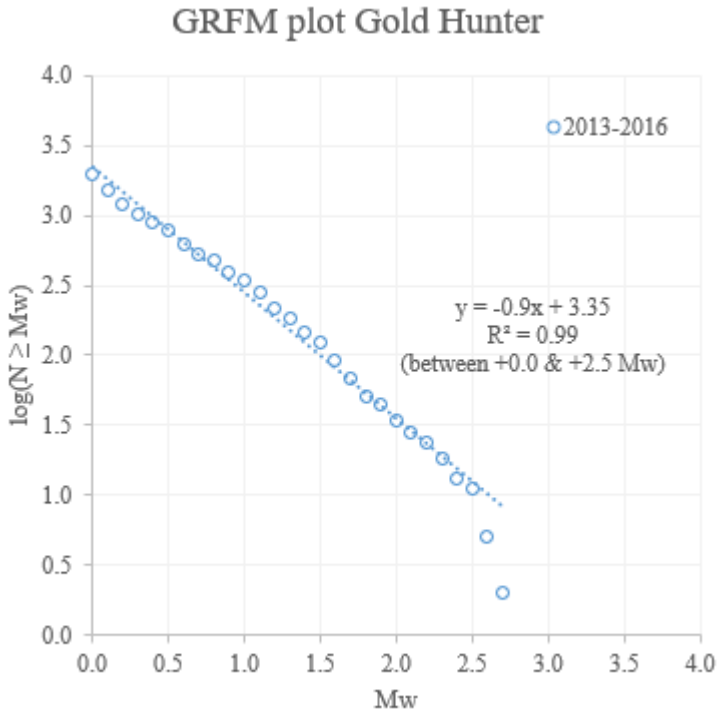
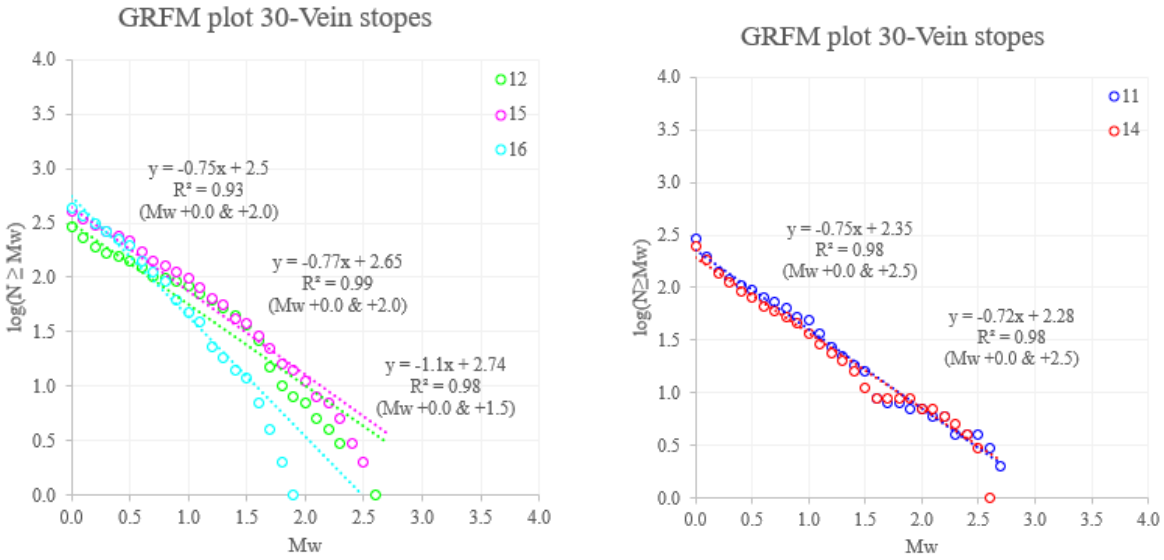


Figure 3.21: Gutenberg Richter Magnitude Frequency plot in Gold Hunter, 2013–2016

Assuming the filter volumes previously presented (*Figure 3.20*), the GRMF relationship has been plotted for each individual stope (*Figure 3.22*). It is observed that the in-stope b-values range from 0.72 to 1.1. The typical interpretation of the b-value, in terms of rockmass response, indicates that a low value (< 1.0) is associated with potential fault-slip or shearing asperities (Mogi, 1962) due to an increase in applied shear stresses (Scholz, 1968). Whereas a higher b-value (> 1.0) represents an increase in material heterogeneity (Mogi, 1962) with the potential for

creeping sections of faults (Wyss et al., 2004). Therefore, the lower b-values in (ascending order form) 14S, 11S, 12S and 15S all infer fault-slip characteristics, while the higher b-value recorded in 16S indicates a lack of structural influence potentially due to a reduction in fracture density or structural persistence in the eastern part of the vein.



(a) (b)

Figure 3.22: Gutenberg-Richter Magnitude-Frequency in 30-Vein stopes (a-b), 2013–2016

3.2.3.2 Event-Time Relation to Mining

The relationship between event-time is well-established in the literature (Whyatt et al., 2002). It is generally accepted that mine-induced events gradually build up as mining progresses, conserving the GRMF dependency (Mendecki, 2013). Therefore, larger seismic events (> +1.5 M_w) generally appear after a certain mining configuration has been reached. For the GH, the relationship between magnitude-time follows the GRMF relationship as well. There is a gradual build-up of lower-magnitude events before the trigger of larger ones (Figure 3.23). This plot includes pillar geometries. Hence the total mine triggered its first +2 M_w event in January 2014. The subsequent large events were gradually released as mining progressed, crudely following the expected b-value event-magnitude release requirement (i.e., releasing ~8 events ≥ +1 M_w). On average, a +2 M_w event occurred every 4.5 weeks in the GH since the first occurrence in the studied catalog. The Lucky Friday deposit released a +2.5 M_L event every 8

weeks at its peak (Whyatt et al., 1996), which compares to a +2.5 M_w release every 14 weeks in the Gold Hunter deposit.

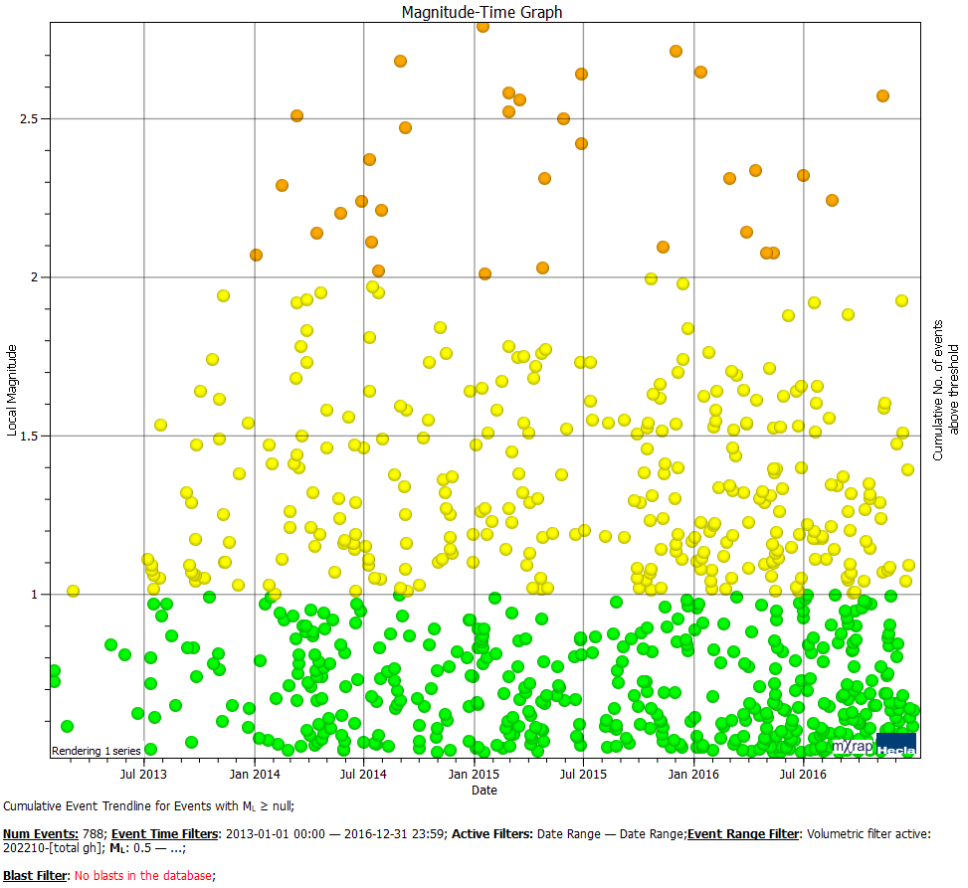


Figure 3.23: Magnitude-Time chart in Gold-Hunter, 2013–2016

The magnitude distribution per production year is shown in the lower plot for the GH (*Figure 3.24*). There is a gradual build-up in events up to +1.5 M_w as mining deepened, peaking in 2015. The drop in larger magnitude events ($\geq$ +1.5 M_w) for the 2016 period is due to stopping production in 11 Stope (December, 2015) and 14 Stope (September, 2014). These two stoping fronts were leading the lower edge of the 4,900L panel towards the upper 5,900L, progressively forming a remnant pillar configuration; the 5,700 Pillar.

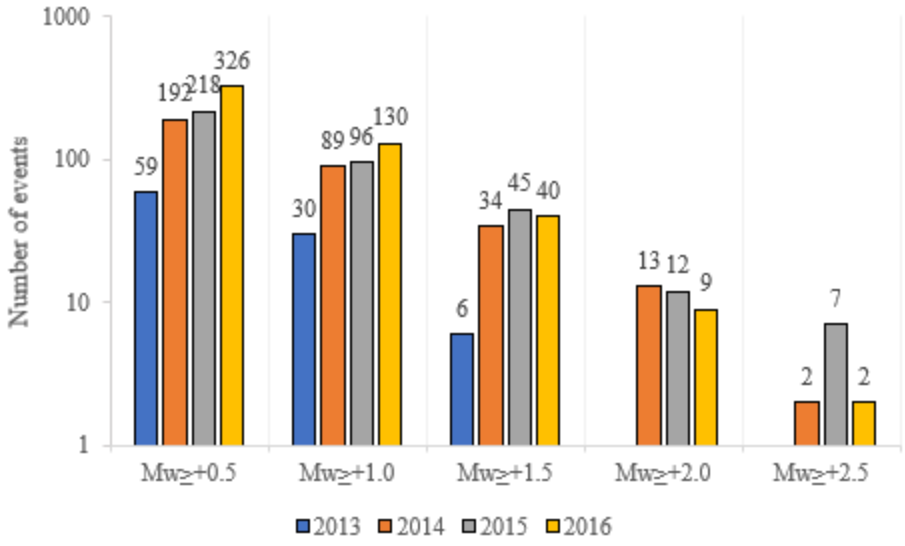


Figure 3.24: Magnitude distribution in the GH per production period, 2013–2016

The magnitude-time graphs have been plotted for each individual stope (*Figure 3.25*). It is observed that the in-stope magnitude-time occurrences depend on the mining activity undertaken and are specific to each stope. The 11S has released six (6) large (> +2 M_w) events while mining towards the 5,900 Panel while forming a pillar geometry. The 5,700 Pillar continued to burst until the mine shutdown 11S in mid-December 2015, having formed a 24.4 m high remnant pillar configuration. An aftershock event followed within 10 months inside the pillar. Neighboring 11S, 14S has released seven (7) large (> +2 M_w) events in the 5,700 Pillar while also mining towards the 5,900 Panel. That stope was shutdown in late September 2014 due to the sporadic release of larger events, leaving a 33.5 m high remnant pillar below the stoping front. An aftershock followed within 9 months inside the pillar after mining stopped in the converging stopes. Most of these events were linked with the F-Series faults, which produced a rockburst in the ramp in 2011 (Hecla, 2013). The 12S saw a flurry of five (5) large (> +2 M_w) events following a fault-slip event which triggered on the western Silver fault, bordering the west side of stope. The 15S has released ten (10) large (> +2 M_w) events, with most of them occurring after 15S Pillar was formed, presenting a remnant pillar height of 15.2 m. The 16S seems to have the maximum magnitude output capped below < +2 M_w. This might be due to the continuous nature of the stoping front (without remnant pillar) and the lack of structural influence within the stope vicinity.

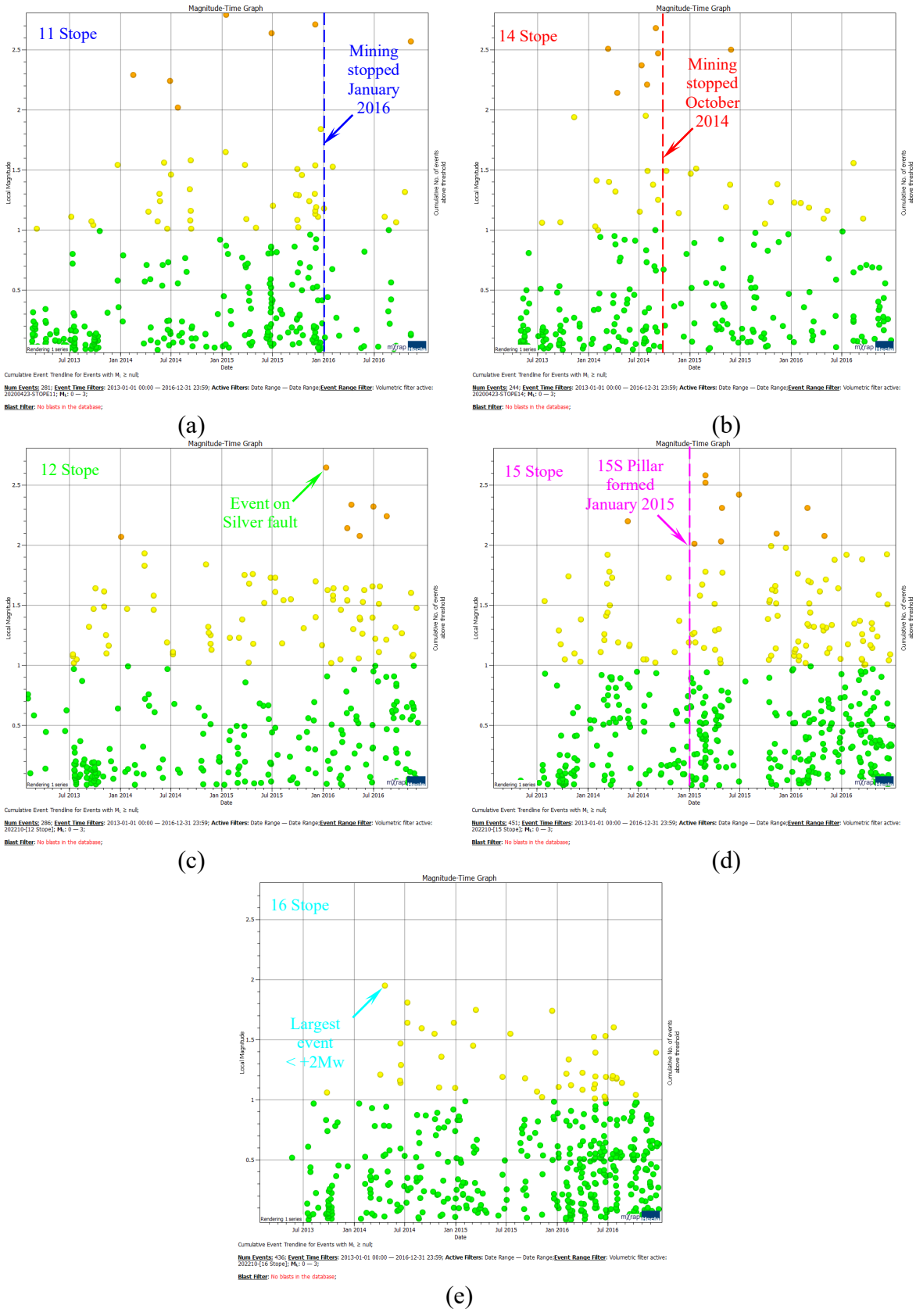


Figure 3.25: Magnitude-Time charts per 30-Vein stope, 2013–2016

The magnitude distribution for stopes is presented below (*Figure 3.26*). It is observed that the stopes behave differently, with 11S releasing the highest magnitude events, while 16S registered the second most notable seismic occurrences without triggering larger +2 M_w. It is also important to note that pillar geometries are present within the stope volumes of 11S, 14S, and 15S. In contrast, 12S has an unfavourable corner geometry created by (the neighboring) 15S leading the mining front by ~25 m, allowing stresses to accumulate in the corner pillar configuration. Unfavourable geometrical layouts (pillars & lagging stope corner) coupled with structural differences may explain the variable magnitude output by these stopes.

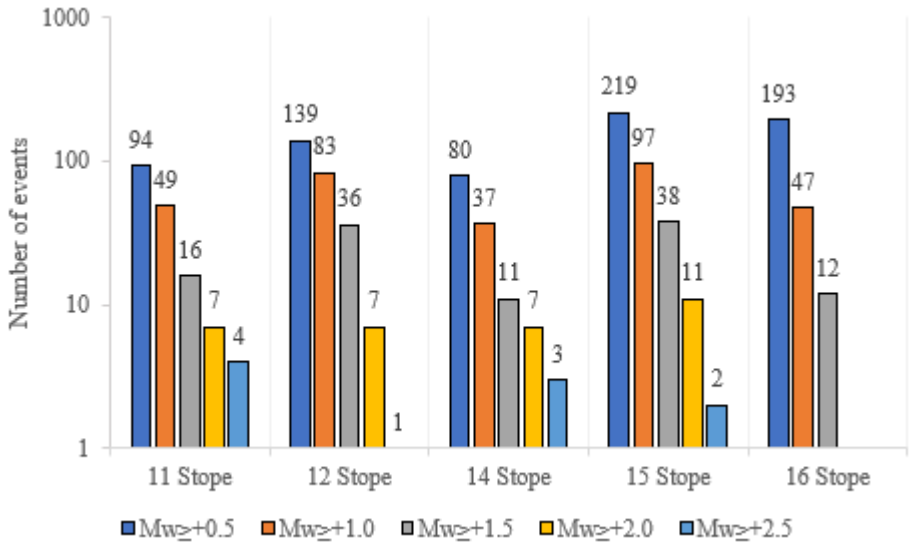


Figure 3.26: Magnitude distribution per 30-Vein stope, 2013–2016

3.2.3.3 Event-Location relation to mining

There is a direct link between mining and the location of seismic focus (Brown, 2021). At the Gold Hunter deposit, mine-induced seismicity often occurs near the active cut, along known (mapped) fault structures, and within pillar configurations. The event-location relationship is visualized by comparing the mine-out geometry to the spatial occurrence of notable seismic events greater than +0.5 M_w (*Figure 3.27*). The associated mining on the 30-Vein was hatched to reference active mining sectors for the period. Notable events have correlated with the F-series faults (F3 & F4) located in the footwall of 30-Vein, clustering around the 5,700 Pillar (*Figure 3.28*). Based on a qualitative event-location assessment (Gibowicz, 2009), the event catalog (which contains 787 notable events) was broadly segregated into 15% fault-slips, 35% pillar

events, and 40% stope events, with 10% being unclassified. Unclassified events occur further than 100 m from known stope extractions, discrete known faults, or pillar geometries.

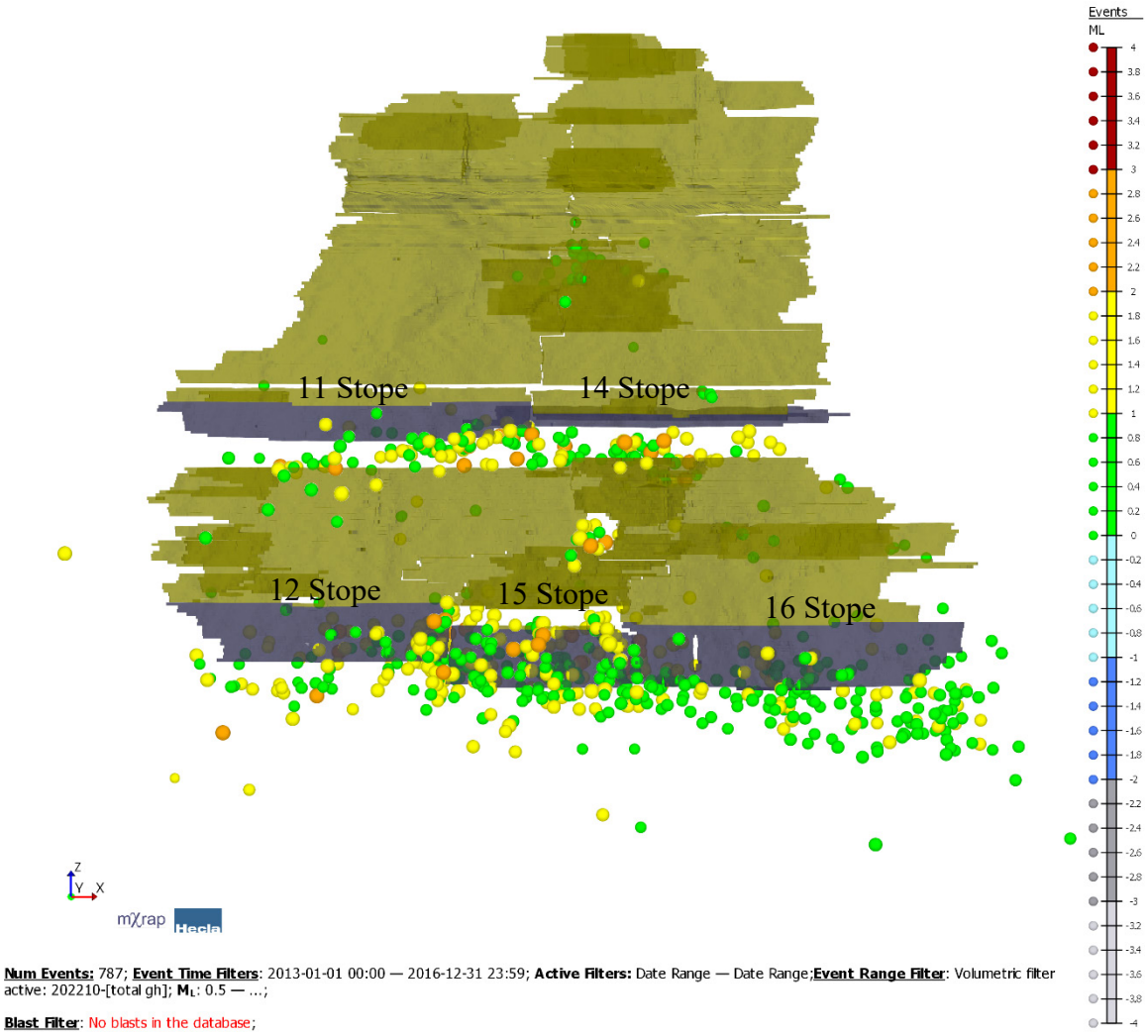


Figure 3.27: Notable seismic events (≥ +0.5 M_w) locations projected on to the GH, the view is looking north, 2013–2016

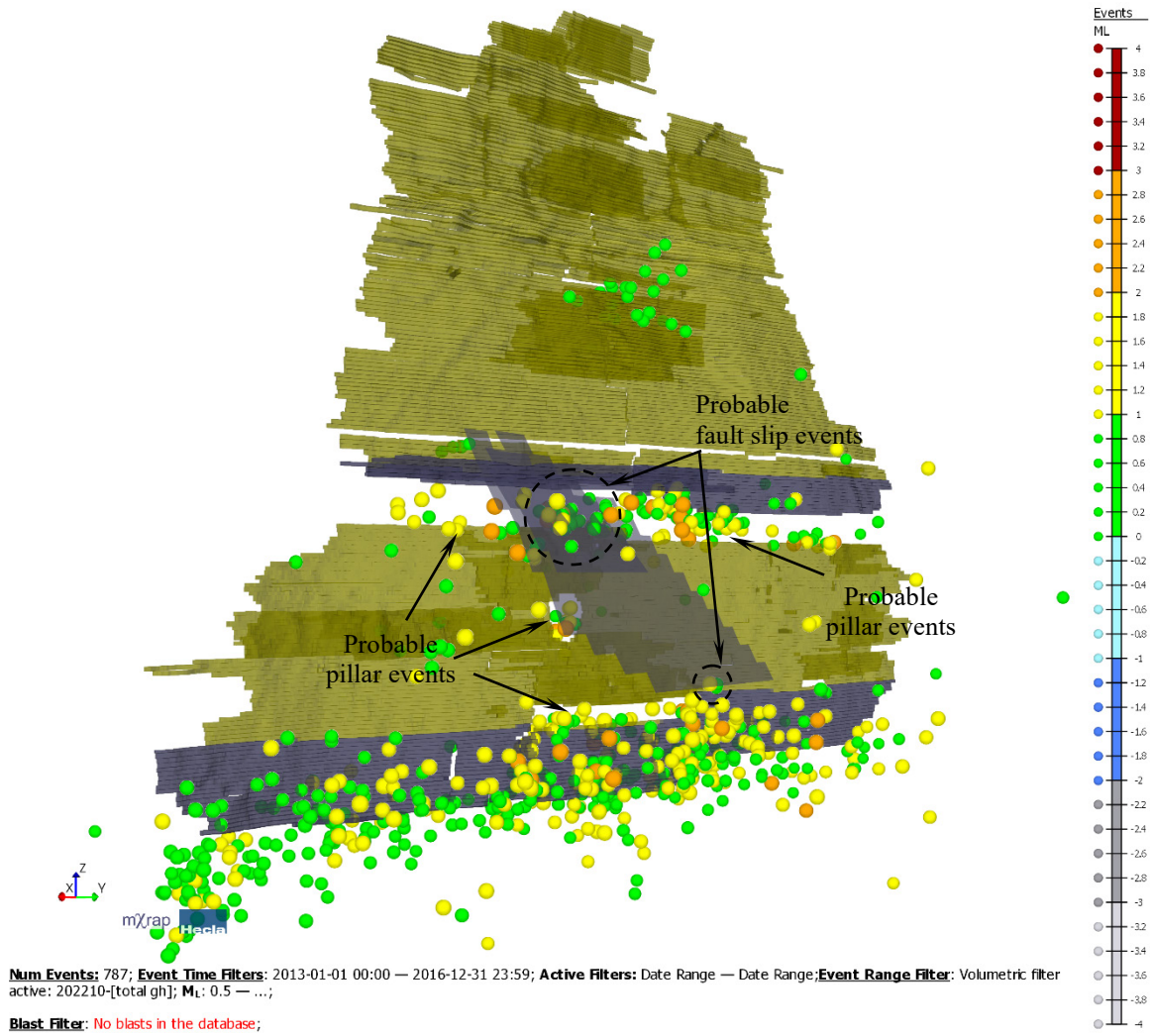
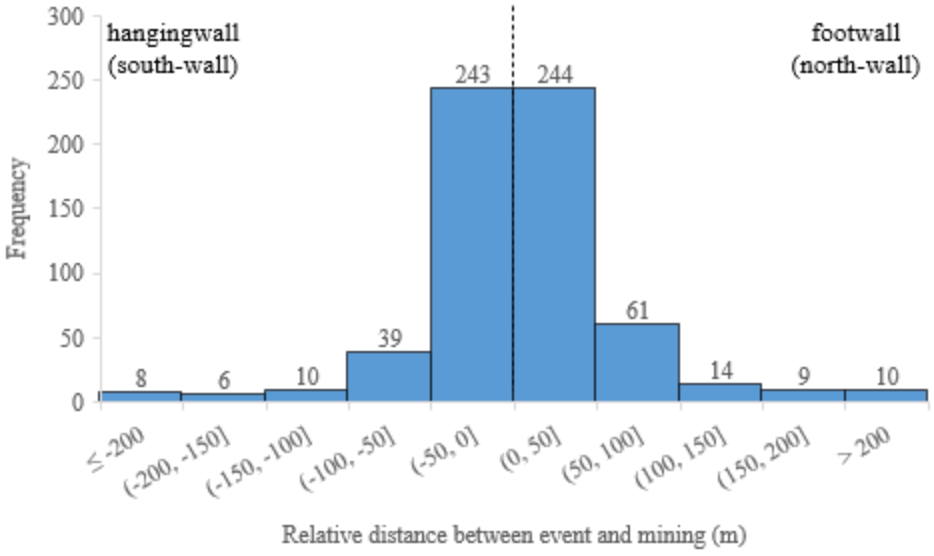


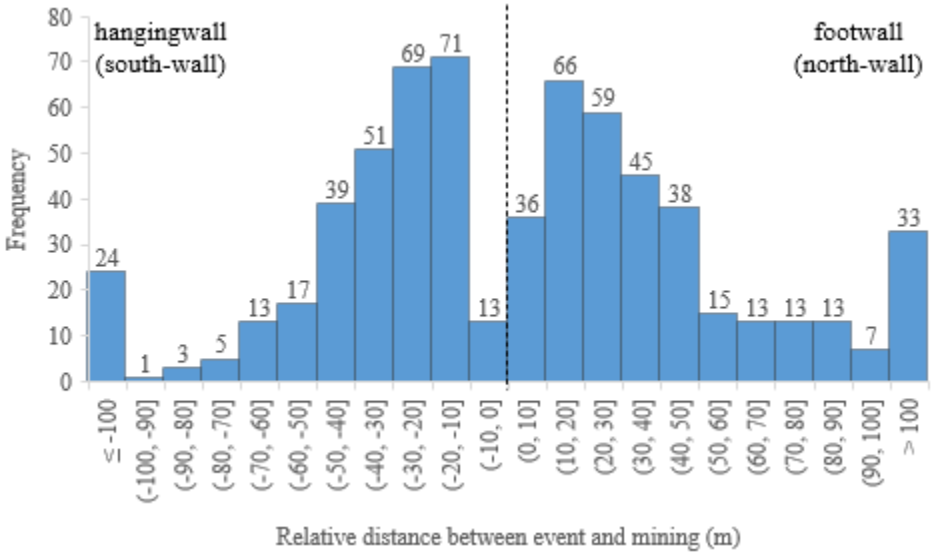
Figure 3.28: Probable fault-slips and pillar events, the view is from the footwall looking southwest towards the F3 and F4 faults, 2013–2016

As was observed in deep tabular South African mines (Joughin & Jager, 1983; Spottiswoode, 1984; Legge & Spottiswoode, 1987), stope advances generate seismic events that bow around the leading edge of the mining front. At the GH period between 2013 and 2016, the spatial-temporal relationship between seismic events and extraction was tested. The relative distance between a recorded notable (> +0.5 M_w) seismic event and a mined-out volume was conserved and referenced within the hangingwall and footwall of the 30-Vein (*Figure 3.29*). Monthly extraction increments were assumed based on available production records. The smallest relative distance between the event-heading was conserved. The spatial-temporal relationship between event locations to monthly mining demonstrates a normal distribution centered around the vein.

However, there is a slightly higher tendency for events locating within the footwall (left skewed distribution). The response is comparable to SA where the events *bow* around advancing stopes. However, this characteristic differs from reports from the LF deposit where the events located predominantly in the footwall, affected by local bedding planes (Board, 1994; Whyatt et al., 2002).



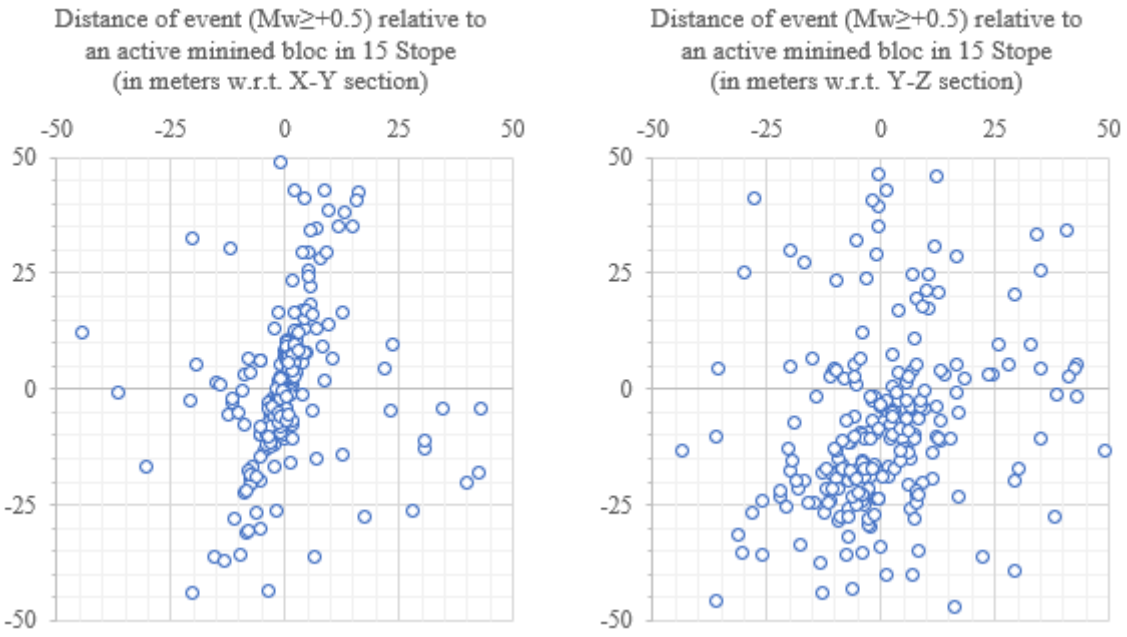
(a)



(b)

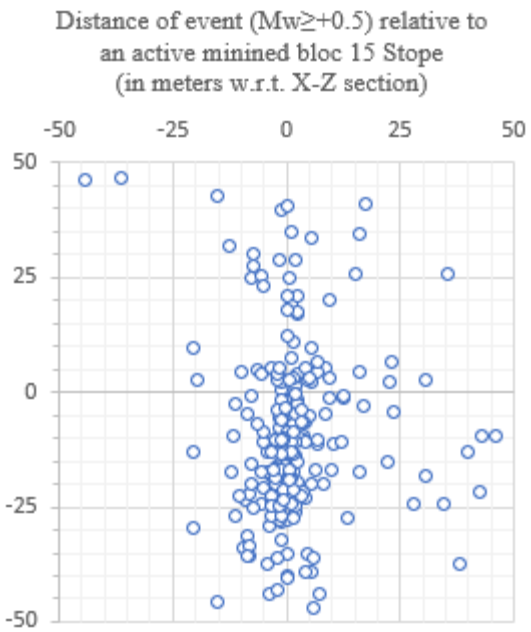
Figure 3.29: Frequency distribution of relative distance between notable events and active mining for (a) 50 m, and (b) 10 m bin widths

To gain further insight into the spatial variability of notable events in relation to mining, the relative distance vector was decomposed into its vector components, assuming the x-y-z frame of reference (i.e., northing-easting-elevation). Assembling these components onto a single reference plane generates a crosshair plot with the central coordinate (0,0) representing the stacking of associated, mined headings. The relationship between the closest active mine heading affected by a notable event, within 50 m of said block, is presented below (*Figure 3.30*). Mine-induced seismicity occurs mainly below the cut (on average 25 m into the floor), adjacent to the face advance (within ± 12.5 m), locating on either side of the footwall or hangingwall. *Figure 3.30*c is marked by a feature trending ~N15°E, which is roughly orthogonal to the strike of the vein. Therefore, the mine-induced events crudely occur on a section relative to the active advancing face.



(a) (b)

Figure 3.30: Spatial distribution of notable events next to active mining for plots equivalent to (a) a longitudinal view (x-z plane), (b) a cross-section view (y-z- plane), and (c) a plan view (x-y plane)



(c)

Figure 3.30: Spatial distribution of notable events next to active mining for plots equivalent to (a) a longitudinal view (x-z plane), (b) a cross-section view (y-z- plane), and (c) a plan view (x-y plane) (cont'd)

3.2.4 Mining Factors Affecting the Seismic Output

Based on the above analysis, it is stipulated that the Gold Hunter mainly produces fault-slip and pillar burst events. Strain-bursting events (directly at the active heading) are less prominent in the more ductile rockmass for notable events. The more ductile argillitic rock unit of the GH tend to crush out in a non-violent manner (*Figure 3.13*). Little to no vitreous quartzites is present in the Wallace & St-Regis formation hosting the 30-Vein, as opposed to the Lower Revett in the historical Lucky Friday deposit. Damage (as seen from rockbursting) is typically observed on events > +1.5 M_w located within ~9 m from the mine openings and has been attributed to fault-slip (Hecla, 2017).

Other mining factors have been observed to affect the seismic output in the GH, such as the mining rate (#events / ton & #energy released / ton mined), the nature of seismic decay following production blasts, seismic release (over time and area mined), and the time-dependent remnant pillar responses.

3.2.4.1 Mining Rate

The mining rate has been compiled for the Gold Hunter, 2013–2016 period (*Figure 3.31*). It can be observed that a production rate of 820 tons per day (~300,000 tons per year), as seen between 2014-2015, released ~0.7 events (≥ +0.5 M_w) per 1,000 tons mined on the 30-Vein. The maximum output was made for an average production of 730 tons per day during the 2016 production, releasing 1.2 notable events per 1,000 tons mined on the vein (about 1.7 times higher output). These mining rates are comparable to those recorded in the Lucky Friday deposit between 1983 and 1993 (Board, 1994). Therefore, reducing the mining rate does not necessarily guarantee a lower seismic event count per tonnage, as seen for 2014–2015 vs 2016 production. The latter mined only the bottom stopes (12S, 15S & 16S).

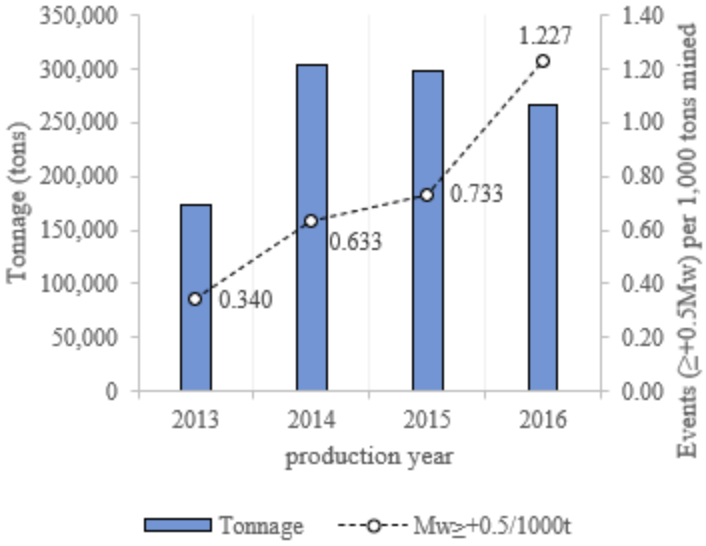


Figure 3.31: Annual seismic-production rate in terms of tons mined in the Gold Hunter

A similar observation occurs when assessing the mining rate through the seismic energy release principal for the Gold Hunter, 2013–2016 period (*Figure 3.32*). The monitoring system calculates the seismic energy (E_s) from the waveform. It can be observed that the higher 820 tons per day rate, as seen between 2014 and 2015, released on average ~645 J/ton on the 30-Vein. However, the maximum output was made for the lower 730 tons per day during the 2016 production, releasing 1,700 J/ton on the vein (about 2.5 times higher output). Therefore, the seismic energy per ton assessment illustrates an even bigger discrepancy between the mining rates when compared directly to the notable event count per tonnage. It appears that the seismic

increase per mining rate is affected by time-dependent incidences in highly stressed abutments (remnant pillar configurations) and large mine-wide fault readjustment (bounding stope faults), where one large event can flood the cumulative energy summation.

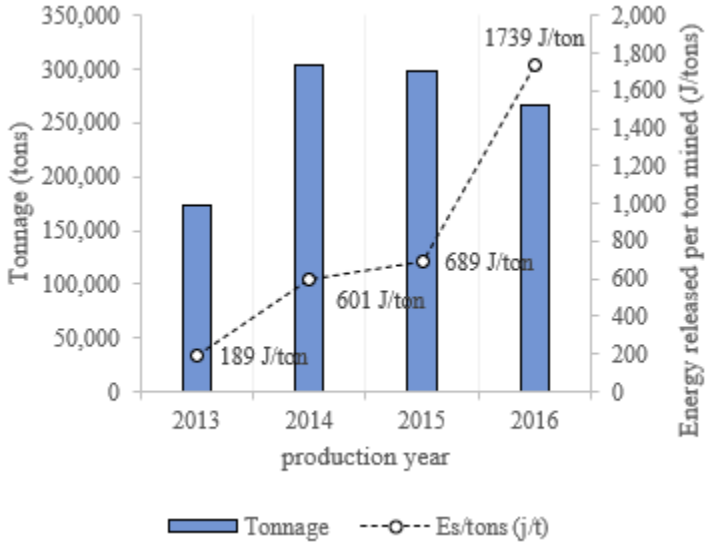


Figure 3.32: Annual seismic-production rate in terms of radiated seismic energy in the Gold Hunter deposit

3.2.4.1.1 Discussion

The mining rate has been identified in the Coeur D'Alene mining district as a technique for controlling rockburst hazards (Whyatt et al., 2002). However, the mining rate (tons / day) was analyzed on a day-of-the-week basis rather than averaged over a production period (say annual). Therefore, it is argued that while the mining rate may affect the seismic outcome in the proximity of the stope face, it does not change the stress build-up in permanent abutments over long periods, releasing energetic events.

Comparing the seismic energy release per ton mined on the 30-Vein with published South African records (in deep gold mines) shows occurrences in the same order of magnitude (*Figure 3.33*). Note that the SA values were taken from Spottiswoode *et al.* (2008). These were averaged from the reported total production tonnages and total energy outputs, where more than 500,000 m^2 of reef were mined over a 4-year period, generating ~10,000 $M \geq +0.0$ events in each case. These reefs share similar geological formations than those found at the LF. The Carbon Leader Reef (CLR) presents the largest seismic energy release by ton mined at 15,310 J/ton. The

Ventersdorp Contact Reef (VCR) presents a seismic energy release of 5,401 J/ton. The 30-Vein stopes (11S, 12S, 14S, 15S & 16S) have released 1,158 J/ton during 2013–2016 production, which falls roughly within one order of magnitude from SA records. The lower rate of range for the GH is attributed to the wider mining width, which generates more tonnage per area. SA practice typically mines veins narrower than 1 m (Budavari, 1983), while the GH average width is closer to 3.65 m. Nonetheless, these seismic energy responses can be grouped and are most likely attributed to the continuity of the vein systems (tabular mine configurations), the presence of quartzite-rich rocks, and the formation of highly stressed narrow abutments resulting from the excavation shape and high in-situ stresses. Due to the higher horizontal stress gradient, and the average mining depth, the GH presents stress-strength ratios similar to those found in ultra-deep SA mines (> 3 km). For wider abutments, as seen in plug shaped orebodies in North American, bulk-type mines experience lower levels of seismicity when compared to deep tabular mines (Brummer, 1999). Unfortunately, readily published data from these mines isn't available for further comparison.

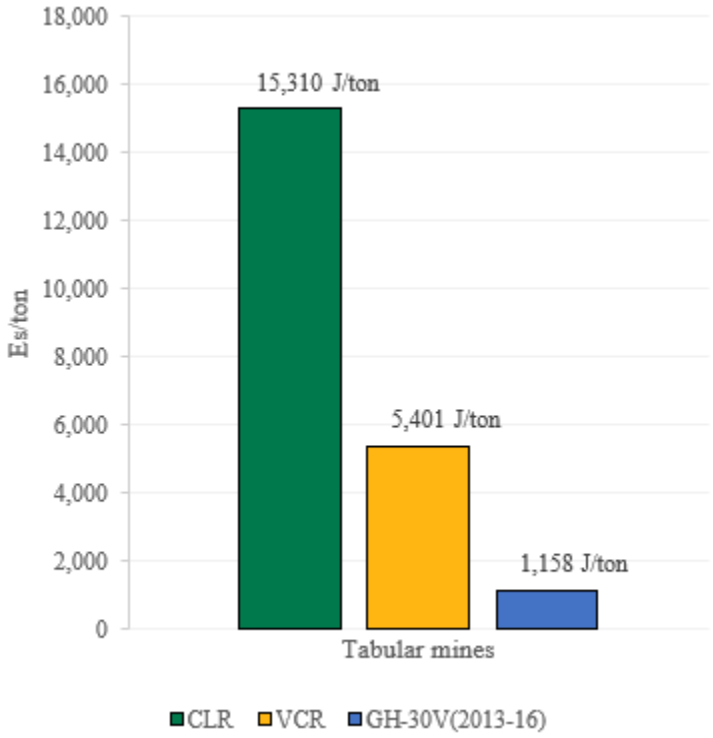


Figure 3.33: Total radiated energy release per ton mined as observed in tabular mines

Comparing the seismic energy release per area mined of the GH to published South African records (in gold mines) shows occurrences on the same order of magnitude (*Figure 3.34*). As previously mentioned, the SA values were reproduced from Spottiswoode *et al.* (2008) and were averaged over a ~4-year span. The CLR, once more, presents the largest seismic energy release by area mined at 49.6 kJ/m^2, while the VCR presents a seismic energy release of 17.5 kJ/m^2, within 4% of the GH attribute of 16.8 kJ/m^2. This assessment eliminated the width dimension bias, allowing us to compare *apples-with-apples*. Based on this data, the Lucky Friday mine might be the most seismically active mine in North America.

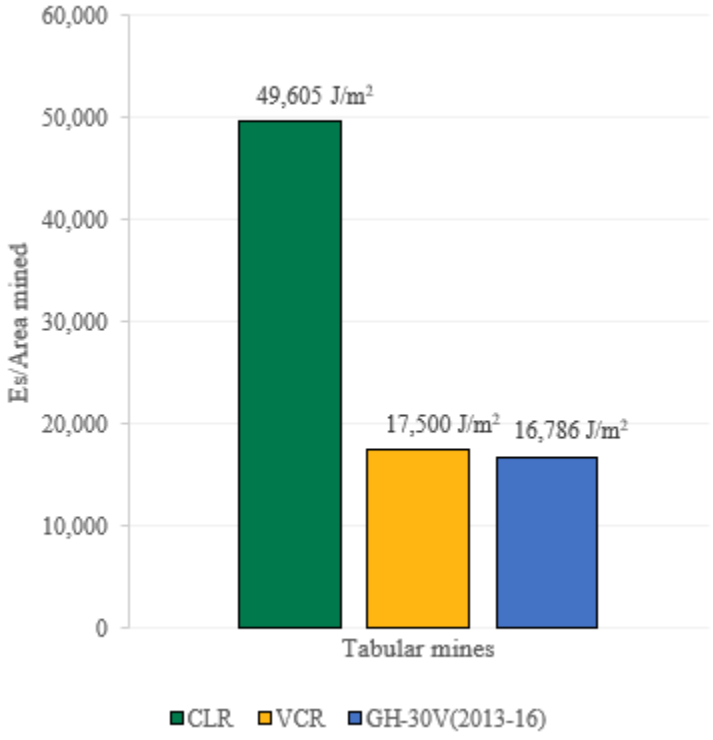


Figure 3.34: Total energy release per area mined as observed in tabular mines

3.2.4.2 Production Blasts

The relationship between mine-induced seismic and stope blasting is well established in the literature (Whyatt & al. 2002). At the Gold Hunter, the lag time between the nearest relevant blast and the occurrence of a significant seismic event was analyzed (Hecla, 2016). The dataset has been extended to complete the 2015–2016 production cycle mined by underhand cut-and-fill on the 30-Vein (*Figure 3.35*). Production blasts are initiated between shift changes, with workers arriving at the headings typically 2-hours following the blast. At that point, ~75% of events ≥

+0.5 M_w have been dissipated or induced, while only ~30% of events ≥ +2 M_w have been observed to occur within the blast clearance period. About 25% of the total mine-induced events ≥ +0.5 M_w present time-dependent response, and these occurrences increase proportionally with increased magnitude release. Therefore, the larger (M_w > +2) events appear less sensitive to immediate blasting, presenting the greatest risk for rockbursts. Fortunately, some of these large events locate in remnant pillars, some distance away from the mining fronts. Due to the size of the output magnitudes (Ortlepp, 1992) and the erratic trigger time distribution (Gibowicz & Kijko, 1994), these large events present fault-slip characteristics. The same conclusion was observed throughout the Silver Valley (Whyatt et al., 2002).

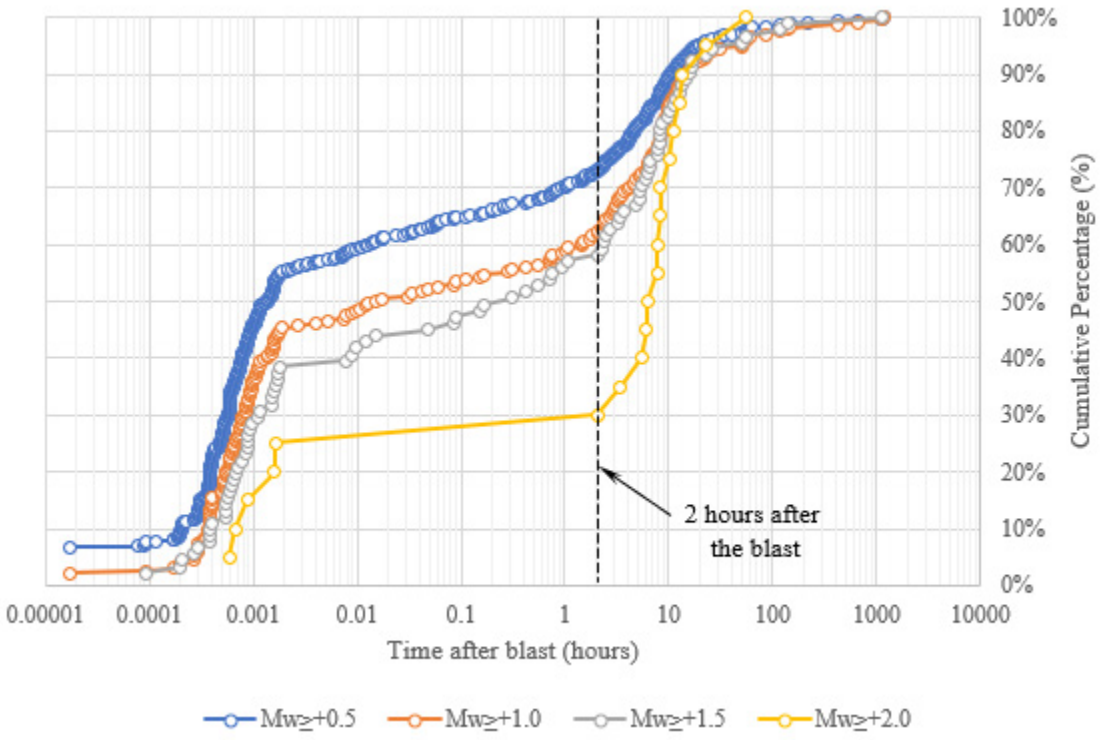


Figure 3.35: Lag time study between end of shift blasts and event trigger, 2013–2016

3.3 Chapter Summary

Chapter 3 presented the mining, geological and geomechanical context of the Lucky Friday mine, focusing on the Gold Hunter deposit. Operations extract the main 30-Vein primarily by the underhand cut-and-fill mining method since 2013. Several faults and related structures bound the

stoping areas. Continuous narrow vein, tabular mines are characterized by high normal stress (many hundreds of MPa) at the face, returning to in-situ values some distance ahead into the rockmass. The GH stope headings yield to these high stresses, inducing fractures that stretch up to 3 m below the cut into the floor. Extracted tabular ore geometries are also characterized by large closures generated at the face, which extend to the mid-stope panel.

The seismic volume filters, constructed to constrain seismogenic stoping zones, were presented. These stoping volumes served as the basis for differentiating the seismic response within individual stoping areas. The seismic review investigated the magnitude-time-location (MTL) relationship with mining for 2013–2016 in the GH at the total and stope scale. Seismic dependencies to mining parameters were also extrapolated and compared with South African publications.

The analyses performed in this chapter resulted in the following conclusions:

1. Notable seismic events group around the stope advance and in remnant pillars. At the heading, the events seem to bow around the leading edge into the HW and FW, extending 100+ m into the rockmass and, on average, ~25 m below the floor. While sensitive to blasting, as 70% of events are released during that period, events greater > +2 M_w appear time-dependent (inducing ~30% release with blasts).
2. Overall, the evidence indicates that most of the larger events (≥ +2 M_w) registered in the GH are fault-slip (shear) related. This upper magnitude range accounts for 87% of the total energy released during the study period. In contrast, the notable events (≥ +0.5 M_w) may likely present a mixture of strain and fault-slip occurrences (especially in remnant pillar locations where confinement is building with load increase on the pillar). The next chapter will further test this idea through numerical stress modelling.
3. It was established that seismic energy illustrates seismic risk better than notable event count. Seismic energy tracking is more representative due to the exponential energy release for increased magnitude incidences, while (say) notable event count stays linear over time.
4. Based on the inferred seismic analyses, fracture density of secondary fault systems may control the seismic outcome in proximity of the abutments (in the stope floor and remnant pillars).
5. Evidence of yielding at the stope face, the presence of primary and secondary related structures, the shallow seismic characteristic (b-value), and the random distribution of seismic occurrences across the stopes suggest that the primary source mechanism, leading to the energy release, is fault-slip.

CHAPTER 4 NUMERICAL ASSESSMENT OF THE SEISMIC CATALOG

4.1 BEM Setup

This chapter assesses the GH seismic database through established seismic processes developed for narrow tabular mines. Utilizing a Boundary Element Method (BEM) code, numerical assessments were undertaken to better comprehend the seismic source mechanism. This deterministic approach separates the modelling effort into two schemes:

1. The grid-based numerical analysis utilizes a planar 3-dimensional construct of the 30-Vein at the GH. The BEM-DD (Displacement Discontinuity) formulation was assumed. Model calibration was achieved by comparing in-stope wall-to-wall closures with simulated results, providing a best-fit estimate of the rockmass Young Modulus. The ERR assessment, as routinely conducted in South African practice (Ryder & Jager, 2002), was employed to examine the mine-wide seismic hazards during specific mining periods. The energy release rates were further compared to seismic records.
2. The block-based numerical analysis improves the accuracy of the 30-Vein construction by generating constant 3-dimensional blocks, capturing the veins meandering. The BEM-FF (Fictitious Forces) formulation was assumed. Stress tensors can be queried at known locations inside the rockmass. Large seismic events were tested for ESS with respect to the corresponding as-built stoping geometries. Inspired by Board (1994) and Salamon (1993), the ESS procedure was integrated into a mine-wide Discrete Fracture Network (DFN) derived from detailed field mapping of faults and related structures within the ramps and stopes of the GH.

Boundary Element codes, which utilize Displacement Discontinuity (DD), are efficient at running stress and displacement analysis for narrow tabular mining fronts (Crouch & Starfield, 1983). A DD element geometry is analogous to a thin two-sided parallel slip (or crack) where the opposing surfaces move relative to each other. For a *virtual* DD thickness, the element reports at its center values for normal (δ_n) and shear (δ_s) displacements, representing closure and ride, respectively.

These deformations are commonly compared with physical convergence measurements taken in tabular mines, primarily in South Africa (Malan & Napier, 2021).

The Boundary Element code MAP3D v68 (Wiles, 2022) was selected for the analyses. MAP3D is based on the indirect Boundary element method (Banerjee & Butterfield, 1981). The model's mesh accuracy was benchmarked against the analytical solution of a planar crack, comparing the stresses and displacements induced by enlarging the span of a reef (Appendix A). The code overestimates the stresses and closures immediately at the edge of a reef by ~20%, improving further away from the leading edge. The overall numerical results compare to within 10% of the expected solution for a mesh equivalent to mining dimensions. MAP3D doesn't assume any edge correction processes (Wiles, 2022). However, further verifications determined a computational error of only ~2.5% between the theoretical and numerical ERR values.

Both BEM schemes assume the following assumptions and specifications:

1. The rockmass assumes homogeneous, isotropic geological conditions (i.e., excludes discrete discontinuities) set in an infinitely elastic medium where E and υ are the primary input parameters. The rockmass strength parameters don't assume a flow rule.
2. The elastic assumption ignores any stress-path dependencies. The complete mining sequence on the 30-Vein was rebuilt from 1997 to 2016 year-end, with the addition of 8 Stope on 80-Vein due to its proximity to 14 Stope. The modelled mining steps extract 11, 12, 14, 15, 16 Stope on the 30-Vein, and 8 Stope on the 80 Vein. The mining steps match production records (survey and tonnages). These were reconstructed in monthly, quarterly, or yearly increments, pending the accuracy of the historical data.
3. The GH infrastructures (e.g., ramps, haulages, slots) are positioned in the footwall and were ignored due to low-stress influence on the mining front.
4. The mesh resolution was determined to match typical cut-and-fill stope advance. The grid-based (DD-element) model assumes an average thickness. The block-based (FF-element) model reproduces the as-built mining widths as measured by mine survey.
5. All external mechanisms impending boundary closure were ignored in the numerical simulations (e.g., backfill and ground support).

Both model constructs are shown below for a mining advance set between 2013 and 2016 (*Figure 4.1* & *Figure 4.2*). The x-y-z axes refer to the easting, northing, and elevation pointers. The displayed mining step integers above value 2 correspond to annual production increments, illustrated by colour. The models present similar mining areas to have occurred on the 30-Vein up to 2016-year end. The main stoping area strikes ~104° and dips vertically. The 80-Vein rests ~30 m north of the 30-Vein (14S) and assumes the same strike. However, the DD-elements (DD square faces) were constructed with a constant element dimension of 3.048 m high by 3.048 m in length with a virtual thickness of 3.048 m. The FF-elements (FF blocks) have been given the same fixed height and length dimension as the DD but with varying thicknesses that range from 3.048 to 10 m (max. thickness found in the slot access into the vein). As previously mentioned, the attributed FF block thicknesses were measured from in-field stope projections. The MAP3D model input parameters are placed in Appendix B.

Both model constructs assume the following in-situ stresses [in MPa]:

$$\sigma_3 = 0.029 * z + 8.8 \quad 4.1$$

$$\sigma_2 = 1.200 * \sigma_3 \quad 4.2$$

$$\sigma_1 = 1.500 * \sigma_3 \quad 4.3$$

where z is the depth (in meters) below the ground surface and the constant (8.8 MPa) accounts for the extra ~300 m overburden above the GH deposit.

with: σ_3 is vertically oriented

σ_2 is horizontally oriented (N50°E)

σ_1 is horizontally oriented (N40°W)

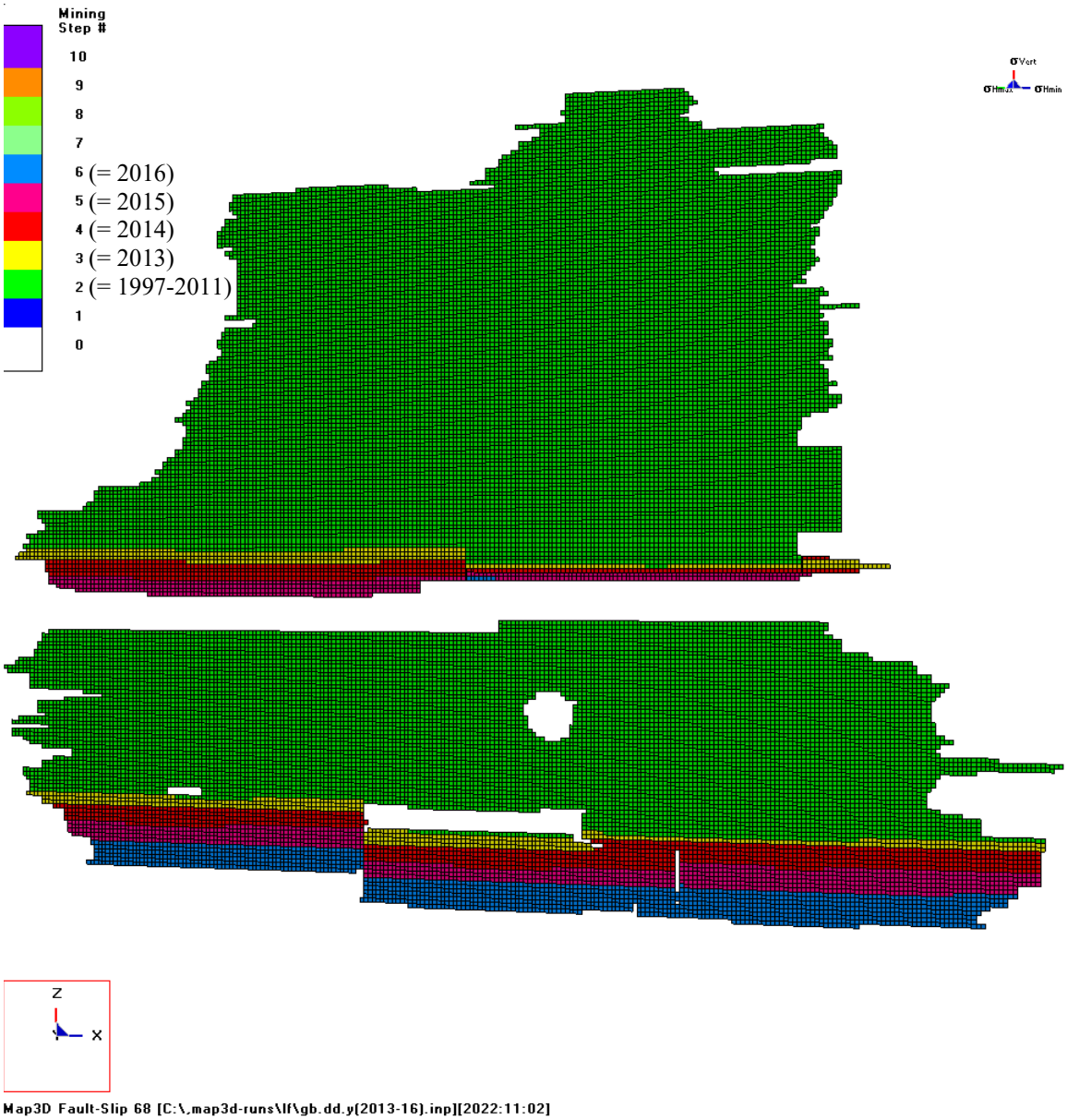


Figure 4.1: Longitudinal view of the grid-based model (DD elements), reconstructing the main 30-Vein of the Gold-Hunter deposit. The view is looking North

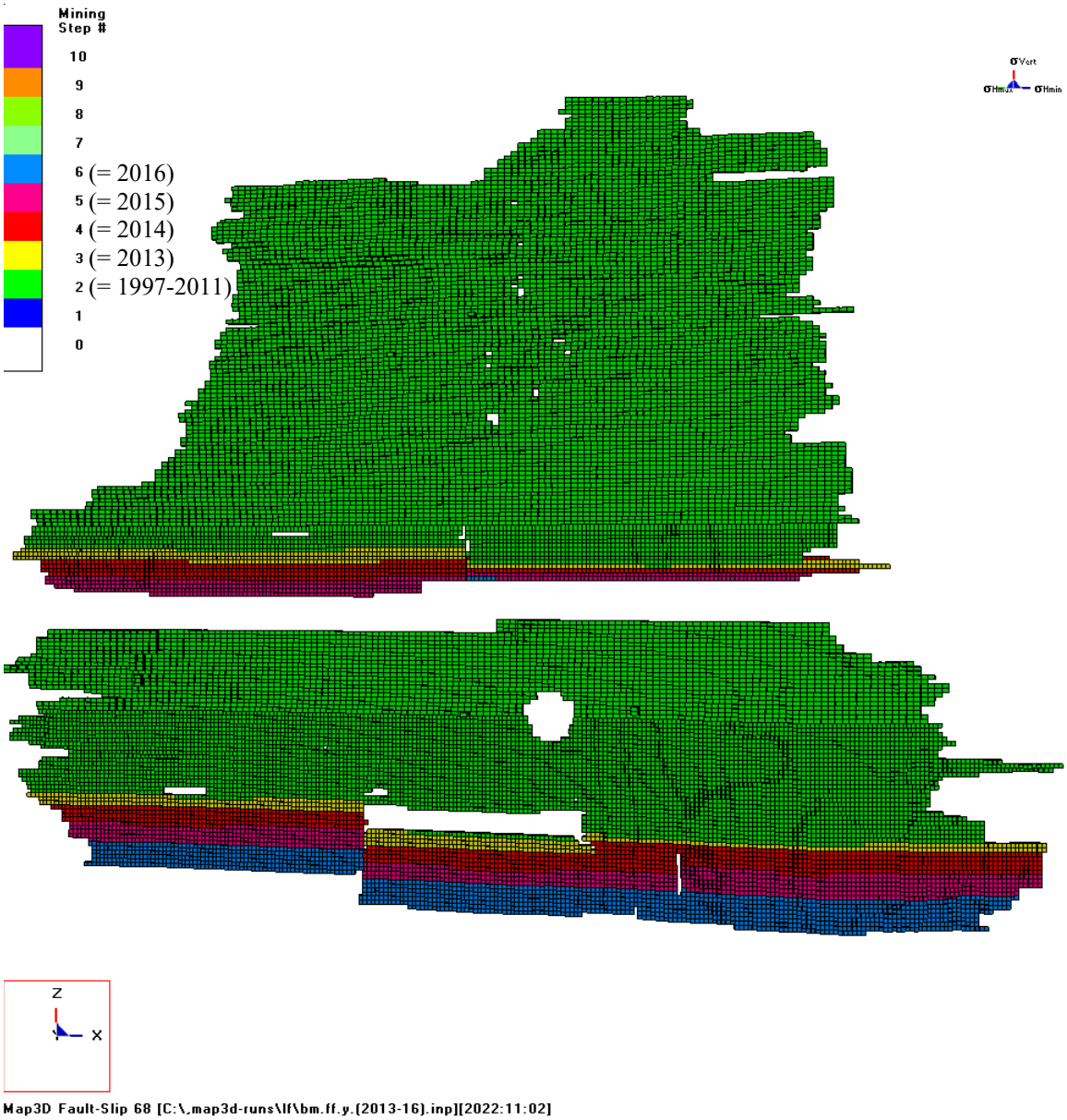


Figure 4.2: Longitudinal view of the block-based model (FF elements), reconstructing the main 30-Vein of the Gold-Hunter deposit. The view is looking North

4.2 Grid-Based Analysis (BEM-DD)

4.2.1 Closure Calibration Procedure & Assessment

As previously discussed in Chapter 2, the bulk of the rockmass in mining narrow reefs behaves elastically as confirmed at the ERPM, and Harmony Gold, in South Africa (Ryder & Officer, 1964; Ortlepp & Nicol, 1963). The uninterrupted extraction of the reef induces large displacements on the stope boundary (observed as closure) while concentrating the stresses ahead of the mining face (fracturing). The theory of elasticity, therefore, provides a framework whereby it is possible to compute the deformations and stresses incident from mining.

From an energy point of view, the induced wall displacements reflect the change in potential energy at the stope boundary (W_t). The latter is a critical component in the energy balance formulation developed by Salamon (1984). For linearly elastic conditions, past studies have attributed up to 50% of the W_t to the energy release (W_r) component (Cook et al., 1966). Mining induced face advance closure (δ_n) values compose the ERR formulation, where South African practice regards ERR > 30 MJ/m^2 as a moderate seismic hazard threshold (Jager & Ryder, 1999).

The wall-to-wall displacements as mining advanced were measured in 555-11-05 (11S) and 635-15-2 (15S) of the GH (Seymour et al., 2016). The in-stope closure responses were presented in **Section 3.1.3.2** (*Figure 3.16*). The numerical procedure developed for calibrating the rockmass to continuous in-stope closure measurements is given herein.

The grid-based model was used to calibrate the elastic rockmass properties of the GH by varying the Young's modulus (E) from lab-scale data, comparing the simulated sets of closures with in-field measurements. Once a set has been reasonably matched, the E of the rockmass is identified.

From a modelling process, the model was sequenced to reflect the actual geometrical change on 30-Vein as observed during the closure monitoring. The mining steps assumed monthly mining increments. These were observed sufficient to drive geometrical changes forcing rockmass displacements. During the monitoring period, all active 30-Vein stopes have been allowed to advance in adjacent stopes as dictated by the production records.

Once the grid-based model was assembled for both stopes, displacement history points were set on DD elements nearest to in-stope instrument locations (see Table 4.1). The effective normal

displacements were monitored on the DD elements as the simulation cycled through the mining steps, capturing the mine-wide geometrical changes. The relative normal displacement (δ_n), simulated on the DD surface, was corrected to exclude the initial displacement of opening the cut. determined by subtracting the absolute displacements simulated before activating the field instruments. Therefore, the model run produced numerical closure recordings (time stamps) matching in-field measurements.

Table 4.1: Displacement history points (at the center of a DD element) with respect to the nearest closure instrument (in metric coordinates)

Stope	DD-dof #	Closure Meter #	x (SI)	y (SI)	z (SI)
11S (5550-11-05)	-	4	17621.7324	24622.6718	-1687.8300
	28894	-	17622.7048	24620.9767	-1687.6786
15S (6350-15-02)	-	5	17830.1788	24572.8108	-1917.1270
	31374	-	17829.9431	24572.7665	-1917.8026

The Elastic modulus reduction process was initiated by setting E = 35.7 GPa (the upper range lab-scale value) while progressively lowering the Modulus to 18.9 GPa by 2.1 GPa increments. The Poison ratio was fixed to reflect laboratory results ($\upsilon = 0.2$) and wasn't varied. Each reduction in Modulus required a model run. The simulated results were grouped and overlayed atop continuously measured displacements, allowing to perform statistical analyses of best-fit test (Appendix C). All the input moduli conserve the *stepped* shape, driven by the underhand mining response. However, the Young Modulus controls the magnitude of simulated convergence (i.e., inversely proportional as higher modulus generates lower displacements).

The E = 29.4 GPa curve offers the best-fit match for both stopes, resulting in the smallest overall root mean square error (*Figure 4.3*). The dashed (blue) line represents the simulated closures. Both datasets match reasonably well, with an average RMSE of 2.54 cm and 1.78 cm for 11S and 15S, respectively. Therefore, the overall elastic property assumed for the GH rockmass is estimated at 29.4 GPa for an overall root mean square error of 2.16 cm.

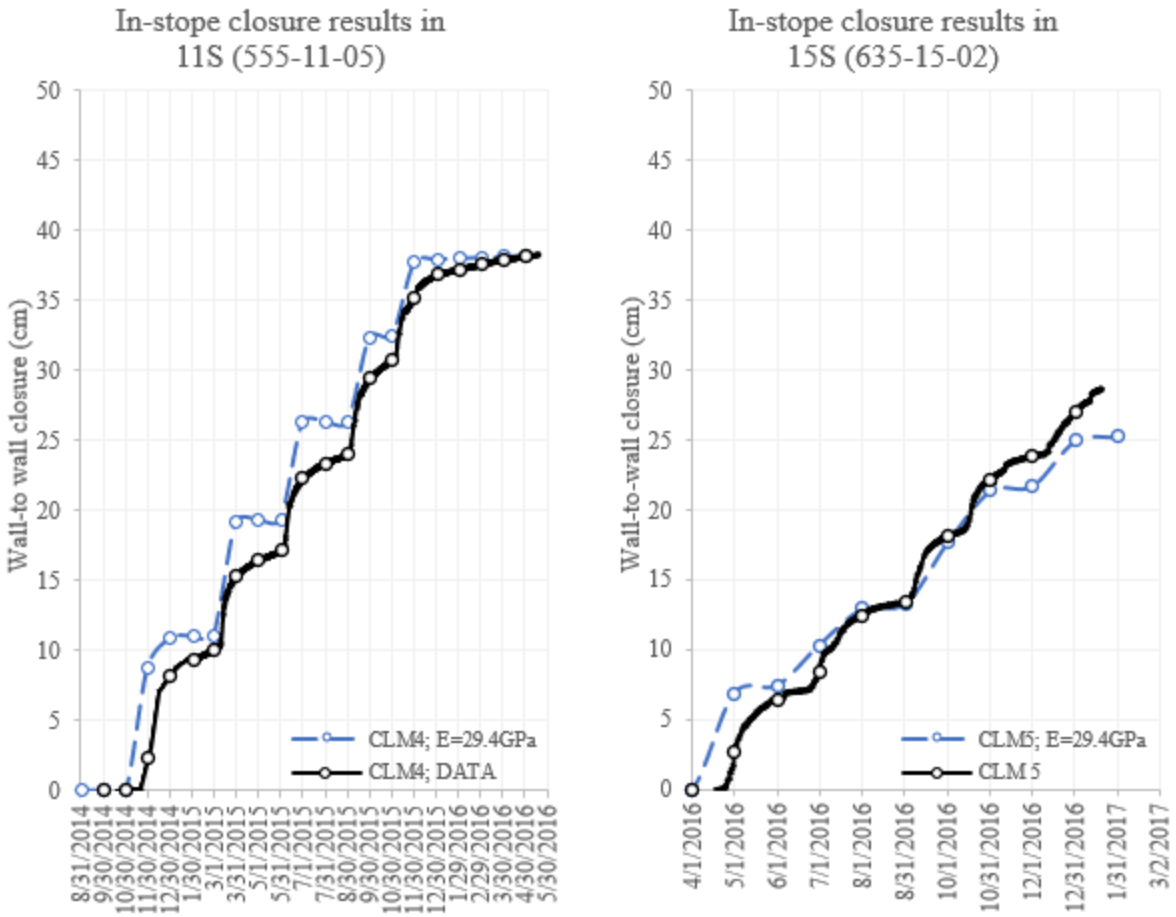
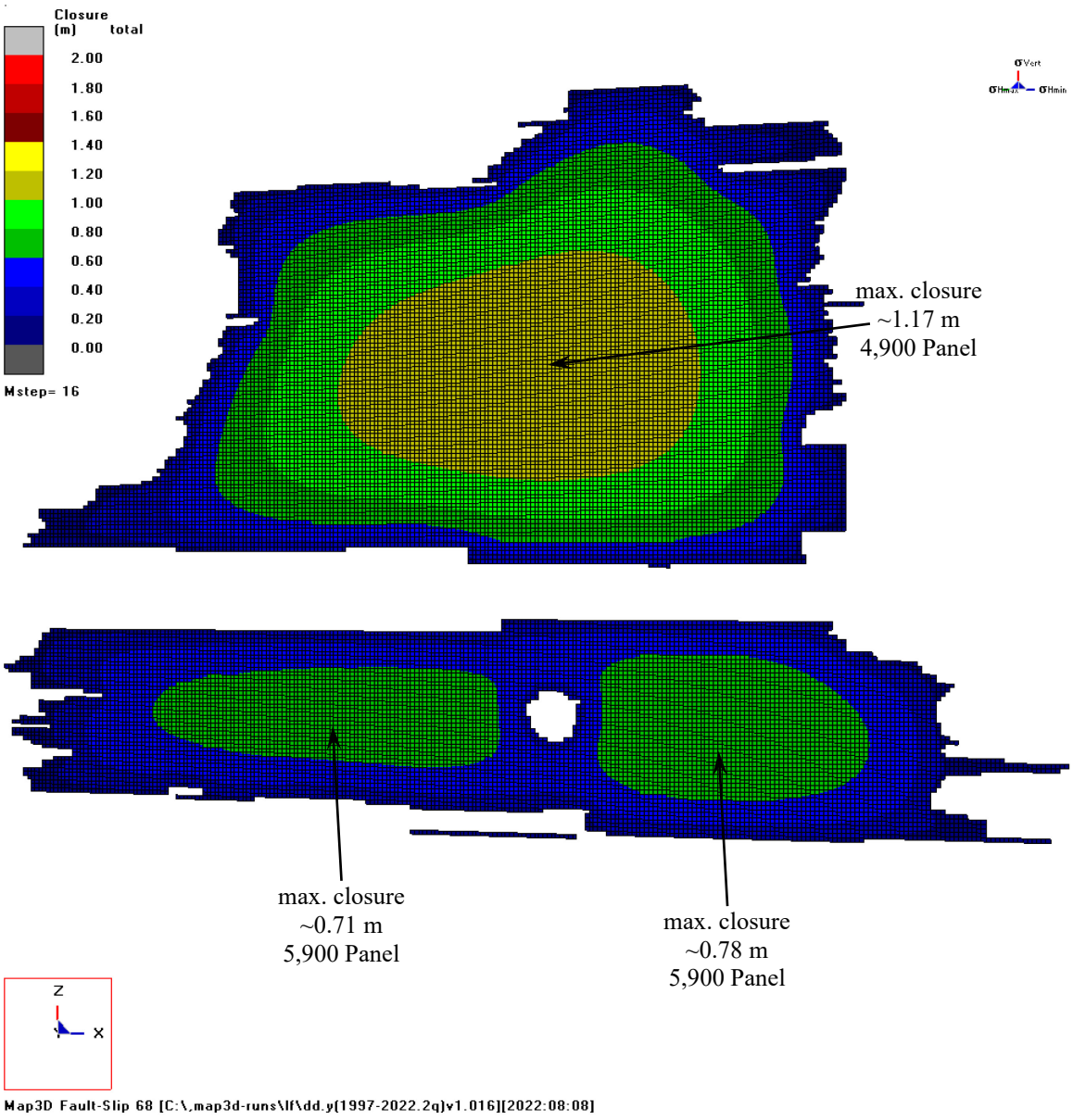


Figure 4.3: Best-fit (E = 29.4 GPa) normal displacement curves in (a) 11S, and (b) 15S

The calibrated E value sits in the upper range lab-scale estimate at ~82%. This value seems to sway from standard rock mechanics practice in North American mines, which assumes a scale effect between in-situ and lab-scale intact results, mainly owing to the presence of geological features (Hoek & Brown, 2019). However, this behavior complies to South African engineering practice in tabular reefs where the in-situ Elastic Moduli match more closely the intact value (Jager & Ryder, 1999). Hence, it is most likely that the extensive continuity of the mined-out vein material, with the small effective extraction front as advanced in thin tabular mining, allows the bulk of the rockmass to respond elastically, minimizing the impact of inelastic structural effects (Gürtunca & Adams, 1991).

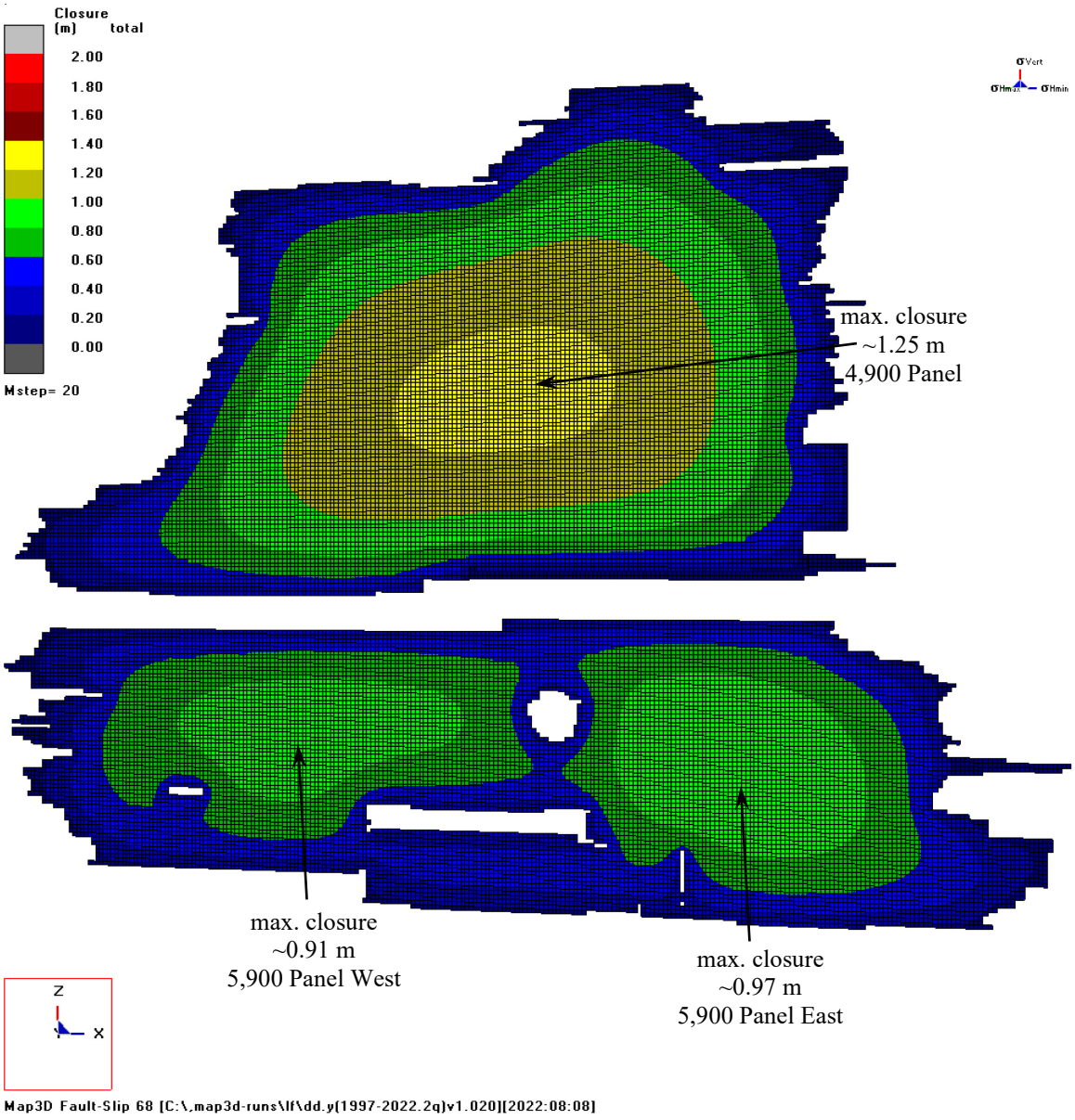
Conserving the calibrated elastic properties, closure estimates across the vein were plotted for two year-end geometries (*Figure 4.4*). It can be observed that maximum closure occurs at the center of each panel, most prominently in 4,900 Panel. These evolve as mining progresses.

Numerically, pillars tend to restrict closures especially in narrow geometries due to the elastic assumption, preventing rockmass yielding.



(a)

Figure 4.4: Normal displacements (δn) on 30-Vein for year-end geometries (a) 2011, and (b) 2016



(b)

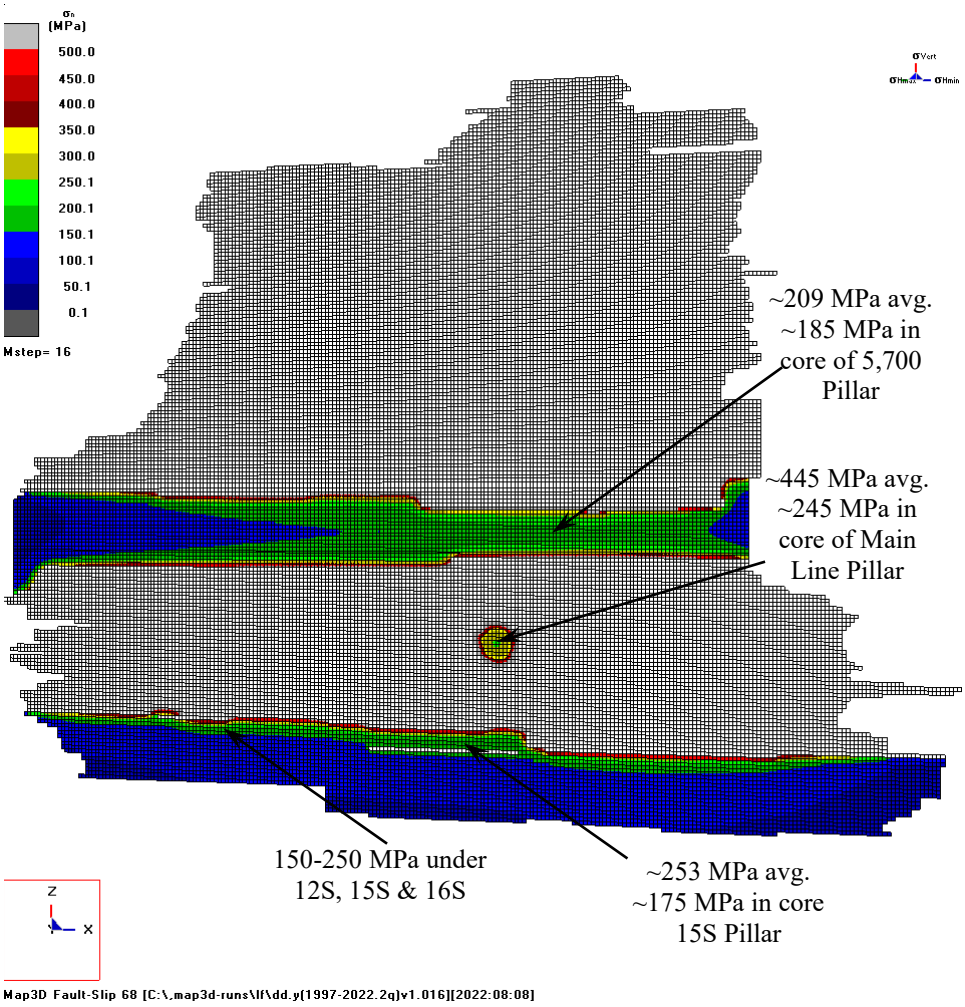
Figure 4.4: Normal displacements (δn) on 30-Vein for year-end geometries (a) 2011, and (b) 2016 (cont'd)

4.2.2 Stress Analysis in Abutments

As was previously discussed in *Chapter 3*, the mine-induced stresses continuously transfer to the abutments of the advancing cut and cumulate in remnant pillars (Budavari, 1983). The uninterrupted extraction of a reef vein induces large stress concentrations at the advancing abutments, often manifested by crushing or bursting of the rockmass (Cook et al., 1966).

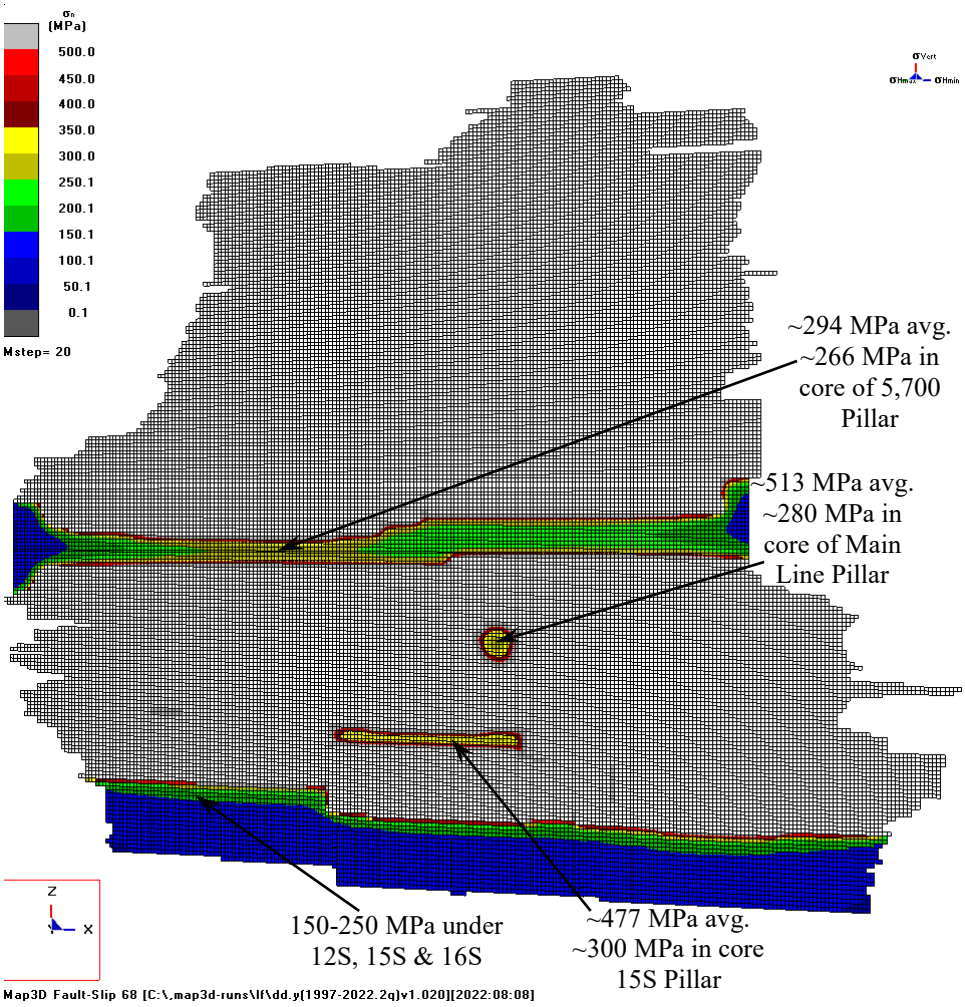
Stresses of complex tabular mining layouts are best analyzed using BEM codes (Crouch and Starfield, 1983). Therefore, the gid-based model has been utilized to assess the normal stresses on the 30-Vein of the GH.

First, the normal stresses (perpendicular to the vein) are plotted in the abutments and remnant pillars for two year-end geometries (*Figure 4.5*). It is observed that the highest average stresses rest in the pillars (250+ MPa) and not in the lower stope abutments (150-250 MPa). The remnant pillar stresses grow as mining extends deeper, increasing on average by 41%, 89% and 15% between the end-of-year layouts in 5,700, 15S Pillar, and Main Line Pillar, respectively. The lower abutment stress stays relatively constant between the stope layouts, although slightly lower in 15S due to a pillar. For both geometries, the zone of high stress migrates with mining.



(a)

Figure 4.5: Normal stresses (σ_n) in lower abutments & in remnant pillars for year-end geometries (a) 2011, and (b) 2016



(b)

Figure 4.5: Normal stresses (σn) in lower abutments & in remnant pillars for year-end geometries (a) 2011, and (b) 2016 (cont'd)

Second, the extent of the induced stresses is significant at the floor into the rockmass. From the stress plot under 12S at the 2016 year-end configuration (*Figure 4.6*), normal induced stress returns within 140% of the pre-mining stress after reaching a depth of 30.48 m. The overstress ratio (σ_1 / UCS) is ~1.15 at that location while it is > 2.5 directly one cut below the stope floor. Yielding at the face is observed in that region. However, the complete extent of the yield is unknown and could possibly extend deeper.

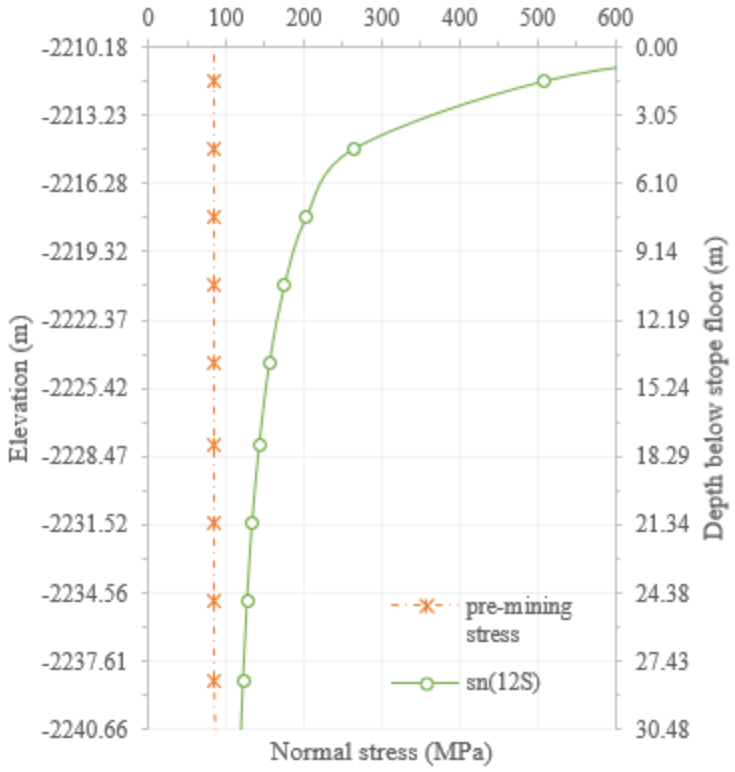
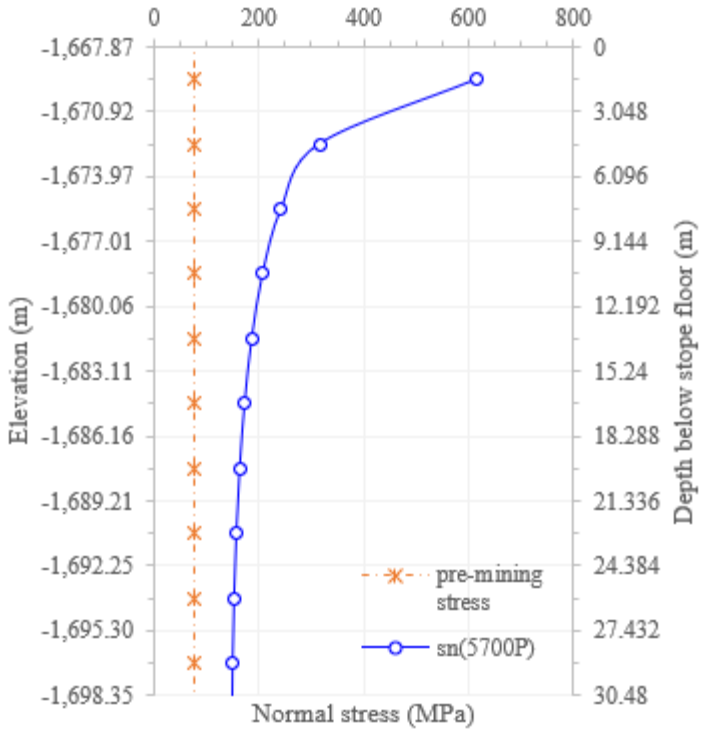
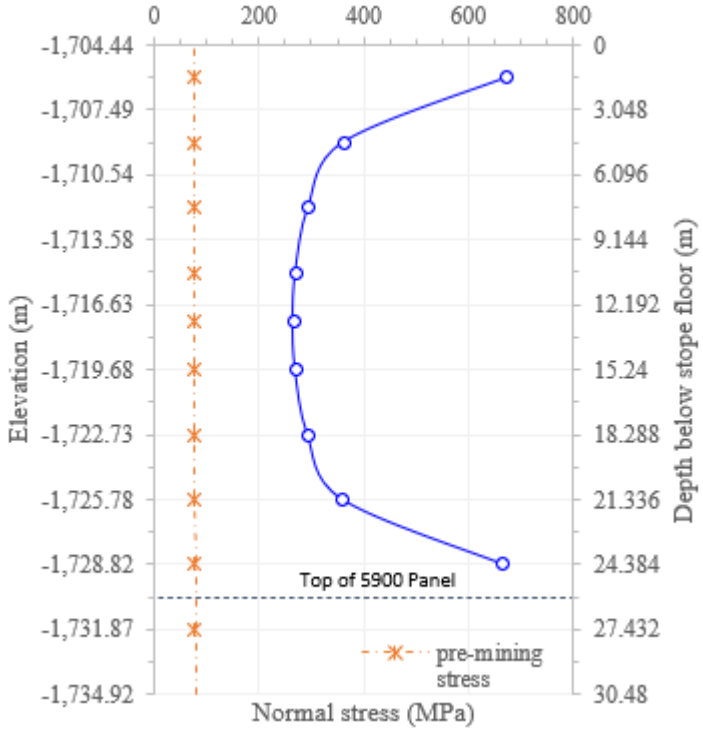


Figure 4.6: Normal stress modeled in abutment under 12 Stope (17,055E) for 2016 year-end geometry

Third, the stresses from the leading edge of two converging horizontal mining fronts will superimpose when within each other's influence (*Figure 4.7*). Normal stresses taken from the formation of the 5,700 Pillar (under 11S & 14S) show signs that the leading edges interact at a pillar height of ~62 m (with normal stresses higher than those observed for deeper conditions in 12S). As the pillar progressively diminishes to ~25 m, the immediate abutments must crush out potentially 1.5 cuts next to the leading edges while the core accumulates high normal (perpendicular) stresses. Not shown here, but the confinement pressures are also high within the pillar core.



(a)



(b)

Figure 4.7: Evolution of normal stress modeled in the 5,700 Pillar for year end geometries (a) 2011 with pillar height ~62 m, and (b) 2016 with pillar height ~25 m

4.2.3 ERR Analysis (BEM-DD)

As examined in *Chapter 2*, the Energy Release Rate (ERR) was empirically derived from deep seismically activate narrow tabular mines to estimate seismic hazard (Cook et al., 1966). The analytical solution associates the pre-mining stress in a block of ground with the post-mining closure induced after extracting the block to the seismic release potential. Mechanical work is defined by multiplying both parameters resulting in the expression as energy over the area mined (MJ/m^2). The ERR provides a practical (deterministic) approach to forecasting the seismic potential of a specific mining sequence or layout. When multiplied by the mined-out area, the ERR value transforms into a component contained in the energy balance formulation, as formulated by Salamon (1983), relating directly to the system's energy dissipation term (i.e., the W_r component). Expanding further, W_r accounts for two independent energy-consuming parameters, which are the (violent) kinetic energy release (W_k) and the (non-violent) strain energy dissipation (U_m). The former relates back to the recorded seismic energy (E_s) captured by the seismic system (Hedley, 1992).

The following section covers the numerical procedure for applying the ERR analysis to a mine-wide grid-base BEM. The energy balance formulation was applied to the extraction sequence studied at the Lucky Friday mine. The objective is to benchmark seismic records against the modeled results. Two main production periods have been identified for the analysis:

1. Mining the GH between 1997 and 2011 (when mining was initiated on the GH).
2. Mining the GH between 2013 and 2016 (when mining restarted, after a one-year work stoppage, with an updated seismic monitoring digitizer).

4.2.3.1 Procedure for Modelling ERR

The calibrated grid-based boundary element model serves as the basis for the energy release analysis. Two additional input parameters need to be incorporated into the grid-base model for each specific mining period: (***i***) the mining sequence on the main vein, and (***ii***) the modeled mining step (e.g., yearly, or monthly geometrical changes). These parameters are mine- and model-dependent, reflecting the geometrical-temporal changes occurring on a mine-scale for an assumed grid resolution.

As the model runs through the selected period, all mined DD elements get tagged to their respective extraction step and stope, and queried for basic values. The extracted DD element block outputs a pre-mining normal stress (σ_n) and a post-mining induced closure (δ_n) taken at the center of the element. The ERR is calculated across the individual DD elements by the following formulation:

$$ERR_{i,j} = \frac{1}{2} \cdot \sigma_{n_{i,j-1}} \cdot \delta_{n_{i,j}} \tag{4.4}$$

where: ERR = energy release rate acting on the DD element [MJ/m^2]
σ_n = stress normal to the DD element [MPa]
δ_n = displacement normal to the DD element [m]
i,j = DD element block number and mining step number, respectively

The ERR is further decomposed into the energy balance components (EBC). The EBC were determined across the extracted DD elements through the following formulations, derived from Salamon (1983, 1984) and Hedley (1992), and adapted to the BEM:

$$W_{t_{i,j}} = \sigma_{n_{i,j=1}} \cdot \delta_{n_{i,j}} \cdot \Delta A_i \tag{4.5}$$

$$W_{r_{i,j}} = ERR_{i,j} \cdot \Delta A_i \tag{4.6}$$

$$U_{m_{i,j-1}} = \sigma_{n^2_{i,j-1}} \cdot \frac{(1-v^2)}{2E} \cdot \Delta A_i \cdot \Delta w_i \tag{4.7}$$

$$W_{k_{i,j}} = W_{r_{i,j}} - U_{m_{i,j-1}} \tag{4.8}$$

where: W_t = potential energy from extracting the DD element [MJ]
U_m = strain energy computed on the DD element pre-mining [MJ]
W_r = elastic strain energy released from extracting the DD element [MJ]
W_k = kinetic energy released from the DD element [MJ]
ΔA = area associated to the DD element [m^2]
Δw = mining width (thickness) of the DD element [m]

The resultant energies were post-processed outside the numerical model code according to the above formulations. A data visualizer (Gem4D) enabled to reference the complete energy series (ERR and EBC) to their DD element id, allowing them to be visually compared to recorded seismic activity at equivalent mining steps. Furthermore, the generated energy values were

compared directly to the Seismic Hazard Potential charts developed by the South African Chamber of Mines Research Organization (COMRO, 1988), to the mine's recorded seismic source parameters (M_w & E_s) and to production tonnages. The proposed energy modelling process is summarized in the flow diagram (*Figure 4.8*).

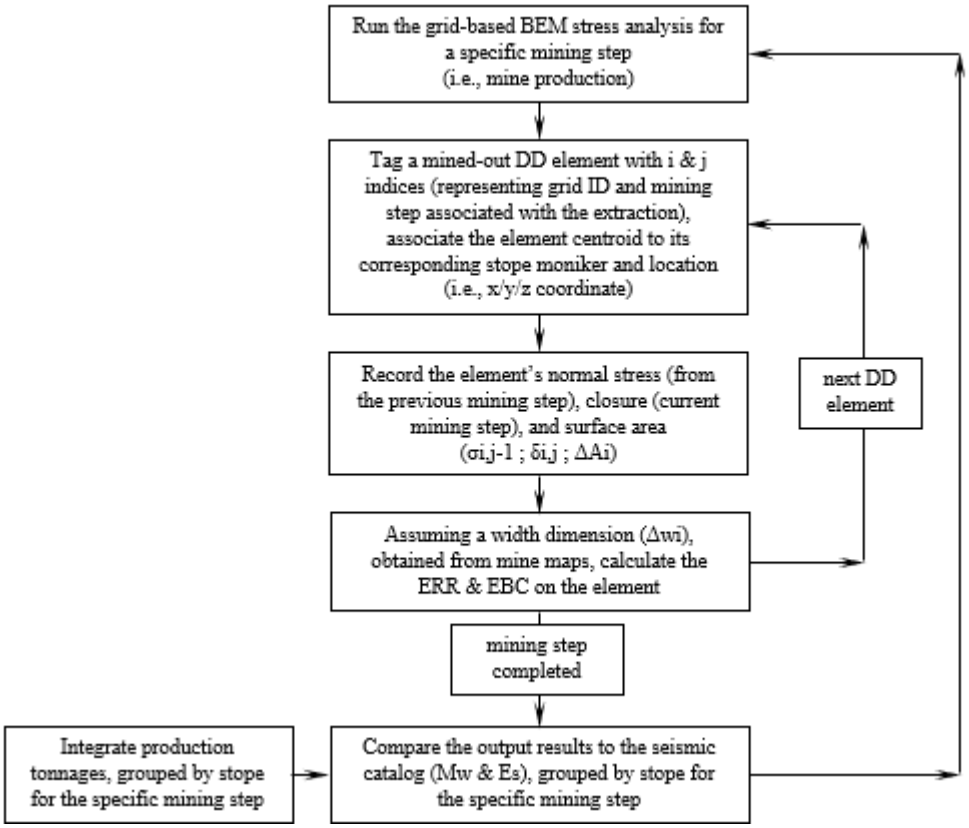


Figure 4.8: Grid-based modelling flow chart of ERR

Due to the applied elastic assumption (i.e., constant elastic properties for a homogeneous rockmass), induced in-field face fracturing conditions (reflecting post-peak material response, see past *Figure 3.13*) and model stress-capping adjustments (as usually applied in South Africa, Spottiswoode et al., 2008) have been ignored in the present energy analysis. The backfill material has not been modeled since infield measurements indicate that it doesn't take any significant load at the immediate face, even after progressing five (5) consecutive cuts underneath the backfill (Seymour et al., 2016). Finally, the proposed energy model ignores explicit discontinuities such as faults but accounts for them indirectly when performing seismic efficiency computations using the ensemble of the seismic data catalog (which contains all event types).

These assumptions provide for consistent and repeatable iterations, reducing potential bias from inputting uncalibrated parameters.

4.2.3.2 ERR calculations in the GH

Two distinct mining periods were evaluated for ERR in the 30-Vein of the GH (***i***) the first mining period occurred between 1997 and 2011 (when mining was initiated on the GH), and (***ii***) the second mining period occurred between 2013 and 2016 (when mining restarted in the GH with an updated seismic monitoring digitizer). Annual mining steps were assumed while monthly increments will be explicitly stated.

4.2.3.2.1 First mining period (1997–2011)

Mining in the Gold Hunter sector started in 1997, initiating on the 4,900 level with two simultaneous overhand and underhand cut-and-fill extraction fronts (*Figure 4.9*). Time markers indicate the year the geometry was formed while an arrow indicates the overhand and underhand mining directions. A second distinct mining horizon was established on the 5,900 level in 2005, forming the onset of the 5,700 (boundary) Pillar between the two converging mining panels. During that period, seismicity was monitored through the Electrolab MP-250 system, consisting of an array of uniaxial accelerometers installed underground around the mining sector (providing source location estimates) coupled with a surface continuously recording Helicorder drum (attributing event size estimates). Seismic activity stayed relatively minor until the latter half of 2007 when a greater number of +1.0 M_L events were onset. The seismic events between 2007 and 2011 were projected onto the longitudinal section. The notable events for that period hold inaccurate locations due to uncertainty on source calibrations. However, their locations were correlated to underground observations such as fault movement or rockmass damage (Hecla, 2013), and their magnitudes were calibrated to the Intermountain West Seismic Network. Mining stopped end of 2011 due to increased rockbursts damaging part of the ramp intersection below 550-14 Stope (probable fault-slip event) and the circular 5,900 Mainline pillar on 5,900L (probable pillar event).

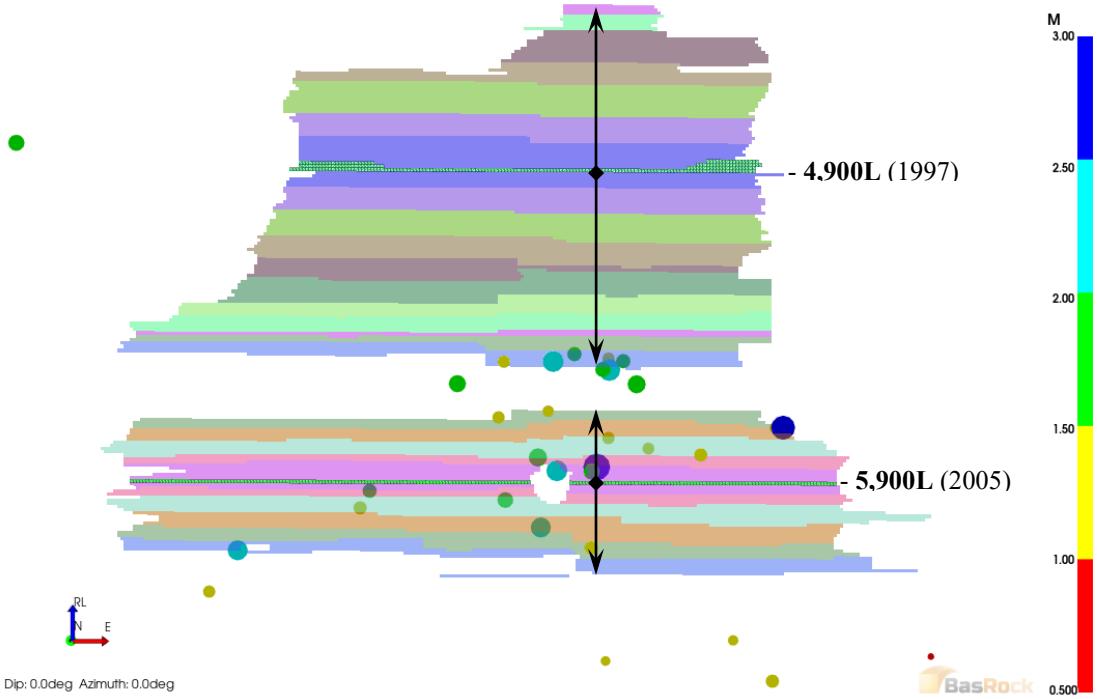


Figure 4.9: Annual extraction sequences with spatial relation to events ≥ +0.7 Mw projected onto the 30-Vein, 2007–2011 (inset arrows indicate the mining directions)

These annual geometrical changes were incorporated into the grid-based model as specified in the procedure (*Figure 4.8*). The individual ERR values were grouped into respective mining steps, representing the GH's average annual release. The average annual ERR values were computed for the first mining period (*Figure 4.10*). As can be seen, seismicity was initiated on the lower 5,900 Panel in 2007, which corresponds to an 11.2 ERR value while reaching its peak at 42.6 ERR in 2011. These ERR onsets match those typically used in South African practice (i.e., 10 ERR indicates slight & 30 ERR indicates a moderate seismic output).

Further investigation into ERR per annual mining step (for year 2007+) reveals that each of the leading longwalls present different ERR values (*Figure 4.11*). These plots were generated by grouping the distinct geometries forming the overhand or underhand fronts (separated by excavated vein material) and averaging the individual ERR values from the DD elements in the mining step. The resulting average mining front ERR reflects the leading-edge value for advancing longwalls and crudely matches the location of the associated seismic activity.

Since the Electrolab seismic system didn't explicitly compute Es values, seismic energy was estimated from recorded magnitudes for that period. These events were converted for seismic

energy by utilizing the E_s to M_w scaling relationship derived from the ESG system between 2013 and 2016, which is:

$$Log(E_s) = 1.86 \cdot M_w + 2.72 \quad 4.9$$

where: E_s = Recorded seismic energy [J]
M_w = Moment magnitude [-]

Seismic efficiency (η%) is defined as the ratio of recorded seismic energy (E_s) to modeled kinetic energy (W_k). This parameter has been computed per total annual increments set between 2007 and 2011 production (*Figure 4.12*). Seismic efficiency varies between 0.0014 and 0.0182%, appearing to increase as the two panels were converging toward the 5,700 Pillar.

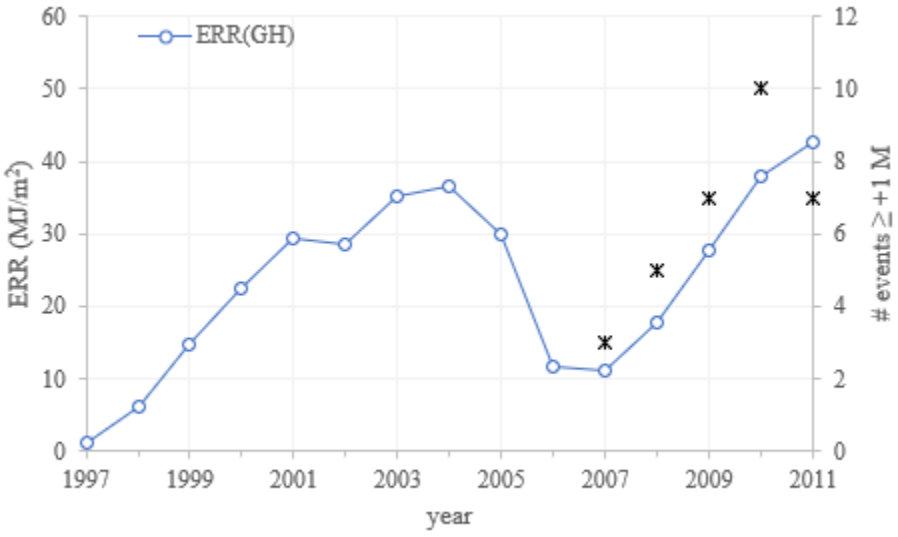
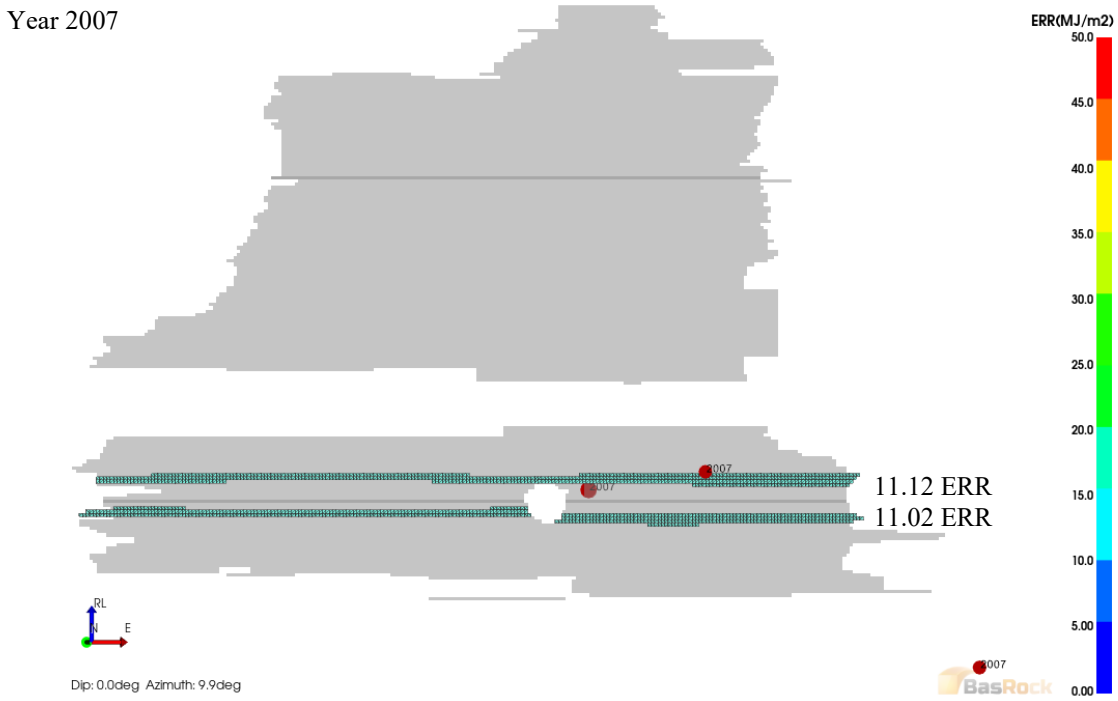
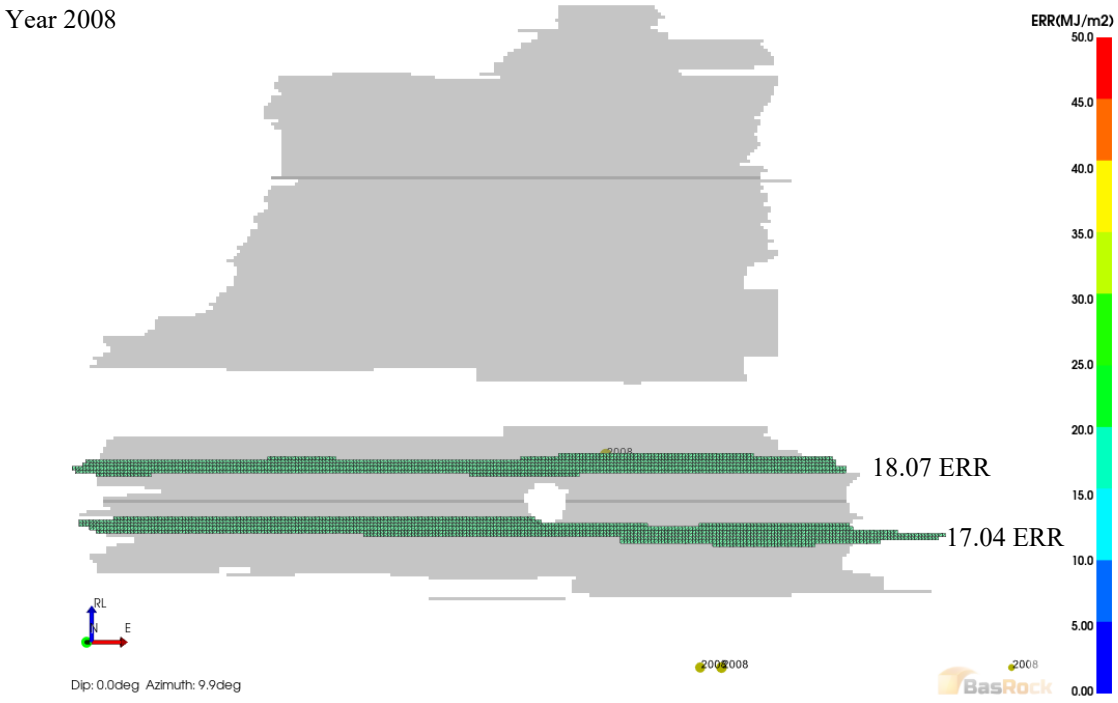


Figure 4.10: Average ERR per total annual extraction period in GH for 1997–2011

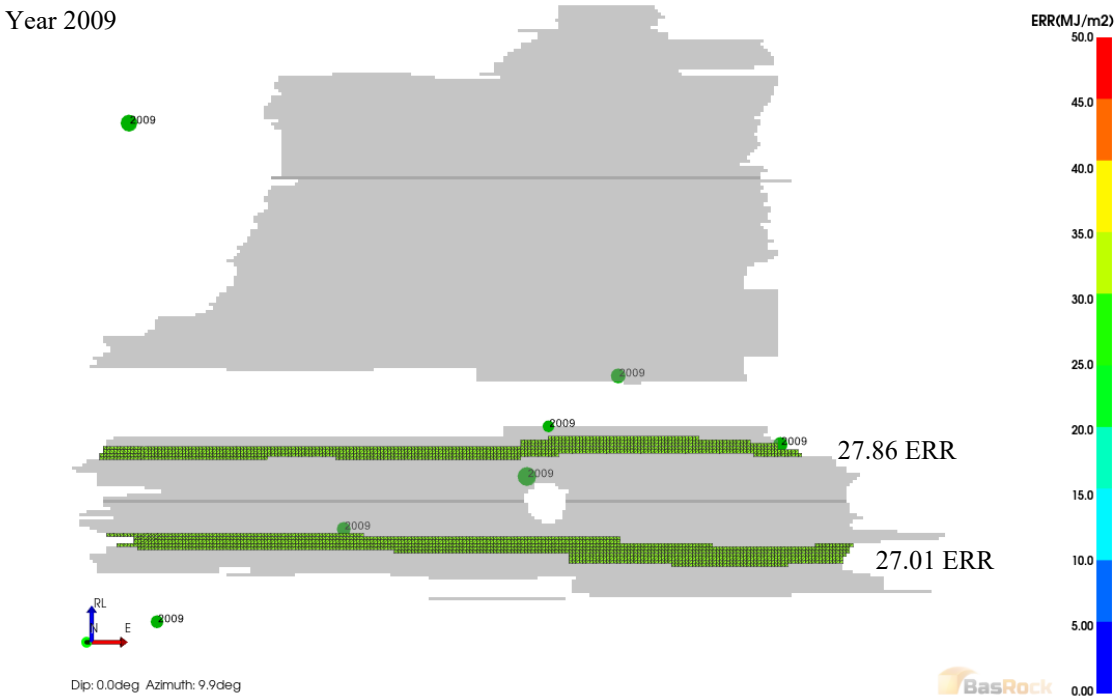


(a)

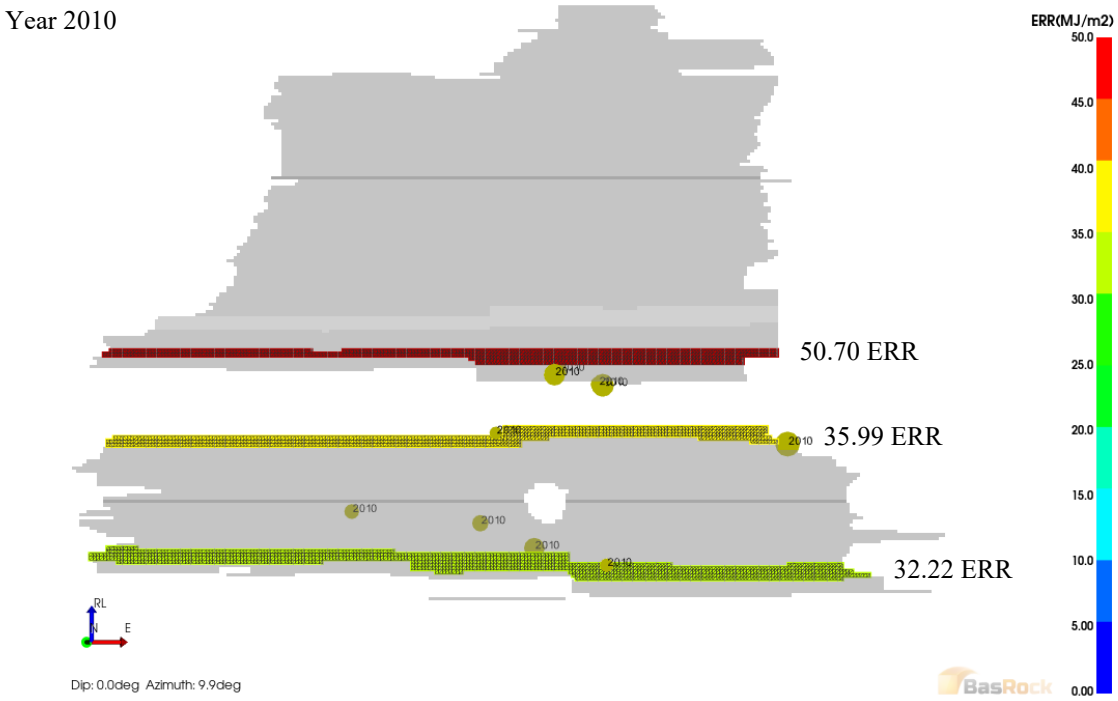


(b)

Figure 4.11: Average annual ERR per longwall in Gold Hunter (a–e) between 2007 and 2011

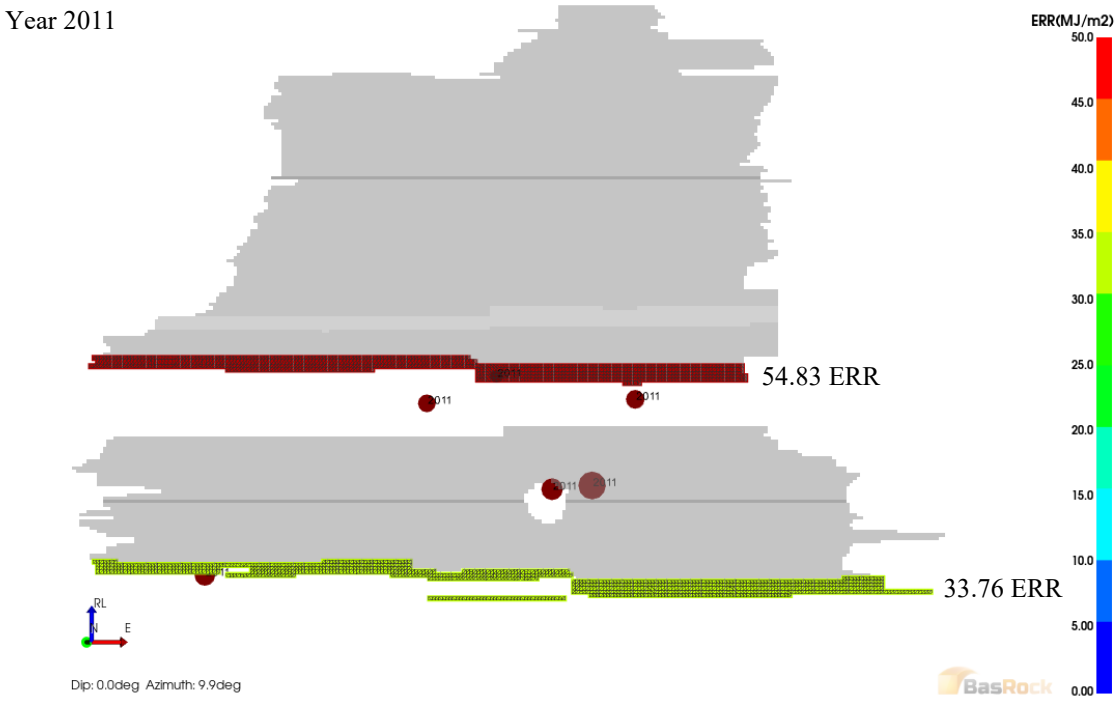


(c)



(d)

Figure 4.11: Average annual ERR per longwall in Gold Hunter (a–e) between 2007 and 2011 (cont'd)



(e)

Figure 4.11: Average annual ERR per longwall in Gold Hunter (a–e) between 2007 and 2011 (cont'd)

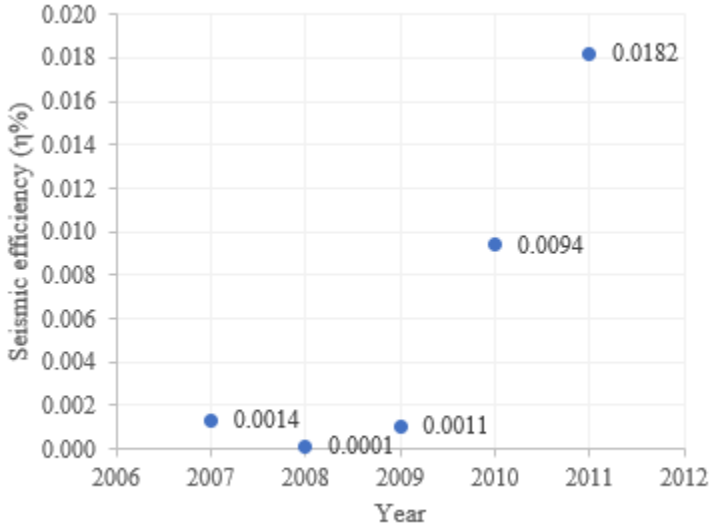


Figure 4.12: Average annual seismic efficiency (η%) computed in Gold Hunter, 1997–2011

4.2.3.2.2 Second mining period (2013–2016)

Mining restarted in the GH sector in 2013, continuing from the previously established geometry with a revised stoping strategy in the 30-Vein (e.g., stress shadowing the 5,700 Pillar from the 80 Vein), and with an updated state-of-the-art full-waveform digitizing system from ESG, significantly improving event source accuracy and precision. Calibration blasts verified the source location accuracy to within 12.2 m in the GH vicinity (ESG, 2016), which falls within the range of accuracy found within mines (Gibowicz & Kijko, 1994). Mining proceeded entirely underhand during that extraction period (*Figure 4.13*). The inset year-stamps indicate year-end geometries, while the arrows indicate mining directions. Large seismic events ($\geq +1$ M_w) recorded during mining were projected onto the longitudinal section. Several mine-scale events (13 events $> +2$ M_w) occurred in the 5,700 Pillar as 11S and 14S were mining toward the 5,900 panel. All mining activities in 14S and 11S were halted in (October) 2014 and in (December) 2015, respectively. Notable seismic events continued to release in the 5,700 Pillar as mining progressed at the bottom of 30-Vein in 12S, 15S and 16S.

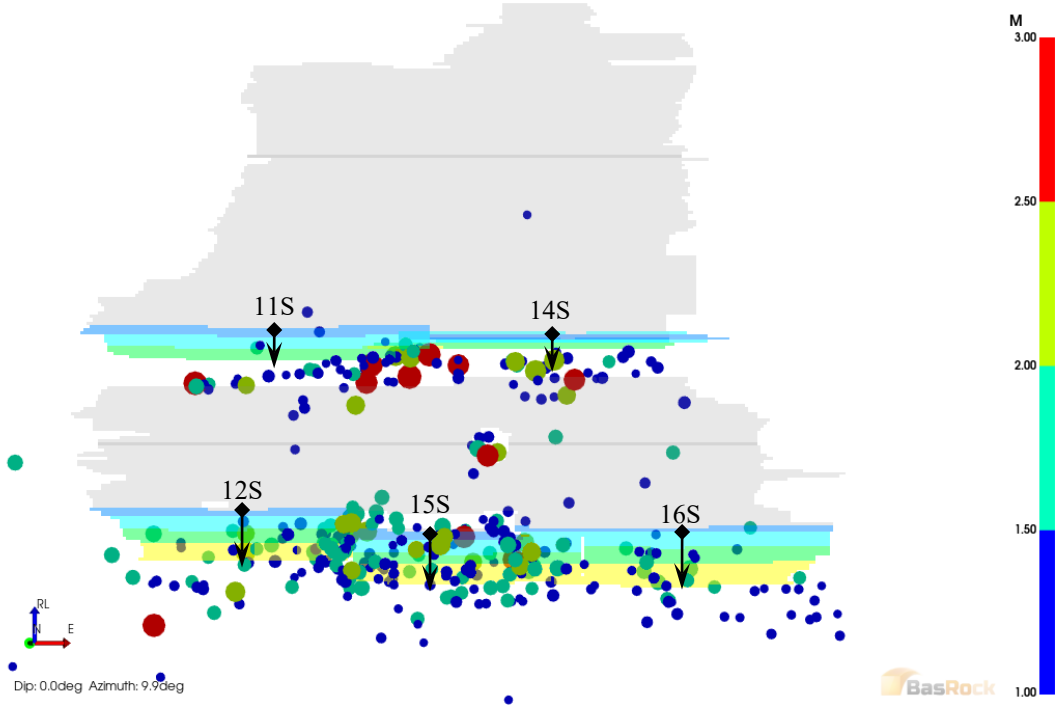
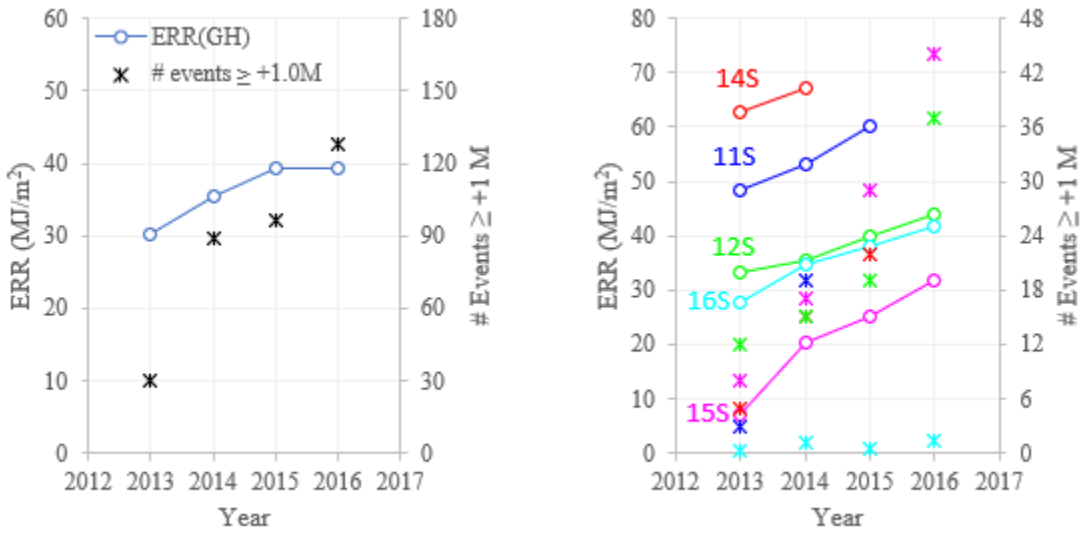


Figure 4.13: Annual extraction sequences with spatial relation to events $\geq +1$ M_w projected onto the 30-Vein, 2013–2016 (inset arrows indicate mining directions)

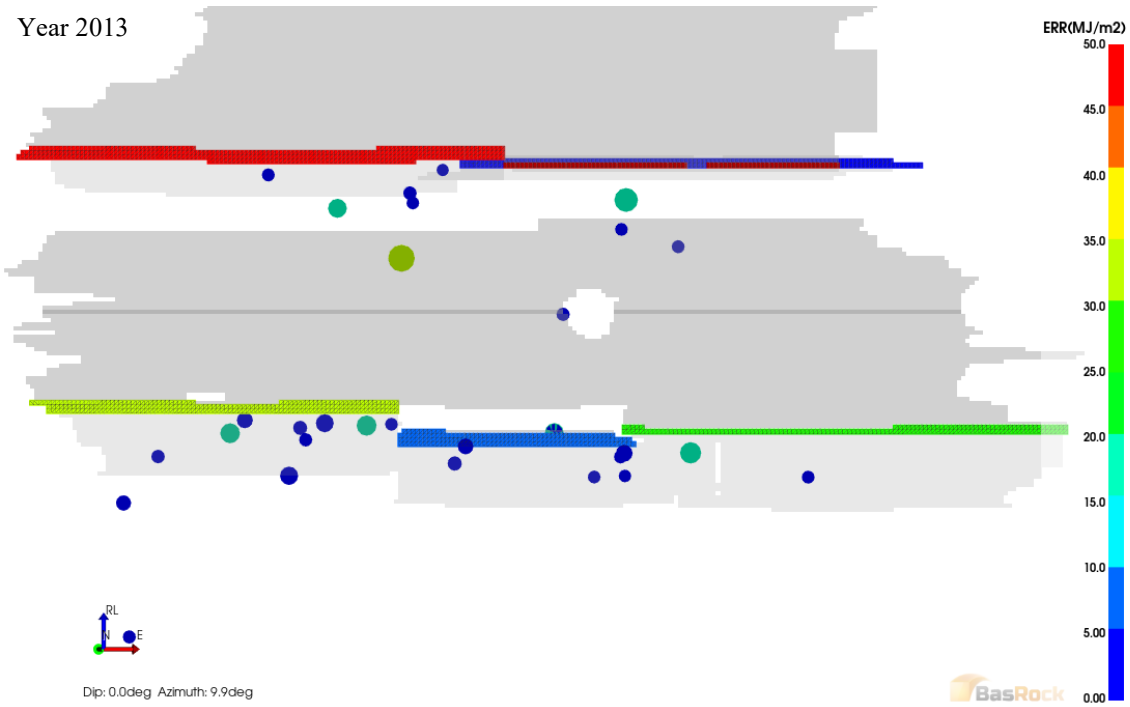
The average ERR per annual extraction was generated for the mining period, assuming total mine (GH) and per stope grouping schemes (*Figure 4.14*). The total mine assessment indicates that mining restarted on the 30-Vein at 30 ERR (releasing over 30 large events in the first year), caping at 39 ERR in 2015. Although mining stopped in proximity of the 5,700 Pillar, high ERR values carried over into 2016, releasing over 120 events >+1 M_w. The release of large events follows the increasing ERR trend for the period. The individual stope assessment reveals the variability of ERR across the 30-Vein. The volumetric seismic zoning filters were used for grouping large seismic event occurrences per stope. In general, 14 Stope presents the highest ERR output with 62.8–67.2, followed by 11 Stope, which output 48.3–60.2 ERR. The 15 Stope computed the smallest ERR values, ranging between 7.1 and 31.6. The lowest ERR value in 15S is most likely attributed to the reduction in simulated closure caused by the mining front's proximity to 15S Pillar. The 15 Stope ERR values saw the greatest increase as mining progressed away from the pillar. Overall, the large seismic events recorded in stope appear to increase with greater ERR outputs except for 16 Stope. The latter seems to be releasing seismicity under a steady-state regime (events are < +2 M_w).



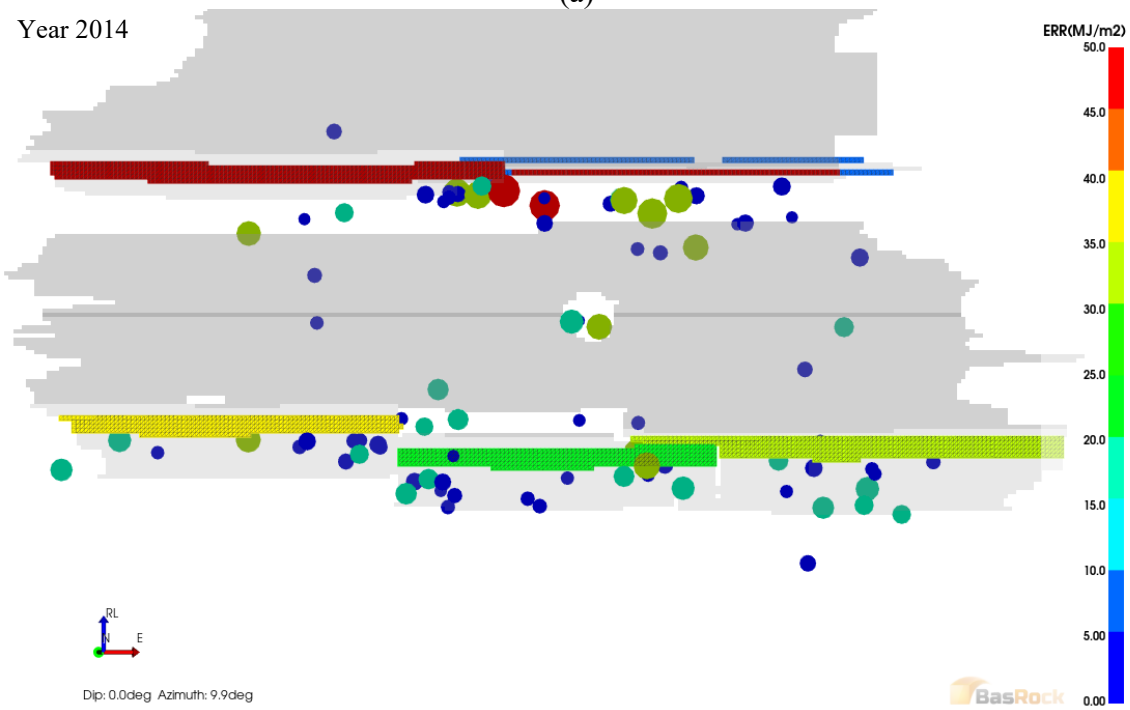
(a) (b)

Figure 4.14: Average ERR per annual production for (a) total mine, and (b) per stope

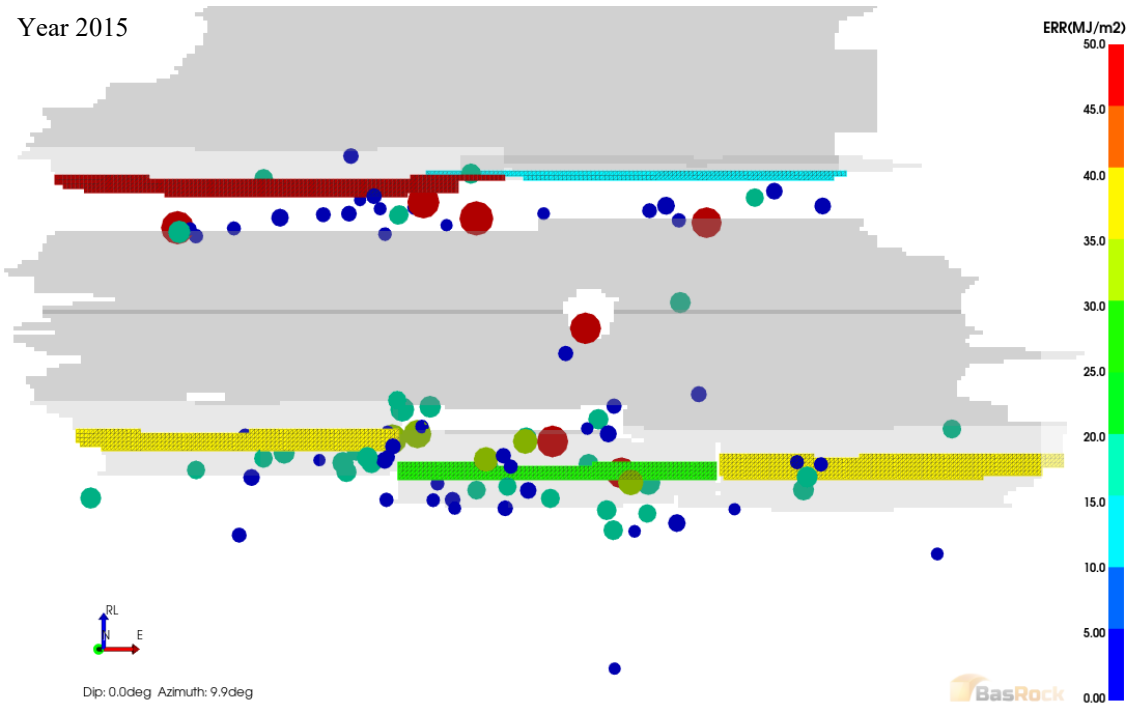
The annual average ERR per individual stope crudely matches the seismic response (*Figure 4.15*).


Year 2013
ERR(MJ/m2)
50.0
45.0
40.0
35.0
30.0
25.0
20.0
15.0
10.0
5.00
0.00
RL
N
E
Dip: 0.0deg Azimuth: 9.9deg
BasRock

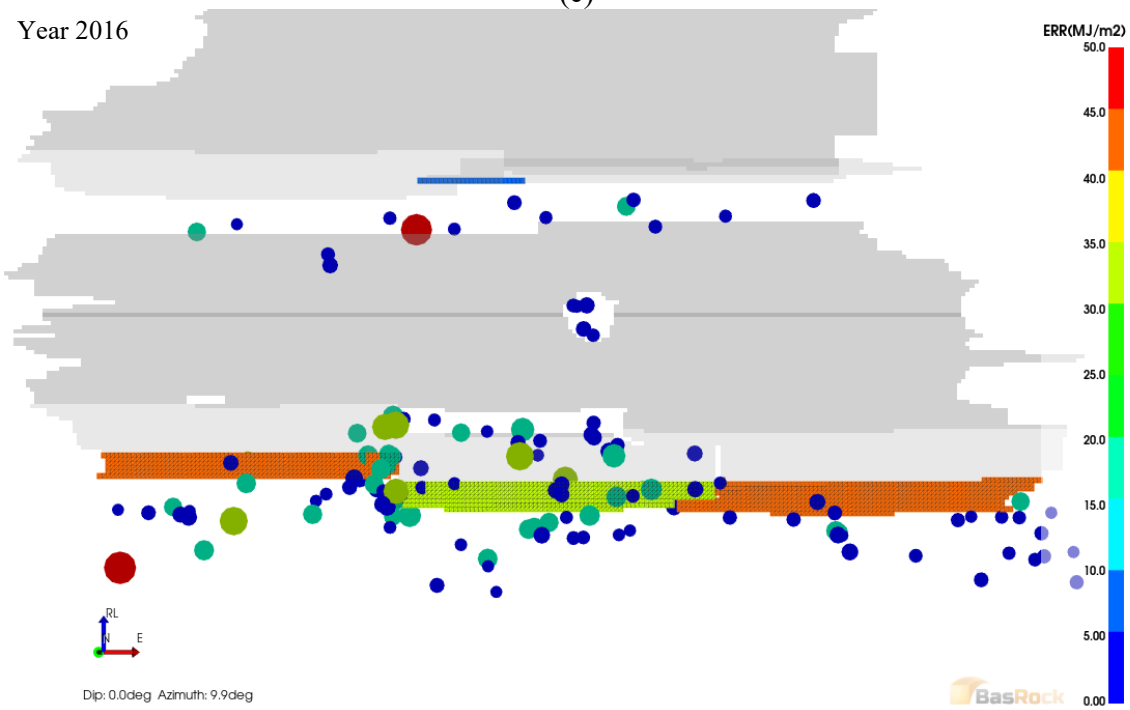
(a)


Year 2014
ERR(MJ/m2)
50.0
45.0
40.0
35.0
30.0
25.0
20.0
15.0
10.0
5.00
0.00
RL
N
E
Dip: 0.0deg Azimuth: 9.9deg
BasRock

(b)



(c)

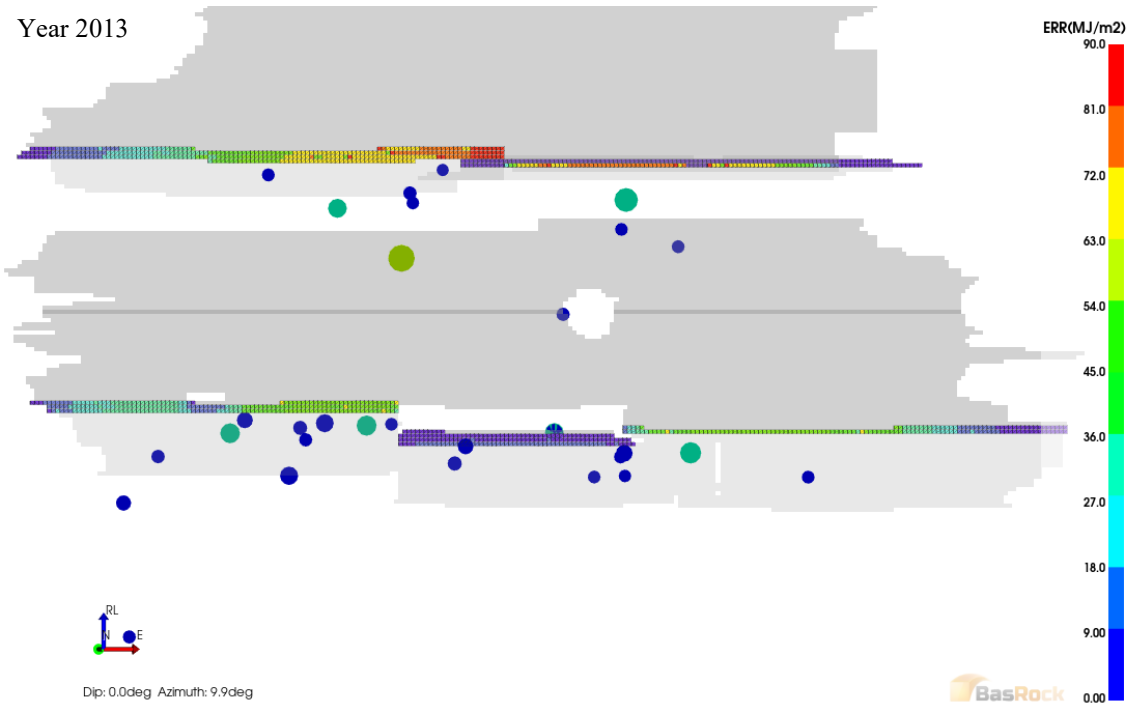


(d)

Figure 4.15: Average annual ERR per stope with associated events ≥ +1 M_w projected onto the 30-Vein for (a-d) 2013–2016, respectively

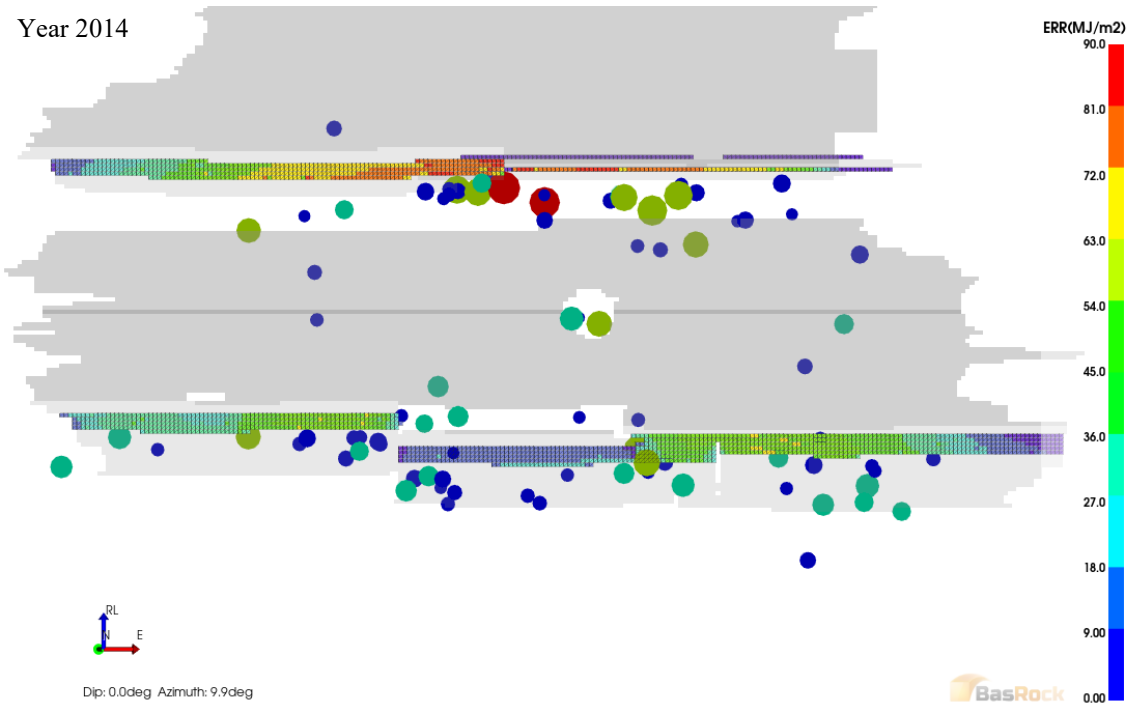
Further investigation into ERR per smaller mining step (monthly increments), reveals that each stope presents zones of varying ERR values (*Figure 4.16*). These plots were generated by

assuming a monthly increment resolution over the period. The ERR values computed on the individual DD-elements were grouped by stope and into yearly sets. Therefore, the annual stope set given by the higher step resolution averages to the stope's annual ERR average previously reported (within ~2% error). Over 48 mining-steps were generated for the period, conforming to mining survey reports. Large seismic events tend to group around higher in-stope ERR values. However, the stopes appear to have different induced seismicity thresholds. For example, seismicity groups around ERR > 60 in 11S, while 12S has a seismic onset at ERR > 35. The lowest ERR threshold is about 20 in 15S, inferring that this stope triggers seismicity at a lower ERR value. Finally, 16S shows little seismic response at 30+ ERR. This assessment remains qualitative but is further expanded upon.

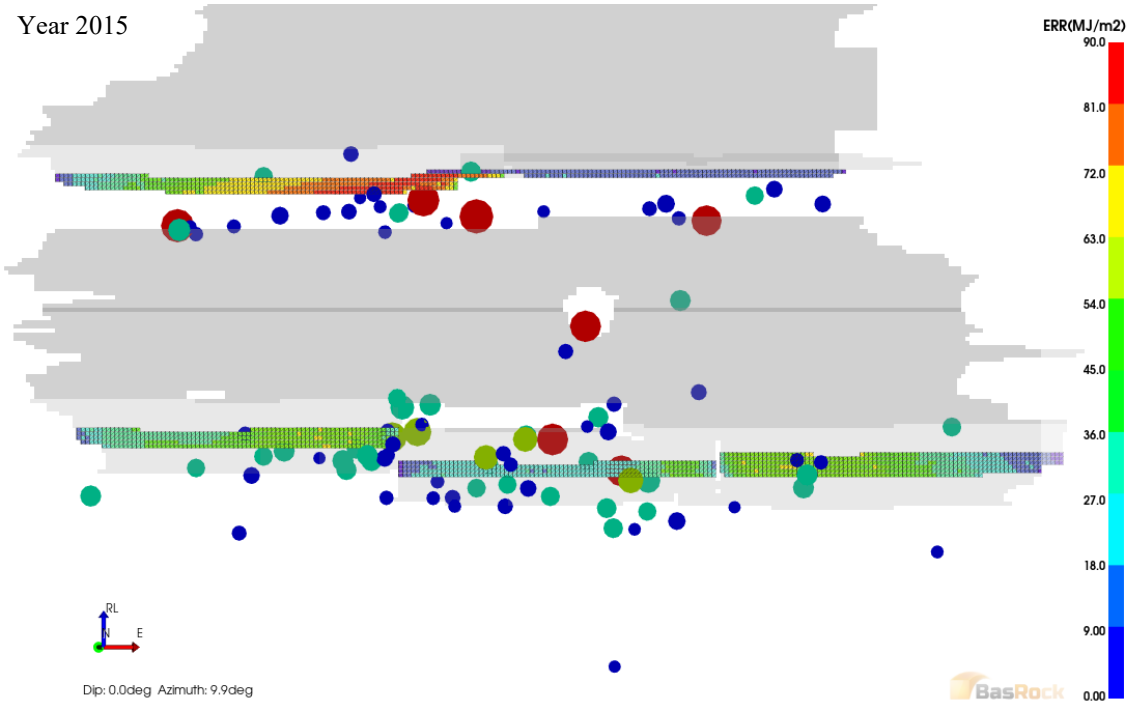


(a)

Figure 4.16: Computed ERR per DD-element from monthly increments grouped by annual production with associated events ≥ +1 M_w projected onto 30-Vein for (a-d) 2013–2016

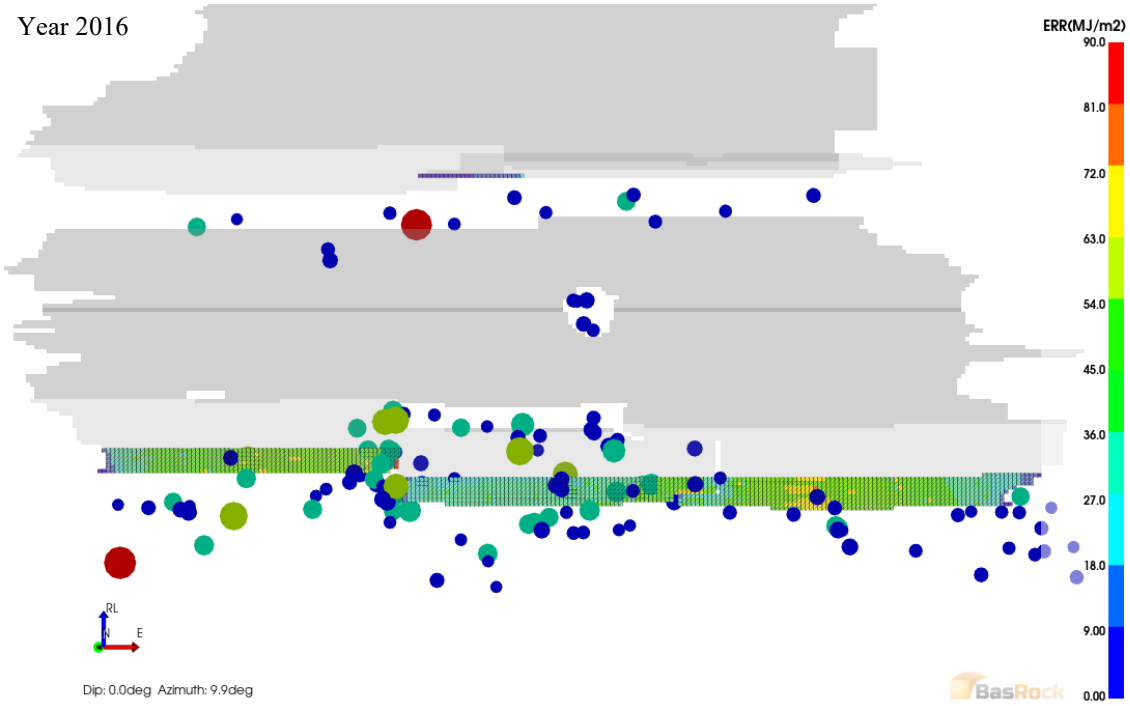


(b)



(c)

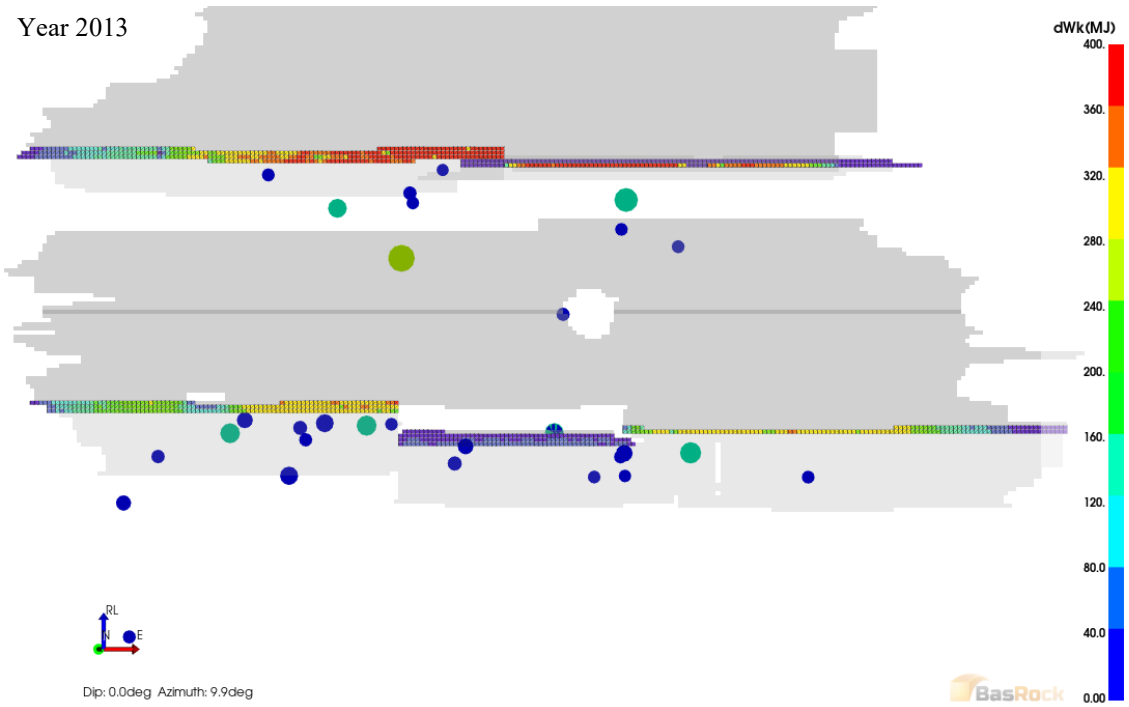
Figure 4.16: Computed ERR per DD-element from monthly increments grouped by annual production with associated events ≥ +1 Mw projected onto 30-Vein for (a-d) 2013–2016 (cont'd)



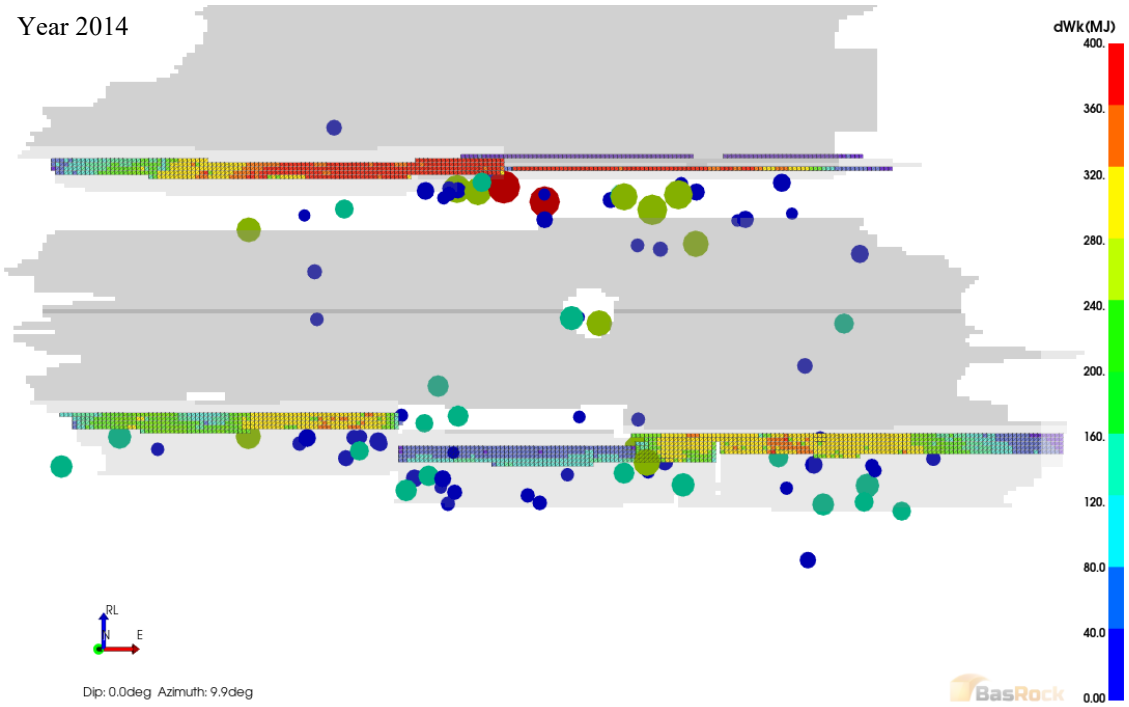
(d)

Figure 4.16: Computed ERR per DD-element from monthly increments grouped by annual production with associated events ≥ +1 Mw projected onto 30-Vein for (a-d) 2013–2016 (cont'd)

The modelled kinetic energy (W_k) has been computed on individual DD-elements for this study period, assuming monthly increments. Recall that W_k is calculated from the energy balance formulations stated previously (eq. 4.5–4.8). Stope thickness (Δw) was derived from infield surveys averaging at 3.65 m for the area. This parameter is used to calculate the strain energy component (U_m) of the mine block. Like the previous ERR plot, elevated kinetic energy occurrences crudely match on location to the seismic response per production year (*Figure 4.17*).

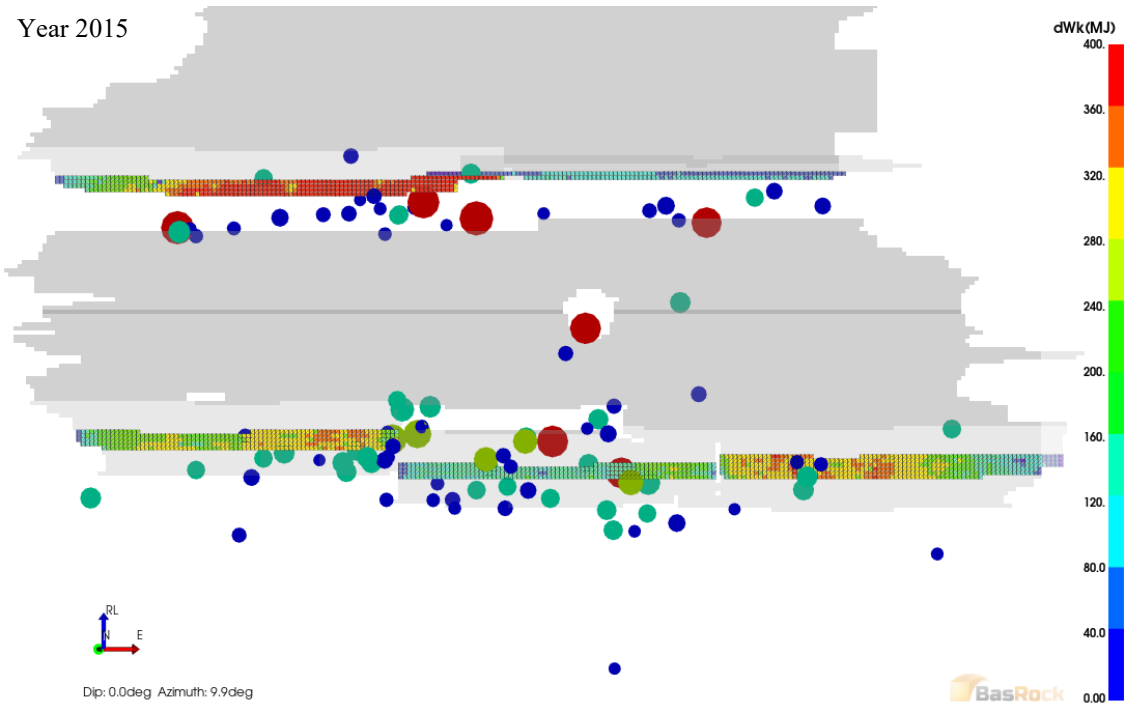


(a)

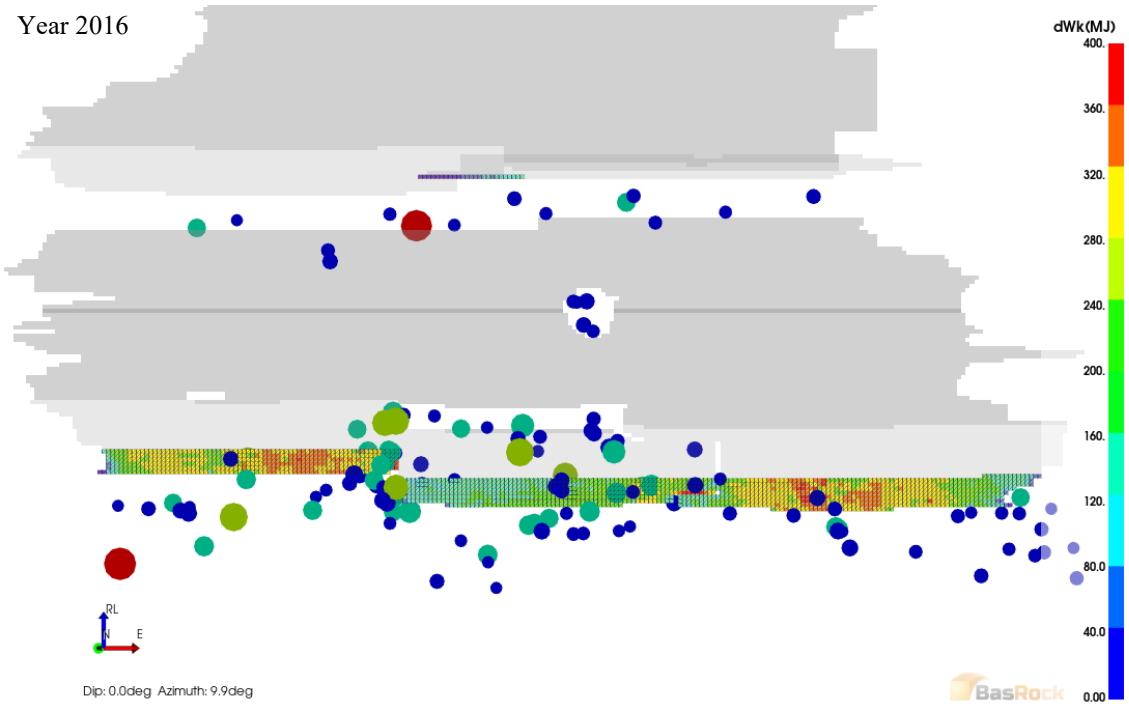


(b)

Figure 4.17: Computed Wk [MJ] per DD-element from monthly increments grouped per annual production with associated events ≥ +1 M_w projected onto 30-Vein for (a-d) 2013–2016



(c)



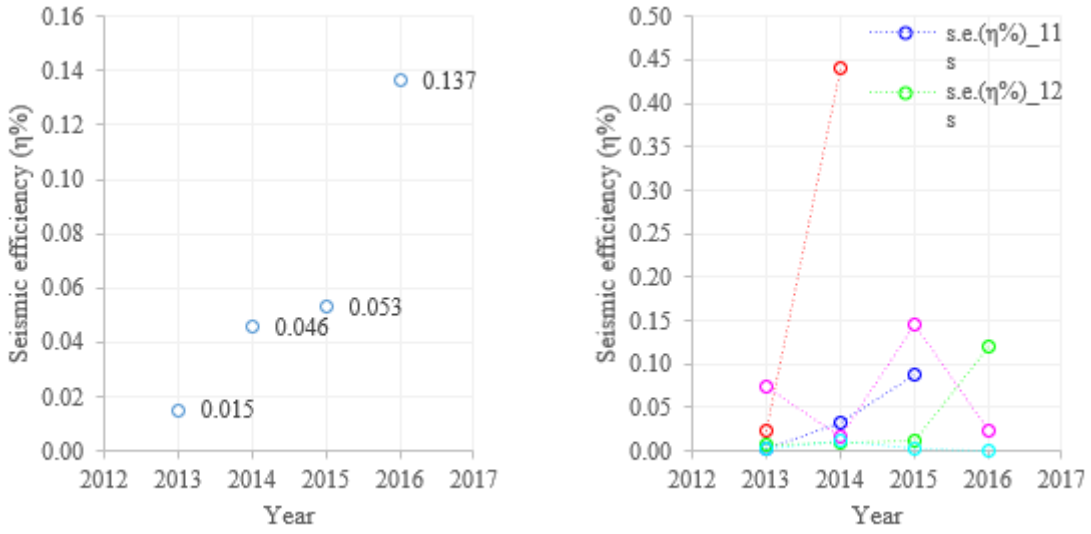
(d)

Figure 4.17: Computed Wk [MJ] per DD-element from monthly increments grouped per annual production with associated events ≥ +1 Mw projected onto 30-Vein for (a-d) 2013–2016 (cont'd)

The seismic efficiency (η%) has been computed for the Gold Hunter sector for yearly production increments set between 2013 and 2016 (*Figure 4.18*). The annual seismic efficiency varies from 0.015 to 0.137%, with an increasing trend that matches observations for the period (i.e., increased occurrence of large events). Upon closer investigation, it was observed that stopes generate different seismic efficiencies, which are most probably due to differences in mine configurations (12S lag pillar with 15S), pillar formations (11S, 14S & 15S), and possibly a lower density of faults crossing the stope (16S). The highest seismic efficiency has occurred in the 5,700 Pillar under 11S and 14S, which are no longer in production. Table 4.2 provides the annual seismic efficiency per stope for the period.

Table 4.2: Summary of seismic efficiency (η%) per stope for the entire period, 2013–2016

s.e.(η%) 11S	s.e.(η%) 12S	s.e.(η%) 14S	s.e.(η%) 15S	s.e.(η%) 16S
0.124%	0.048%	0.253%	0.052%	0.004%



(a) (b)

Figure 4.18: Average annual seismic efficiency (η%) computed for Gold Hunter, 2013–2016

4.2.3.2.3 Discussion & Comparison to South African Practice:

Seismic efficiency ratios (η%) measurements were gathered in SA mines at the CLR and the VCR by Spottiswoode *et al.* (2008), revealing that these efficiencies can be as low as 0.4% and 0.2%, respectively. Cook (1976) also found that several gold mines of the Witwatersrand System displayed a seismic radiation efficiency of ~0.1%. These values are an order of magnitude larger than those calculated for the GH in 2011 onwards, only better matching the last production year, which output η% of 0.137% in 2016. However, combining the two production periods of the GH shows a steadily increasing exponential growth for seismic efficiency (*Figure 4.19*). The growth can be attributed to two factors: increased precision of the recorded seismic energy and an increased occurrence of larger events as mining progressed deeper and formed remnant pillars.

The former (energy output), the radiated seismic energy release during the first period, needed to be estimated from the magnitude. This was achieved by utilizing the E_s-M_w scaling relationship produced by the GH during the second mining period. However, when assuming other E_s-M_L relationships, such as those derived from SA practice, there is a jump in seismic efficiency for that period. This is represented by the yellow markers in *Figure 4.19*, which assume Spottiswoode & McGarr's (1975) energy-magnitude[1] formulation. Abercrombie (1995) demonstrated that smaller earthquakes ($M_w < 2$) present a smaller E_s / M_w ratio when compared to larger ($M_w > +4$). The SA scaling relationship may account for several larger events (> +2 M_w), skewing the seismic energy upwards. Therefore, it is unclear what causes this discrepancy, but the GH scaling law seems to underestimate the seismic energy output computed from magnitude when compared to SA practice for the first period. The magnitude of an event at the GH is calculated from the output seismic moment (M_o), which matches published sets (Hanks & Kanamori, 1979), so the integrity of the magnitude scale remains.

For the second (increases in seismic efficiency), seismologists have associated higher seismic efficiencies for higher outputting magnitude events, computing up to 5% for large M_w events (McGarr, 1984). In addition, higher radiated energies have been observed in events with increased slip velocity due to higher driving stresses (Kanamori, 2001). It is likely that as mining continues to deepen (growing the mined-out area), seismic energy releases will continue to increase exponentially due to occurrence of higher magnitude events in abutments and remnant

[1] Es = 10^(1.5 ML - 1.2); in [MJ]

pillars. On the other hand, the kinetic energy response computed by the grid-based BEM will continue to increase linearly at a slower rate. Over time, the seismic efficiencies will most likely see an increase from current estimates in the GH.

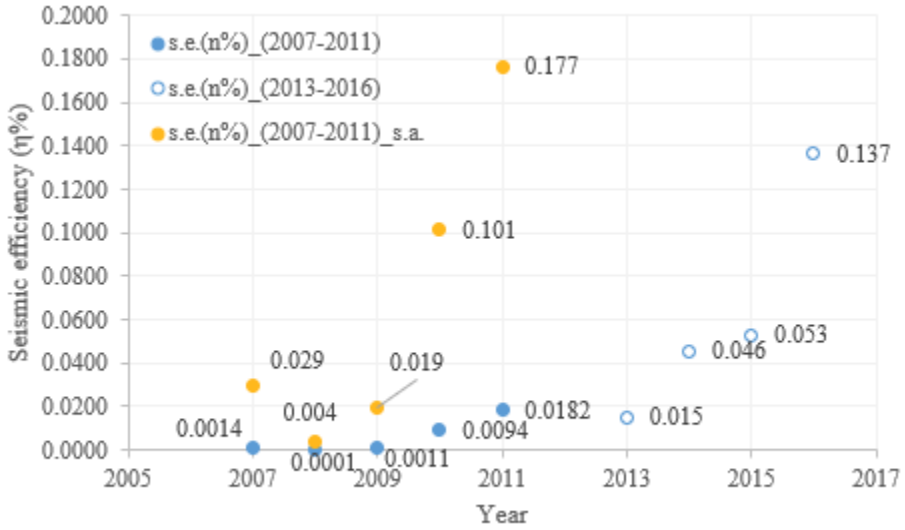
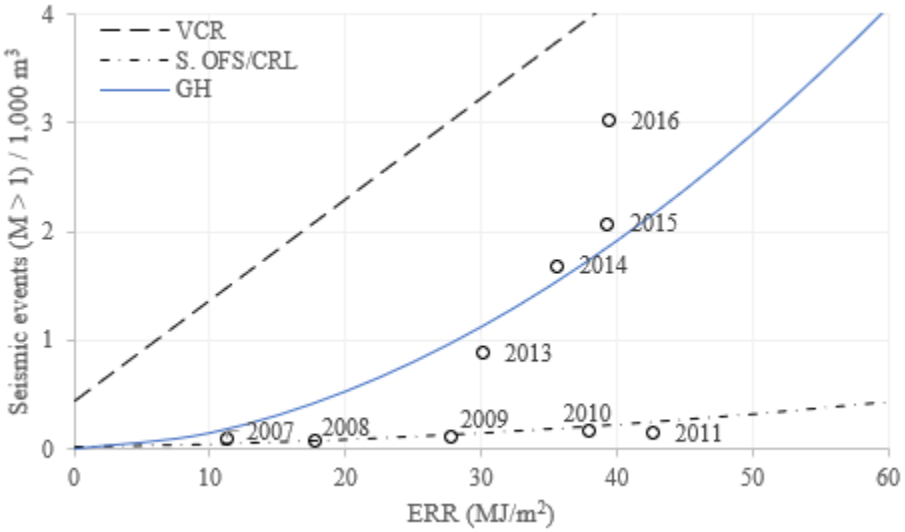


Figure 4.19: Seismic efficiency comparison between GH and SA energy-magnitude scaling relationship

The annual ERR computed from the grid-based analysis was plotted against the occurrence of seismic events (M > 1) normalized over 1,000 m^3 of extracted ore (*Figure 4.20*). This configuration represents the relation between the frequency of large events, local ground conditions, and energy release rate, often cited as the Seismic Hazard Potential chart (for rockbursting and seismic occurrences) developed by COMRO (1988) and seen in tabular hardrock mines handbooks like that of Jager & Ryder (1999). The designs related to the VCR and the Southern O.F.S. and Central Rand Mines were plotted in the figure. Note that the VCR plot was borrowed from the rockbursting relationship to energy release, as it is assumed that large events (M > +1) were needed to cause rockbursts to manifest. The GH's annual ERR markers (*Figure 4.20*a) are bound within the two SA design plots. In addition, the 30 ERR value indicates the onset of one (1) large event per 1,000 m^3 mined. This ERR threshold is often regarded in SA design for the onset of moderate to severe seismicity (Jager & Ryder, 1999). The GH Seismic Hazard Potential trend line was derived from the computed events, better agreeing with the second mining period. Overall, the GH trend presents an RMSE of +0.578 seismic events (M>1) / 1,000 m^3 for the 2007–2016 mining period.

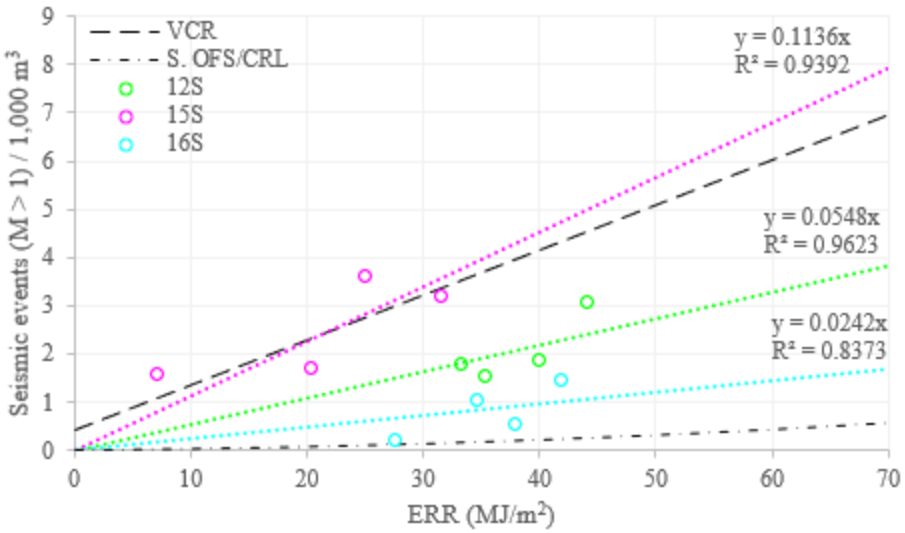
The ERR for individual stopes was also plotted on the design chart (*Figure 4.20*b-c). It can be readily seen that different stopes present different onsets for moderate seismicity. Based on these figures, 15S presents the highest seismic potential for ERR to incidence of seismic events for the bottom stopes, matching those extrapolated from the VCR. For the higher ERR outputting stopes, 14S represents the highest seismic risk. Therefore, these design charts are empirically derived from different mining layouts within the GH. Mines should perform their own assessment to validate the ERR threshold for evaluating mine layouts and mining sequences (Jager & Ryder, 1999). It is important to realize that strictly assessing the incidence of seismic events greater than +1 M_w might be misleading when compared to the seismic energy radiated by the events. For example, one (1) single +2 M_w event radiates 32 times more energy than the previous integer magnitude decreases. Therefore, thirty-two (32) +1 M_w events are needed to radiate an equivalent energy release to one (1) single +2 M_w event. Stopes with lower b-values are most affected as the requirement for triggering the next (more energetic) integer event necessitates fewer events. This is the case for 11S where its seismic hazard is low when compared to the other stopes; although the cumulative seismic release was higher.

Overall, the GH's seismic efficiency and the ERR analyses show similar trends as those captured in South African mines, demonstrating a strong relationship between seismic occurrence in narrow continuous tabular mines (Brummer, 1999).

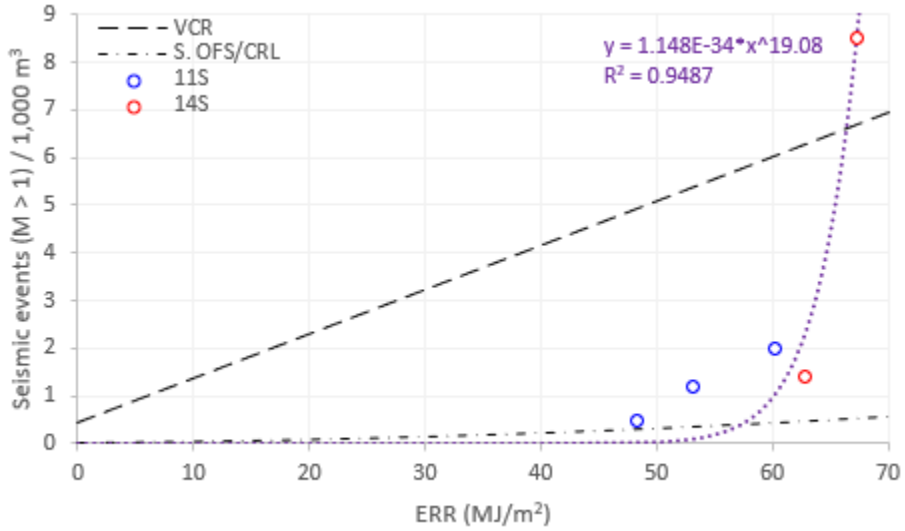


(a)

Figure 4.20: Seismic response in GH (a–c) compared to SA practice



(b)



(c)

Figure 4.20: Seismic response in GH (a–c) compared to SA practice (cont'd)

4.3 Block-Based Analysis (BEM-FF)

This section pushes Ryder's (1987) ESS formulation further by incorporating Salamon's (1993) methodology for identifying slip initiation. Salamon adjusted the original ESS analytical solution by comparing the active shear stress (τ_a), acting at the center of a circular fault surface, to the static shear stress (τ_s) resisting the slip onset (termed ESS_S — where the suffix refers to the static shear stress component used in the computation). A slip is presumed to initiate (at the centroid of

the discontinuity) when the active shear beats the static shear stress ($\tau_a \geq \tau_s$). When slip occurs, the slip point experiences a static stress drop ($\Delta\tau$) where the static shear strength drops to the residual slip strength, breaking all asperities along the fault. Therefore, the static stress drop is calculated from the difference between the static-dynamic slip envelopes (τ_s - τ_d) instead of being set to a specific value, as proposed in Ryder's original methodology. Cohesion can be integrated into the static friction strength. Importantly, Salamon's formulation assumes a fracture size dependency when estimating seismic source mechanisms (i.e., assumes complete slip upon rupture). Hence, initiated discontinuities slip to their maximum preset fracture length (2·Ls).

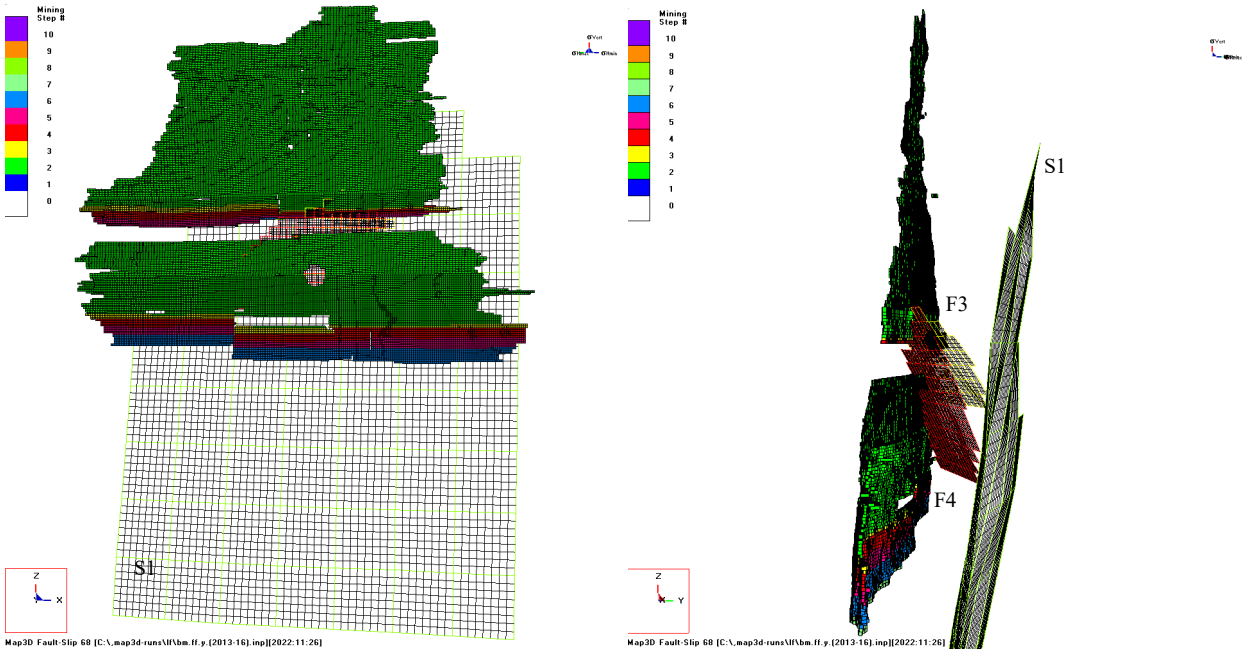
Applying the ESS_S analysis offers insight into fault slip potential, therefore, the seismic moment (M_o) and moment magnitude (M_w). Because of the higher geometrical precision with FF constructs, recorded seismic events in the GH were investigated for slip initiation. This also provides an opportunity to calibrate the static friction angle. In addition, a DFN generated from mapped joint sets enabled to validate the fault-slip potential further as well as the frictional properties defined by the Mohr-Coulomb slip criterion.

4.3.1 ESS Analysis (BEM-FF)

The block-based boundary element model serves as the basis to investigate the seismic records by the ESS_S analysis. The rockmass was set to the previously calibrated elastic properties (E = 29.4 Gpa, G = 12.4 GPa & υ = 0.2). The FF-element construct of the 30-Vein has been previously presented (previous *Figure 4.2*). Additional fault constructs, the S1 and the two F-series faults (F3 & F4) have been digitized into the FF-BEM (*Figure 4.21*).

The following section covers the numerical procedure for assessing the ESS_S slip onset in the GH sector through the block-based model. The objective was to test the fault slip potential and to derive reasonable frictional properties by evaluating the seismic records and structures in the rockmass:

1. Assess the slip initiation of recorded notable events (> +0.5 M_w) with respect to the mine geometry and digitized faults.
2. Compare the simulated seismic outcome for fault-slip generated from a Discrete Fracture Network (Itasca, 2023) with seismic records.



(a) (b)

Figure 4.21: The block-based (FF-element) geometries with the S1, F3, and F4 faults

4.3.1.1 Procedure For Modelling ESSs

The modelling procedure for testing ESSs (slip initiation) requires the active shear stress to be compared with the static shear stress acting at a point in space around the mining vicinity. To meet this requirement, the stress tensor at any point in space inside the grid-based model must be extractable. Therefore, calculation nodes with know x-y-z coordinates have been placed in the model to track numerous stress tensors as mining progresses. Notable events (which hold a hypocenter coordinate) and planar discs (which are characterized by a centroid coordinate) can be approximated as calculation nodes inside the model. Each computation point is tested for slip initiation at a specific mining step, reflecting the mining state.

Each grid node provides the principal stress vectors allowing to determine, through stress transformation processes (Timoshenko & Goodier, 1970), the normal and shear stress of an oriented discontinuity plane. The stress transformation formulations are as follows in the principal plane:

$$\tau_a = (\sigma_1 - \sigma_3) \cdot sin\theta \cdot cos\theta \qquad 4.10$$

$$\sigma_n = \sigma_1 \cdot sin^2\,\theta + \sigma_3 \cdot cos^2\,\theta \qquad 4.11$$

where: τ_a = active shear stress [MPa]

σ_n = normal shear stress [MPa]

θ = angle between the fault plane and σ_1 [°]

σ_1, σ_3 = major and minor principal stresses [MPa]

If the orientation of the failure plane is unspecified, the critical plane orientation is assumed and defined by:

$$\theta_S = 45° - \frac{\varphi_s}{2} \tag{4.12}$$

To evaluate the slip initiation of recorded seismic events, each computational node was tested for the following condition (Ryder, 1988):

$$CEV_S = \frac{(\sigma_1 - \sigma_3) \cdot \sec(\varphi_s)}{2} - \frac{(\sigma_1 + \sigma_3) \cdot \tan(\varphi_s)}{2} \tag{4.13}$$

where: CEV_S = coulomb ESS vector computed from static friction angle (Ryder, 1988)

The CEVs suffix refers to the static friction angle component used the computation of the term.

The node initiates slip when the following condition is met:

$$CEV_S \geq 0.0\ MPa \tag{4.14}$$

In this case, the normal and shear stresses are computed for the critical joint orientation providing slip. However, the true fault orientation remains unknown at that location. This analysis only confirms the existence of a favourable orientation causing the maximum probable slip.

To evaluate slip initiation of the centroids within the DFN, each computational node was tested for the following condition:

$$ESS_S = \tau_a - \tau_s \tag{4.15}$$

$$ESS_S \geq 0.0\ MPa \tag{4.16}$$

Therefore, slip initiates at a computational point when the active shear stress beats the static frictional strength.

Since the disc centroid references a discrete structure orientation, the principal stresses are transformed to reflect those orientations, calculating the active shear, the normal, the static shear and the dynamic shear stresses. Recall that the static strength of the fault surfaces is given by:

$$\tau_s = C + \sigma_n \cdot tan(\varphi_s) \quad 4.17$$

where: τ_s = static shear stress [MPa]
C = cohesion [MPa]

While the dynamic strength of the surface is given by:

$$\tau_d = \sigma_n \cdot tan(\varphi_d) \quad 4.18$$

where: τ_d = dynamic shear stress [MPa]
φ_d = dynamic friction angle [°]

The static stress drop ($\Delta\tau$) is defined as the difference in the static and dynamic strength at the onset point:

$$\Delta\tau = \tau_s - \tau_d \quad 4.19$$

When simulating planar fractures, Salamon's (1993) formulation assumes complete slip, along the whole fracture size ($2 \cdot L_s$) immediately after slip has been initiated. This assumption is conserved throughout the subsequent section.

Assuming the circular slip model (Brune, 1970), the seismic source parameters were derived from the following formulation (Salamon, 1993):

$$M_o = \frac{8(1-v)}{3\left(1-{}^{v}/_{2}\right)} \cdot \Delta\tau \cdot {L_s}^3 \quad 4.20$$

where: Mo = seismic Moment [N·m]
$\Delta\tau$ = static stress drop at slip onset [Pa]
L_s = slip radius [m]
G = shear modulus assumed [Pa]
υ = Poison ration assumed [1].

The M_o relationship to the moment magnitude (M_w) is calculated by the following formulation (Hank and Kanamori, 1979):

$$M_w = \frac{2}{3} \cdot \log(M_o) - 6.01 \quad 4.21$$

where: M_w = moment magnitude [1]

M_o = seismic moment [N·m]

The seismic energy (E_s), if needed, is computed directly from the E_s-M_w scaling relationship established from the GH (eq. 4.9).

4.3.2 ESS_S Analysis of Recorded Seismic Events (2013–2016)

The seismic catalog provides the location coordinates of notable events ($\geq +0.5$ M_w) in the GH. The source locations of these events were integrated into the block-based model as computational nodes (x,y,z coordinates). The block-based model was run with annual production steps, reflecting the annual stress change induced by the extraction sequence. At the end of each mining step, the stress tensor of the corresponding seismic events having occurred during that period was extracted. The computational nodes were then tested for the CEV_S. The static friction angle was reduced by iteration from an upper bound value (i.e., 90°) until the slip condition was satisfied (i.e., $CEV_S \geq 0.0$ MPa), tagging the angle which met the minimum slip requirement. The following flow chart summarizes this process (*Figure 4.22*).

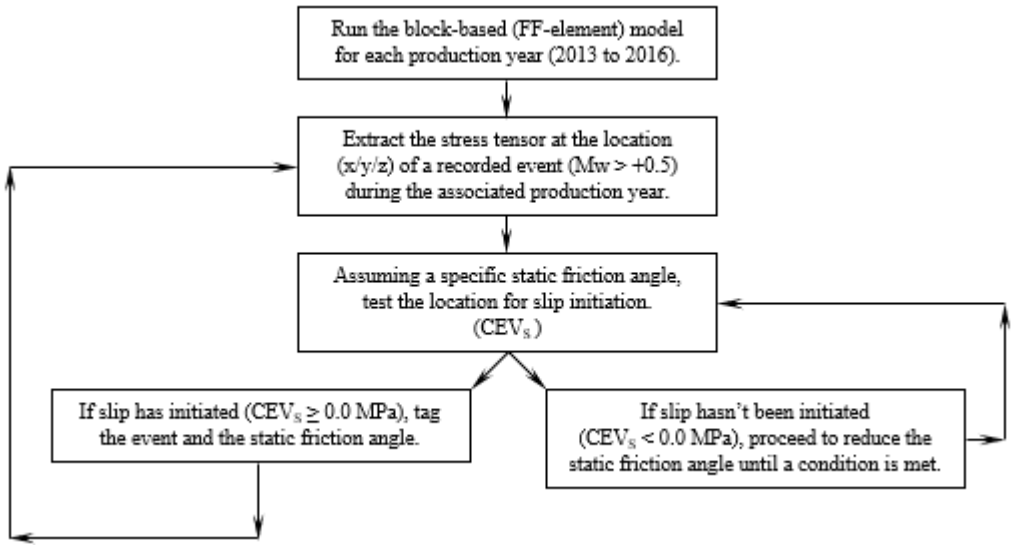
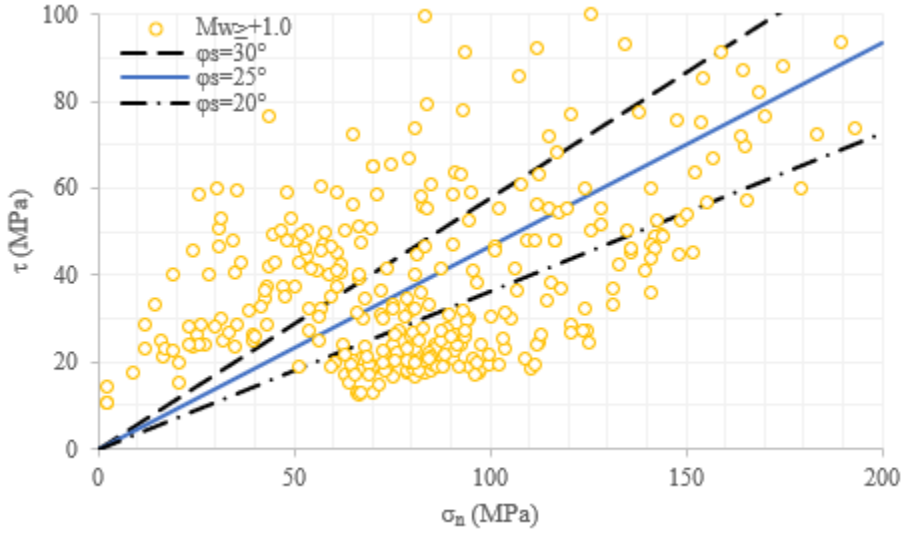


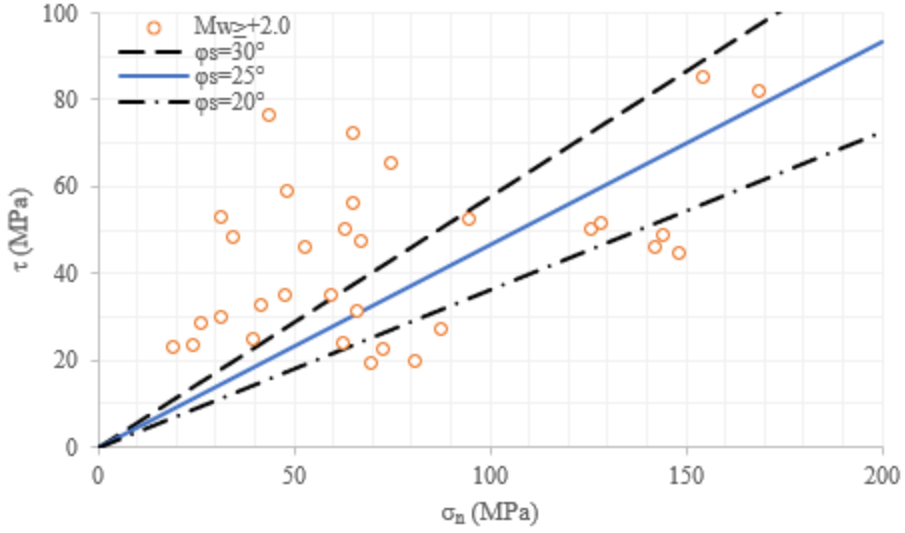
Figure 4.22: Block-based model flow chart for investigating CEV_S

The results of the analysis are plotted in the Mohr-Coulomb space for events greater than +1 M_w and +2 M_w (*Figure 4.23*). The seismic events (yellow markers) represent the minimum normal and shear stress requirement to initiate slip at that location. A series of static strength envelopes, assuming 20–30° static friction, were integrated into the plot. The seismic events which fail to meet the slip condition are represented by the markers locating below the strength envelope.

Inversely, the events which initiate slip are represented by markers locating above a set strength envelope. For events ≥ +1 Mw (n = 322), 66%, 54%, and 43% have initiated slip for a static friction angle of 20°, 25°,and 30°, respectively. For events greater than +2 Mw (n = 34), over 79%, 71%, and 56% have initiated slip for a static friction angle of 20°, 25°, and 30°, respectively. Overall, 50% of the notable seismic events (n = 734) recorded between 2013–2016 have computed favourable slip initiation for a static friction angle set to 25°, releasing > 64% of seismic energy.



(a)



(b)

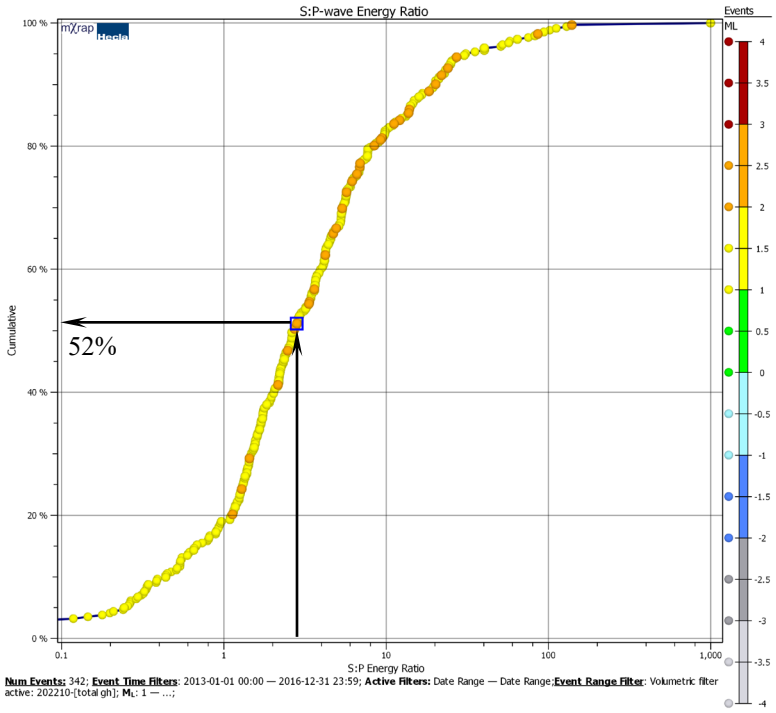
Figure 4.23: Mohr-Coulomb slip strength criterion sensitivity analysis (a-b)

To establish confidence in the static friction angle estimate, the E_s / E_p ratio as well as the spatial occurrence of events with relation to faults were further examined.

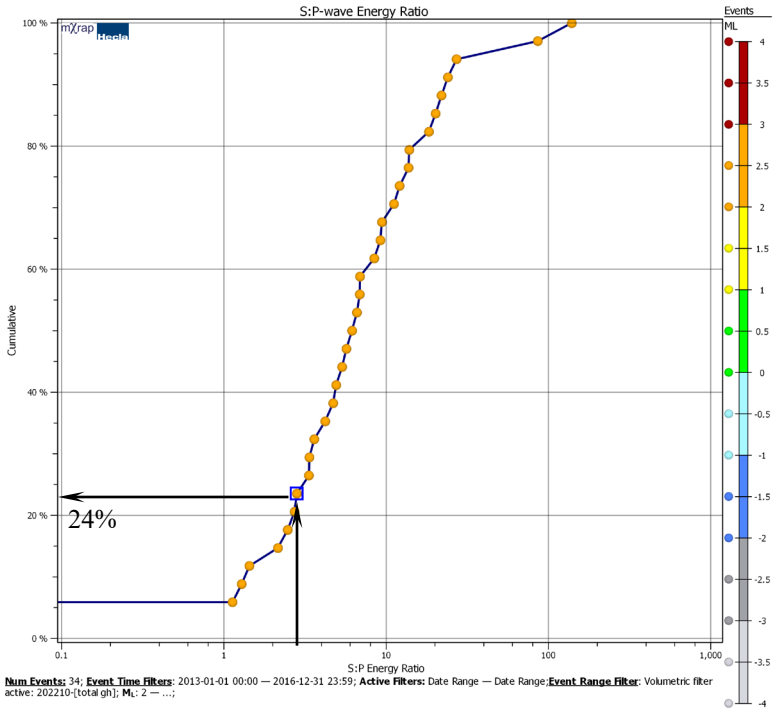
The energy ratio infers the focal mechanism, helping engineers attribute a seismic source mechanism to an event based on source parameters (Mendecki, 2013). Fault-slip (pure shear) mechanisms show the highest S-wave (E_s) to P-wave (E_p) ratio of energy. On the other hand, a lower E_s / E_p ratio of energy indicates non-shear mechanisms. Literature often attributes **non-shear** events to E_s / E_p < 3 (Hudyma & Potvin, 2010), with **pure-shear** events falling on the higher end of the spectrum at E_s / E_p > 10 (Boatwright & Fletcher, 1984). A mixed failure mode populates the interstice between these boundaries. Morkel *et al.* (2019) cautions that event processing techniques within the mining industry affect the confidence of resulting E_s / E_p inferences. Since mines rely on different seismic suppliers, data processing software and have variable arrays; this may explain the discrepancy in the literature for setting definitive E_s / E_p diagnostics for focal mechanisms.

At the GH, a damaging fault slip event has been recorded with an E_s / E_p ratio as low as 1.5. Damage consisted of large rocks having heaved the floor into the stope cut. The source mechanism was attributed to be fault-slip due to the large particle distribution of heaved (damaged) blocks. Fault slip was subsequently confirmed based on the size of the released magnitude (> +2 M_w) and the presence of in-stope structures successfully linked with its hypocenter (Hecla, 2017). It was concluded that the structure slipped after the cut was widened. Based on this assessment, a reasonable classification of fault slip events in the GH is at an E_s / E_p greater than 3.

Investigating the recorded shear-to-compression ratio response of large events provides the following plots (*Figure 4.24*). Setting the E_s / E_p to 3 classifies 48% and 76% of events larger than +1 M_w and +2 M_w, respectively, into the site-derived fault slip category. This outlook further confirms the determined static friction angle of 25°.



(a)



(b)

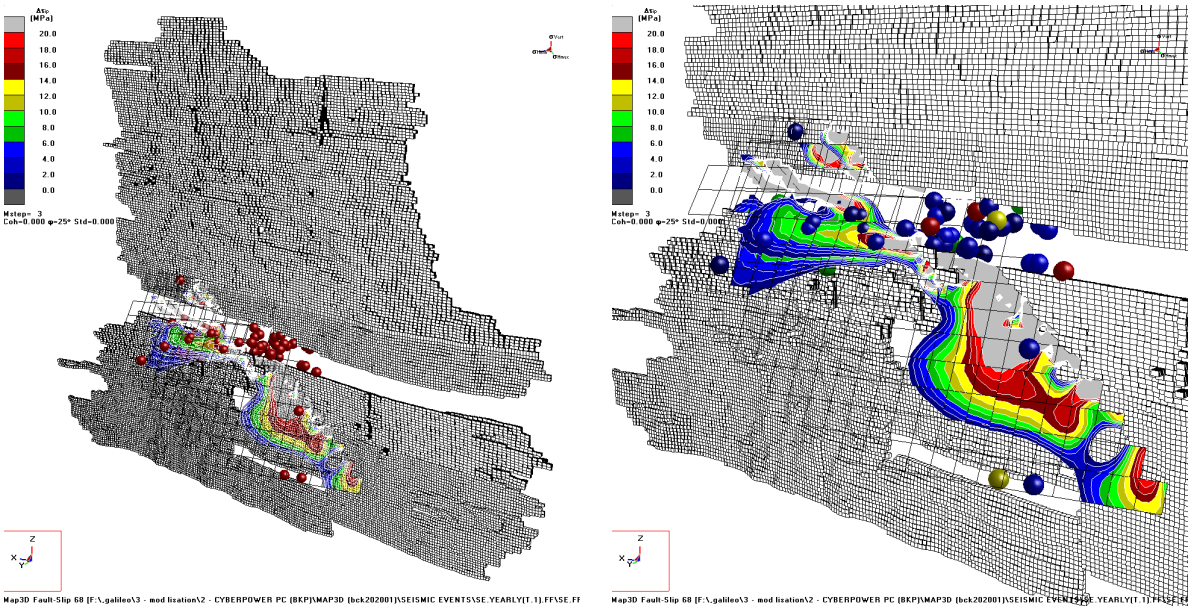
Figure 4.24: The Es/Ep in GH for events (a) ≥ +1 M_w & (b) ≥ +2 M_w, 2013–2016

The relationship of events in proximity to known fault structures was assessed (*Figure 4.25* & *Figure 4.26*). For the discrete F-series faults (F3 & F4), the modeled slip potential, identified as

positive CEV_S lobes in the lower figures for $\phi_s = 25°$, fits reasonably well with the occurrence of notable events. These specific faults have slipped in the past (Hecla, 2013) and continue to record movement. In total, 29 events ($M_w > +1$) have occurred within 12 m of these structures, releasing ~434 MJ and accounts for ~50% of the total energy recorded between 2013–2016.

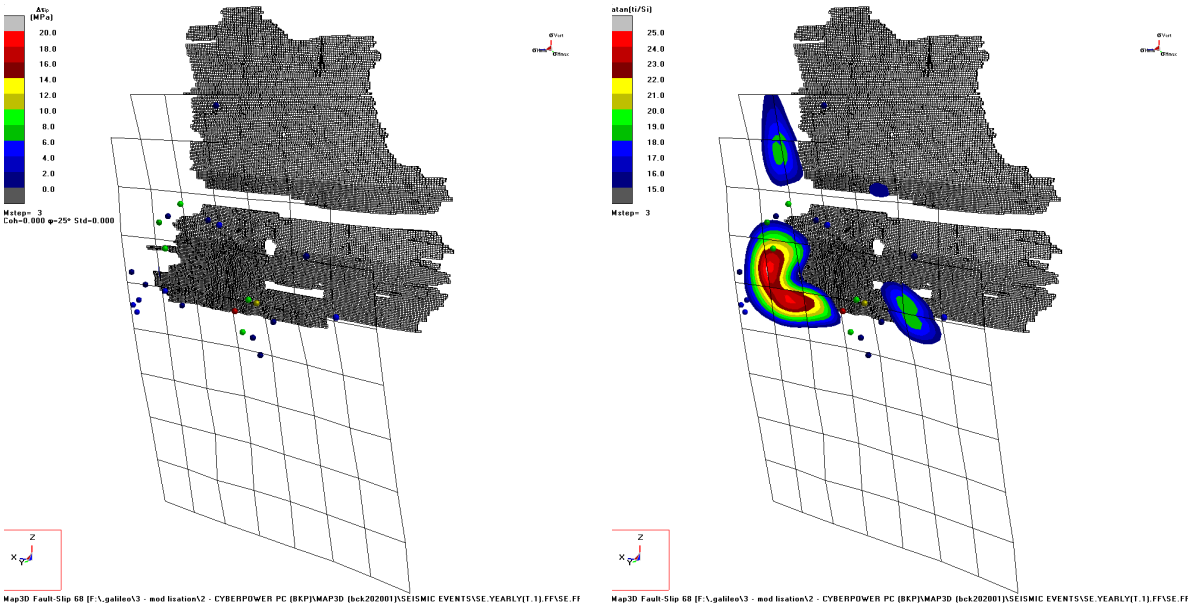
For the S1 fault (*Figure 4.26*), the modeled slip potential had to be significantly reduced (down to 15°) to match event occurrences. However, the S1 experienced only 23 events greater than +0.5 M_w recorded within 12 m of the structure, with only 12 events greater than +1 M_w, for the study period. The energy release near S1 is negligible when compared to the total energy released at the mine. Therefore, the seismic potential of the S1 appears negligible for that period, matching the modelling effort.

Based on these two surveys (the E_s / E_p ratio and the slip potential relationship with seismic occurrences on faults), the most probable static friction angle to be applied in the GH for numerical simulation was selected to be 25°.



(a) (b)

Figure 4.25: Slip potential on F3 and F4 with recorded notable events within 12 m from the structures, 2013–2016



(a) (b)

Figure 4.26: Slip potential on S1 with recorded notable events within 12 m from the structure where (a) shows no slip at φ_s = 25°, and (b) slip initiation regions for φ_s reduced from 15–25°

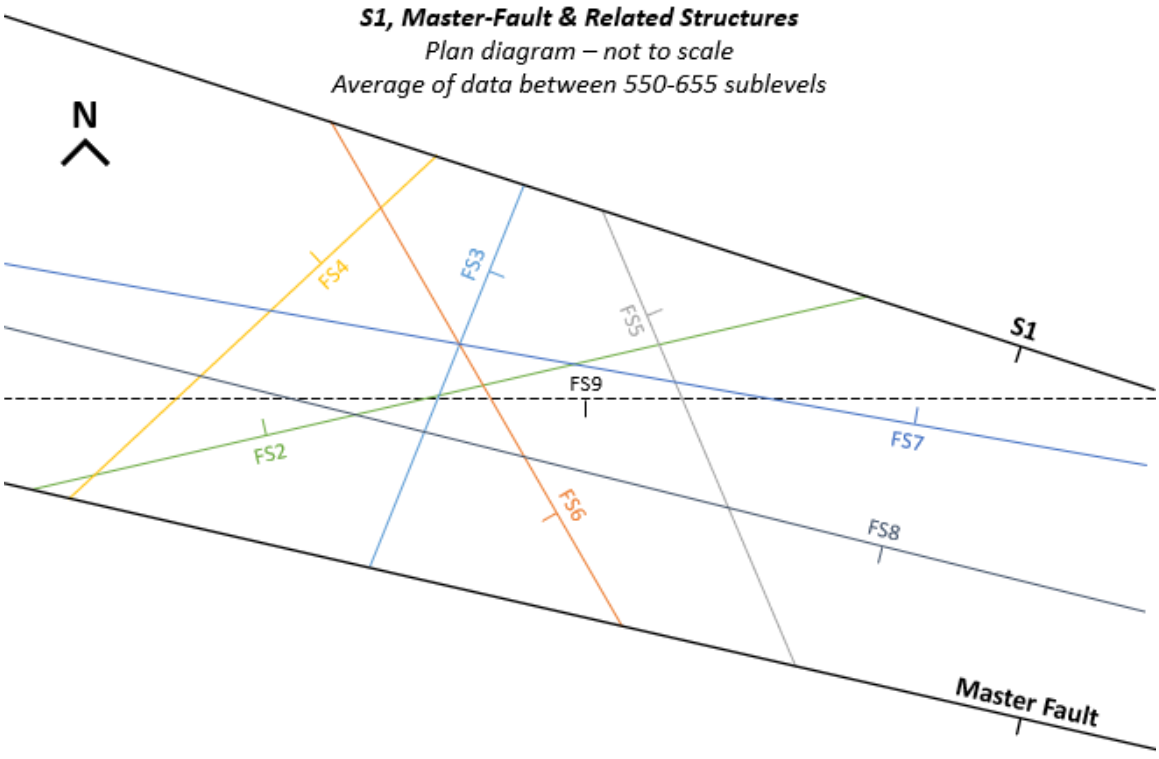
4.3.3 ESS Analysis of DFN

4.3.3.1 DFN Generation (for Density, Position & Size)

Several conjugated faults and related structures exist within the bounding fault system and have been linked with seismic activities at the mine (i.e., FS-2). Past studies done on the LF deposit have identified bedding planes to contribute significantly to seismicity (Board, 1994). Recognizing this association, an extensive mapping campaign was undertaken in the ramps (DeVoe & Meyers, 2017) and in the stopes (Smith, 2021) of the GH to digitize secondary joint sets. All captured structures persist through the exposed drift surfaces (*Figure 4.27*). Over 2,400+ structures have been mapped and digitized for location, dip-direction and dip (*Figure 3.7*). These fracture sets (FS) have been grouped into families, generating eight distinct groups that include the bedding (*Figure 4.28*).



Figure 4.27: Persistent in-stope fracture set visible on the South rib in 15 Stope (JRC ~2)



fracture set:	fs-2	fs-3	fs-4	fs-5	fs-6	fs-7	fs-8	fs-9
trend/plunge:	ne/n	ne/s	ne/n	nw/n	nw/s	we/n	we/s	bedding
dip.dir./dip:	347/58	112/55	317/59	067/67	240/71	010/65	194/75	180/60

Figure 4.28: Typical structural layout in the GH vicinity (DeVoe & Meyers, 2017)

Based on field data, a Discrete Fracture Network (DFN) was constructed by Itasca (2020), assuming an average fracture density of ~0.07 discontinuities per unit length (P10), equivalent to an average spacing of 14 m. The centerline of the ramp infrastructure (5500–6550L) served as the scanline for DFN generation. The position of each discontinuity follows a uniform distribution in space through the homogeneous Poisson point process (Bæcher et al., 1977).

The fracture size limit was set between 10 and 300 m. The lower bound limit was set to the length of the smallest mapped fracture. Since all mapped discontinuity traces remained concealed to the drift height of 5 m, the exposures were assumed to be semi-trace lengths (Priest & Hudson, 1981). The upper bound was derived by linking related fracture sets across the different ramp intercepts, estimating the maximum trace length provided above. Several relationships between magnitude, fault size, stress drop, and slip exist in the literature (Zoback & Gorelick, 2012; Stein & Wysession, 2003). Therefore, the current fracture size condition limits the microseismic onset by generating events approximately greater than +0.5 M_w (*Figure 4.29*).

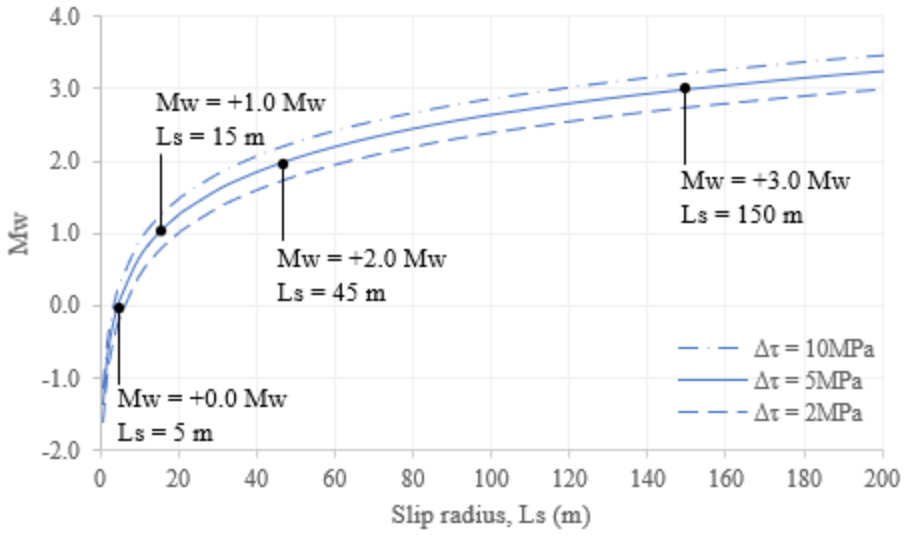


Figure 4.29: Slip radius to moment magnitude relationship given a static stress drop

A negative exponential distribution governs the fracture size (Priest, 1992), with the exponent coefficient (λ) adjusted to 0.1 from its original power-law iteration (*Figure 4.30*). The DFN assumes a mean fracture size (full length) of 10 m, resulting in an arithmetic average of 27 m. Therefore, these lower-bound structures occur more frequently, while the occurrence of the upper-bound fracture size (> 100 m) is less frequent.

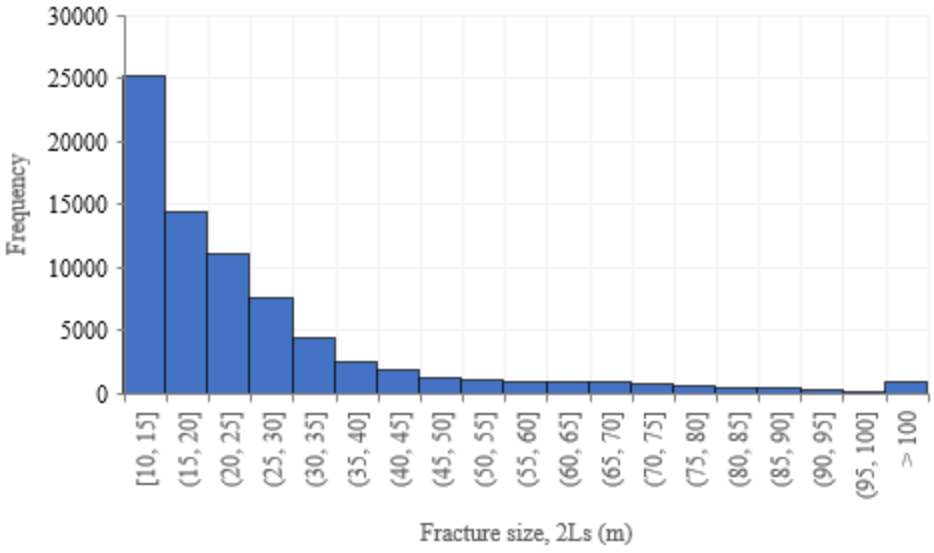


Figure 4.30: Histogram of adjusted fracture sizes (2Ls)

Over 75,000+ structural elements representing the mapped fracture sets were generated in the vicinity of the GH (*Figure 4.31*). The modeled domain extends to an approximate 1,000 m x 550 m x 700 m block dimension, entirely covering the 30-Vein construct while reaching 2,400 m below ground surface (~100 m under the current mining front). This DFN is used throughout the study. However, as will be described in the next subsection, the disc orientation was ignored following calibration efforts and a new methodology was developed for identifying favourable fracture sets.

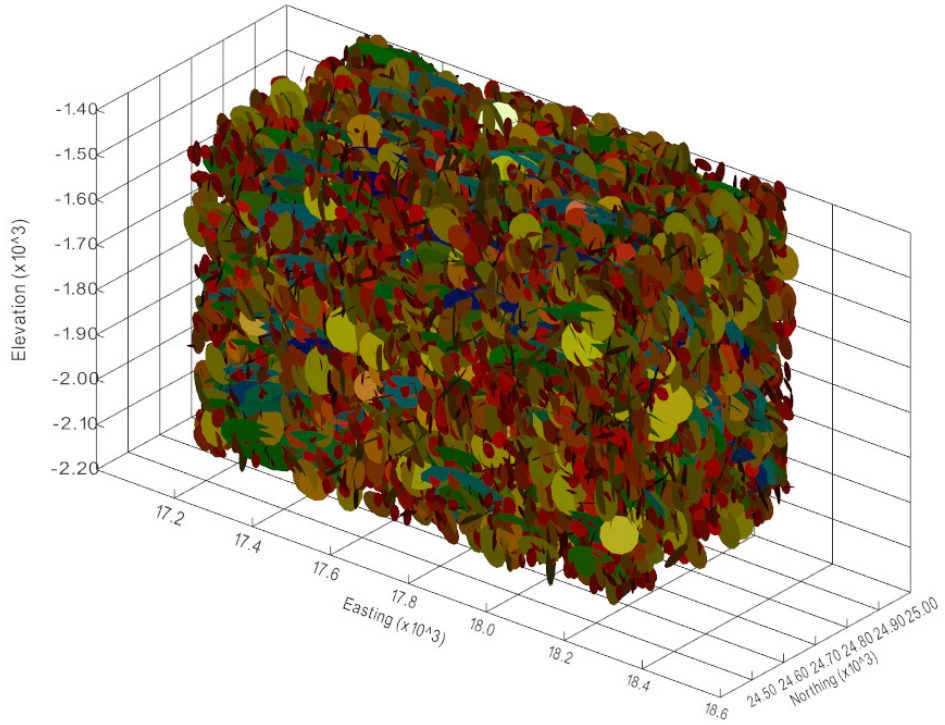


Figure 4.31: DFN catalog of mapped related structures showing fracture size ≥ 30 m

4.3.3.2 Fault-Slip Assessment based on ESS of the DFN

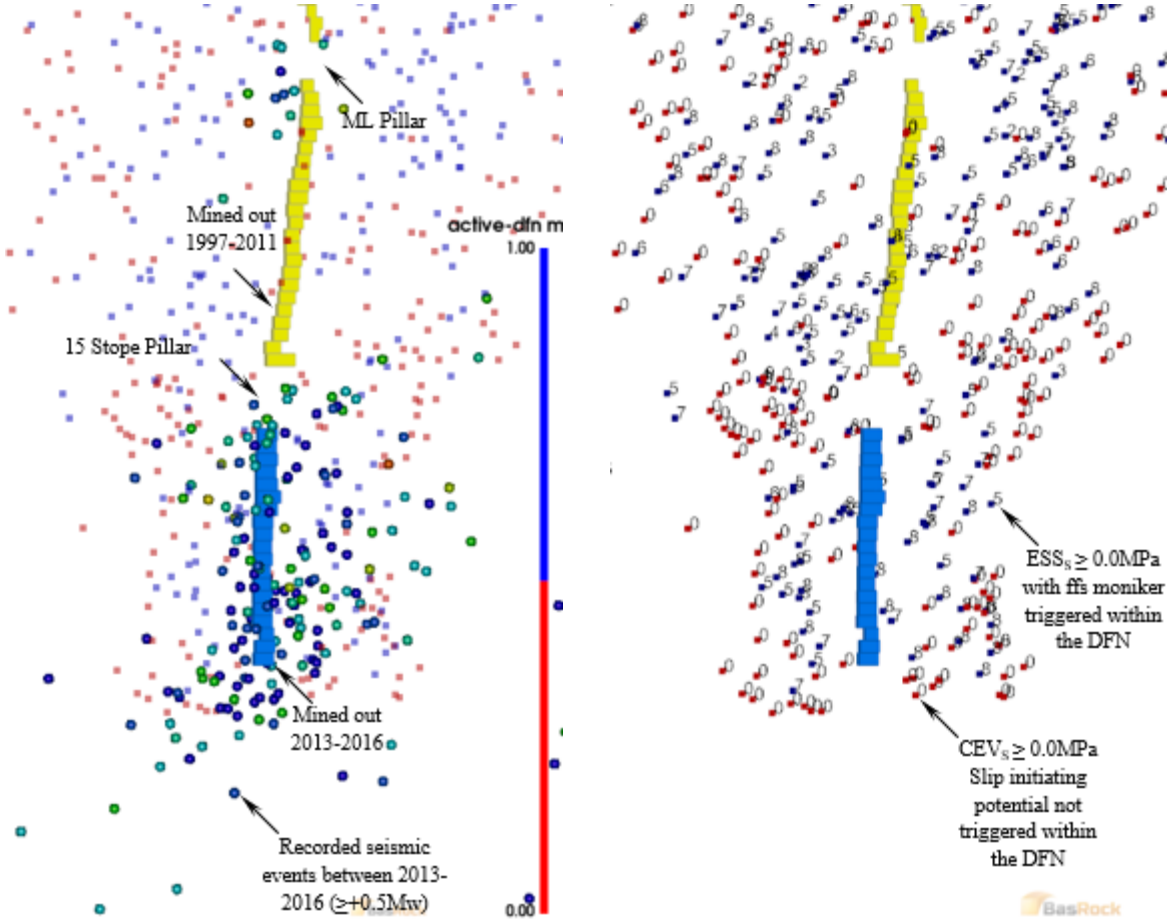
The block-based model (FF-element) was used to benchmark the seismic potential of the DFN catalog against 2013–2016 data. For this case, the DFN centroids were integrated into the BEM model as computational nodes. Each DFN centroid was tested for slip initiation flowing the outlined CEV_S procedure (eq. 4.13-4.14). The stress tensor was readjusted to the in-plane structure orientation attributed by the DFN catalog and tested for slip initiation given the $ESS_{S(DFN)}$ formulation. Hence, tagged $ESS_{S(DFN)}$ markers represent initiated DFN structures given

a positive $ESS_{S(DFN)}$ value ($\geq$ 0.0 MPa). For this process, the calibrated static friction angle of 25° was set as the input parameter.

As can be seen on the lower 15 Stope cross-sections (*Figure 4.32*), the registered CEV_S and $ESS_{S(DFN)}$ events have been plotted and projected onto the section, composing the seismogenic zone, as well as recorded events. These components were computed from the resulting mine-induced stresses formed by the 2013–2016 extraction step (blue blocks). The seismic zone extends vertically through the entire 30-Vein and captures the entire seismic envelope response since mining was initiated in 15S. Since the updated seismic digitizing system came online in 2013, only the events in proximity of formed pillars and recent extraction fronts can be compared to simulated occurrences for this case analysis. Therefore, the simulated events in proximity to the 1997–2011 mine-out geometry (yellow mine blocks) have possibly already slipped while developing those stopes but have not been captured within the digitized seismic database.

Focusing on the lower 15S abutment, the registered CEV_S events occur more frequently than the $ESS_{S(DFN)}$ events. These locate mainly on the outer boundary of the seismogenic zone, showing the maximum slip initiation extent for the set static friction. The simulated seismic envelope encompasses most of the recorded notable events ($\geq$ + 0.5 M_w) generated in that area as well. However, there appears to be fewer released $ESS_{S(DFN)}$ events directly at the mining front abutment when compared to the recorded seismic occurrences. Overall, the CEV_S events bound the recorded events more accurately (*Figure 4.32*a).

Further investigation indicates that the DFN presents a dependency on dip direction where the south-dipping faults tend to release in the northwall while the north dipping faults occur most specifically in the southwall (*Figure 4.32*b). Consequently, the DFN presents a heavy dependency for releasing FS-7 and FS-5 in the southwall and FS-8 in the northwall of the mining front in 15S. The FS-7 and FS-8 series strike parallel to the stope. In practice, it has been demonstrated that large fault slip occurs when the mining direction is towards an oblique-oriented structure (Ng et al., 1993; Gill et al., 1993). Therefore, these two sets are more likely to slip *continuously* as mining progresses offset from them, releasing under lower magnitude outputs. In addition, these initiated DFN events tend to locate at the floor elevation of the cut, while there exists the potential for deeper seated events, as has been inferred by the triggered CEV_S events, better matching the recorded seismic data.



(a) (b)

Figure 4.32: Cross-section through 15 Stope showing CEV_S (in red) and ESS_S (in blue) where (a) compares simulated with recorded seismic events, and (b) identifies fracture sets prone to initiate slip. The view is looking due West

To counter these discrepancies, a new procedure was developed to test the most likely fault set to initiation at the DFN centroid location. Therefore, the stress tensor at each centroid was rotated to the in-plane stresses (normal & shear) for each mapped fracture set orientation in the GH (*Figure 4.28*). The most favourable fracture set (FFS) is selected based on the highest output ESS_S value, prompting the fault sets to *compete* for maximum slip potential where the highest positive $ESS_{S(FFS)}$ values ($\geq$ 0.0 MPa) is conserved. The slip event is registered for that set.

It is important to note that the proposed procedure contrasts with the traditional DFN definition (Fisher, 1995) because the attributed fracture set orientation at each centroid was left unspecified. However, the new $ESS_{S(FFS)}$ technique was developed to account for this omission and allowed to

compare against recorded seismic events, providing further opportunity to calibrate for frictional properties as will be demonstrated herein.

To assure clarity, the proposed algorithm for the $ESS_{S(FFS)}$ technique is depicted below (*Figure 4.33*).

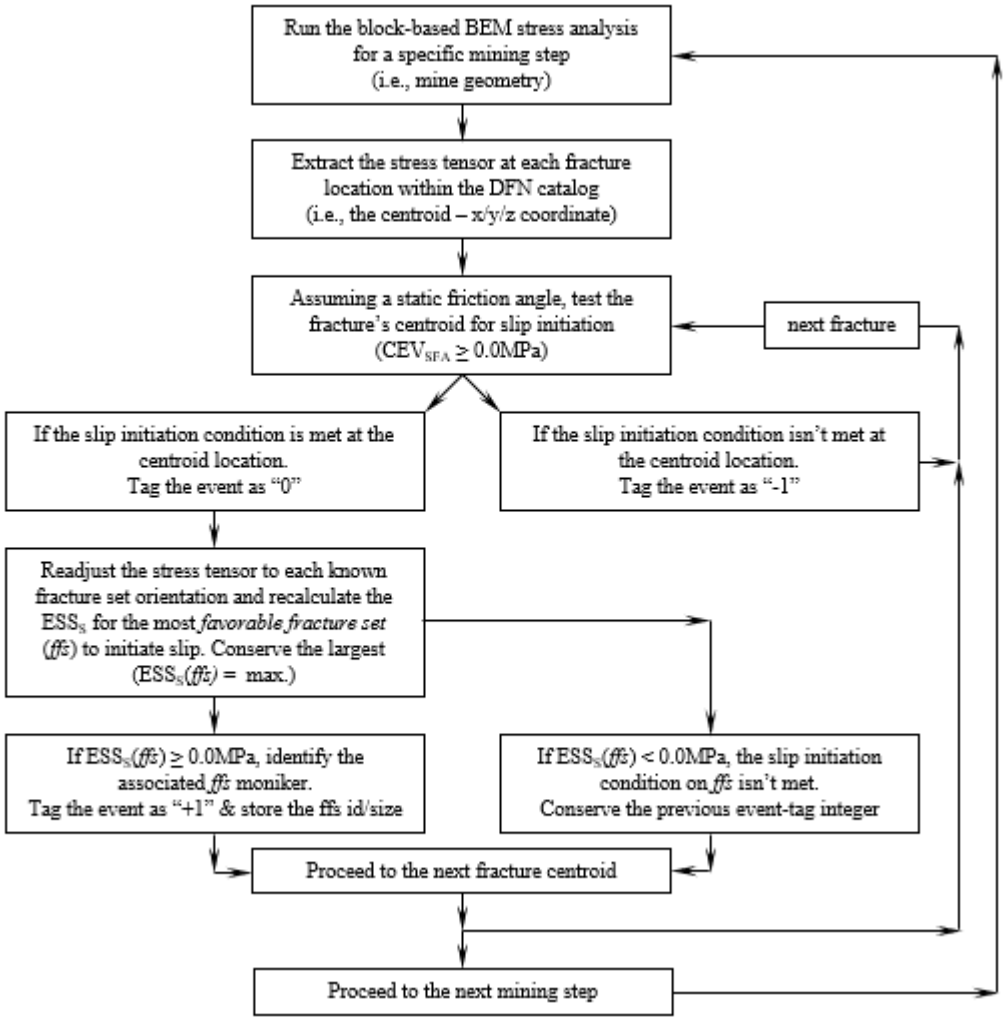


Figure 4.33: Modelling flow chart for $ESS_{S(FFS)}$

Applying the $ESS_{S(FFS)}$ algorithm to the induced stress state given by the 2013–2016 extraction results in the following observations (*Figure 4.34*). Focusing once more on the lower 15 Stope cross-section, the registered CEV_S events occur less frequently than the $ESS_{S(FFS)}$ events. The CEV_S events still position themselves on the outer seismogenic boundary, showing that there exists slip potential unrelated to know mapped structure sets. The seismic envelope remains the same as previously identified (*Figure 4.32*). Overall, the new $ESS_{S(FFS)}$ events match the

recorded notable event occurrences more accurately, seating deeper below the mining floor as well. Upon further investigation of the selected ffs in the unspecified-DFN, the dip direction dependency still arises where south-dipping faults tend to release in the north wall while north dipping faults occur most specifically in the south wall (*Figure 4.34*b).

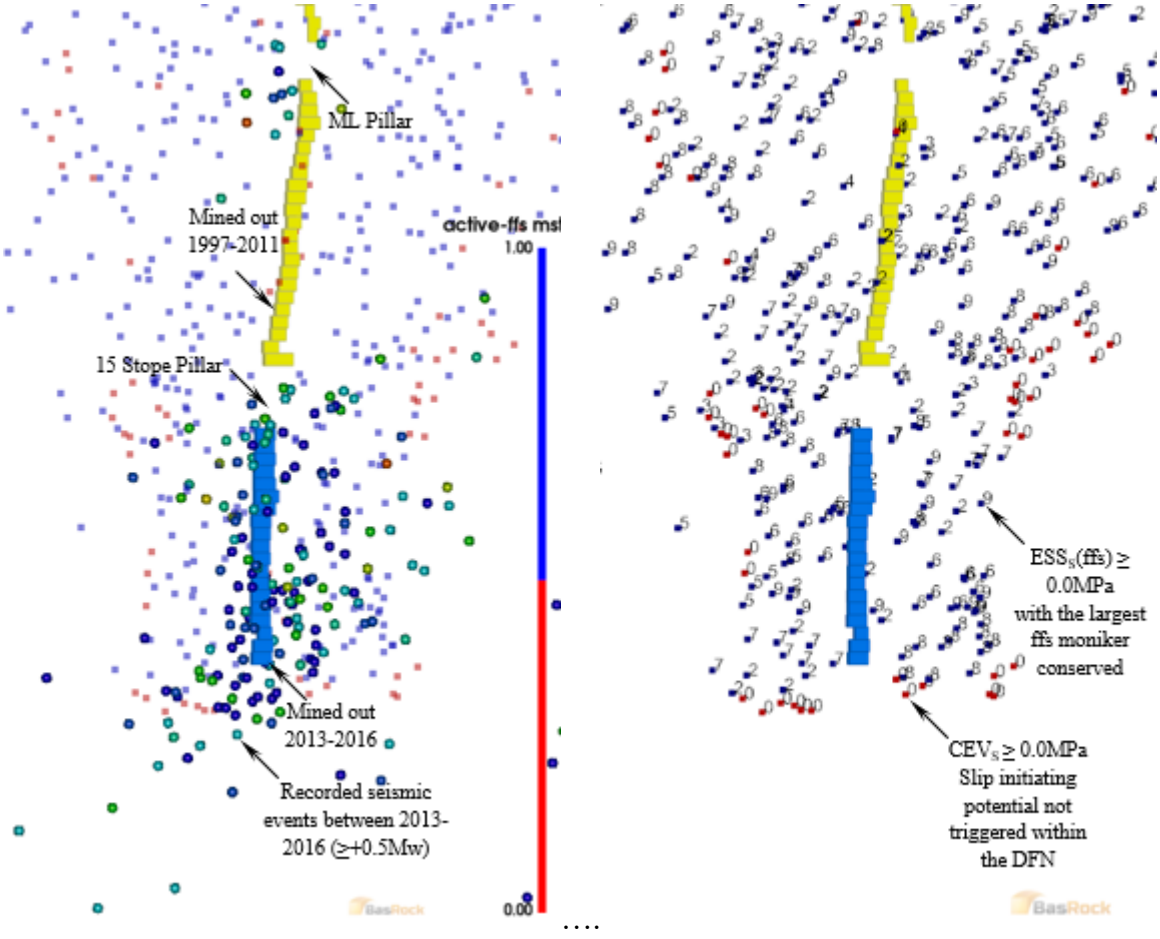


Figure 4.34: Rerun analysis on cross-section through 15S showing FFS results for CEV$_S$ (in red) and ESS$_S$ (in blue) where (a) compares simulated with recorded events, and (b) identifies favourable fracture sets prone to initiate slip. The view is looking due West

This is expected as the principal stresses flow under the floor, forcing structures to potentially clamp or slip based on orientation (Board, 1994). However, the unspecified-DFN allows additional fracture sets to develop slip. The FS-2 is seen to occur more frequently in the lower abutment of the southwall, while FS-6 is more apparent in the northwall. This occurrence matches in-field observations as the F-series are seismogenic (equivalent to the FS-2 orientation). In addition, these new orientations are oblique to the mining cuts. One may expect that they can

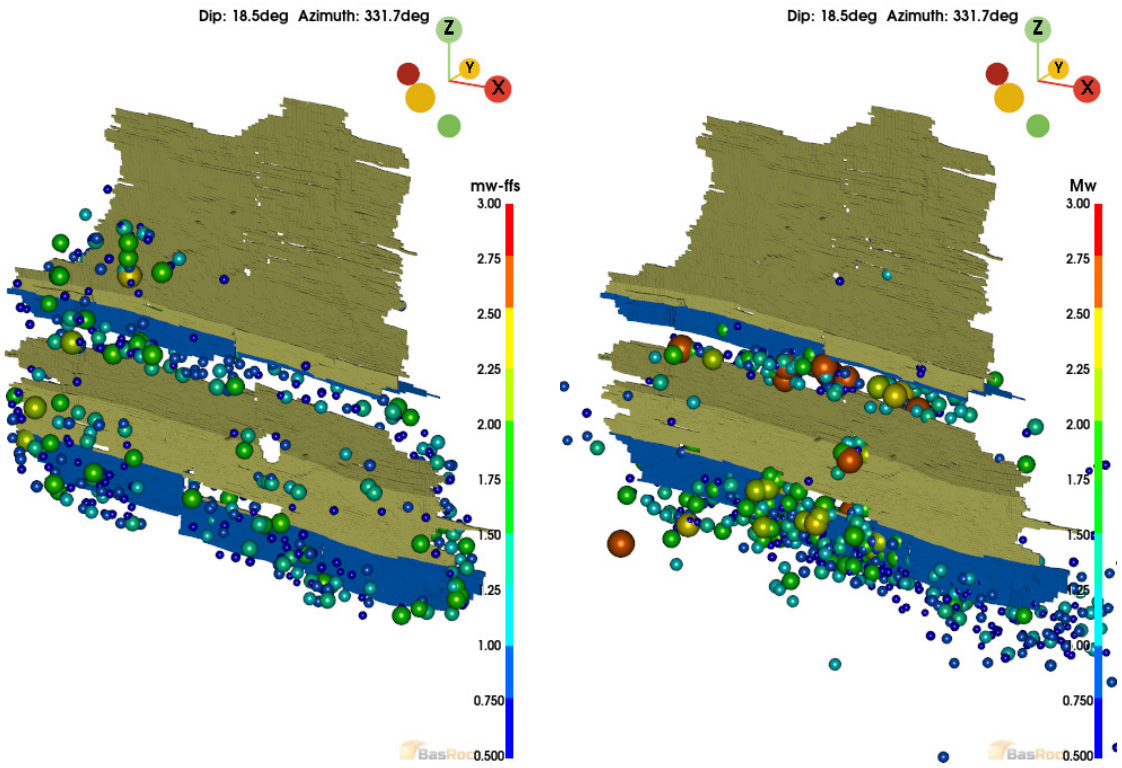
develop the highest seismic potential as mining progresses laterally toward them. Therefore, the unspecified-DFN with the associated $ESS_{S(FFS)}$ procedure provides more accurate seismic responses, better matching simulated seismic responses to recorded events.

Considering that slipped events cannot remobilize in a subsequent mining step (Salamon, 1993), the unspecified-DFN was queried for $ESS_{S(FFS)}$ events, which have initiated during 2013–2016. The seismic potential (M_w estimates) was derived for induced events by setting the dynamic friction to 22.5° (i.e., 90% of its static counterpart). The initiated structures were assumed to have completely slipped, given their fracture size attribute defined by the DFN, like that proposed by Salamon (1993).

The simulated seismic events have been visually compared with recorded events (*Figure 4.35*). For the 30-Vein production period set between 2013–2016 (blue blocks), over 580 notable events ($\geq +0.5$ M_w) were simulated as compared to 788 recorded events. The largest simulated seismic event for this dataset is +2.48 M_w, comparing crudely to the max +2.79 M_w recorded event. It is important to remind the reader that the goal of this simulation is to gain insight into the deterministic seismic response mechanism when compared to recorded events, not necessarily to match the stochastic nature of the actual occurrences.

This said, the simulated seismic events locate well below the floor abutments of the stopes, and bow around the active mining fronts, extending behind past production sectors (yellow blocks). This behavior matches the recorded seismic response for notable events, although less notable events have occurred in proximity of these previously mined out areas. However, after further inquiring the seismic catalog, smaller seized events ($< +0.5$ M_w) in the GH tend to extend well behind active mining fronts. Therefore, the simulated system might overestimate the seismogenic envelope for notable events in proximity to previously mined-out areas.

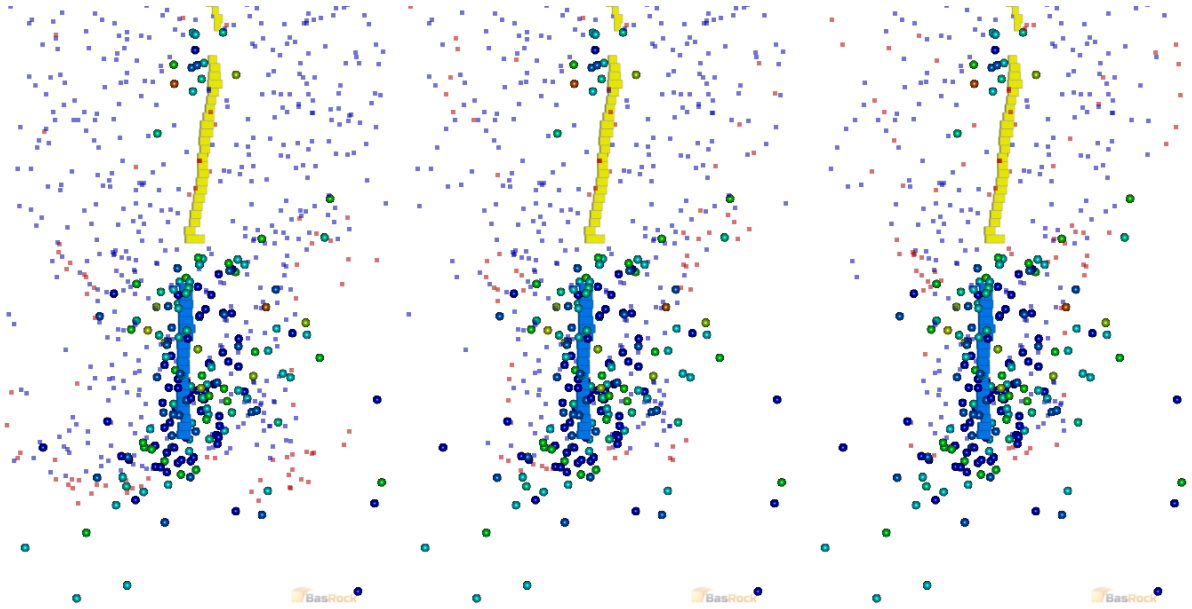
The remnant pillar configurations generate synthetic seismic activity similar to the recorded events, although the simulated events do not appear to locate directly in the core of these geometries.



(a) (b)

Figure 4.35: Isometric view of (a) simulated, and (b) recorded notable events

A parametric analysis was performed on the (static & dynamic) frictional properties as well as the fracture size (adjusted the DFN size from 2·Ls to Ls). Utilizing the computed induced stresses resulting from the 2013–2016 extraction, the static friction angle was adjusted to 20° and 30° in the $ESS_{S(FFS)}$ algorithm, allowing to reanalyze the unspecified-DFN (*Figure 4.36*). The base case ($\varphi_s = 25°$) was used to evaluate the results. Focusing once more on the lower 15 Stope abutment, the static friction angle controls the extent (or size) of the seismogenic zone around the 30-Vein geometry. The lower bound static friction angle obtrudes the seismic envelope, extending laterally past recorded events, while the upper bound static angle tightens the initiating events to the stope for lateral and floor occurrences. In addition, the lower bound static angle produces the deeper-seated events, better matching recorded events. However, the base case analysis continues to present the ideal match, only slightly underestimating the occurrence of floor events.



(a) (b) (c)

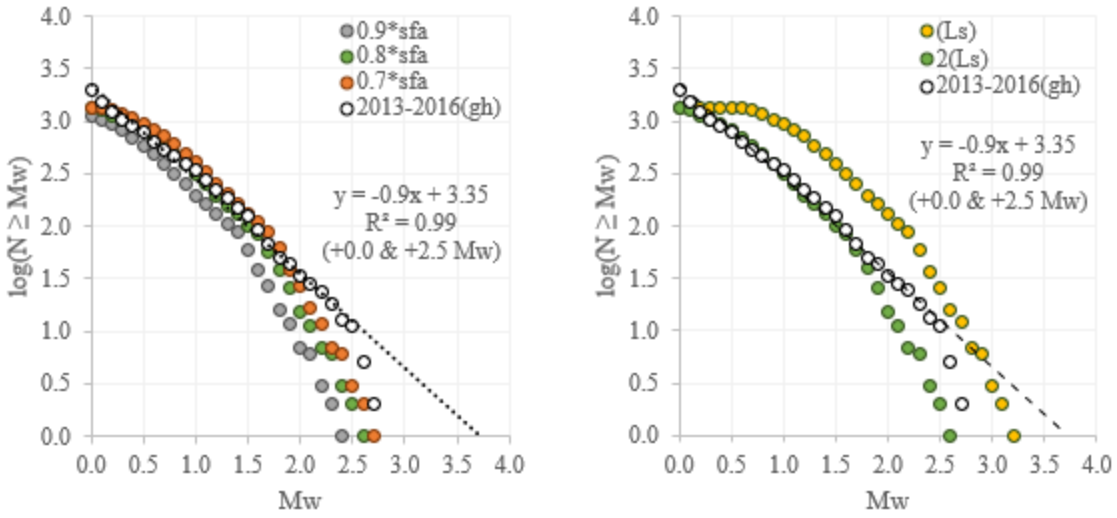
Figure 4.36: Comparison between simulated fault slips on FFS with relation to recorded seismicity for varying static friction angles (20°, 25° & 30°). The view is looking West

When filtering out the previously slipped events (pre-2013 extraction), the seismic potential (magnitude) was revaluated for the $ESS_{S(FFS)}$ events by reducing the dynamic friction ratio from 0.9 to 0.7 by 0.1 increment. Although the relative amount of initiated fault slip remains unchanged, the reducing dynamic friction angle progressively increases the registered static stress drop ($\Delta\tau$), potentially increasing the output magnitude of the event. The GRMF plot was generated for the three friction ratio cases (*Figure 4.37*a). The three plots present very similar b-values (~0.9), comparing reasonably well with the recorded events for the same period. As expected, the lower friction angle ratio (0.7) generates the largest event magnitude (+2.71 M_w), as opposed to the two other ratios of 0.8 and 0.9, releasing a maximum event size of +2.65 M_w and +2.48 M_w, respectively. All three curves present a roll-off, which is typically observed in seismology, although slightly underestimating the frequency of events >+2 M_w. This may be attributed to smaller fracture size, limiting the moment magnitude output by restricting the slip area. However, the dynamic-to-static friction ratio of 0.8 agrees the most with the recorded data for events up to +1.75 M_w.

Assuming the 0.8 friction ratio, the fracture size specified in the DFN was doubled (i.e., fracture size assigned in the DNF equals Ls) and compared with the previous results (*Figure 4.37*b). Due

to the slip length assumption (which accounts for complete slip upon initiation), doubling the fracture size increases the occurrence of the events with the maximum registered magnitude at +3.2 M_w. Interestingly, the b-value remains the same (~0.9) for increased slip length.

This analysis provided further confidence in the unspecified-DFN procedure and the resulting frictional properties calibrations (φ_s = 25° & φ_d = 20° with cohesion = 0.0 MPa).



(a) (b)

Figure 4.37: Recorded vs simulated GRMF response in GH for (a) varying dynamic friction angle, and (b) varying slip lengths

4.4 Chapter Summary

Chapter 4 presented the general BEM model setup for the grid-based (DD-element) and block-based (FF-element) analyses, utilizing the MAP3D v68 software. Assuming the infinite homogeneous elastic medium assumption, the extraction on the 30-Vein (and part of the 80-Vein) was reconstructed for two early production periods. Model calibration efforts relied on matching the elastic rockmass response to in-stope closure measurements. Following successful calibration, the two main models were constructed.

The grid-based (DD-element) model was built for ERR (Cook et al., 1966), where specific modelling procedures were developed for mine-wide assessment. The latter approximates the stope shapes to a single 3-dimensional plane.

The block-based (FF-element) model was built to push the ESS (Ryder, 1987) analysis further, allowing to assess fault initiation (ESS_S) and to calibrate the frictional properties. The latter matches the 3-dimensional shape of the stopes. The block-based model was further tested by incorporating a DFN where mine-induced stresses were mapped onto the structure centroids (represented by discs) and tested for slip initiation and extent.

The analyses performed in this chapter resulted in the following conclusions:

1. For the grid-based model, the global ERR analysis of the GH has resulted in design curves matching those published in South Africa. The ERR of 30 MJ/m^2 corresponds to the moderate seismic occurrence, defined here as one (1) seismic event greater than +1 M_w per 1,000 m^3 extracted vein material. However, individual stopes were observed to produce different ERR thresholds (as low as 10 MJ/m^2 in 15S), resulting from dependencies to local layouts and variability of fracture densities.
2. Continued application of the grid-based model has resulted in annual GH seismic efficiency (η%) estimates, ranging between 0.015% and 0.137% for the 2013–2016 production period. Although low, the resulting upper range in 2016 matches SA research, which has found global seismic efficiency values ranging between 0.2% and 0.4% at the VCR and CLR mines, respectively. Other mines of the Witwatersrand System have shown seismic efficiencies of ~0.1%.
3. From the block-based model, CEV stress analysis on exact locations (x, y, z coordinates) of recorded notable seismic occurrences have numerically demonstrated that 54% of events (> +1 M_w) and 71% (> +2 M_w) show the potential to release fault-slip events. These results match well with E_s / E_p ratios (set to above 3), which were queried from the ESG seismic system, providing further confidence in the dominance of the shear mechanism in notable events (> +0.5 M_w) induced in the GH.
4. A DFN was integrated into the block-based model, and the ESS_S procedure was applied at the centroids for identifying slip initiation and the CEV potential. The analyzed mining period (2013–2016) poorly matched seismic records in 15S, while the resulting CEV events better matched these records. Therefore, the unspecified-DFN with the $ESS_{S(FFS)}$ analysis was developed and retested for the mining period. The simulated $ESS_{S(FFS)}$ induced seismic events better compared with notable events recorded in 15S.
5. The ESSS calibration efforts for static and dynamic frictional properties, as well as fracture lengths, have been undertaken for the mining period (2013–2016). The efforts have resulted in adopting φs = 25° and φd = 20°, with cohesion set to zero. These properties provide the best match with seismic records in 15 Stope (sensitivity on the static friction angle) and within synthetic GRMF plots (sensitivity on the dynamic friction angle) of the complete GH. The fracture length variability, set to fracture size equates to Ls or 2(Ls), bound the global GRMF plot of released events recorded during 2013–2016.

CHAPTER 5 FORECASTING MINE-INDUCED SEISMICITY

5.1 Deepening Mine Conditions in the Gold Hunter Deposit

As mining is planned to progress in the GH, the engineering department must develop feasible ore recovery designs centered around sound engineering practice. Based on current resource and reserve estimates (*Figure 5.1*), the potential mining depth will eventually reach 8,000L at a depth of ~2.7 km below the surface. In addition to the ongoing operational challenges (e.g., air cooling and material handling), the mine must be mindful of increased seismic hazards imposed by deepening (Hudyma, 2010).

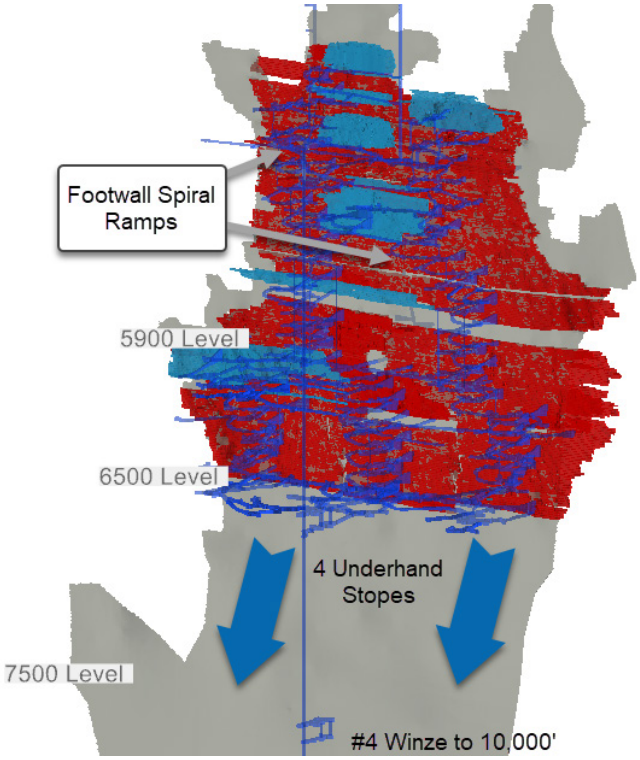


Figure 5.1: Resource and reserve estimate in the GH (Hecla, 2022)

As the GH continues its descent below the 6,500L, the mine-planning engineer requires the following inputs to manage seismic hazards at depth:

1. Description of the primary seismic source mechanisms contributing to large-scale seismicity.

2. Estimates of a likely number of events per magnitude range (e.g., > +1 M_w), which may be expected, providing estimates for frequency occurrence (e.g., occasional or frequent) and likely location relative to mine geometries (Board, 1994).
3. Estimates for likely rockmass damage imposed by large-scale seismic hazards with potential strategies for limiting personnel exposure (Hudyma et al., 2017).

These inputs will allow engineering to plan adequately for the following:

1. Select the most favourable mining method or sequencing to minimize seismic hazards.
2. Offset permanent infrastructures (such as ramps and main haulages) from seismically active zones and develop appropriate protocols for personnel re-entry into stopes after blasting (limiting exposure).
3. Install heavy dynamically rated bolts with chain-link forming a high kinetic energy absorbing ground support system at critical locations throughout the mine or in-cycle in stope development, limiting the rockmass damage potential.

The above inquiries do not require an exact prediction of the magnitude, time, and location of events but rather an incisive forecast of the general seismic behavior from which the rockbursting risk can be assessed. Therefore, the previously developed seismic hazard charts and methods were validated against new mining conditions.

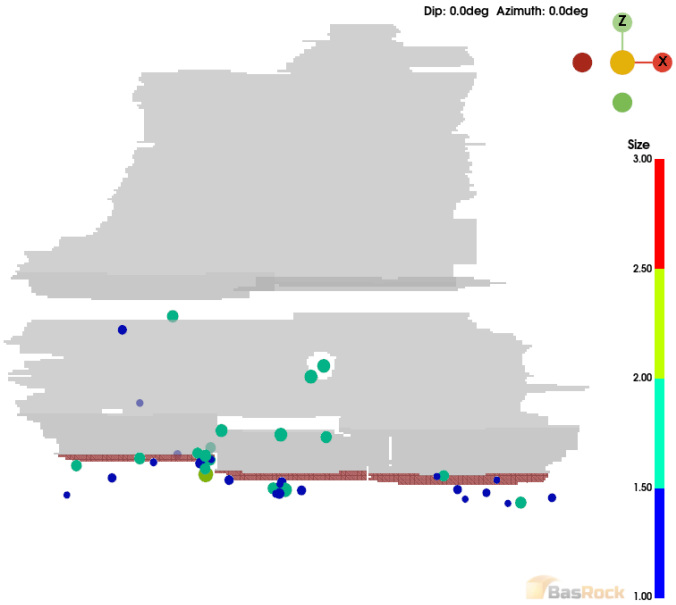
5.2 Validation of Developed Seismic Design Chart

This section will attempt to validate the previously derived seismic design charts (i.e., ERR and ESS) against two subsequent mining periods that occurred after 2016:

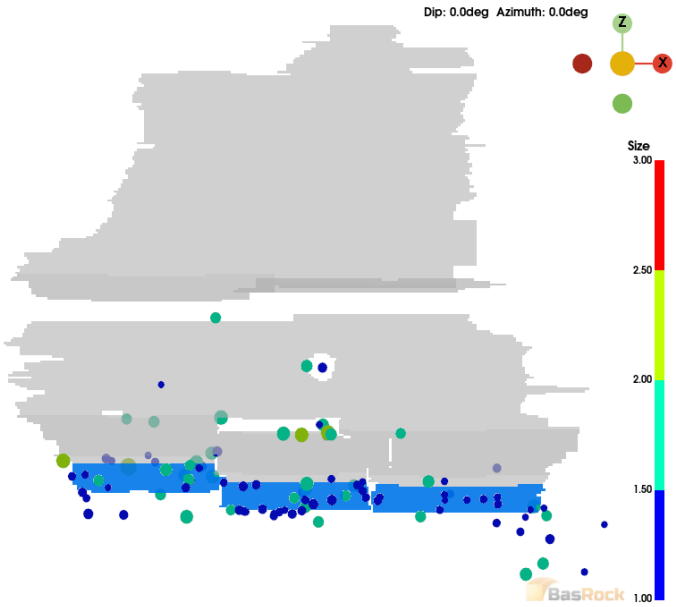
1. Mining period 2017–2019, where the mining rate was reduced by over 85% due to a mine-wide work stoppage.
2. Mining period 2020–2021, where a new mining method (termed the Underhand Closed Benching) was implemented in the 30-Vein, presenting a similar average extraction rate for the period but focused on the lower stopes.

5.2.1 Back Analysis of Subsequent Mining Periods

Both these mining periods have collectively deepened the mining front on the 30-Vein by ~50 m since 2016 year-end (*Figure 5.2*). This roughly represents an increase in the total area mined of ~10%.



(a)



(b)

Figure 5.2: Mining on 30-Vein with projected large seismic events (> +1 M_w) for (a) 2017–2019, and (b) 2020–2021

The grid-based model computed the ERR per year within each mining period. These results were integrated into the ERR forecast plot previously derived from 1997 to 2016 (*Figure 5.3*). The RMSE of the new period is +0.822 as compared to the GH trend error of +0.578. Therefore, the chart over-predicts seismic occurrence. As observed, the number of occurring seismic events larger than +1 M_w has significantly reduced during those mining periods except in 2017. A higher mining rate impacted the latter in the first quarter of that year, which inevitably released an increased number of larger seismic events better matching the GH trend. However, the subsequent mining years present distinct operating characteristics where the mining rate (during 2017–2019) was reduced to ~15% of that typically observed in LFUL while staying within 87% of that for a new mining method (during 2020-2021). The slight increase in ERR reflects the impact of mining depth observed from 2019 onward by ~48 m. Overall, these new results show a drop of ~1 large seismic event (M_w>+1) per 1,000 m^3 mined from those previously analyzed. Nonetheless, these new results stay bound within South African practice.

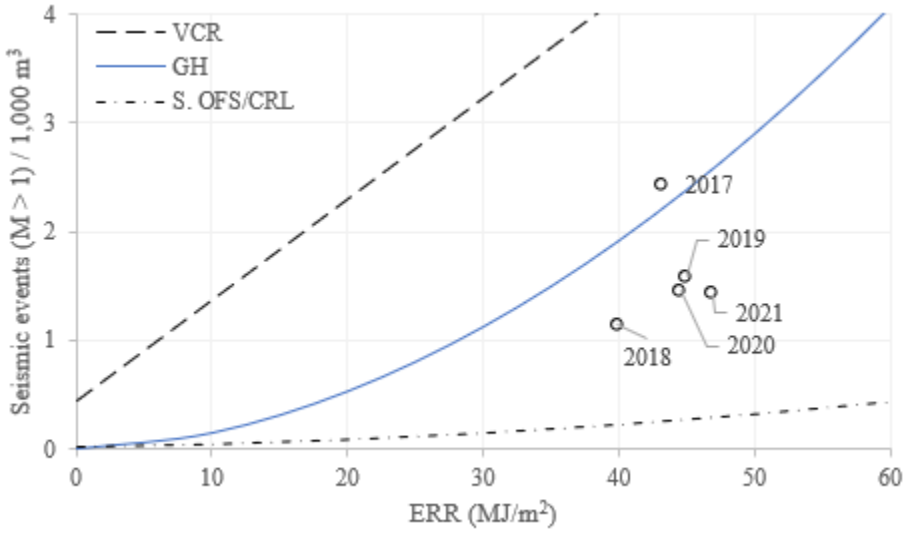


Figure 5.3: ERR forecast comparison with those recorded during subsequent mining

The normalized annual magnitude distribution of large seismic events for the three periods is presented in *Figure 5.4*. The number of events has been normalized to one production year within each mining period. Also, the 2013 production year has been omitted because it consisted of a ramp-up period from the 2012 work stoppage. As can be seen, the release of notable events (M_w > +1) has decreased by 87% and 51% for both periods, 2017–2019 and 2020–2021,

respectively. The maximum magnitude release has also reduced. The decreased mining rate period caps capped around +2 M_w release, while the new mining method capped below +2.5 M_w.

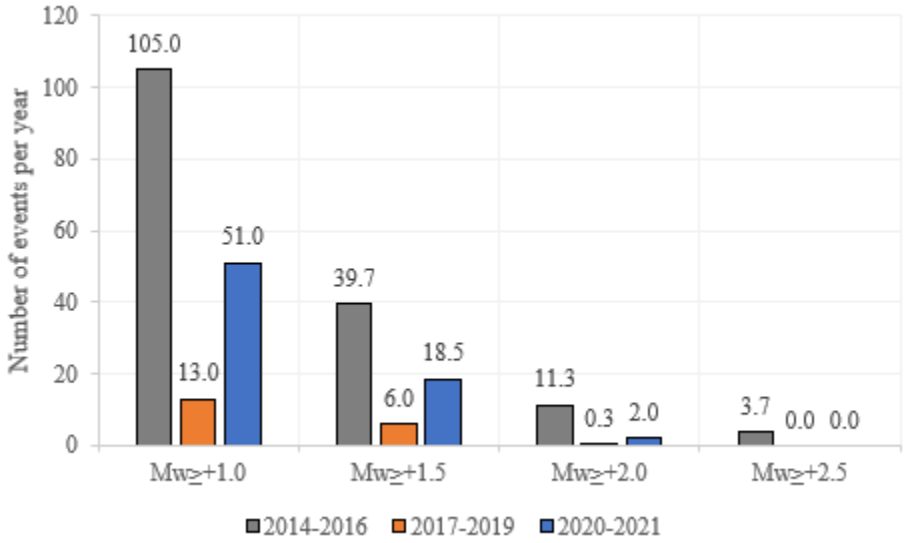


Figure 5.4: The normalized annual occurrence of seismic events by mining period in GH

There is a general decrease in output seismic release for increasing mining depths. The rockmass seismic response has deviated from the established LFUL mining trend. Table 5.1 relates the largest seismic event occurrence to its location within the mine geometry.

Table 5.1: The largest events recorded in Pillars and mining abutments per mining period

Mining Period	Largest. Pillar Event	Largest. Stope Abutment Event	Mining Depth from Surface
2014–2016	+2.79 M_w	+2.34 M_w	2,237 m
2017–2019	+1.70 M_w	+2.15 M_w	2,255 m
2020–2021	+2.08 M_w	+2.35 M_w	2,285 m

5.2.2 Discussion on the Effects of Mining Conditions

Literature indicates that certain mine factors affect seismic output, such as the rock type, extraction method and layouts, mining depth and extent (Gibowicz, 2009), mining rate (Hudyma et al., 2017), and the seismic decay after large production blasts (Vallejos & McKinnon, 2011). In practice, deep narrow tabular mines have shown larger seismic outputs per ton mined due to localized stresses loading thinner abutments (Brummer, 1999). Continuous narrow veined

orebodies present a softer loading response due to loads arduously transferred to distal abutments. As extraction proceeds, remnant pillars (left behind due to poor grade or established by converging mining fronts) negatively affect seismic response (White et al., 2002).

Therefore, the effects of mining conditions on seismic response related to the GH are further investigated in this section. First, the new mining periods were affected by a change in the production rate, which can be crudely derived from the normalized tons per year extraction sequence plot (*Figure 5.5*). The daily production is estimated at ~790 tons per day (2014–2016), ~120 tons per day (2017–2019), and ~690 tons per day (2020–2021). Note that in the last period, mining occurred exclusively in the bottom 30-Vein stopes, therefore, presenting an increased mining rate.

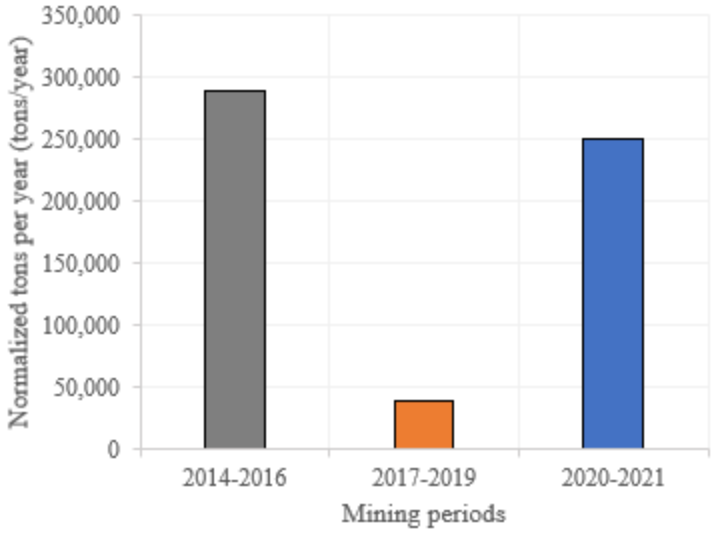


Figure 5.5: Normalized tons per year for each mining period in GH

For the second period, the LF mine developed a new mining method (Board & al., 2023) to induce fault-slip on structures in 30-Vein stopes and fully implemented the technique in 2021 across the main lower production stopes (12S, 15S, and 16S). The Underhand Closed Bench (UCB) mining method relies on destressing (completely fragmenting) the floor in advance of the mining front (*Figure 5.6*). A long-hole pattern is drilled along the entire floor line (targeting 8.5 m in depth) of the cut, with the blast shooting each side separately (two blasts per stope). Note that the blast does not require a relief cut, resembling a confined trench cut blast rather than a long-hole design. The confined blasted rock swells into the top drill cut, where operations

remove the ore until the previous floor line is re-established and proceed with backfilling the cut with cement paste backfill. Mining re-enters into the next cut below the paste sill beam and extracts the fragmented material in a shrinkage manner with little to no additional blasting, progressively securing the stope walls with ground support. This is repeated over two cuts (~4.2 m high), continuously working under an engineered back until the next drill cut is re-established 8.5 m below the previous. This mining method steps away from the standard cut-and-fill practice, requiring blasting with every advance into the cut, and introduces a bulk mining system on the vein. Several proactive control measures for seismic release were observed during the initial trials of the method. These will be further elaborated on in this section.

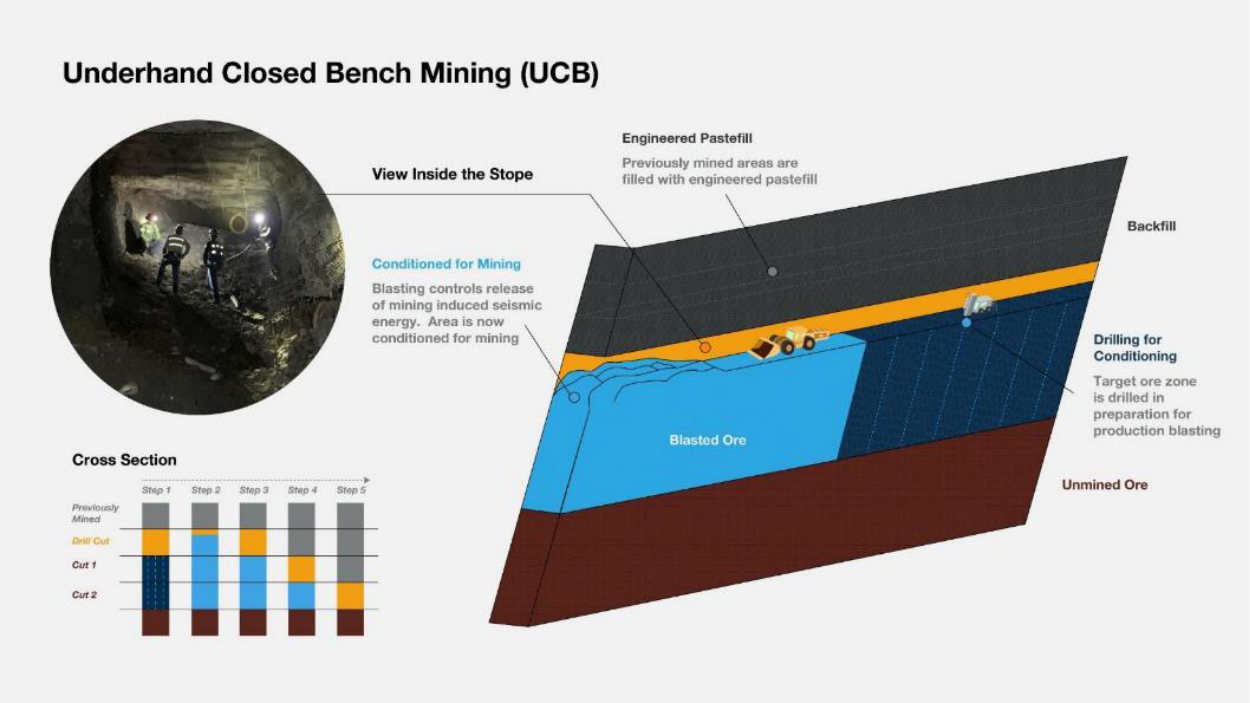


Figure 5.6: The Underhand Close Benching (UCB) mining method (Hecla, 2022)

5.2.2.1 Change in Energy Release per Mining Period

As previously demonstrated, the kinetic energy (W_k) estimate was determined by subtracting the strain energy in the mined block (U_m) from the ERR value. Assuming an average seismic efficiency of 0.137%, *Figure 5.7* compares the forecast of W_k release with recorded seismic release (E_s). The 2016 production year was inset in the assessment since all of the mining on the 30-Vein occurred in the lower stopes after 2015. As can be seen, the forecast energy levels are considerably higher than the recorded energy releases for all subsequent mining periods past

2016. Seismic efficiency was reduced on average to ~0.02% for those periods, inferring a possible change in rockmass response.

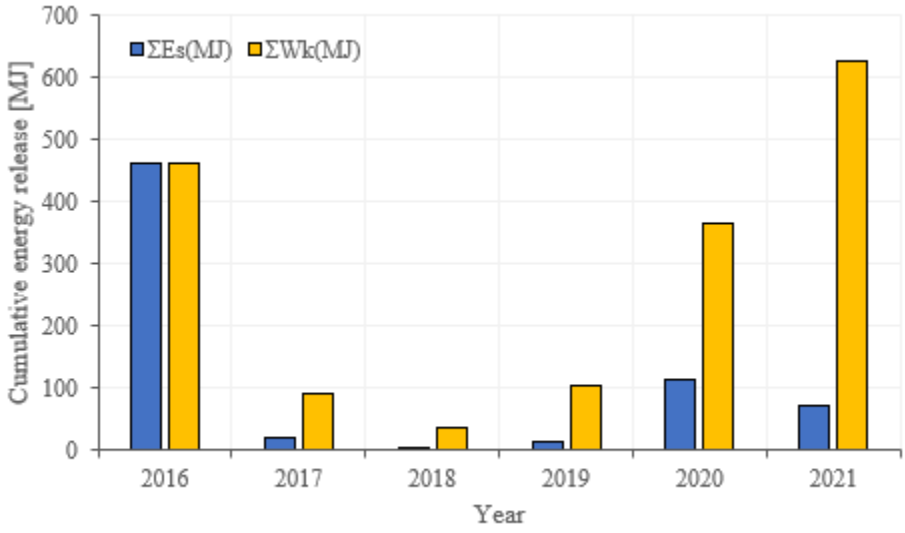


Figure 5.7: Energy release forecast by production year in GH

Translating these findings into energy release per ton (J/ton) produces the following plot (*Figure 5.8*). The same behavior emerges where the modeled W_k overestimates the release per mined ton.

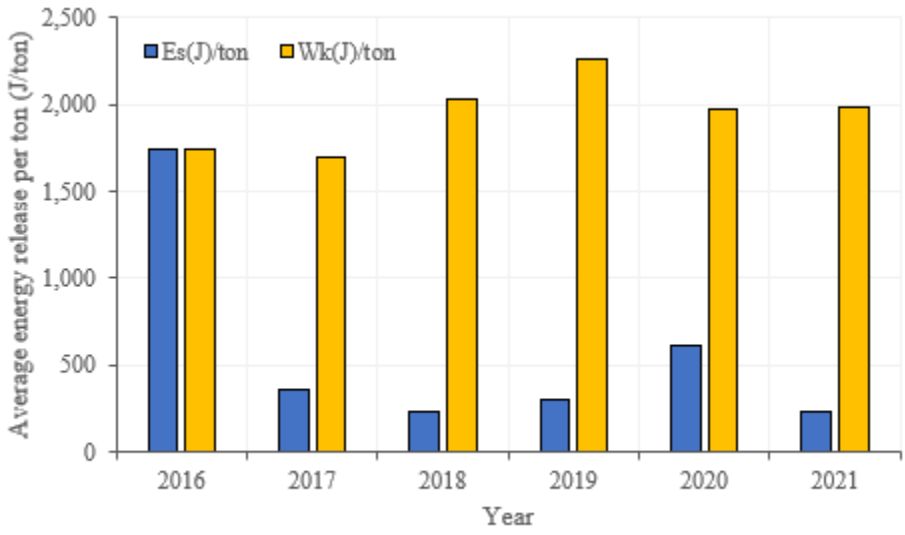


Figure 5.8: Energy release per tons forecast by production year in GH

5.2.2.2 Change in Seismic Response per Mining Period

The magnitude distribution of occurring seismic events represents a typical method of examining the seismic characteristic of a rockmass response (Wesseloo, 2014). The changes in geology, mining geometry, and exploitation methods facilitate these changes (Mendecki, 1997). The Gutenberg-Richter Magnitude-Frequency plots for the LFUL (2014–2016), LFUL with reduced mining rate (2017–2019), and the UCB (2020–2021) mining are provided below (*Figure 5.9*). The b-value is often used to interpret the rockmass failure mechanism. Low b-values (< 1.0) indicate a potential for asperities on faults (Mogi, 1962) and an increase in applied shear stresses (Scholz, 1968). Higher b-values (>1.0) represent increasing material heterogeneity (Mogi, 1962) or creeping sections of faults (Wyss et al., 2004). Here, all mining periods reflect clear fault-slip potential (b-values < 1.0). However, the slope of the two latest periods has significantly steepened following distinct operational changes, resulting in a reduction of large events. Thus far, the roll-off at large magnitudes shows events capping below +2.5 M_w for UCB and the reduced LFUL mining rate, while the maximum event size for the LFUL method exceeds +2.5 M_w.

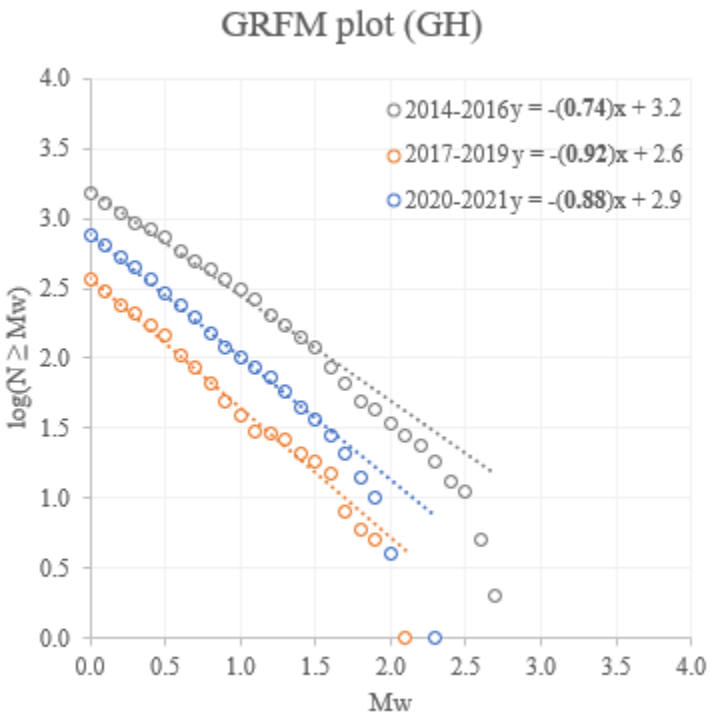


Figure 5.9: Gutenberg-Richter Magnitude Frequency plot per mining period in GH

The time of occurrence after production blasts represent a method for examining time-dependent seismic behavior. Events typically observed after blasting are grouped into two broad categories: (***i***) induced, or (***ii***) triggered. The adjective *induced* describes seismicity resulting from notable stress changes leading to failure, whereas *triggered* describes incremental stress change leading to the same outcome (McGarr & Simpson, 1997). In practice, induced events are characterized to occur hours following the blast, while triggered events can linger beyond the expected seismic decay (Gibowicz, 1993). The lag time between large seismic events (> +1 M_w) with respect to blasting was assembled and highlights the difference in response between the mining methods in 15 Stope (*Figure 5.10*). Note that the 2017–2019 events were excluded from this analysis due to irregular blast times incurred by the work stoppage. The 2020–2021 period results in around 88% of the induced events occurring within 2 hours following production blasts. In contrast, less than 60% of events were induced within this same time window for the LFUL method, meaning that 40% of large events were triggered outside the blast window.

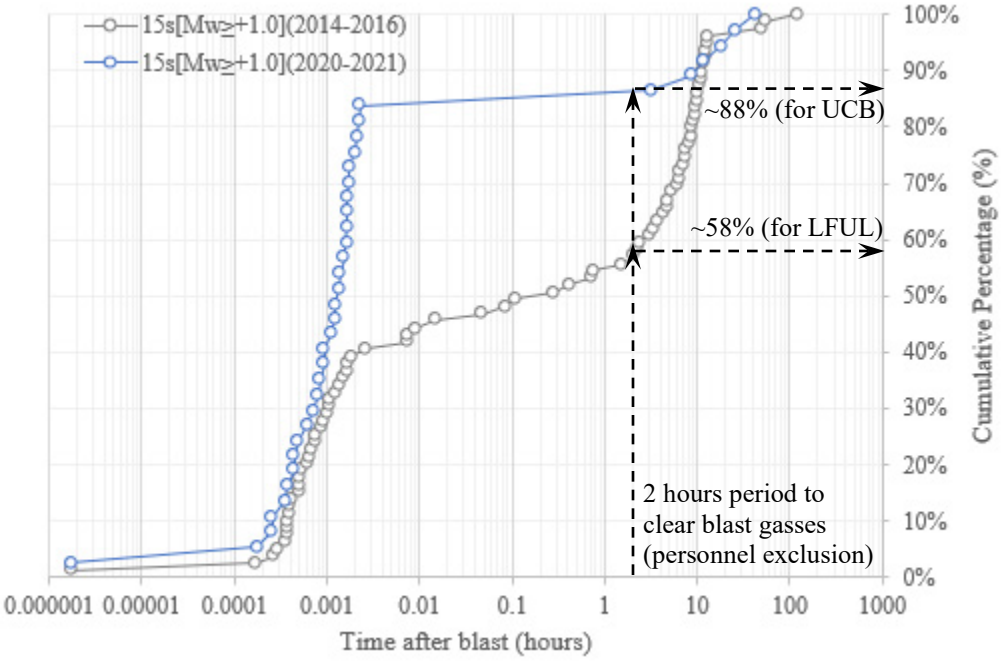


Figure 5.10: The lag time between blasting and large seismic events in 15 Stope

The spatial distribution of events (hypocenters) with respect to mining represents a method for examining rockmass failure types (Carusone, 2018). In practice, event clusters that stay bound to a fixed region in the rockmass infer the existence of a large geological structure, while moving

seismic clusters that follow the mining advance indicate a mixed strain and fault-slip release environment. Several techniques are developed to capture de change in seismic response based on event occurrences (Cortolezzis & Hudyma, 2018). As previously presented, the relative distances of notable events (> +0.5 M_w) were decomposed into vector components for the period 2020–2021 and compared with previously analyzed responses (*Figure 5.11*). The locations of the events stay bound to the mined bloc (< 50 m), although new occurrences seem to be grouped closer to the cut. The seismic source mechanism is therefore assumed to have stayed the same.

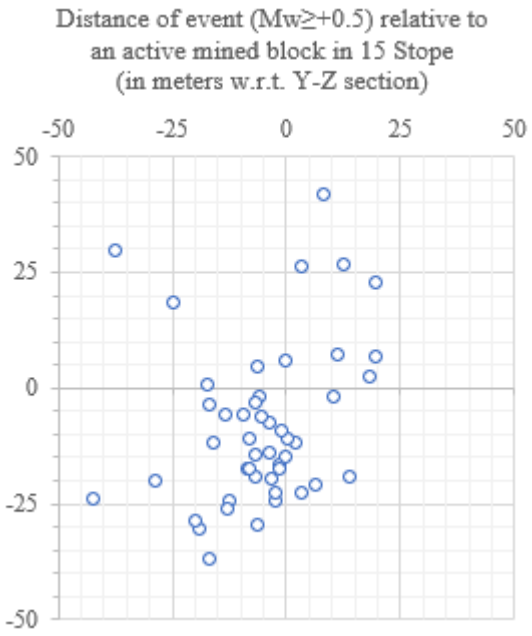


Figure 5.11: Seismic occurrence of notable events, 2020–2021

These plots reinforce the general concept of changed rockmass response in the GH since modifying the mining conditions post-2016.

5.2.2.3 Resulting Impact of UCB on Seismicity & Production

The UCB has significantly increased productivity in the lower 30-Vein as nearly 90% of the total production is extracted from the bottom stopes (12S, 15S, 16S) since 2016. The tonnage extracted from the three lower 30-Vein stopes is compared between production years (*Figure 5.12*). Note that the mine also operated in the upper 11S and 14S in 2014–2015 (ignored in the figure), with mining progressing exclusively on the lower 12S, 15S & 16S in 2016. Between 20017 and 2019, most of the mining was performed by salaried staff. Mining resumed afterward

with the development of the UCB method, which was fully integrated into the active 30-Vein stopes in late 2020. The 2016 and 2021 mining periods present identical extraction conditions where the lower 12S, 15S and 16S secured most of the ore production on the 30-Vein. Comparing both production years, UCB mining in 2021 (271,787 tons) shows a rough 40% increase in productivity over the last full year of LFUL in 2016 (190,746 tons).

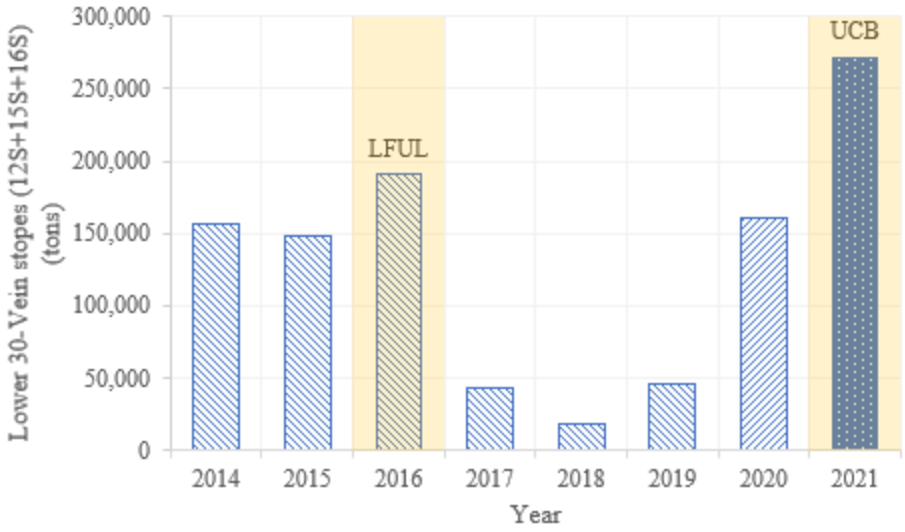


Figure 5.12: Annual production tonnage taken from lower 30-Vein stopes (12S, 15S & 16S)

A comparison of the cumulative seismic energy release (in MJ) recorded by the seismic system in the lower 30-Vein stopes, as a function of time for production years 2016 and 2021, is shown below (*Figure 5.13*). The release of periodic large seismic events explains the stepped characteristics present in both curves. Based on the ratio of total energy release per annual tonnage, the LFUL averages a seismic energy release rate of ~833 J/ton in 2016 and ~250 J/ton from UCB mining in 2021.

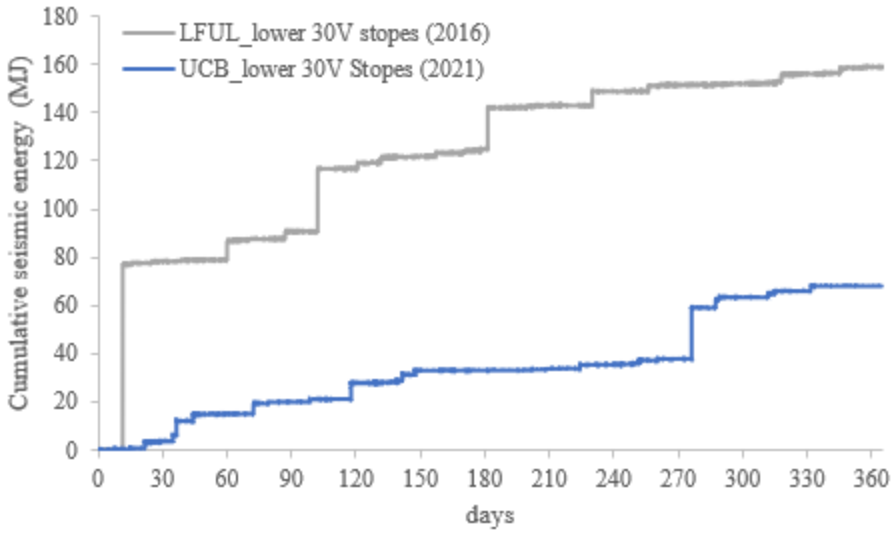


Figure 5.13: Cumulative seismic energy release recorded in lower 30-Vein stopes, comparing the last year of LFUL mining (2016) with one complete year of UCB (2021)

Investigating the distribution of recorded seismic energy per mining activity provides further insight into the seismic output behavior (*Figure 5.14*). The recorded energy is grouped into activities composing the mining cycle. The activity *during active mining* represents the period when miners are inside the stope extracting the cut (drill and blast or mucking fragmented ore). The activity *within 12h of a UCB blast* tallies the seismic energy released following a mass blast (only applicable to 2021). The activity *during other activities* accounts for backfilling and cement paste cure practices before slotting back into the vein (i.e., no change in potential energy occurs at that time on the vein). As can be seen, the LFUL released ~774 J/t during active mining operations, while UCB released ~30 J/t for the same activity. Most of the total seismic energy in the UCB method (~85%) gets released within the blasting operations. The Omori (1894) energy decay analysis reveals that 96% of the seismic energy, following a 48h period after the blast, is released within the first 3 hours (*Figure 5.15*). The seismic event count per hour quickly decays to background noise after reaching that time interval.

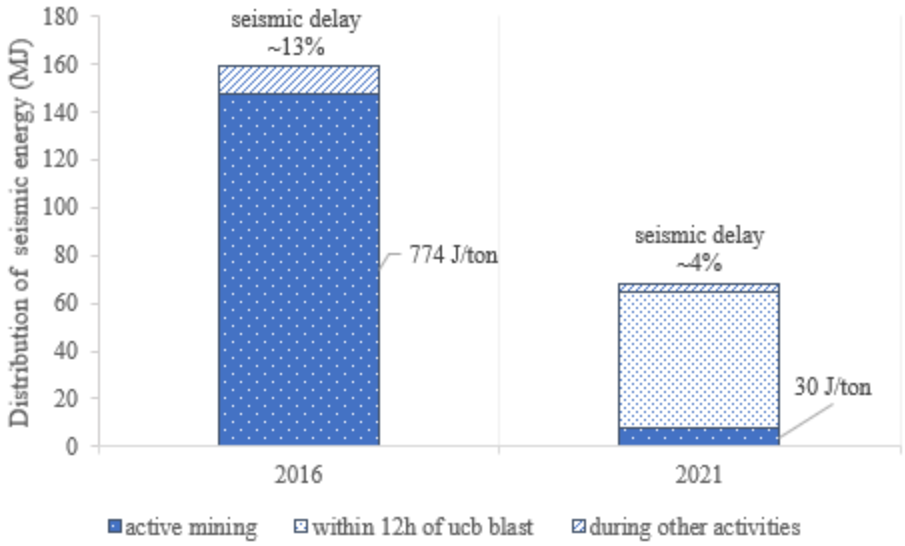


Figure 5.14: Distribution of the annual seismic energy release in active 30-Vein stopes, comparing the last year of LFUL mining (2016) with one complete year of UCB (2021)

A typical seismic delay employed at the mine consists of a 12-hour standdown period where the labor force is held out from the seismically active stope. Seismic exclusions successfully reduce risk by limiting personnel exposure (Hudyma et al., 2017). Since transitioning into the UCB mining method, seismic delays have reduced from 13% to 4% annually. To account for a small uncertainty in large event occurrences for UCB (*Figure 5.10*), a mandatory 12-hour exclusion period is enforced in the stope after each UCB blast. Since, in any given stope, a UCB blast is done about every 2 months, the 12-hour exclusion accounts for ~4% mining downtime. However, two blasts typically occur per day on any given LFUL stope, imposing a similar exclusion period would result in an uneconomic mining method.

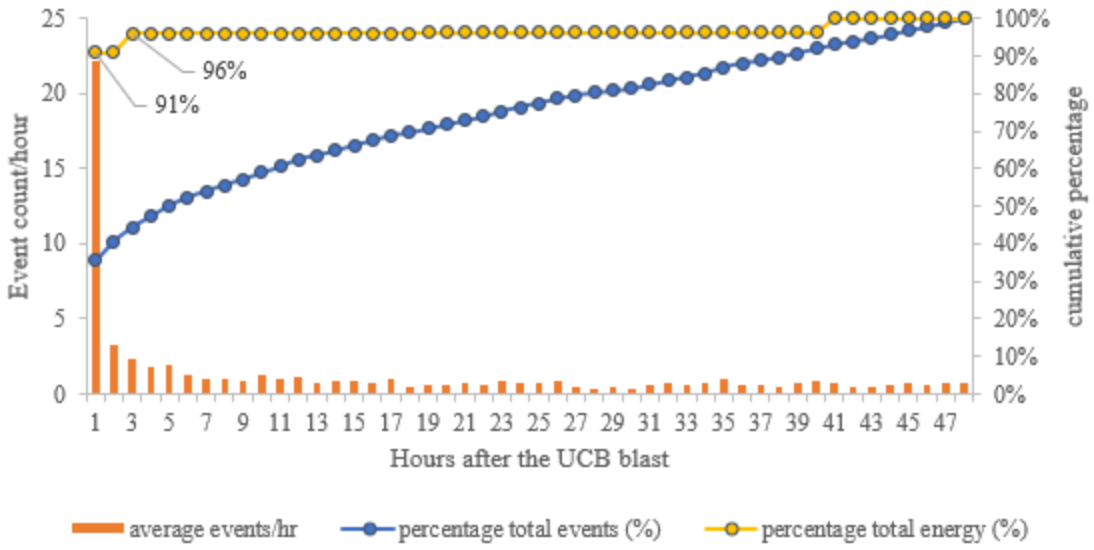


Figure 5.15: Omori chart for energy release captured in 48h following UCB blasts (n=31)

5.3 Mechanisms Affecting Seismic Response

5.3.1 Investigating the Mechanism of Seismic Control in UCB

The mechanism offering seismic control with the UCB mining method is investigated. The elastic block-based FF-model was used to examine a specific UCB extraction sequence in 15 Stope. The modeled seismic source mechanism assumes a fault-slip type response. The induced stresses caused by incremental volumetric changes imposed by the mining sequence were superimposed onto the unspecified DFN centroids. The Excess Shear Stress procedure for initiating slip identified favourable fault structure (FFS) orientations, tracking new fault slip onsets as they occur per mining step. The ESS analysis was further examined by validating the slip region of the FFS by assessing its slip extent. The FFS defines the structure's orientation, the DFN catalog attributes the fracture size (L_s). The total slip extent was computed on 3-dimensional discs representing the induced fractures. The moment magnitude (M_w) of each structure was calculated from the resulting static stress drop ($\Delta\tau$) and the fracture size was approximated from the total slipped region calculated from the slipped area. The generated seismic event locates at the FFS centroid marker, indicating movement onset. The simulated UCB seismic response was then compared against: (***i***) actual seismic records obtained from the

UCB blasts, and (***ii***) measured against a simulated LFUL extraction sequence. This section develops on the numerical procedure outlined in **Section 4.3.3** and presents the findings.

5.3.1.1 Modelling Procedure for Simulating a Seismic Response

Ryder's (1987) Excess Shear Stress serves as the basis for this analysis. Unspecified DFN centroids are tested for slip initiation at each mining step of the numerical modelling process (described in more detail below). Slip is initiated when the driving active stresses are beaten, meaning $ESS_S \geq 0.0$ MPa (Salamon, 1993). The fracture set displaying the largest slip initiation potential at the DFN centroid is tagged in the numerical data catalog for the specific mining step. The output catalogs are then compared between mining step interval querying for new fault-slip occurrences. The previously developed procedure (*Figure 4.33*) has been utilized to determine the favourable fracture set (FFS) that initiate maximum slip at the centroid marker.

Once the FFS have been identified, a numerical scheme was developed to generate point clouds over the initiated FFS centroids matching their specified orientation and fracture radius. The faults are represented by planar discs commonly used in fault-slip analysis (Wiles, 2014). This process sets the point cloud density at one point per square meter (1 point/m^2) over the surface area. Past studies have assumed sparser spacings tagging fault boundaries (vertices & edge centers) with intermediate points leading toward the centroid (Cao et al., 2018). The complete set of point clouds were reintegrated into the grid-based model as calculation nodes (x-y-z coordinates). The sequenced FF-element model is then rerun, compiling the stress tensor on the point cloud markers acting as the three-dimensional structures. Slip potential is verified at each point along the fault when it has reached its initiated mining step. The total slipped area is estimated from the positive ESS values derived from the original formulation (Board, 1994), meaning $ESS_D \geq 0.0$ MPa. This procedure is summarised in the following flowchart (*Figure 5.16*).

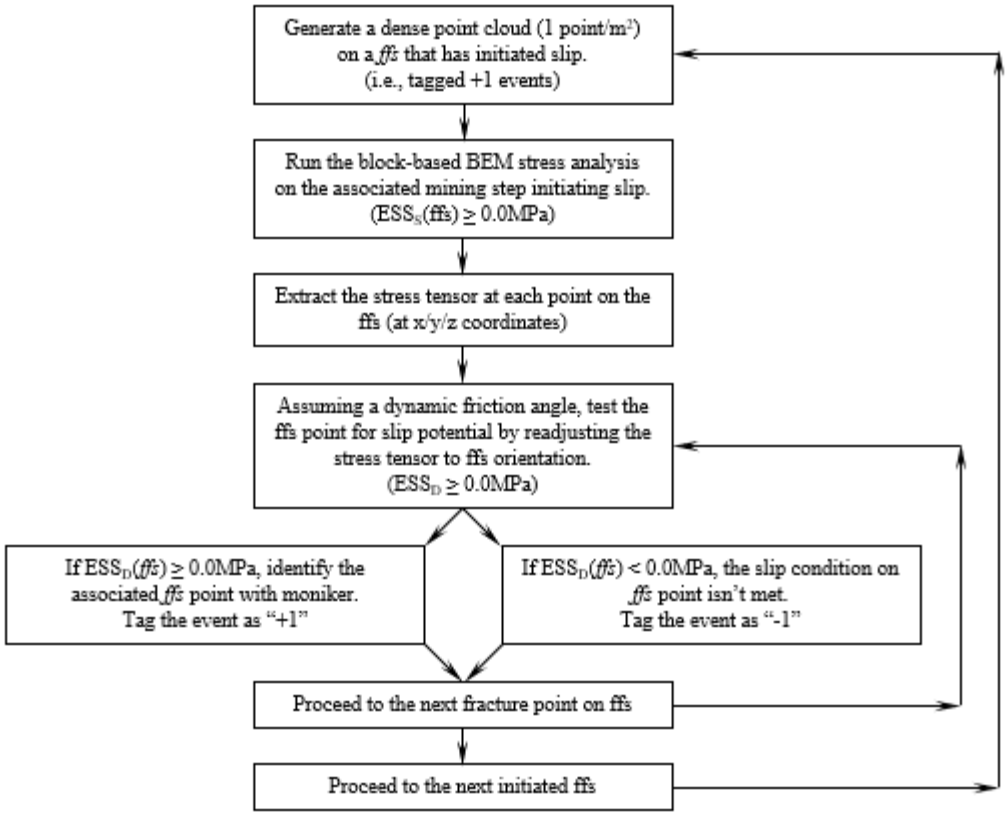


Figure 5.16: Modelling flow chart for ESS_D analysis

Recall that the modeled faults have already indicated shear movement, indicating that there is at minimum a slip extent close at the disc center. Therefore, the stress tensor at each point cloud marker is rotated to fit the preferred fracture set orientation through standard stress transformation processes (Timoshenko & Goodier, 1970). The shear and normal stress components acting on a plane are then compared to a Mohr-Coulomb slip condition to determine if dynamic shear failure is possible. For clarity, the ESS formulations are herein reiterated:

$$\tau_s = C + \sigma_n \cdot tan(\varphi_s) \quad 5.1$$

$$\tau_d = \sigma_n \cdot tan(\varphi_d) \quad 5.2$$

The slip initiation criteria (ESS_S) is onset at the centroid of the structure for the following condition (Salamon, 1993):

$$ESS_S = \tau_a - \tau_s \quad 5.3$$

$$ESS_S \geq 0.0\ MPa \quad 5.4$$

The slip region (ESS_D) is approximated from the point cloud for the following condition (Ryder, 1987):

$$ESS_D = \tau_a - \tau_d \quad 5.5$$

$$ESS_D \geq 0.0\ MPa \quad 5.6$$

where: ESS_D = ESS determined from the dynamic frictional strength [MPa]

The following frictional properties were assumed in the model:

$\varphi_s = 25°$

$\varphi_d = 20°$

Cohesion = 0.0 MPa

The dynamic friction angle is set to 80% of its static counterpart ($\varphi_d = 20°$), reflecting the lower bound ratio found in the literature (Byerlee, 1978). These frictional properties were derived from mine-wide calibration efforts (Chapter 4).

The area of positive ESS_D on the fault surface is then used, along with the static stress drop ($\Delta\tau$) to estimate the seismic moment (M_o) by the method of Hedley *et al.* (1985). A site-specific scaling relationship between seismic moment (M_o) and moment magnitude (M_w) was used to estimate M_w. The following formulae resume the process:

$$M_o = \frac{8(1-v)}{3\left(1-\frac{v}{2}\right)} \cdot \Delta\tau \cdot {L_s}^3 \quad 5.7$$

$$M_w = \frac{2}{3} \cdot \log(M_o) - 6.01 \quad 5.8$$

where: $\Delta\tau$ = static stress drop computed at centroid [Pa]
L_s = equivalent circular slip radius [m]
M_o = seismic moment [N·m]
M_w = moment magnitude [1]

The seismic magnitude estimate is determined from the static stress drop generated at the initiation point (center of the structure) and the equivalent slip radius is derived from the total

slipped area on the fault. The area of positive ESS_d on the fault surface accounts for the slip. The equivalent circular slip radius (Ls) is determined from the following formulation:

$$Ls = \sqrt{\frac{A_t}{\pi}} \tag{5.9}$$

where: A_t = Cumulative slipped area on the point cloud [m^2]

L_s = Equivalent circular slip radius [m]

5.3.1.2 A Case Study of UCB in 15 Stope

The block-based (FF-element) model was reconstructed to match the geometrical changes imposed by an actual UCB production sequence in 645-15-03 (15 Stope), which occurred in late 2020 (*Figure 5.17*). The faint line (running vertically along 30-Vein) indicates the section line further reference in the study This cut incurred two UCB shots, destressing the west and east portion of the cut. To simulate UCB mining, the lower cuts were extracted from the model in one mining step. This is equivalent to extracting three (3.048 m high) cuts as the original drill design called for ~10 m holes. Both UCB blasts were modeled as one through the described extraction method. The blast energy was ignored in the simulation, assumed to be consumed during ore fragmentation and the thrown into the above drill cut. However, the simulated fragmented ore was softened entirely so as not to cause back-pressures inhibiting stope boundary closure. This assumption fits reasonably well with the field observations where the restored UCB drill sills registered over 0.16–0.23 m of relative (post-blast) wall-to-wall convergence (Board et al., 2023). These in-field observations match previous in-stope measurements taken in traditional LFUL cuts (Raffaldi et al., 2019).

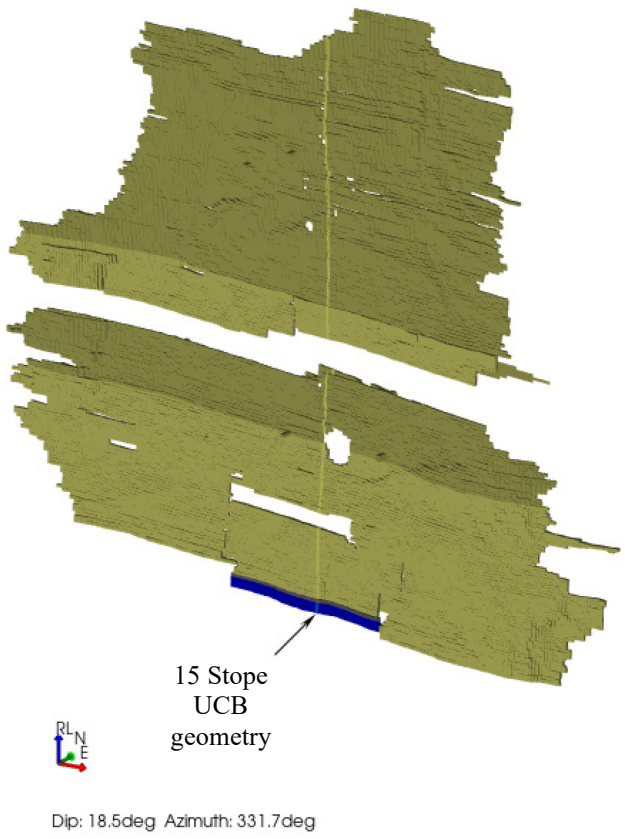
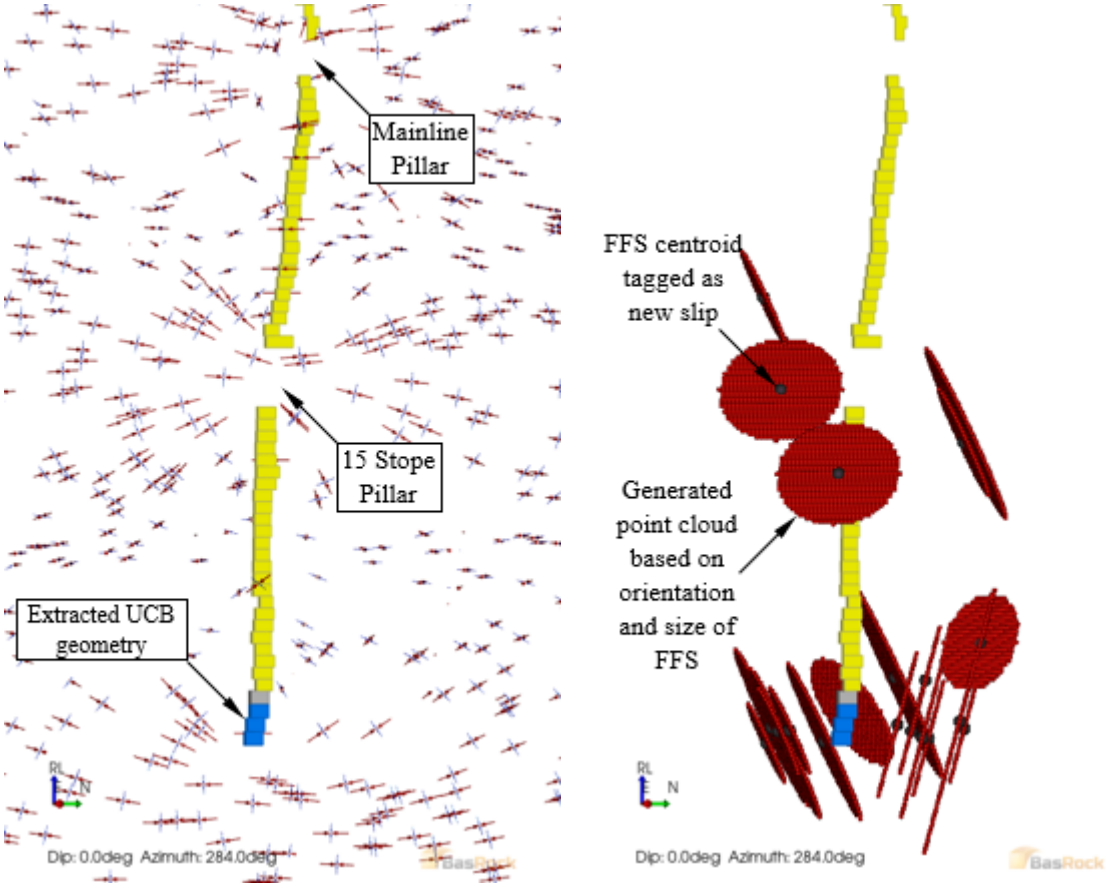


Figure 5.17: Modeled UCB geometry utilizing the block-based (FF-element) BEM in 15S

The undefined DFN catalog (accounting for more than 75,000+ centroids) was integrated into the numerical model via computational nodes (*Figure 5.18*). Each DFN centroid registers the stress tensor induced by mining up to the drill cut (in gray), extracting the drill cut, and the subsequent UCB cuts (in blue). The principal stress vectors resulting from the final UCB extraction sequence are illustrated on a cross-section through 15 Stope (*Figure 5.18*a). For each mining step, these stresses were superimposed on the unspecified-DFN centroids. These hold three possible outcomes after running the complete model sequence and tested for slip initiation, where the centroid either: (***i***) remained stable at the final extraction point (i.e., no slip), (***ii***) slipped during a mining step leading to the drill cut extraction (i.e., previously slipped), or (***iii***) initiated slip during the UCB extraction sequence (i.e., new slip). The processed computational nodes were queried for new fault slips incurred by the final mining step. These were isolated for further processing, where the favourable fracture set were assessed for each initiated centroid and the

fracture size assigned from the DFN catalog. Once the geometries were attributed, the three-dimensional point cloud series were constructed for all tagged FFS exhibiting new slip onset during UCB extraction (*Figure 5.18*b).

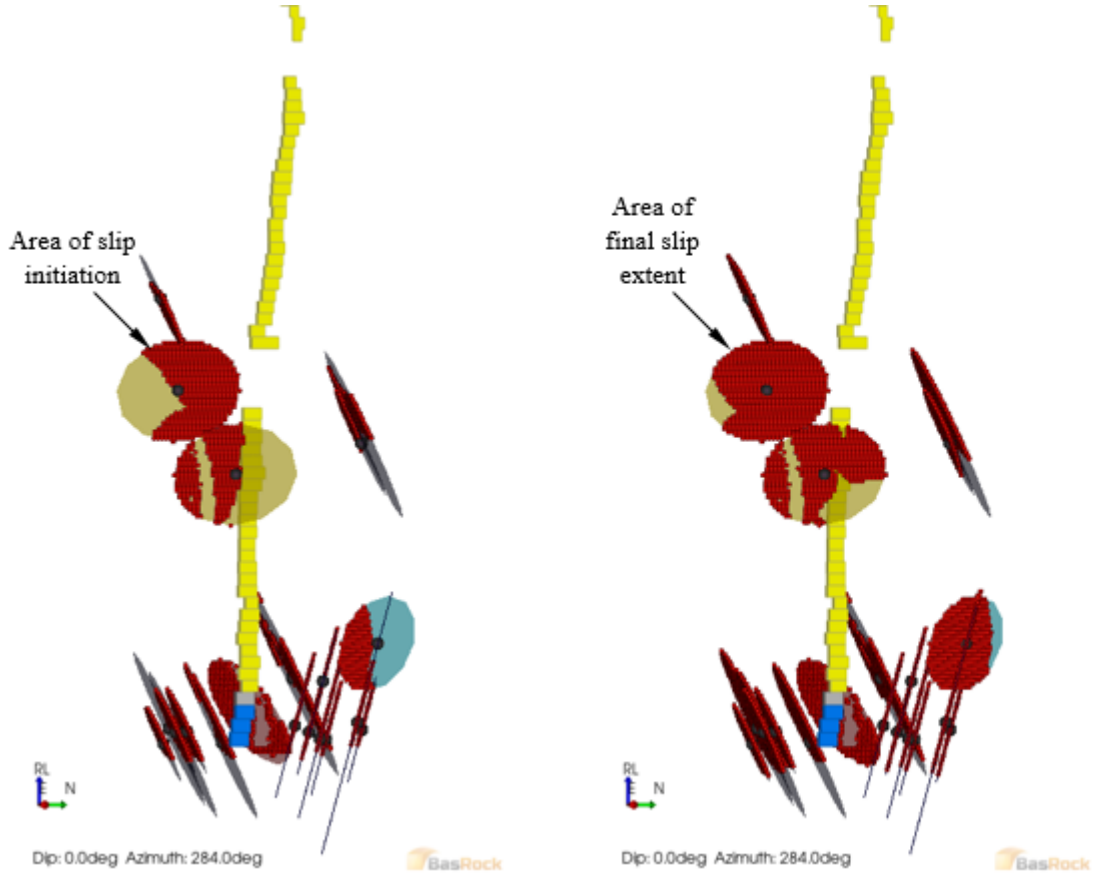


(a) (b)

Figure 5.18: Cross section through 15S showing the (a) major (red) and minor (blue) principal stress vectors induced after extracting the UCB geometry, and (b) construct of slipped structures

The slip behavior of the related UCB fault slip events is plotted below (*Figure 5.19*). The ESS_S and ESS_D procedures were applied on individual FFS. These plots differentiate between the slip onset and the slip extent characteristics. As can be seen, the slip onset, illustrated by the red area indicating $ESS_S \geq 0.0$ MPa in *Figure 5.19a*, extends and touches the centroid of the FFS, indicating slip initiation. The slip extent progresses further outwards on the disc plane (marked by the red area indicating $ESS_D \geq 0.0$ MPa in *Figure 5.19b*. The total slip efficiency, defined as the ratio of the total fault area over the slipped area, can be computed for the final state. On

average, the UCB seismic events present a seismic slip efficiency (slipped area over total digitized surface area) of ~0.8.



(a) (b)

Figure 5.19: Cross section through 15S showing the simulated UCB events for (a) slip initiation, and (b) slip extent

The seismic source parameters for simulated UCB events were computed from the computed results (*Figure 5.20*). These estimates provide event magnitude positioned over the FFS centroid. The actual seismic events (> +0.5 M_w) recorded during the UCB blasts in 15S overlay the resulting simulated events. The observed and simulated UCB events locate in proximity of the mining front as well as in the remnant pillars well behind the leading edge. It was found that faults dipping at moderate angles toward the stope show significant seismic potential. These seismically active structures group to fault families FS2-FS7 and FS6-FS8 in the south-wall and north-wall of 30-Vein, respectively. The 15S Pillar shows a preference for fault orientation as well. The location and magnitude range of modeled slip events compare reasonably well

between simulated and recorded events for the UCB blast, where 23 events with magnitude > +0.5 M_w have been registered by the simulation (ranging from +0.44 M_w to +1.74 M_w), with 7 events located in remnant pillars, as compared with 15 recorded events with magnitude > +0.5 M_w induced by the UCB blasts (ranging from +0.50 M_w to +1.96 M_w), with one (1) recorded event locating in the remnant pillar. Finally, the seismic energy release is 2.66 MJ simulated against 8.18 MJ recorded.

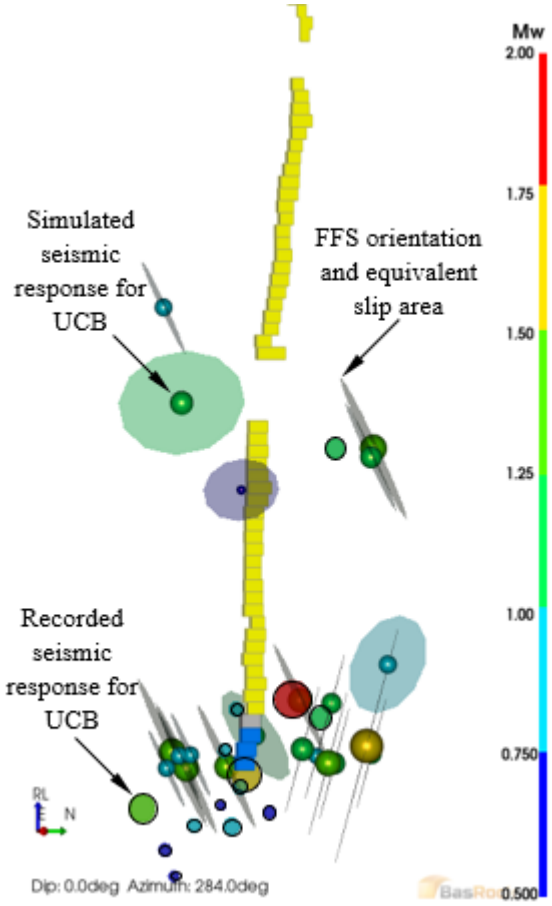


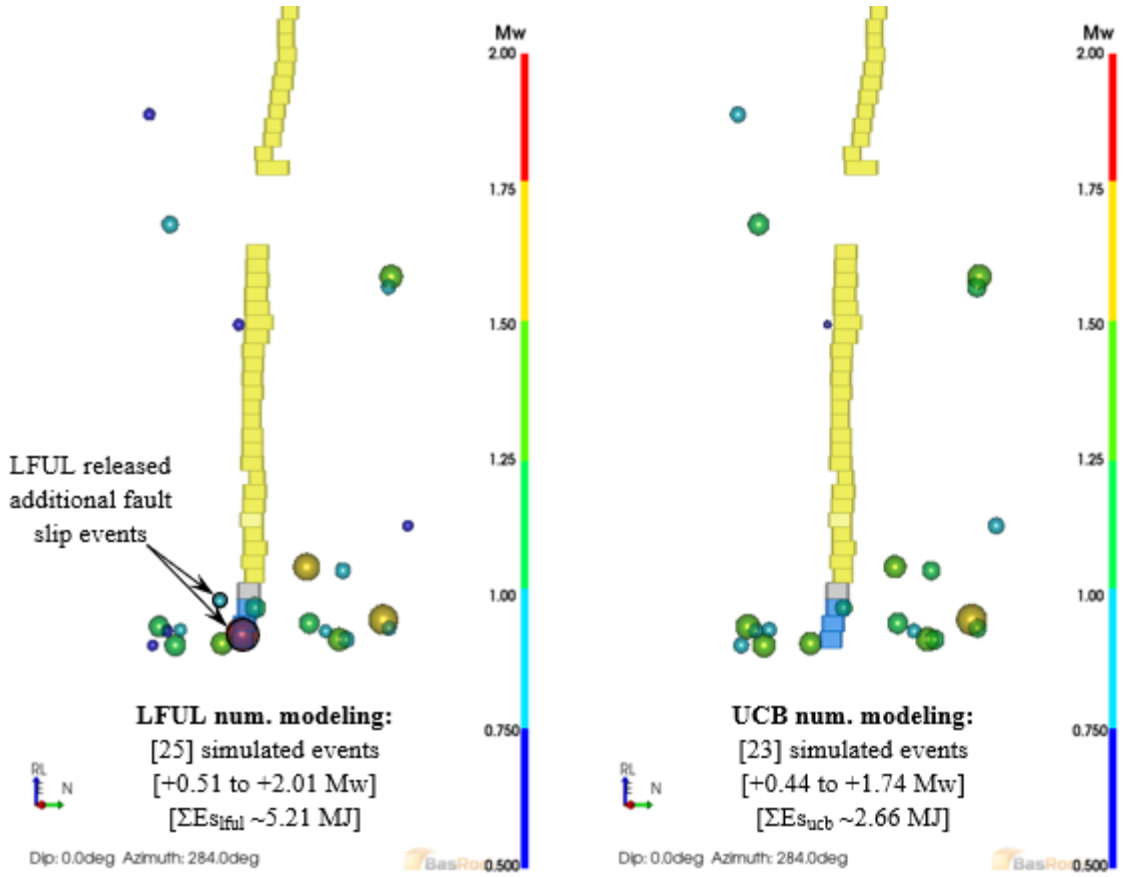
Figure 5.20: Cross section through 15S showing the simulated fault slip events vs recorded notable seismic response of UCB projected onto the section

The comparison of simulated to recorded events suggests that the UCB extraction provides sufficient mined volume to result in stress changes around the mining front. UCB extracts an equivalent of ~1/6 of the vein's total strike length, sufficient to induce slip on most of the DFN-simulated favourable fault sets close to the stope. Based on the calibrated friction angles, north-dipping (FS-2 & FS-7) and south-dipping (FS-6 & FS-8) fault structures prefer to slip in the hangingwall (southwall) and the footwall (north-wall) of the 30-Vein mining front. Recorded

seismicity indicates that all this energy release occurs within hours of the UCB blast, followed by a quiescent period until the new structures near the mining front are mobilized with the next blast. Additionally, highly stressed portions of some faults cutting through the vein floor (FS-2 or FS-6) may be extracted by the blast, thus preventing them from further energy release. Finally, the stress wave accompanying the blast does not appear to affect the fault slip onset.

5.3.1.3 Reduction in Energy Release (LFUL vs UCB)

To investigate the observed reduction in cumulative seismic output by UCB, the block-based (FF-element) model was sequenced for successive cuts extraction using the LFUL method. The incremental mining advance of the LFUL was simplified by extracting the complete cuts in succession equivalent to the UCB volume. The same fault slip initiation and slip extent processes were utilized to compare seismic response between methods (*Figure 5.21*). Overall, the LFUL sequence triggered slip on comparable near-stope wall structures while generating two (2) additional events adjacent to or in advance of the cut. The incremental mining process of single-cut extraction in LFUL produced greater magnitude ranges with a higher cumulative energy output almost double of that cumulated for UCB. However, the most significant impact of UCB appears to be extraction of faults in the immediate floor of the stope where the mining-induced stresses are highest, and slip produces the largest energy releases with the most significant potential for damage to stope via floor heave.



(a) (b)

Figure 5.21: Cross section through 15 Stope showing simulated seismic response for (a) LFUL, and (b) UCB

To investigate the impact of mining-induced stress change on faults between the two mining methods, the BEM model was flexed further to determine the influence of the stress path at the initiation point of common faults located in the stope wall of the stope. The change in shear and normal stress at an FFS centroid was extracted for both LFUL and UCB as the extraction sequence progressed (*Figure 5.22*). The stress paths show the position of peak shear stress on the simulated fault surface and its relation to the slip condition on the fault. The initial stress state (prior to mining) is the same for both methods until the mining face approaches the fault location, causing normal confinement to increase. The UCB mining stress state arrives at the static slip condition at lower shear and normal stress, consequently producing a lower stress drop and, overall, lower seismic energy release. This results from the large zone of decompression (relaxation) around the stope walls immediately after the UCB is shot (pushing the stresses into

the floor). In contrast, the LFUL, with its smaller mining advance, triggers the fault in the immediate wall to slip at higher shear and normal stress, consequently producing higher static stress drops and, thus, larger seismic energy release.

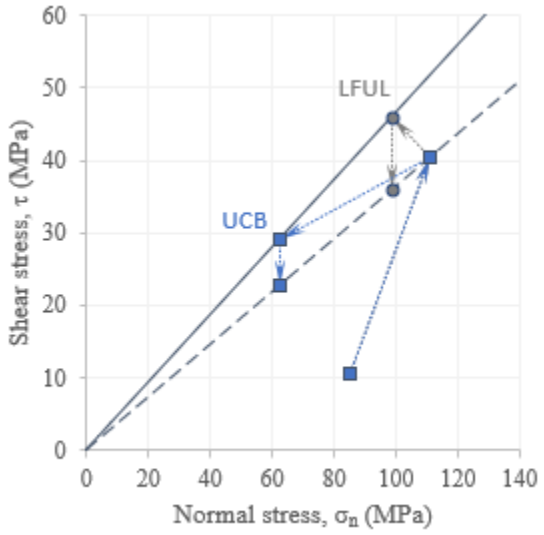


Figure 5.22: Stress path of a near stope fault slip triggered by LFUL, and induced by UCB

Both mining methods indicate similar slip efficiency ratios of ~0.7. However, the seismic source size measured by the mine-wide seismic system indicates that notable events to have higher slip radii for the LFUL method (*Figure 5.23*). These mechanisms add further confidence in explaining the discrepancy in seismic energy release observed in-field between both mining methods.

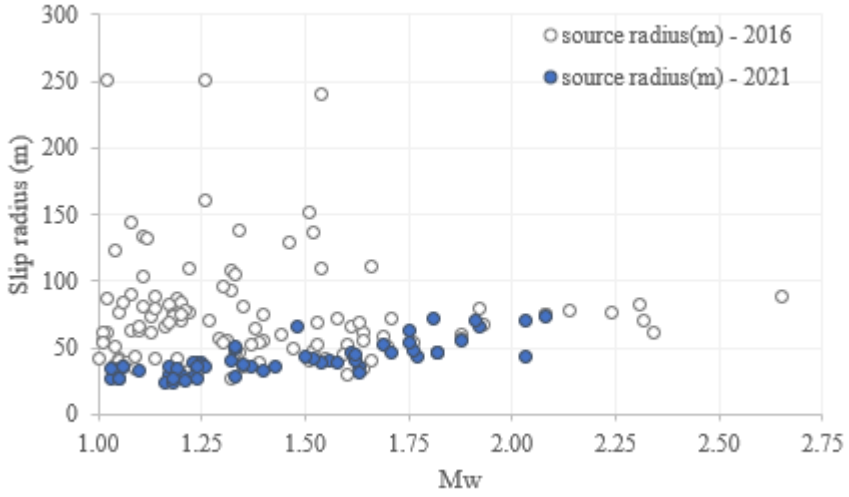


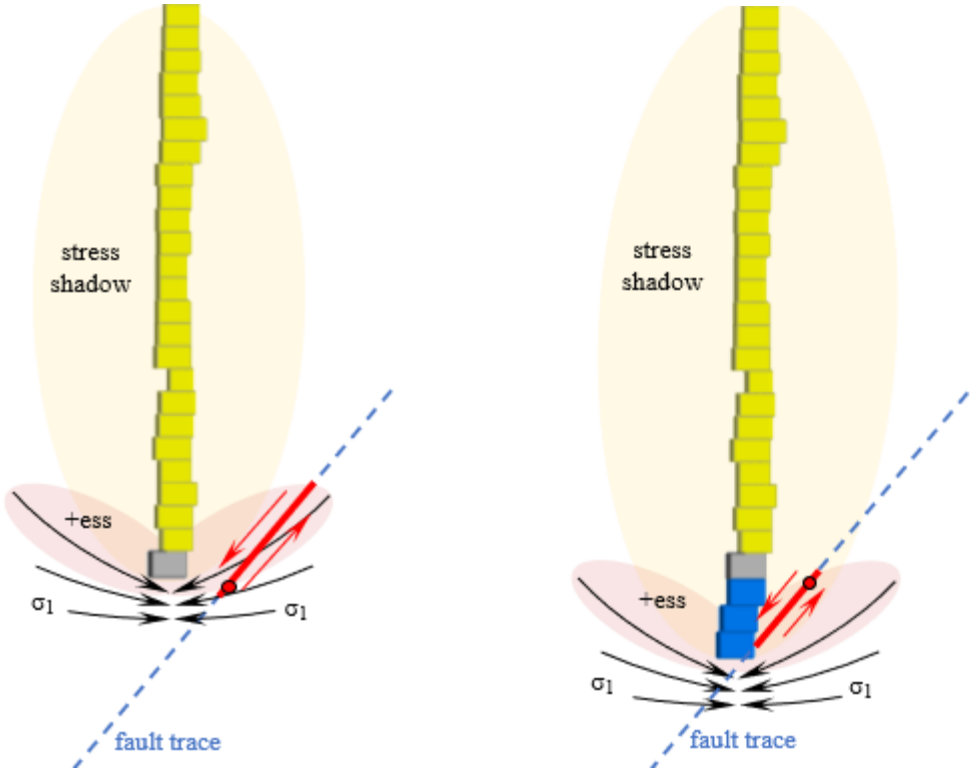
Figure 5.23: Slip radii obtained from the ESG seismic system, 2016 and 2021

Based on the seismic observations and the modelling results, seismic control through UCB appears to be the result of two main mechanisms (*Figure 5.24*):

1. The large UCB (destress) blast fragments the floor rock, potentially extracting critically oriented faults in the ore directly beneath the incoming mining front. These faults transect the zone of greatest stress concentration in advance of the face. The incremental advance of the LFUL face over them would have typically triggered these fault slip responses (reflected in events with larger slip areas). The fragmented-swelled ore that fills the UCB stope immediately after blasting provides the additional benefit of reinforcing the stope walls with a back-pressure. Thus, the damage to the stope from seismic events induced by the blast is minimized.
2. The deep vertical extent of the blasting zone causes an immediate stress redistribution around the stope bottom, stress-shadowing the stope walls at the drill cut level. This reduces the normal stresses on the faults in the vicinity of the stope floor, pushing the zone of higher stresses below the UCB floor.

Based on these observations, seismic control via the UCB method relies on:

1. Ensuring a sufficient drill-and-blast depth into the stope floor to either extract or induce slip on the structures around the immediate stope walls within the production shot.
2. Successfully fragmenting the rock volume below the stope floor, which preconditions the stope walls over a large strike length of the mining front, lowering the influence of the critical stress path on structures. This is opposite to the incremental mining method that progressively loads stresses onto faults, slowly bringing them to a critical state in which slip could trigger at an unknown time.
3. Conforming to a continuous mining front to ensure that the change of potential energy in the stope vicinity can occur unobstructed. Unmined geometries produce remnant pillar configurations that trigger time-dependent energy releases – these events are less likely to be induced by a UCB blast.



(a) (b)

Figure 5.24: Concept of near stope fault slip response for (a) LFUL, and (b) UCB method

5.3.2 Seismic Release Mechanism in Pillars

Investigating the simulated UCB events located in remnant pillars reveals that these events were triggered due to the progressing stress changes within those geometries caused by the global extraction on the 30-Vein (*Figure 5.25*). Therefore, a significant amount of volume on the main vein needs to get mined out before the critical stress state on a through-going structure creeps to its slip limit. The stress changes incurred by LFUL or UCB mining methods need to be significant in order to trigger a single large event response in those pillars. Hence, fault slip pillar events will continue to trigger independent of the mining method. However, the magnitude of the stress transfer to the remnant pillars will decrease as the mining front extends deeper into the rockmass, caused by an increased geometrical distance between the active face and the remnant. Therefore, it is possible that the frequency of large pillar events will decrease in consequence.

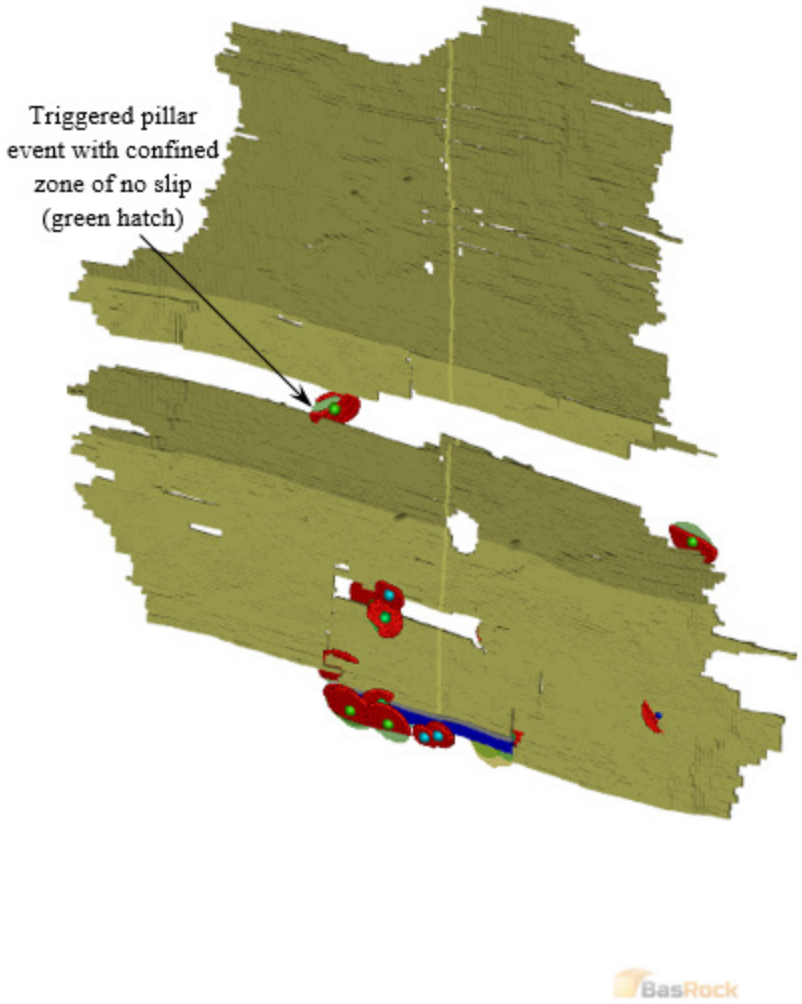


Figure 5.25: Triggered pillar events from the UCB analysis

The pillar events attributed to fault slip on structures are conceptualized below for an increasing mining depth (*Figure 5.26*). As previously examined, the pillar's core presents a zone of high confinement restraining slip to run through it, for all structure orientations until the trigger point has been reached (*Figure 5.26*a). As the mining front progressively increases (say after an annual production period), the incremental stress changes compounded around the remnant pillar configuration. Consequently, the confined pillar halo decreased allowing slip to trigger on the initiation point of the structure (*Figure 5.26*b). The unclamping of the trigger point is potentially achieved under a higher normal confinement, consequently generating a higher static stress drop with increased rupture velocity (Madariaga, 1976). The mobilized structure rapidly expands into the previously locked slip region. The final slip length may overshoot the ESS slip length due to increased rupture velocity, extending the slip region into the footwall of the stope.

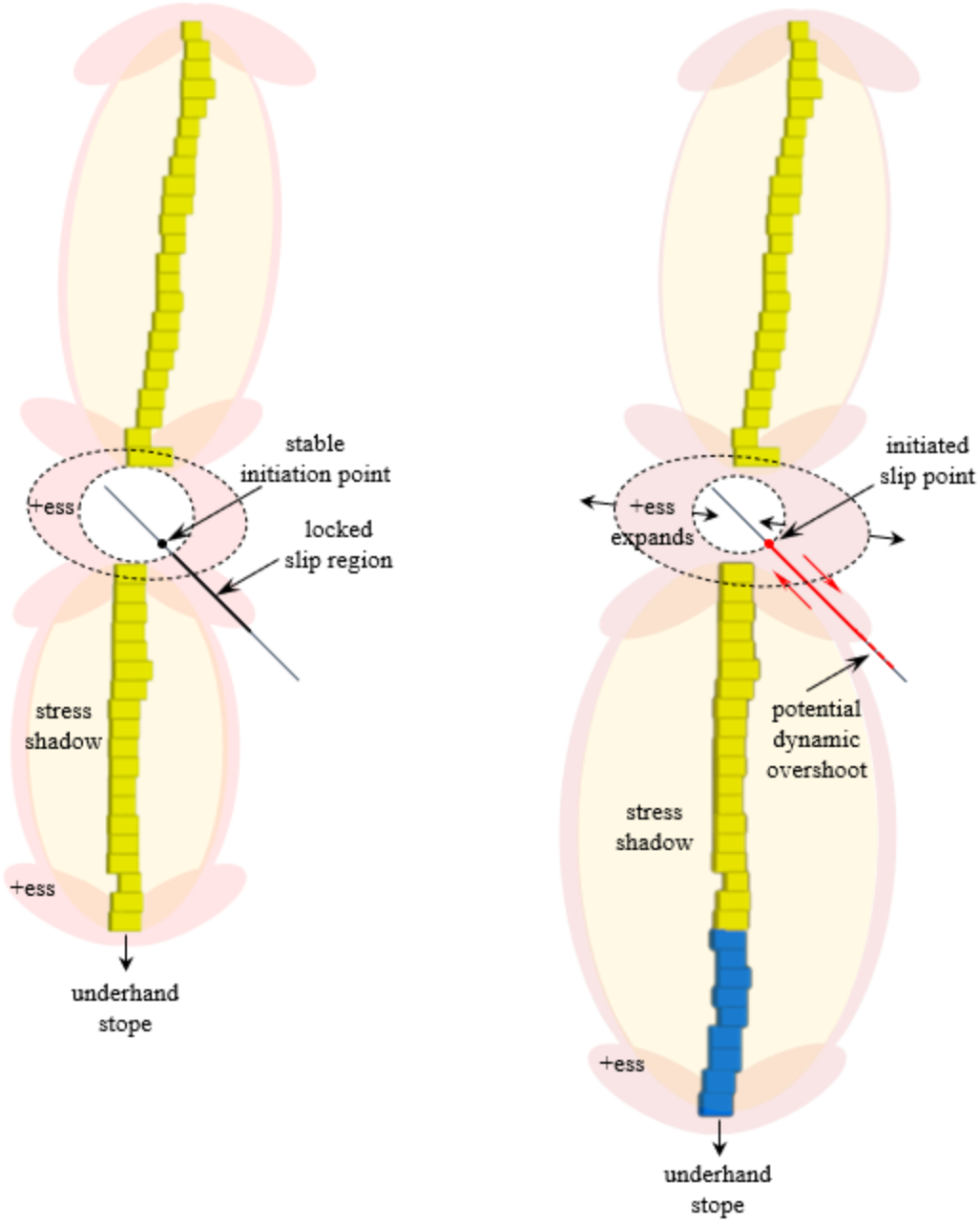


Figure 5.26: Concept of fault slip response in proximity of pillar where (a) presents a stable structure, while (b) shows the structure to have triggered due to increased mining depth

These fault slip pillar events exhibit high static stress drops with potentially lower slip radii restricted by the confined pillar core, similar to stick-slip ruptures along rough surfaces (Harbord

et al., 2017). For narrow continuous tabular mines, there are also other types of pillar failure mechanisms documented in literature such as foundation failures induced by squat pillar configurations (Jager et Ryder, 1999). The fault slip source mechanism was attributed to 50% of recorded notable events (> +0.5 M_w) in the GH, increasing to 70% for larger (> +2 M_w) events. It is therefore possible that both mechanisms exist within the GH remnant pillar configurations.

5.4 Forecasting Seismicity as Mining Progresses

5.4.1 Tracking Magnitude-Time-Location

To address seismic risk on a daily basis, long-term planning has to be complemented by short-term seismic forecasts to provide a likelihood of an event occurring within an active mining front. These evaluations are often derived from daily changes in seismicity at the mine. Large-scale magnitude events pose the greatest risk to an operation, especially when occurring on shift. Spottiswoode (2010) posed two key statements, which need to be true, in order to systematically forecast for large event occurrences:

1. There must be an apparent change in event rate or event characteristic before large events.
2. The observed change in event rate or event characteristic differs from the numerous smaller events.

Several techniques exist within the mining industry to forecast large events based on routine seismic monitoring of (primary or secondary) source parameters, such as the Cumulative Apparent Volume (Mendecki, 1993) or the Energy Index (van Aswegen & Butler, 1993). These techniques are often cited as short-term seismic hazard indicators where past seismic events, leading to large events, are scrutinized within a discrete volume and time window for apparent triggering patterns. This process requires several back-analysis iterations to adequately calibrate a method for reliable warning of new event occurrences. Short-term seismic hazard indicators have produced mixed results in the industry as these have resulted in as many successful alerts as false positives (Nordström et al., 2020; Spottiswoode, 2010). Their merit, however, revolves around inferring rockmass behavioral trends for daily, routine assessments (Simser et al., 2015; Dehn et al., 2018).

Another source *trigger* for inducing seismic response arises during or after operational blasts (Whyatt et al., 2002). At the Gold Hunter, the LFUL method has demonstrated that ~70% of events occur ~2.5 hours after the blast (between shifts), while with the UCB ~90% of the events are released during the same period. Hedley (1992) argues that the explosives contribute little to stimulate seismic release, rather it is the change in the mine geometry, which forces stress to redistribution within the rockmass leading to the events. Therefore, continuously extracted narrow tabular mines, of South Africa and Coeur D'Alene, appear more sensitive to stress change (hence blasting).

Examining the blast impact in terms of radiated energy response instead of event occurrence reveals another picture. Utilizing 15 Stope as a case study, a plot of cumulative seismic energy release in relation to the transition toward UCB mining is assembled (*Figure 5.27*). The dotted line represents the cumulative seismic energy as captured by the seismic system within the stope boundary (from mid-2020 to January 2022). The mining progression of consecutive cuts is draped atop the cumulative energy release line, which (the blue line) represents a normalized advance of a cut in 15 Stope (i.e., each integer interval represents the extraction of a physical cut, from start to completion). UCB blasts (xs') and seismic events (circles) greater than +1 M_w are illustrated by markers. The seismic events are referenced to match the mining advance. The jumps in the cumulative energy plot are apparent in the figure. These relate to the release of large energetic events producing a stair-stepped appearance (recall that one increase in magnitude integer produces 32 times more energy). The step increase occurs most often with UCB blasts while mining progresses under a quasi-seismic quiescent period. Therefore, the radiated energy release follows a relatively linear trendline highlighting the relationship between UCB blasts and seismic energy release. Although not guaranteed, as some UCB blasts have released seismic events with low energy outputs (see cut 7 in the figure), the cumulative energy plot of the stope appears to want to catch up to the expected energy level. The radiated energy release rate follows a constant trend line (~1.635 MJ/cut) for UCB mining in 15 Stope over 8 cuts (> 1 year). The Cut-0 (yellow hatched area in the figure) represents the transition from LFUL to the UCB method. Notice the sporadic release of seismic events during the advance of that transition cut, clearly illustrating the seismic characterization of the underhand cut-and-fill method.

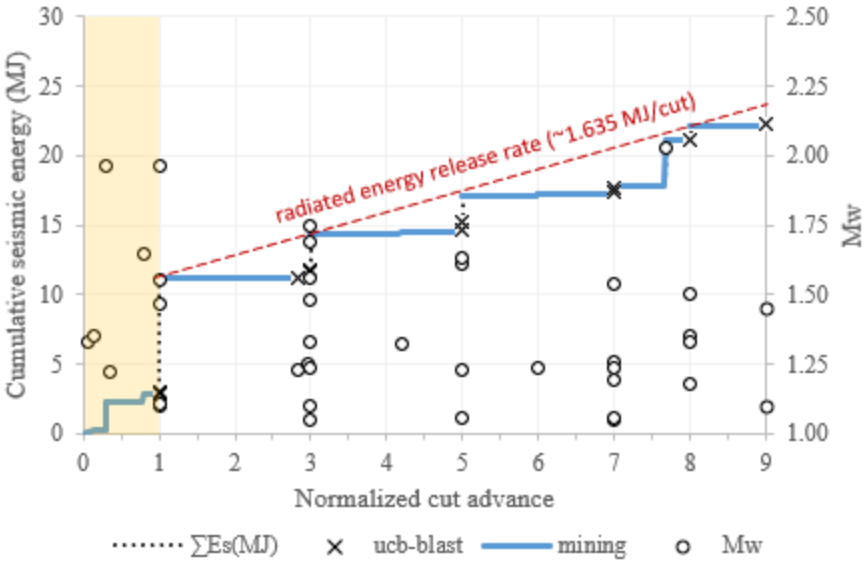


Figure 5.27: Cumulative seismic energy release as a function of advancing the cuts in 15S, mining period set between July 2020 and December 2021

An energy *deficiency* develops between the recorded energy output and the trendline, where radiated seismicity eventually catches up to the expected energy state for the stope volume. This is clearly observed while mining Cut 7 where the UCB blast conducted to destress the mining front induced several notable events with low radiated energy outputs. Consequently, an event of +2 M_w occurred in 15S Pillar while mining the destressed cut. Upon completing the cut, the energy released by the subsequent UCB blast further caught up to the expected energy trendline.

Spottiswoode *et al.* (2008) reported similar trends for South African mines, where the radiated seismic release follows a near-linear release with the mining area. Previously, Brink (1984) has successfully used the cumulative energy (and event count) per time in selected areas, at Western Deep Level Mine in South Africa, to delineate burst-prone structures.

The short-term seismic hazard can be related to a magnitude estimate through the scalar relationship between E_s-M_w derived from the seismic data. First, the relationship between seismic energy and moment is presented for the period in 15 Stope (*Figure 5.28*). The E_s-M_o relationship for 15 Stope during the mining period is:

$$log(Es) = 1.24 \cdot log(Mo) - 8.59 \qquad 5.10$$

Note that E_s is expressed in Joules [J] and M_o in Newton-meter [N·m]. This expression is derived for the same dataset (in 15 Stope) using the quantile-quantile (QQ) plot, which provides a better fit to the highest-density zones (Harris & Wesseloo, 2015).

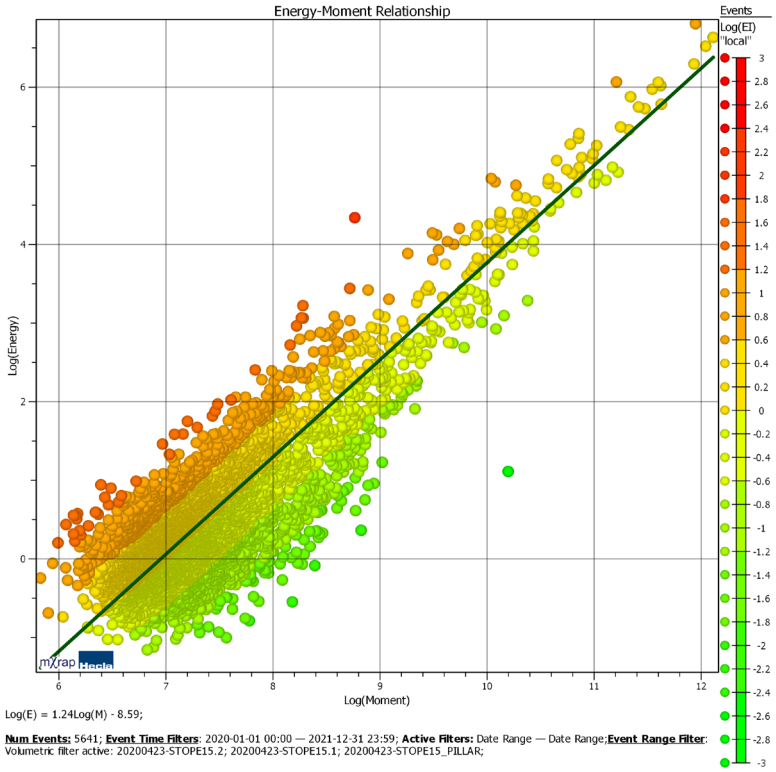


Figure 5.28: Seismic energy – seismic moment relationship in 15S, 2020–2021

Substituting the seismic moment (M_o) by the moment magnitude (M_w), utilizing Hank & Kanamori's (1979) scaling formulation (eq. 5.8), the following local energy-magnitude relationship appears:

$$M_w = \frac{\log(E_s) - 2.59}{1.86} \qquad 5.11$$

From this point, the accumulating energy deficiency, as defined by the difference between the trendline and the cumulative seismic release, is now readily evaluable for magnitude, time, and location within the stope boundary of 15 Stope.

5.4.2 Procedures & Applications

The Energy Buildup procedure, presenting the logic for forecasting radiated energy release as it is being captured by the seismic system, has been summarized below (*Figure 5.29*).

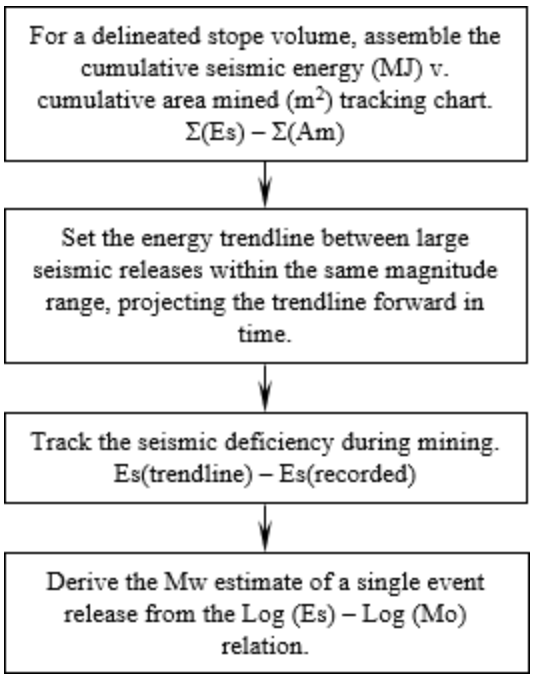


Figure 5.29: Flow chart of the Energy Buildup procedure

The seismic energy forecast procedure was back-calculated against the energy recorded during UCB blasts in 15 Stope. The trend line was set at the energy peaks of Cut 1 and 3. The energy deficiency, as observed before the UCB blasts, was estimated for the drill cut and compared to actual seismic recording post-blast (< 24 hours). In addition, a single equivalent magnitude value was determined for the actual and the forecast energy releases. The results are summarized in the table below.

Table 5.2: Comparison of forecast to recorded seismic energy release in 15 Stope

Mining cut	Energy induced by UCB (MJ)	Energy Deficiency (MJ)	Error	Equiv. M_w released	Forecast M_w	Error
3	3.24	3.24	0%	2.11	2.11	0%
5	2.44	3.09	-21%	2.04	2.10	-3%
7	0.43	3.61	-88%	1.63	2.13	-23%
8	0.69	1.50	-54%	1.75	1.93	-9%
9	0.18	2.00	-91%	1.43	2.00	-28%

Note that cut 3 was used as the anchor point for setting the trend line from cut 1. The overall errors for the subsequent cuts (5–9) indicate that the energy release and equivalent magnitude forecasts were overestimated. However, two (2) out of the four (4) cuts present reasonable

magnitude estimates with no significant energy release while mining the destressed rockmass. This method allows to track of the seismic hazard per individual stope volumes as well as that of the total mine.

The cumulative energy release with respect to the mining area was assembled for the Gold Hunter between 2013 and 2021 (*Figure 5.30*). The Energy Buildup procedure was applied to the total mine dataset with adjusted seismic relations. Two forecasting trendlines were set for the entire database. It is noted that one large (mine scale type) event flooded the energy tracking system. This event had an equivalent energy-magnitude release of +3.1 M_w, resulting in the significant jump on the energy plot (~308 MJ). Prior to that event, the large-magnitude releases were in the +2 to +2.79 M_w range. Inherently, each increase in magnitude release produces 32 times more radiated energy. Therefore, these large mine scale events can disrupt the Energy Buildup tracking scheme. However, each magnitude range set can be independently evaluated. The 2021 end of year energy deficit forecasts +2.91 M_w.

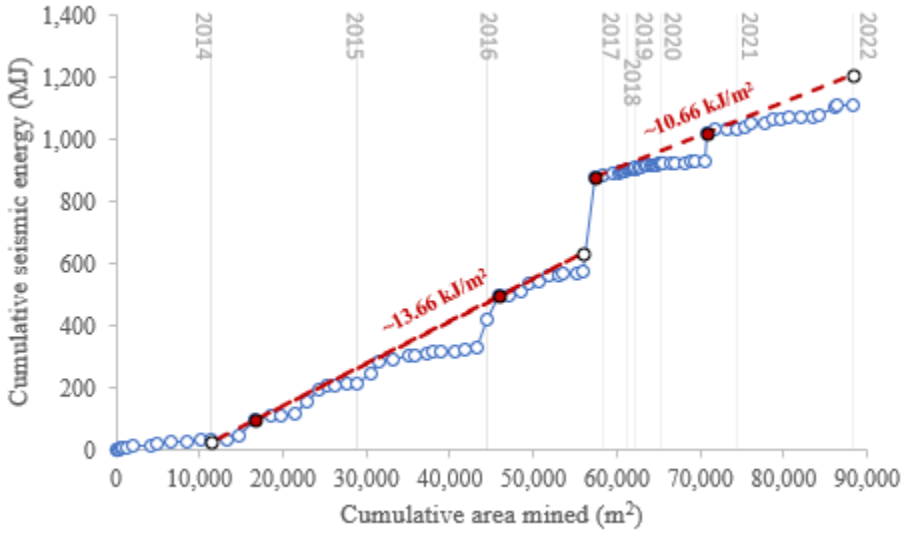


Figure 5.30: Conceptual tracking of energy build-up for Gold Hunter

The GRMF relation provides estimates for the number of events expected to release within a magnitude range before inducing the next integer magnitude increase (McGarr, 1984). This type of forecast seems to better apply to tabular than bulk-type mines due to smaller variations in mining rates and geometry over the life of mine (Hedley, 1992). Keeping track of the sum of released smaller events, since the last major occurrence, can provide a probability of triggering

the next major event. The GRMF plot for the Gold Hunter is assembled (*Figure 5.31*). Utilizing the b-value (~0.9) and having kept track of the smaller event released (+2 M_w) post 2017 indicates that the probability of inducing the forecast equivalent +2.91 M_w event is 63% for the GH at year end 2021.

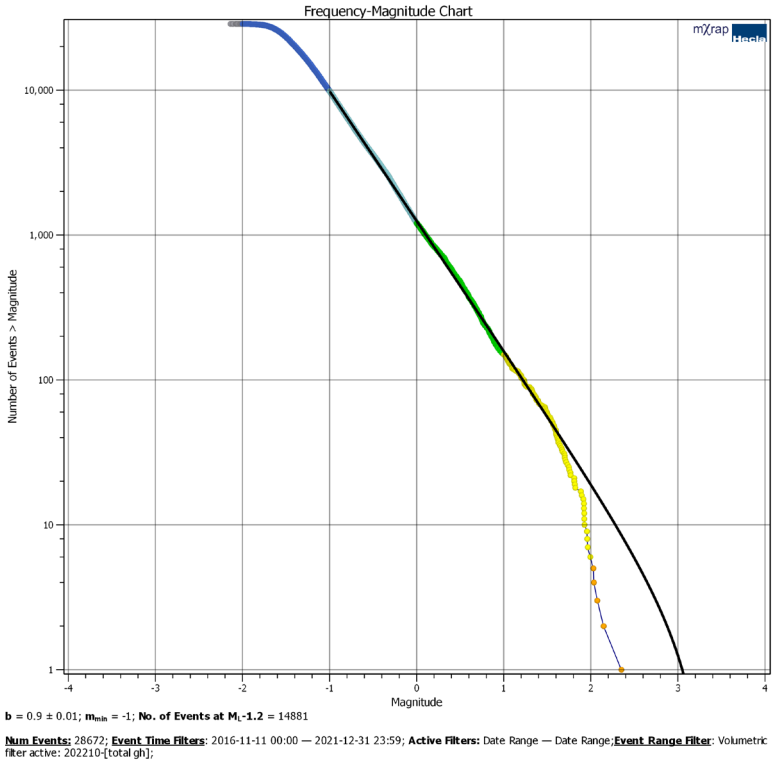


Figure 5.31: GRMF for the GH between 2016-11-11 and 2021-12-31

5.4.3 Discussion on Forecasting Seismic Energy Release

It is generally accepted that there is no reliable technique for predicting seismic occurrences at mines. The effective management of seismic hazards relies on understanding the seismic characteristic of magnitude release, time of occurrence, and affected location(s). However, a fair forecast provides valuable insight, allowing engineers and operations to plan contingencies. Hence, numerical modelling (intended for design) complemented with short-term and daily seismic assessment is the most reliable process for evaluating seismic hazard (Spottiswoode, 2010).

The Energy Buildup procedure tracks the cumulative seismic energy release with respect to mining area. As was observed in the case example above, there is a strong correlation between these two parameters (Spottiswoode et al., 2008).

The radiated seismic energy is a primary source parameter calculated from the waveform, often characterizing the intensity an event. The seismic energy controls high-frequency radiation and drives strong ground motion (Mendecki, 2013). Therefore, seismic energy relates better to the damage potential outside the source volume. As was seen in the past figures, small seismic events contribute very little to the cumulative seismic energy release. Most significant jumps occur from large events (> +1.5 M_w). Seismic energy can vary for the same event magnitude release.

Radiated seismic energy, as measured by the digital seismic system, is produced by the elastic strain wave released from the hypocenter of a seismic event (Gibowicz & Kijko, 1994). The total energy is computed from the primary and the secondary wave components. Several physical parameters (in the medium) can affect the resulting seismic waves energy. Brittle failures tend to release more energy due to higher static stress drops. Similarly, much more seismic energy is released in shear than in tensile failures (Gale, et al., 2001). A slow rupture and slip velocity radiate less seismic energy (Mendecki, 2013). An increase in source size decreases the predominant frequencies of the seismic wave. In contrast, increased rock strength, elasticity, and stress increase the co-seismic deformation rate, inherently increasing the amplitude of the released seismic wave (hence higher energy). Waves transitioning from hard to soft ground will slow down (low frequency) while seeing an increase in amplitude. Low frequencies decay slower.

Continuously extracted tabular mines, such as those found in South Africa and in Coeur D'Alene, appear more sensitive to mining geometry changes (Hedley, 1992). Seismic occurrences relate closely to the advancing mining front, as well as in remnant pillars. Particularly in the Coeur D'Alene mining district, a strong correlation exists between the production blasts and the onset of seismicity, which follows with or shortly after blasting (Whyatt et al., 2002). Greater lag time (between a blast and seismic response) arise for fault-related events.

This can be tracked with this procedure. Several trendlines can also be set per stope.

5.5 Chapter Summary

Chapter 5 presented the application of the seismic design charts to subsequent mining periods (after 2016). The chapter illustrated the challenges that arose when forecasting seismic occurrences. The subsequent studied periods were observed to be operated under different mining conditions, possibly affecting the rockmass response. Two subsequent mining periods were reassessed for seismic hazards.

Most notably, it was postulated that a new mining method (UCB) implemented in the 30-Vein (between 2020 and 2021) has changed the rockmass response. This idea was tested through a numerical analysis where a complete UCB blast cycle was modelled in the block-based (FF-element) model containing the DFN catalog. Assuming the newly developed procedure for identifying favourable structures to initiate slip, seismicity was simulated and compared to recorded events captured during UCB. Good agreement was obtained in proximity at the face and pillars, providing confidence in the proposed modelling technique. The comparison to the LFUL method followed, where the UCB model was repurposed for incremental mining by extracting individual cuts up to the total mined-out shape. The LFUL simulation produced a different fault slip response near the mining face, while pillar events remained indifferent to the change in mining technique.

The mine-induced seismic response is variable. Therefore, a cumulative energy per mined area was proposed to track the potential seismic hazards as mining progresses.

The analyses performed in this chapter resulted in the following conclusions:

1. Two (2) subsequent mining periods were examined, which deviated significantly from traditional LFUL settings. The first production interval (2017–2019) consists of a general slow-down of mining that lasted ~3 years, averaging to ~120 tons per day. The second interval (2020–2021) encompasses the commissioning of a new mining method (UCB) across the lower 30-Vein stopes, averaging to ~690 tons per day for the period. The mining rates fall within 15% and 86% of that typically executed for LFUL daily production (~790 tons per day). In addition, the mining depth increased by ~48 m on the lower 30-Vein stopes over those two mining periods.
2. These two (2) subsequent periods were analyzed for annual ERR and were compared to the forecasting ERR design charts (derived in the previous chapter). The modelled trendline was observed to overestimate the seismic event release potential for both subsequent mining periods (RMSE +0.822). The largest induced events in the abutments and pillars stayed below those recorded during the 2014–2016 period.

3. Analysis of the forecasted kinetic energy release per subsequent mining period was compared with actual seismic records. The results show that the model significantly overpredicts seismic output (E_s/ton). The seismic response appears to have changed for the subsequent periods when compared to the LFUL (between 2014 and 2016). The b-value (which continues to indicate slip potential for subsequent mining periods) has significantly steepened and reduced the overall size of large events, capping below +2.5 M_w while exceeding this size for the traditional LFUL method. For the mining UCB period, the release of large events (> +1 M_w) within 2 hours following a production blast has increased from 58% to 88% in 15S. The relative positions of notable events (> + 0.5 M_w) stayed about the same, occurring on average ~28 m from the stope profile and extending up to 100 m into the abutments.
4. For the UCB mining period, the 2021 production year accounts for the complete implementation of the new method across the lower 30-Vein stopes, which has increased extraction by roughly 40% compared to the 2016 LFUL production. Yet, the seismic energy release rate was lower for 2021 at ~250 J/ton mine compared to 833 J/ton in 2016. Further investigation into the energy release distribution per planned activity type has identified that UCB exhibits lower seismic energy release during active mining periods (when miners actively remove material from the stope). UCB resulted in ~30 J/ton released during active mining in 2021 compared to ~774 J/ton LFUL in 2016. Most recorded seismic releases (~85%) occurred within hours following the production blast. Seismic stand-downs for re-entry into the stopes, which restricts access to the stoping area for one shift (12 hours), have decreased from 13% to 4% of the total production time since implementing UCB.
5. A UCB mining sequence in 15S was implemented into the calibrated block-based (FF-element) model. Following the procedure derived for unspecified-DFN, ffs meeting the positive ESS_S criterion were identified and isolated for further analysis. The complete slip extent on each ffs structure has been assessed (positive ESS_D) by rerunning the model with constructed 3D surfaces (assuming 1 point/m^2) corresponding to the ffs orientations. As previously observed, FS2-FS7 and FS6-FS8 continue to show preferred slip potential in the south-wall and north-wall of 30-Vein, and the average total slip efficiency was ~0.8. The simulated seismic events compared reasonably well with actual recorded data taken from UCB blasts in 15S, falling within the maximum magnitude range and locating in proximity of the stope. The UCB model triggered additional pillar events (in 15S Pillar and 5,700 Pillar).
6. The model was rerun for an LFUL simulation, where each cut was extracted in sequence for the same mining volume. It was found that the incremental mining method induced additional events and provided increased magnitude estimates (+2.01 M_w maximum event) when compared to the UCB extraction (+1.74 M_w maximum event). The seismic energy output by the LFUL simulation was ~96% larger than that output by the UCB simulation. This analysis suggests that faults behave differently between the methods. The UCB method tends to induce faults to slip, potentially under lower normal confinement offered by the deep destress blast. In contrast, the LFUL tends to trigger faults to slip by slowly allowing stresses to build until they reach the critical state and release.

7. It was concluded that the seismic control via the UCB method relies on several factors, which include sufficient destress length and depth, successful fragmentation of the ore and the continuity of the vein system. Time-dependent energy releases in pillar configuration were unaffected by the simulated mining method and will most likely continue to occur.
8. Developed a model and procedure for forecasting fault-slip seismicity at the stoping and mine-wide level.

CHAPTER 6 CONCLUSION, CONTRIBUTIONS AND RECOMMENDATIONS

6.1 Summary & Limitations

Mining was initiated on the 30-Vein of the Gold Hunter in 1997 through narrow cut-and-fill stopes utilizing incremental production advances assured by conventional drill-and-blast methods. The vein has a significant strike length of over 600 m (as well as a continuous dip), requiring the body to be split into several staggered mining horizons. The abutting stopes can develop considerable strike lengths (>200+ m each). Overhand and underhand mining directions were first established on the vein. Operations remove the ore from the vein in horizontal cuts, with certain stopes leading the others on mining depth. Due to proximity, active headings on separate advancing cuts were constrained from converging toward one another when mining is within 45 m. A single stope advances to securely mine out the gap while the other cut remains static. This procedure manages the formation of end-line (dip) and horizontal sill (strike) pillars. The interaction between active cuts stays limited, allowing seismic occurrences to be attributed to the effect of the leading stope. Due to an increased abutment area, it was recognized that converging mining fronts (i.e., two leading longwall edges) present a higher seismic risk for an overhand operation. To prevent their development, the underhand direction was adopted exclusively on the 30-Vein since 2013, mining downward on the vein. The 30-Vein is analogous to extending a slit (or a crack) where most seismic incidences are located in stope abutments where the stresses are the largest (e.g., below the floor cut or in neighbouring pillars). The average mining depth reached ~2.27 km below the ground surface at the year-end of 2016, bequeathing this study with detailed engineering layouts, tonnages, and robust seismic records since mining started in the GH.

As the Lucky Friday mine continues its inchmeal descent towards the ultra-depth marker (defined as mining depth > 2.7 km), stresses will increase in the advancing fronts and remnant abutments. The main driver behind the seismic review of previously (documented) production periods was to extract (benchmark) sound engineering guidance, which will help forecast seismic hazards at increasing depth on the 30-Vein. The idea for the assessment was to link past (spatial-temporal) seismic records associated with mine changes and production tonnages to derive a site-specific

empirical design chart and the primary source mechanism. Two specific mining periods were selected for the benchmark: (***i***) 1997–2011, and (***ii***) 2013–2016. This notion isn't new in literature; however, the mining potential offered by a single leading vein system under relatively low extraction rates (~800 tons/day) allows a better study of stress transfers and their effects on seismic occurrences.

Therefore, the Gold Hunter's tabular mine geometry offers a unique opportunity to study the sector's onset and persistence of mine-induced seismicity. This thesis considers that recorded seismicity results from stress changes induced by mining, causing failures within the rockmass (Cook, 1963a). Therefore, historical stope layouts, production tonnages, and seismic occurrences were collected and combined to derive the seismic source mechanism through deterministic failure processes – primarily through the ERR and ESS.

Large seismic events ($M_w > +2.5$) in the Coeur D'Alene mining district have been well connected with fault slip failures (Whyatt et al., 2002). Specifically, at the historical LF deposit, events as large as +4 M_L have occurred (Blake & Hedley, 2003). However, notable events (> +0.5 M_w) have also been attributed to local and related structures, including bedding planes (Board, 1994). Therefore, the present study assumes that seismic events have a deterministic source mechanism, but the faults appear randomly. This study revolves around notable events in the GH, where it was assumed that at least 50% of all recorded notable events present a shear-slip response. This hypothesis was confirmed through simple elastic numerical modelling, utilizing the ESS in a BEM code, where 61% of all recorded notable events have shown fault-slip potential (for $\varphi_s = 25°$), accounting for 64% of the seismic energy released in the GH between 2013 and 2016.

The following sections summarize the findings while highlighting the limitations of applied analyses.

6.1.1 Seismicity at the Lucky Friday Mine (Chapter 3)

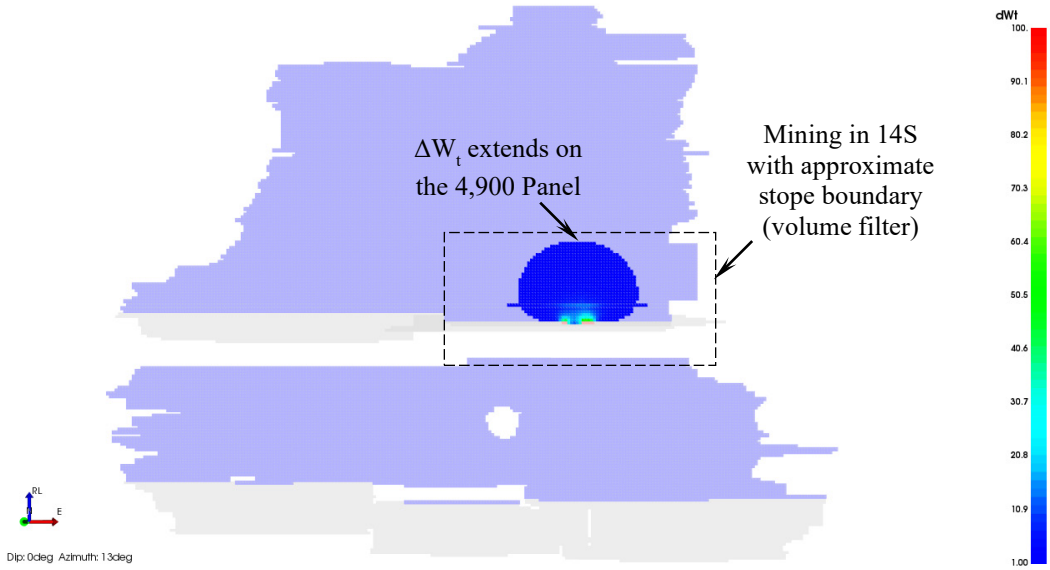
Chapter 3 covers the mining context at the Lucky Friday mine, with attention set on the current mining horizons of the Gold Hunter deposit. Underhand production layouts for mining the (main) 30-Vein were provided. The GH sits in the Wallace formation, characterized by softer, vertically oriented, thinly-bedded argillites to siltites with increasing quartzite and siderite mineralogy closer to the vein packets. The GH sector is bounded by major fault sets and

populated by several secondary-related fracture sets. Rock mechanics properties were provided, including lab-scale strength measurements and in-situ stress estimates done in the LF deposit. The rockmass response to mining a tabular deposit was investigated through numerical modelling (BEM), confirming analytical responses. Normal stresses and displacements were computed in the abutments and provided in-stope closure estimates. This numerical model served as the baseline for subsequent modelling.

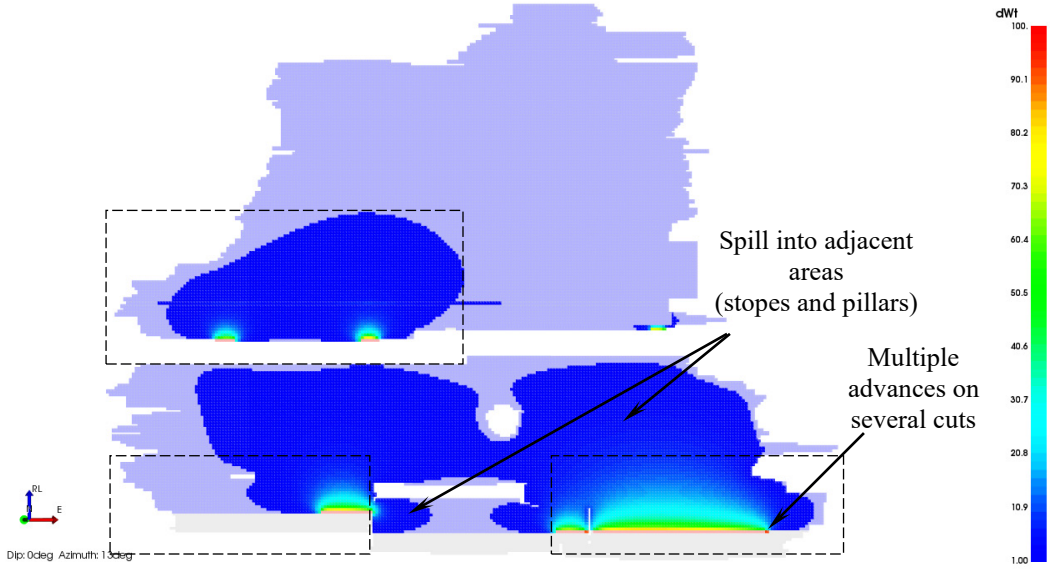
Furthermore, a seismic review investigated the magnitude-time-location (MTL) relationship with mining. Based on established contiguous zoning filters encompassing individual mining areas, seismicity was assessed per stope and globally for the GH sector during the mining period 2013–2016. Although seismic occurrences were captured during 1997–2011, the quality of the source parameters in the first mining period was less accurate. Several mining factors affecting the seismic output were investigated, such as dependencies on the mining rate, production blasts, seismic energy release over time, and remnant pillar configurations. Finally, empirical comparisons were made to South African practice, where striking correlations emerged, solidifying that deep, narrow tabular mines are comparable and most seismically active.

6.1.1.1 Limitations

The major limitation related to the seismic assessment of stopes revolves around determining the correct volume filter applied over the stoping area, which captures events related to ore mining. All seismic events occurring within a seismogenic zone are assumed to be related to that specific stope activity (*Figure 3.20*). These fixed volume filters were designed to group the seismicity within their respective stoping geometries, supporting the causation leading up to their manifestation. These volumes extend over the stoping areas, providing significant coverage into the lower and top abutments by several hundreds of meters (Gibowicz, 2009). Since most stopes share an end-line boundary (11S with 14S; 12S with 15S; 15S with 16S), attention was set to avoid overlapping filters in an effort to prevent the potential for double-up on event counts. Therefore, stopes may have triggered events outside their respective filter volume when mining close to those boundaries, spilling events over into the next volume filter (*Figure 6.1*). This is due to the large extent of the change in potential energy (stope closure) induced by the cut extraction. There was no effort to correlate these *spilled* events to their source volume.



(a)



(b)

Figure 6.1: Change in potential energy (ΔW_t) over the mined-out 30-Vein, resulting from extraction in (a) 14S exclusive, and (b) multiple stopes

Linking seismic events in remnant pillars to the exact stoping area presents the same challenge (*Figure 6.2*). The change in potential energy (ΔW_t) induced by multiple active cuts combines to an extent through the entire mining panel, communally affecting pillar responses. This becomes even more challenging for time-dependent seismic responses. Major faults can also disrupt causality in the same way as pillars do. Mine-wide events, termed adjusting events, occur because of the total extraction extent of the vein. These are also time-dependent, arising

randomly in pillars and on major faults. This was most noticeable in 2016 when only the lower 30-vein stopes were advanced, yet significant occurrences continued in the 5,700 pillars. Therefore, breaking the relationship with the provoking stope, yet providing no direct method for linking these back to individual stope blasts.

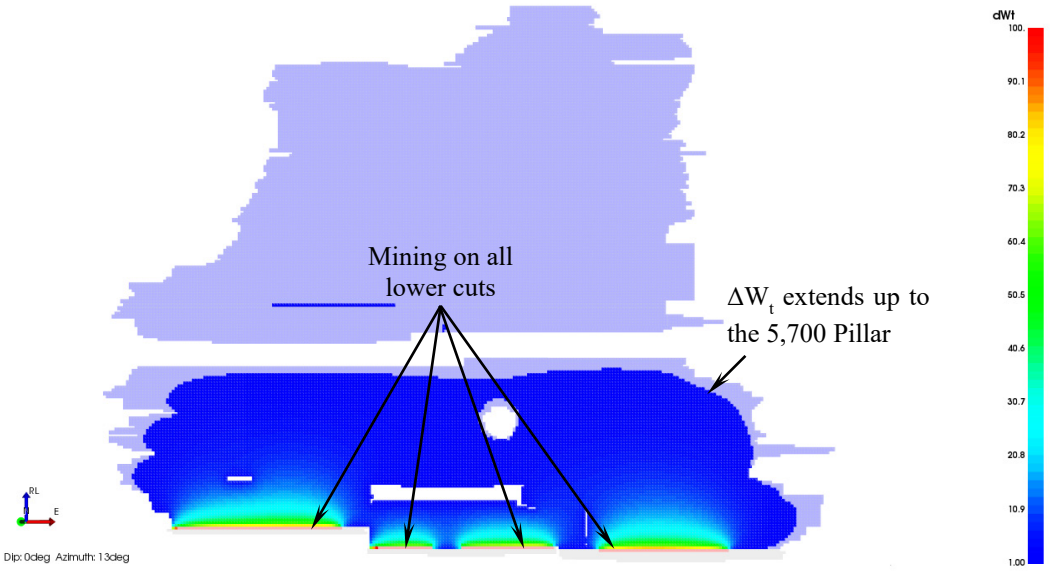


Figure 6.2: Change in potential energy (ΔW_t) over the mined-out 30-Vein, resulting from exclusively extracting the bottom 30-vein stopes

The inherent seismic source location error (± 12 m) is another limitation of this study, as events can easily locate into adjacent stope volumes. This resolution error is significant when comparing simulated events with actual recordings in the proximity of stope faces. Unfortunately, no proven method exists in the literature for improving the error resolution post-processing. This issue has to be tackled through improved sensor array designs and improved velocity models, which account for mine opening (Hudyma, 2010).

However, the global GH (or total mine) volume filter groups all the seismic events across the mine and links them to the global geometrical change occurring on the main 30-Vein. Identifying and delineating noise is also an issue (Woodward et al., 2017). Some noise may have been introduced into this data filter, from development and ore pass, but these present minimal impact on the overall assessment, focusing on notable and large events.

6.1.2 Numerical Assessment of the Seismic Catalog (Chapter 4)

Chapter 4 covers the general BEM model setup for the grid-based (DD-element) and block-based (FF-element) analyses using the MAP3D software. The main numerical modelling assumptions and specifications were presented, selecting the infinite homogeneous elastic medium assumption. The model construct reproduced for the two mining periods, exclusively on the 30-Vein and (part of) the 80-Vein (which provided stress shadowing to the 5,700 Pillar). These two mine-wide constructs reproduced the mining sequence of the GH since mining initiated on the 30-Vein. Model calibration efforts centred around reducing mesh size dependencies (selecting appropriate grid size construct) and matching in-stope closure measurements in 11S and 15S. These were achieved and resulted in defining the elastic mechanical properties for the rockmass, established at $E = 29.4$ GPa and $\upsilon = 0.2$. Following successful calibration, stresses in the abutments and pillars were derived and presented.

The grid-based (DD-element) model was utilized for ERR (Cook et al., 1966) and ESS (Ryder, 1987) analyses, where specific modelling procedures were developed for the mine-wide application. The ERR was determined for the two mining periods and compared to seismic occurrences of notable and large events. Energy balance formulae were derived for the BEM and applied to these two mining periods. Annual seismic efficiency ratios (E_s / W_k) were obtained for global and per-stope settings. The results correlate with South African seismic design charts and practice (COMRO, 1988).

The block-based (FF-element) model was utilized to push the ESS analysis further, allowing an assessment of fault initiation (ESS_S) and the frictional properties. In addition, following the work from DeVoe & Mayer (2017) and Smith (2021), a DFN was constructed (Itasca, 2020) and tested for fault-slip potential in a mine-wide environment. A novel procedure was created which allows the fault sets to *compete* for slip potential, termed the unspecified-DFN. The results (from the traditional DFN and the unspecified-DFN) were compared to recorded seismicity in 15S. Several sensitivity analyses on frictional properties allowed to calibrate these for the Mohr-Coulomb slip criterion and confirmed the fracture size distribution.

6.1.2.1 Limitations

The major limitation related to computing the empirical ERR index is adequately computing the normal stress ahead of the advancing face. The constitutive material assumption of the rockmass, as well as input of backfill material into the model, have been shown to impact the modeled horizontal stress in the abutment. First, South African practice often utilizes numerical processes to limit the stress at the working face (*Figure 6.3*). Three main models exist, namely the (homogeneous) elastic rockmass response, the constant stress cap (crushing) model, and the strength weakening (yielding) model. These constitutive laws were developed to approximate the relaxation of the reef ahead of the face. The output ERR (one-half the product of the stress and the displacement) is significantly reduced for the weakening model, requiring precision calibration efforts (Spottiswoode, 1997). The most common material response is the stress cap model, assuming a stress cap between 240 and 400 MPa (Ryder & Jager, 2002). Due to the intense face yielding observed at the GH at the stope headings (*Figure 3.13*), the most realistic constitutive model would be somewhere between the last two cases (i.e., crushing and yielding). Although average yielding depth estimates were provided, in-situ stress measurements must be collected across all the stopes to provide strength estimates ahead of the face, ideally across several stopes.

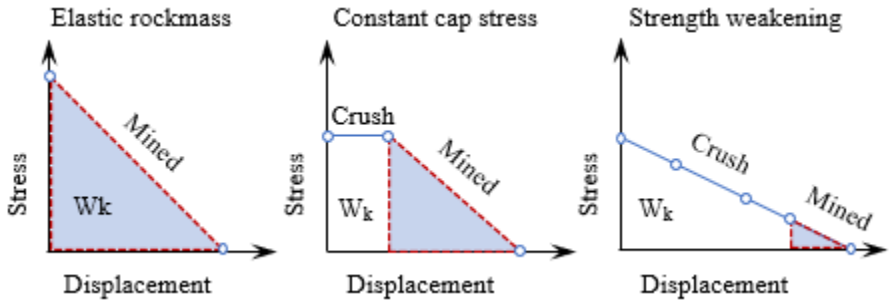


Figure 6.3: Schemes for reducing stress in the mined-out block (a) elastic rockmass assumption, (b) constant cap (crushing) stress assumption, (c) consecutive strength weakening (yielding) assumptions (Spottiswoode et al., 2008)

Second, excluding backfill has an impact on ERR computations. Whyatt et al. (1992) have determined through a parametric study for underhand mining that omitting the backfill model reduces the stress ahead of the face by roughly 10%, impacting up to 9 m ahead of the face.

Furthermore, their model also indicated that excluding backfill altogether increases the ERR by 42% compared to the backfilled case (Whyatt et al., 1992). The latter condition arises from the condition that the ERR, although readily calculated from the mined block, is also intricately tied to the change in potential energy component (ΔW_t) through the energy balance formulations (Salamon, 1984). Cook (1967) realized that half the change in potential energy is equal to the energy release component (W_r) in his original concept of energy balance. This has been validated for the elastic assumptions (Salamon, 1974). Therefore, closures at midspan affect the change in potential energy generated by mining the cut. Whyatt *et al.* (1992) have demonstrated the variation in (half-) closure along the mid-span of the stope between fill assumptions, where the closure at midspan was reduced by ~20% (*Figure 6.4*). Several backfill constitutive models exist, such as the spring approximation (utilized by Whyatt et al., 1992) or the South African hyperbolic function (Ryder et Jager, 2002), which models the strain-hardening response of the backfill material. However, current in-stope paste pressure measurements (Raffaldi et al., 2019) haven't yet reached the onset of strain hardening after deepening the mining front by five cuts (~15.24 m), making backfill calibration inefficient. Therefore, the best assumption at the moment is to keep the more conservative ERR index value without correcting for backfill response.

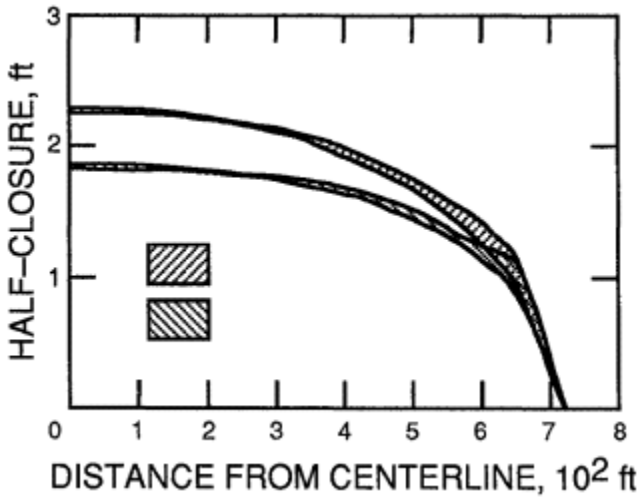
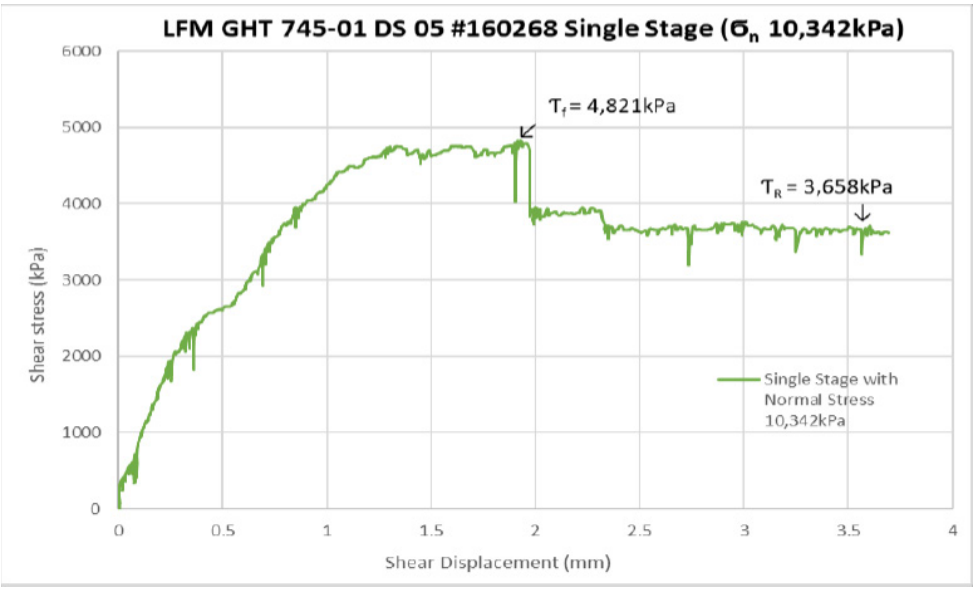


Figure 6.4: Range of half-closures (closure divided by 2) of the stope as a function of distance from the panel midspan, assuming various rockmass properties and fill assumptions (Whyatt et al., 1992)

A third major limitation concerns the validity of the output seismic energy release (E_s) values computed by the mine seismic system. The first study period (1997–2011) relied on a scaling formulation to estimate E_s from the magnitude of an event. For the same dataset, the E_s outputs by the GH scale relationship were lower than those derived from E_s-M relations published in SA (*Figure 4.19*). Therefore, the GH estimate for Es may be lower due to planarity of the seismic array, which is mainly located in the footwall of the 30-Vein, and the high dependence on uniaxial geophones. Since geophones have a physical spring that moves inside the sensor, they are sensitive to the orientation at which the seismic wave hits the sensor (Hudyma, 2010). The E_s-M_w scaling relationship in the GH needs to be further investigated, especially if energy release rates are to be compared with other deposits or mines.

To follow suit, another major limitation related to computing the ESS relies on selecting the appropriate (static and dynamic) frictional properties. Although thorough calibration efforts were developed and compared those results with mine-induced seismicity, the final calibrated estimates for friction were determined to be $\varphi_s = 25°$, $\varphi_d = 20°$ with cohesion set to zero. For planar opened unfilled joints such as those found at the GH (with JRC~2), the static friction angle falls below the typical values found in the literature for quartzite formations at ~30° (Ryder, 1987; 1988). However, as often seen in the GH, most joint surfaces display talc and chlorite alterations, potentially reducing shear strength. Observations made by Barton (1973) indicate that a range of fault gouges, shear zones (applicable to GH), and low-strength rock joint types can group within a static friction angle range between 20° and 30°, assuming zero cohesion (see Wyllie, 2018, p.131). To acquire additional insight (complementary to the study), single- and multi-stage direct-shear tests were conducted by Montana Technological University in late 2022 (*Figure 6.5*). Core samples from the 7500L were collected in argillites (and quartzites) lithology and sent to a rock laboratory. The selected fractures for testing were open joints, most likely representing bedding plane surfaces, as these are the easiest fracture sets to identify in the core. The joint surfaces were characterized as planar with some alteration. Preliminary direct-shear test results on the argillites series have indicated the peak and residual friction angles to be 22.5° and 15.3°, respectively. These results are encouraging as the calibrated friction properties fall within the range of the direct-shear results. In addition, the direct-shear test below illustrates an explicit stress drop behaviour (*Figure 6.5*a). Talky material was observed to form on top of the

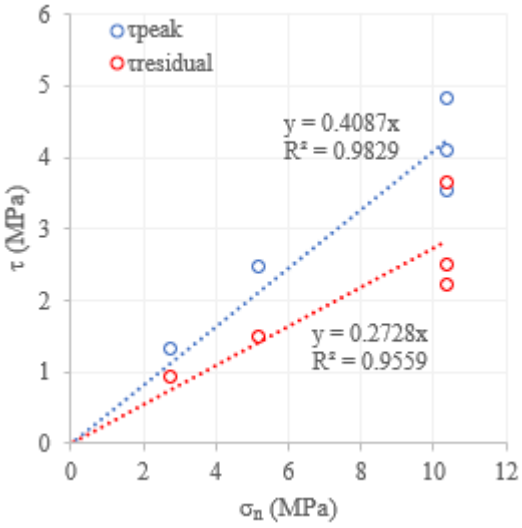
joint surface after the trial had run to completion and the surfaces unmatted. Although encouraging, these need further investigation, potentially for all fracture sets.



(a)



(b)



(c)

Figure 6.5: Preliminary direct-shear results on core from 7500L, in argillites: (a) single stage result at highest normal stress, (b) surface structure condition pre-test, (c) static and residual strength estimates

6.1.3 Assessing the Seismic Source Mechanism (Chapter 5)

Chapter 5 began by illustrating the mining depth potential that exists at the GH and identifies key seismic input inquiries which need to be addressed for adequate engineering planning efforts to minimize seismic hazard. The application of developed seismic design charts (ERR and ESS) was benchmarked against two (2) subsequent mining periods at varying mining rates: (***i***) 2017–2019 (~123 tons per day), and (***ii***) 2020–2021 (~685 tons per day on the lower stopes exclusively). The formulated ERR design chart over predicted seismic incidence for both subsequent periods by ~1 event per 1,000 m^3 mined. For both subsequent mining periods, the largest seismic events in abutments and pillars did not exceed those recorded during the 2014–2016 period, contrasting with the ESS expectation of increased size events for mine deepening.

It was highlighted that the subsequent mining periods differed significantly from the previous base case, with the first subset period presenting a low extracted area mined. At the same time, the second incorporated a completely new mining method affecting the rockmass response. The impact of mining conditions on seismic release was illustrated through changes in energy release, seismic response (MTL), and the positive impact UCB has on seismicity and production.

The mechanisms affecting seismic response were further investigated for UCB to understand the impact on fault slip. The calibrated block-based (FF-element) model was utilized to simulate the UCB extraction in 15S (645-15-03) through simple numerical processes. The modelling scheme relies on extracting the fragmented cuts, excluding blast energy provided by the production shot. The unspecified-DFN was integrated into the model, assuming (static & dynamic) Mohr-Coulomb frictional strength properties, and validated the slip initiation potential on centroids. The frictional properties were set to $\varphi_s = 25°$, $\varphi_d = 20°$ and null cohesion, based on previous calibration efforts. The new ffs structures that have slipped during the UCB extraction were further analyzed for slip extension as done by Board (1994). Seismic energy and magnitude estimates were derived from scaling formulae and compared to UCB results. A reasonable comparison was achieved on event count, location, magnitude ranges, and cumulative seismic energy release. Furthermore, the analysis was rerun for a mining sequence simulating LFUL extraction. Most importantly, it was concluded that the LFUL (triggers) while UCB (induces) faults to slip – presenting a difference in fault response. Hence, the new mining method mainly affects the rockmass response at the mining front. However, the pillars and, most probably, the

distal bounding faults may continue to present a triggered (time-dependent) seismic response independent of the mining method.

This chapter aimed to guide planning engineers in investigating seismic potential as mining deepens. Therefore, a method for simultaneous seismic events was derived and presented through a case example based on Ryder's ESS concept integrated into Salamon's (1993) and Board's (1994) modelling processes. This method relies on tracking the related structures in the mining environment, digitizing them (as discs), and incorporating them into a BEM model. As the mining sequence is simulated, the induced stresses are mapped onto the faults, and tested for slip initiation and extent. Seismic parameters (E_s & M_o) are calculated for slipped structures. This method can potentially be extrapolated to the total mine geometry quickly and efficiently. It is essential to remind the reader that this method does not claim to predict the seismic outcome but instead allows one to forecast the (general) magnitude, occurrence, and the (general) location of resulting events.

6.1.3.1 Limitations

The major limitation related to the modelling of Ryder's ESS resides in using the simplified Mohr-Coulomb strength assumption. It has been long recognized (at the laboratory scale) that most rocks obey the fundamental empirical laws of friction (Byerlee, 1978; Dieterich, 1978). In nature, the constitutive friction model leading to and propagating the ride may be affected on a large scale. In the developed ESS formulation, utilizing circular discs, it is assumed that the fault initiates at the centroid when active shear stress beats the static shear strength. However, the disc may have already entered a state of slip initiation elsewhere across its surface without initiating the trigger point. These assumptions generalize the complexity of fault movement where rock bridging (splays or jogs) or cohesion variability (asperities) may exist along the discontinuity (Scholz, 2019). The ESS implicitly accounts for this process, arguing that the positive ESS trigger point, which meets the critical fault strength, will initiate infinite energy at the initiation point, shearing through all resistive asperities (Ryder, 1987; 1988).

The potential for multiple events on a single fault also exists, as recorded on the F-series faults crossing into the 5,700 Pillar (*Figure 4.25*). These events often appear to be time-dependent, releasing outside the blasting period. Engelder & Scholz (1976) have recognized that faults undergo self-roughening processes as sliding occurs, creating oriented grooves on the surface

plane. When the stresses evolve around the structure (say, induced by mining), these grooves can act as new asperities, allowing shear stress to build back up onto the discontinuity for further episodes. Stick-slip mechanisms, such as those studied by Dieterich (1978), may also provide the mechanism to support the ability of a fault to regain its coefficient of friction due to the time of stationary contact.

In addition, the fragmented ore (from the UCB blast) was softened until the stresses were relieved from the volume. Although confirmed by in-field closure measurements, this assumption may differ from a modelling standpoint. Since the fragmented ore stays below the stope floor, it potentially adds uniformly distributed back pressures onto the UCB'ed stope boundary (acting as ground support). The fragmented ore's ability to do work may consume part of the energy release, providing additional justification for the recorded seismic energy discrepancy found between mining periods (*Figure 5.13*). However, these assessments can only be performed by a numerical code that can track each energy component.

Finally, it is recognized that the first-order faults need to be integrated into the numerical assessment as they present specific locations for triggering large seismic events in response to the total mine extraction. Historically, the Lucky Friday mine released two large (+4 M_L) bounding structures within the LF deposit (Whyatt et al., 1996). These mine-wide faults have the potential to release massive amounts of energy, especially when mining arrests orthogonal to its surface, leaving unmined contacts. In certain situations, these contacts can act as asperities, initially preventing the fault from moving until sufficient stress builds up, rupturing the contact and allowing dynamic slip over an increased area (Board, 1994).

The developed elastic BEM model presents several areas for improvement; however, these simple procedures prove valuable to quickly assess different layouts at an increasing mining depth. In addition, this methodology parses efficiently through a large DFN catalog, identifying the most critical fracture sets. These *selected few* can then be run under more complex slip mechanisms in a discontinuum model (e.g., UDEC, 3DEC, PFC). Since explicit structures propagate or dilate (Brady & Brown, 2006), discontinuum models predict better stresses across discontinuities than continuum models (Bobet et al., 2008). However, grouping and clustering the slipped regions on an explicit fault may present challenges.

6.2 Contributions

The section below highlights the accomplishments and contributions made as part of this thesis.

An extensive evaluation of high-quality seismic data was conducted for the GH deposit. This is the only seismic database that offers uninterrupted time coverage for the complete mining duration of a tabular vein since 1997. The studied seismic period ranges from 2007 to 2021, with a gap in production in 2012 due to a mine stoppage, which allowed for a significant seismic system upgrade. The post-processing performed by the site engineers on all notable events (≥ +0.5 M_w) and the continuity of the recorded data illustrate the quality of the seismic database used in the study. The seismic catalog was linked through spatial-tempol methods with historical mine records such as mining layouts, tonnages, and surveys. The available mine records were adjusted for monthly or yearly intervals and separated into stopes, with the later period (2013+) providing the most precise information at the stope scale. All the data was checked, validated, and organized into comparable formats.

A benchmark seismic analysis was conducted for a specific mining period from 2013 to 2016 at the mine scale. This period was selected due to its higher accuracy. Based on magnitude-time-location, the seismological principles were applied to investigate the seismic source mechanism, which indicated a primary fault-slip source. The analysis was conducted in detail and structured at the mine and stope scale. This North American seismic database is the only one that has been reasonably compared with the current South African mine, published by Spottiswoode *et al.* (2008), in the Witwatersrand basin (which hosts the deepest and most seismically active mines worldwide). The mining rate was observed to have the most significant impact, represented by Joules / m^3. The Lucky Friday mine (GH deposit) releases similar energies per area mined as observed in other deep, narrow tabular hardrock mines.

External engineering reports were collected and treated as input parameters. These were limited to (1) laboratory rock test results (Agapito & Associates, 2011), (2) paste stability analysis (Seymour et al., 2017), and (3) in-stope closure measurements (Seymour et al., 2016; Raffaldi et al., 2019). These documents were purposefully selected to help advance the analyses presented in this thesis. The source data was verified, and my interpretations were made (unless otherwise cited).

A BEM code was tested and selected to reconstruct the geometry of the main 30-Vein of the Gold Hunter since mining was initiated in 1997 up to 2021. Model construction details, numerical mesh dependency analysis and detailed model benchmarking of stress and closure on a tabular narrow reef were performed (see Appendices). Two (FF & DD-element) models were successfully built with the mining step ranging from an annual step to a monthly advance. Each model hosts a numerical seismic analysis scheme, relying on established deterministic concepts: Cook's ERR and Ryder's ESS. The contribution made in this thesis lies in successfully integrating these analytical concepts into a numerical code for mine-wide application. The input parameters were kept as simple as possible and relatable to in-field observations. The models assume an elastic, homogeneous rockmass. The basic material input parameters (E & ν) were taken from laboratory results and successfully calibrated to match in-field measurement data, providing increased confidence in the model construct.

A numerical ERR procedure was developed and successfully implemented into the calibrated DD-BEM. The ERR outputs were linked with mine records at the mine and stope scale for the mining periods between 1997-2011 and 2013-2016, where most studies only analyze the absolute or effective increase in release rate per mining step (focusing on limiting the energy jumps). The GH data was directly compared with the empirical design chart (COMRO, 1988) developed for South African tabular mines. To the author's knowledge, such direct comparisons haven't been made for North American mines.

A numerical ESS procedure was developed and successfully implemented into the calibrated FF-BEM. The ESS was used to assess the notable events between 2013 and 2016. This provided further confidence in the fault slip source, where 50% presents the potential to slip and represents 64% of the cumulative seismic energy release. To build on the work of Salamon, Board, and Linkov, a synthetic fracture network was built for the GH from field mapping assembled by the site geologists (capturing over 2,400+ fault intercepts). Itasca (2021) built the base DFN; however, calibration efforts undertaken in this thesis have revealed that the DFN database for an unspecified fault orientation provided a better correlation with seismic records (2013–2016). Therefore, the unspecified DFN was born out of this assessment, where a new approach also emerged to calibrate the frictional properties of discontinuities from seismic records.

To further test their integrity, the numerical seismic forecast schemes were validated for subsequent mining periods between 2017 and 2019, and 2020-2021. The ERR empirical chart derived for the GH identified (correctly) lower seismic energy releases for both periods. This highlights the sensitivity in the applicability of the empirical chart as both periods underwent significant changes in mine setting, including a change in mining method (converted from LFUL to the UCB). The ESS analysis was utilized to simulate a case study of UCB in 15S, using the unspecified DFN scheme. The simulated fault-slip events matched the seismic records in terms of event count, general locations, and magnitude release range with unprecedented accuracy at such a small scale. The ESS analyses captured changes between mining methods. They gained insight into the fault slip mechanism for UCB, demonstrating the versatility of the method (i.e., sensitivity to stress and geometrical changes). The forecasting schemes directly compare to seismic system records (E_s, M_o & M_w).

Understanding that seismicity will likely remain unpredictable, a process for tracking short-term seismic hazards was developed in this thesis based on several interactions with mine personnel. The biggest contribution lies in selecting to track the cumulative seismic energy release by cumulative area mined, formalizing the energy tracking process and demonstrating its applicability through another case example in 15S for several UCB blasts.

Finally, a numerical seismic assessment of mine-induced seismicity in a deep, narrow tabular deposit was developed in this thesis. The presented results do not transpose directly to other orebodies or mines. However, based on the assumption that a seismic event is deterministic at its hypocenter, the methodology can be applied to other seismically active mines. These processes can help mine staff evaluate their primary source and enable them to perform simple numerical assessments to forecast fault-slip with outputs directly comparable to those in the seismic catalog.

6.3 Recommendations for future work

Numerous improvements can be made to the present study. For the grid-based model, additional efforts should be made to refine ERR assessment's of Wk component. This can be achieved by integrating and calibrating the backfill material response. The in-field mid-panel closure, which is currently unknown, can be utilized to calibrate the fill’s strain-hardening response. These measurements can be acquired relatively simply by core drilling into the mid-panel from the

ramp. The absolute compaction of the fill could be estimated from the measured fill crossing. The simulated mid-stope closure estimates (without backfill) can guide these intercepts.

Develop a procedure to identify strain-type events located in pillar geometries or under the stope floor. Mines typically use the E_s / E_p ratio to distinguish between strain and shear-type events. The E_s / E_p ratio for shear-type events in the GH was assumed to be > 3.0 based on (limited) fault-slip event occurrences; these parameters need further investigation. However, similar to the ESS assessment performed on extracted stress tensors, the brittle shear ratio (Castro et al., 2012) or the burst potential index (Mitri et al., 1999) could validate the strain potential at the source location. This procedure could provide the basis for a statistical assessment of seismic event type (based on deterministic failure types) in relation to mine geometry when a notable event occurs at the mine.

For the block-based model, integrate the bounding first-order faults (such as the mine scale Silver, S1, and Paymaster faults) into the numerical model scheme based on geological constructs. Track the potential slip extent on the digitized faults resulting from annual (or quarterly) production on the 30-Vein. The ESS procedure, with the estimated friction properties, would allow computing an explicit magnitude estimate and ride direction. During annual planning, mining sequences for different layouts can be simulated to validate fault stress management strategies.

Develop a procedure for identifying the different fracture sets within the core. The unspecified-DFN approach does not differentiate the frictional properties between fracture sets – these are assumed constant in this study. Oriented core drilling, or the measured differences between the alpha and the foliation angle of the core, could assist in this effort. Once a fracture set tagging scheme has been developed, additional fault characterization and direct-shear tests should be commissioned.

Finally, this study aimed to produce simple numerical methods, derived from field measurement, that site engineers can routinely apply to help guide layout design as the mine deepens at the GH. Seismic occurrences (magnitude-time-location) cannot be adequately **predicted** with this methodology (or any other). All the recommendations given in the limitation sections should be further investigated as the experience with the forecasting models grows.

REFERENCES

Abercrombie, R.E. (1995). Earthquake source scaling relationships from -1 to 5 ML using seismograms recorded at 2.5-km depth. Journal of Geophysical Research: Solid Earth, 100(B12), 24015-24036.

Adhikari, G.R. (2007) Ground vibration and structure response due to rockbursts at Kolar gold fields, India. Journal of Mines, Metals & Fuels, (5), 14–152.

Agapito & Associates (2011). Hecla Limited Ambient Temperature Rock Mechanics Properties Test Results. Internal report.

Aki, K., & Richards, P.G. (1980). Quantative seismology: Theory and methods. New York, 801.

Andrieux, P. (2005). Application of rock engineering systems to large-scale confined destress blasts in underground mine pillars. (Doctoral dissertation) Université Laval (Canada).

Andersen, L.M., & Spottiswoode, S.M. (2001). A hybrid relative moment tensor methodology. Rockbursts and Seismicity in Mines, 5, 81-89.

Armatys, M. (2012). Modification des classifications géomécaniques pour les massifs rocheux schisteux. (Master thesis) Ecole Polytechnique Montreal (Canada).

Bæcher, G.B., Lanney, N.A., & Einstein, H.H. (1977, June). Statistical description of rock properties and sampling. In US Rock Mechanics/Geomechanics Symposium (pp. ARMA-77).

Baig, A., & Urbancic, T. (2010). Microseismic moment tensors: A path to understanding frac growth. The Leading Edge, 29(3), 320-324.

Banerjee, P.K. and Butterfield, R. (1981). Boundary element methods in engineering science. McGraw-Hill, New York.

Barton, N. (1973). Review of a new shear-strength criterion for rock joints. Engineering geology, 7(4), 287-332.

Barton, N., & Choubey, V. (1977). The shear strength of rock joints in theory and practice. Rock mechanics, 10(1-2), 1-54.

Beck, D.A. (2000). The engineering management of induced seismic failures in deep-level hard rock mining. (Doctoral dissertation) University of Queensland (Australia).

Beeler, N., Tullis, T., & Weeks, J. (1994). The roles of time and displacement in the evolution effect in rock friction. Geophysical Research Letters, 21(18), 1987-1990.

Beus, M.J., & Chan, S.S. (1980). Shaft design in the Coeur d'Alene Mining District, Idaho: Results of in situ stress and physical property measurements (Vol. 8435). United States Bureau of Mines, 39p.

Bewick, R.P., Valley, B., Runnalls, S., Whitney, J., & Krynicki, Y. (2009). Global approach to managing deep mining hazards. ROCKENG (CABUS), 3, 3994.

Bizzarri, A. (2011). On the deterministic description of earthquakes. Reviews of Geophysics, 49(3).

Bizzarri, A., Cocco, M., Andrews, D., & Boschi, E. (2001). Solving the dynamic rupture problem with different numerical approaches and constitutive laws. Geophysical Journal International, 144(3), 656-678.

Blake, W. (1972). Rock-burst mechanics. Quarterly of Colorado School of Mines, 67(1), 1–64.

Blake, W., Board, M.P. and Brummer, R.K. (1998). Destress Blasting Practices − A Review of the Literature and Current Industrial Practice, report from the Itasca Consulting Group and Richard Brummer Associates to CAMIRO −Mining Division, Sudbury, Canada, 96 p.

Blake, W., & Hedley, D.G. (2003). Rockbursts: case studies from North American hard-rock mines. SME.

Board, M.P. (1994). Numerical Examination of mining-induced seismicity. (Doctoral dissertation) University of Minnesota (USA).

Board, M.P., & Fairhurst, C. (1983). Rockburst control through destressing-a case example. In Rockbursts: prediction and control. Symposium, 91-101.

Board, M.P., Rorke, T., Williams, G., & Gay, N. (1992). Fluid injection for rockburst control in deep mining. Paper presented at the 33th US Symposium on Rock Mechanics (USRMS).

Board, M.P., Johnson, W.B., Neville, C., Armatys, M. (2023) Development of the Underhand Closed Bench Mining Method for Control of Fault Slip Seismicity at Hecla's Lucky Friday Mine. Internal report.

Boatwright, J., & Fletcher, J. B. (1984). The partition of radiated energy between P and S waves. Bulletin of the seismological society of America, 74(2), 361-376.

Bobet, A., Fakhimi, A., Johnson, S., Morris, J., Tonon, F., & Yeung, M.R. (2009). Numerical models in discontinuous media: review of advances for rock mechanics applications. Journal of geotechnical and geoenvironmental engineering, 135(11), 1547-1561.

Brace, W. F. (1964). Brittle fracture of rocks. State of stress in the earth's crust., 111–174.

Brace, W., & Byerlee, J. (1966). Stick-slip as a mechanism for earthquakes. Science, 153(3739), 990-992.

Brady, B.H. (1990). Keynote lecture: Rock stress, structure and mine design. Rockbursts and Seismicity in Mines, 2, 311-321.

Brady, B.H., & Brown, E. T. (2006). Rock mechanics: for underground mining. Springer science & business media.

Brink, A.V.Z. (1984). Rock burst prediction research-development of an early warning system. Acoustic Emission/Microseismic Activity in Geologic Structures and Materials, 3.

Brown, L.G. (2021). Quantifying discrete seismic responses to mining. Canadian Geotechnical Journal, 58(7), 1023-1035.

Brown, L.G., & Hudyma, M. (2017). Identifying local stress increase using a relative apparent stress ratio for populations of mining-induced seismic events. Canadian Geotechnical Journal, 54(1), 128-137.

Brown, L.G., & Hudyma, M.R. (2018). Mining induced seismicity in Canada: a 2017 update. In ARMA US Rock Mechanics/Geomechanics Symposium.

Brummer, R.K. (1999). Simple truths about rockbursts. In South African Rock Engineering Symposium, 2.

Brune, J.N. (1970). Tectonic stress and the spectra of seismic shear waves from earthquakes. Journal of Geophysical Research, 75(26), 4997-5009.

Budavari, S. (1983). Response of the rock mass to excavations underground. Rock Mechanics in Mining Practice. The South African Institute of Mining and Metallurgy, MS(5), 55-76.

Budavari, S. (2003). Rock engineering aspects of the evaluation of mining layouts proposed for the extraction of gold-bearing reefs at ultra-depths. Safety and Environmental Aspects of mining, 63, 45–87.

Bukowska, M. (2006). The probability of rockburst occurrence in the Upper Silesian Coal Basin area dependent on natural mining conditions. Journal of Mining Science, 42(6), 570-577.

Byerlee, J.D. (1967). Theory of friction based on brittle fracture. Journal of Applied Physics, 38(7), 2928-2934.

Byerlee, J.D. (1968). Brittle-ductile transition in rocks. Journal of Geophysical Research, 73(14), 4741-4750.

Byerlee, J.D. (1978). Friction of rocks. In Rock friction and earthquake prediction, 615-626.

Byerlee, J.D., & Wyss, M. (1979). Rock friction and earthquake prediction (Vol. 6): Springer.

Cai, M. (2013). Principles of rock support in burst-prone ground. Tunnelling and Underground Space Technology, (36) pp. 46–56.

Cai, M., & Kaiser, P. (2018). Rockburst phenomenon and support characteristics. Laurentian University, Laurentian.

Cao, W., Shi, J. Q., Si, G., Durucan, S., & Korre, A. (2018). Numerical modelling of microseismicity associated with longwall coal mining. International Journal of Coal Geology, 193, 30-45.

Carusone, O., & Hudyma, M. (2017). Variations in apparent stress and energy index as indicators of stress and yielding around excavations. In Underground Mining Technology (ACG), 5, 205-218.

Castro, L.A.M., Carter, T.G., & Lightfoot, N. (2009). Investigating factors influencing fault-slip in seismically active structures. CANUS rock mechanics symposium, 3, 1–12.

Castro, L.A.M., Bewick, R.P., Carter, T.G. (2012) An overview of numerical modelling applied to deep mining. Innovat Numer Model Geomech, 393–414.

Caw, J.M. (1956). The Kolar Gold Field. Mine and Quarry Engineering, 22, 258–306.

Chambon, G., Schmittbuhl, J., & Corfdir, A. (2006). Frictional response of a thick gouge sample: 2. Friction law and implications for faults. Journal of Geophysical Research: Solid Earth, 111(B9).

Coates, D.F. (1959). Energy Released In Rockbursts. Rock Mechanics (USRMS), 3.

Coates, D.F. (1965). Rock mechanics principles. Geoscience Abstracts.

Collins, D.S., Toya, Y., & Hosseini, Z. (2016). Use of Seismic Deformation and Stress Inversion Analysis to Help Improve the Understanding of Rock Mass Response to Excavation. In ARMA US Rock Mechanics/Geomechanics Symposium, 16(0525).

COMRO (1988). An Industry Guide to Methods of Ameliorating the Hazards of Rockfalls and Rockbursts. Johannesburg: Chamber of Mines Research Organization.

Cook, N.G.W. (1963a). The basic mechanics of rockbursts. Journal of the Southern African Institute of Mining and Metallurgy, 64(3), 71-81.

Cook, N.G.W. (1963b). The seismic location of rockbursts. Rock Mechanics-Proceedings of the Fifth Symposium. Pergamon Press.

Cook, N.G.W. (1964). The application of seismic techniques to problems in rock mechanics. International Journal of Rock Mechanics and Mining Sciences, 1(2), 169-179.

Cook, N.G.W. (1965a). The failure of rock. International Journal of Rock Mechanics and Mining Sciences, 2, 389–403.

Cook, N.G.W. (1965b). A note on rockbursts considered as a problem of stability. Journal of the Southern African Institute of Mining and Metallurgy, 65(8), 437-446.

Cook, N.G.W. (1967). Design of underground excavations. 8th U.S. Rock Mech. Symp., Minnesota 167-193.

Cook, N.G.W. (1976). Seismicity associated with mining. Engineering Geology, 10, 99-122.

Cook, N.G.W., Hoek, E., Pretorius, J., Ortlepp, W., & Salamon, M. (1966). Rock mechanics applied to the study of rockbursts. Journal of the South African institute of mining and metallurgy, 66(10), pp. 695–705.

Cook, N., Fenton, C., Lancaster, F., More-O'Ferall, R., Nienaber, W., van Schalkwijk, A., . . . Waterman, D. (1978). An industry guide to the amelioration of hazards of rockbursts and rockfalls. Chamber of Mines of South Africa.

Cortolezzis, D., & Hudyma, M. (2018). Application of sequential spatial clustering and fractal dimension to caving seismic event parameters of time, distance, and intensity. In Block and Sublevel Caving (ACG), 4, 799-814.

Coulson, A.L., & Bawden, W.F. (2008). Observation of the Spatial and Temporal Changes of Microseismic Source Parameters and Locations, Used to Identify the State of the Rock Mass in relation to the Peak and Post-Peak Strength Conditions. US Rock Mechanics Symposium (USRMS), 42.

Crouch, S.L., Starfield, A.M., & Rizzo, F.J. (1983). Boundary element methods in solid mechanics.

Cundall, P.A., & Lemos, J.V. (1990). Numerical simulation of fault instabilities with a continuously-yielding joint model. Rockbursts and Seismicity in Mines, 2, 147-152.

Davis, R., & Salt, G. (1986). Strength of undulating shear surfaces in rock. Geotechnique, 36(4), 503-509.

Dehn, K.K., Butler, T., & Weston, B. (2018). Using the energy index method to evaluate seismic hazards in an underground narrow-vein metal mine. In US Rock Mechanics/Geomechanics Symposium (pp. ARMA 18-1027).

DeVoe., T. & Meyers, J. (2017) Major Faults, F Series Faults, Northwest & Northeast Faults 5500 to 6550 Mine Levels and Sublevels, Gold Hunter Mine, Mullan, Idaho USA. Internal report

Dieterich, J.H. (1972). Time-dependent friction in rocks. Journal of Geophysical Research, 77(20), 3690-3697.

Dieterich, J.H. (1978). Time-dependent friction and the mechanics of stick-slip. Rock friction and earthquake prediction, 790-806.

Dieterich, J.H. (1992). Earthquake nucleation on faults with rate-and state-dependent strength. Tectonophysics, 211(1-4), 115-134.

Dieterich, J.H., & Kilgore, B. D. (1994). Direct observation of frictional contacts: New insights for state-dependent properties. Pure and Applied Geophysics, 143(1-3), 283-302.

Drescher, A., & Fairhurst, C. (1987). Failure of soil and rocks. Ground Engineer ref. book, 611-618.

Duplancic, P. (2001). Characterisation of caving mechanisms through analysis of stress and seismicity. (Doctoral dissertation) University of Western Australia (Australia).

Durrheim, R.J. (2010). Mitigating the risk of rockbursts in the deep hard rock mines of South Africa: 100 years of research. Extracting the science: A century of mining research, 156-171.

Durrheim, R.J., Roberts, M.K.C., Haile, A.T., Hagan, T.O., Jager, A.J., Handley, M.F., Spottiswoode, S.M. & Ortlepp, W. (1998). Factors influencing the severity of rockburst damage in South African gold mines. Journal of the Southern African Institute of Mining and Metallurgy, 98(2), 53-57.

Durrheim, R., Anderson, R., Cichowicz, A., Ebrahim-Trolloped, R., Hubert, G., Kijko, A., Van der Merwe, N. (2006). The risks to miners, mines, and the public posed by large seismic events in the gold mining districts of South Africa.

Durrheim, R., Anderson, R., Cichowicz, A., Ebrahim-Trollope, R., Hubert, G., Kijko, A., Van der Merwe, N. (2011). Risks posed by large seismic events in the gold mining districts of South Africa. In: Daya Publishing House.

Duvall, W.I., & Stephenson, D.E. (1965). Seismic energy available from rockbursts and underground explosions. Transactions of the Society of Mining Engineers, 232(3), 235–240.

Emanov, A. F., Emanov, A. A., Fateev, A. V., Leskova, E. V., Shevkunova, E. V., & Podkorytova, V. G. (2014). Mining-induced seismicity at open pit mines in Kuzbass (Bachatsky earthquake on June 18, 2013). Journal of mining science, 50, 224–228.

Engelder, J.T., & Scholz, C.H. (1976). The role of asperity indentation and ploughing in rock friction—II: Influence of relative hardness and normal load. In International Journal of Rock Mechanics and Mining Sciences & Geomechanics Abstracts, 13(5), 155-163.

ESG (2016) calibration report for Gold-hunter. Internal report.

Esterhuizen, G.S. (1997). An improved method for the assessment of deep mine layouts using elastic models. Proc. 1st Southern African Rock Engineering Symposium, pp. 197-204.

Fairhurst, C. (1990). Design of excavations in high rock-stress conditions. Rockburst and Seismicity in Mines, 2, 421-423.

Fairhurst, C. (2004). Fundamental considerations relating to the strength of rock. Colloquium on rock fracture, Ruhr University (Germany). Original publication date 1971, 55, 1-56.

Fairhurst, C., & Cook, N.G.W. (1966). The phenomenon of rock splitting parallel to the direction of maximum compression in the neighborhood of a surface. International society of rock mechanics, 1, 687-692.

Gale, W.J., Heasley, K.A., Iannacchione, A.T., Swanson, P.L., Hatherly, P., & King, A. (2001, July). Rock damage characterisation from microseismic monitoring. In US Rock Mechanics/Geomechanics Symposium (ARMA).

Gane, P., Hales, A., & Oliver, H. (1946). A seismic investigation of the Witwatersrand earth tremors. Bulletin of the Seismological Society of America, 36(2), 49-80.

Gibowicz, S.J. (1990). Seismicity induced by mining. In Advances in geophysics (32), 1-74.

Gibowicz, S.J. (1993). Keynote address: Seismic moment tensor and the mechanism of seismic events in mines. Rockbursts and Seismicity in Mines, 3, 149-155.

Gibowicz, S.J. (2009). Seismicity Induced by Mining: Recent Research. Advances in geophysics, 51, 1–53.

Gibowicz, S.J., Young, R., Talebi, S., & Rawlence, D. (1991). Source parameters of seismic events at the Underground Research Laboratory in Manitoba, Canada: Scaling relations for events with moment magnitude smaller than -2. Bulletin of the seismological Society of America, 81(4), 1157-1182.

Gibowicz, S.J., & Kijko, A. (1994). An Introduction to Mining Seismology. San Diego: Academic Press.

Gill, D.E., & Aubertin, M. (1988). Évaluation du potentiel de coups de terrain dans les mines d'Abitibi: Unite de recherche et de Service en technologie minerale de l'Abitibi-Temiscamingue.

Gill, D.E., Aubertin, M., & Simon, R. (1993). A practical engineering approach to the evaluation of rockburst potential. Rockburst and Seismicity in Mines. Balkema, Rotterdam, 63-68.

Goodman, R.E. (1989). Introduction to rock mechanics (2nd edition). Wiley New York.

Griffith, A.A. (1921). The phenomena of rupture and flow in solids. Phil. Trans. R. Soc. Lond. A, 221(582-593), 163-198.

Griffith, A.A. (1924). The theory of rupture. First Int. Cong. Appl. Mech., 55-63.

Guha, S.K. (2013). Induced earthquakes. Springer Science & Business Media. 314p.

Gürtunca, R.G., & Adams, D.J. (1991). Determination of the in situ modulus of the rockmass by the use of backfill measurements. J.S. Afr. Inst. Min. Metall., 91(3), 81-88.

Gutenberg, B., & Richter, C.F. (1955). Magnitude and energy of earthquakes. Nature, 176(4486), 795-795.

Hadjigeorgiou, J. (2012). Where do the data come from? Mining Technology, 121(4), 236-247.

Hanks, T.C., & Kanamori, H. (1979). A moment magnitude scale. Journal of Geophysical Research, 84(B5).

Hardy, H.R.J. (2003). Acoustic emission/microseismic activity. Activity: Principles, Vol. 1.

Harris, P.H., & Wesseloo, J. (2015). mXrap software, version 5. ACG, University of Western Australia (Western Australia) https://mxrap.com/

Hart, R., Board, M.P., Brady, B., O'Heam, B., & Allan, G. (1988). Examination of fault-slip induced rockbursting at the strathcona mine. US Symposium on Rock Mechanics, 29.

Hasegawa, H.S., Wetmiller, R.J., & Gendzwill, D.J. (1989). Induced seismicity in mines in Canada—an overview. Pure and applied geophysics, 129(3-4), 423-453.

Heal, D., Hudyma, M., & Vézina, F. (2005). Seismic Hazard at Agnico-Eagle's Laronde Mine Using MS-RAP.

Hecla Limited (2013). Rockburt in 54 ramp. Internal report.

Hecla Limited (2016). Lag Time Analysis Report. Internal report.

Hecla Limited (2017). Rockburt in 15S. Internal report.

Hecla Limited (2022). Technical report Summary on the Lucky Friday Mine, Idaho, USA. S-K 1300 Report, prepared by SLR, 218 p.

Hedley, D.G.F. (1992). Rockburst handbook for Ontario hardrock mines. Canmet, 305 p.

Hedley, D.G.F., Bharti, S., West, D., & Blake, W. (1985). Fault-slip Rockbursts at Falconbridge Mine. In 4th Conference on Acoustic Emission/Microseismic Activity.

Hencher, S.R., & Richards, L.R. (1989). Laboratory direct shear testing of rock discontinuities. Ground Engineering, 24–31.

Hildyard, M.W., Napier, J.A.L., Spottiswoode, S.M., Sellers, E., Linzer, L.M., & Kataka, M.O. (2006). New criteria for rockmass stability and control using integration of seismicity and numerical modelling.

Hobbs, S.W., Campbell, A.B., Griggs, A.B., & Wallace, R.E. (1965). Geology of the Coeur d'Alene district, Shoshone county, Idaho (Vol. 478). US Government Printing Office.

Hoek, E., & Bieniawski, Z. (1965). Brittle fracture propagation in rock under compression. International Journal of Fracture Mechanics, 1(3), 137–155.

Hoek, E., & Brown, E.T. (1980). Empirical strength criterion for rock masses. Journal of the geotechnical engineering division, 106(9), 1013-1035.

Hoek, E., Grabinsky, M., & Diederichs, M. (1991). Numerical modelling for underground excavation design. Institution of Mining and Metallurgy Transactions. Section A. Mining Industry, 100.

Hoek, E., Carranza-Torres, C., & Corkum, B. (2002). Hoek-Brown failure criterion-2002 edition. Proceedings of NARMS-Tac, 1(1), 267-273.

Hoek, E., Carter, T.G., & Diederichs, M.S. (2013). Quantification of the geological strength index chart. In ARMA US Rock Mechanics/Geomechanics Symposium.

Hoek, E., & Martin, C. (2014). Fracture initiation and propagation in intact rock–a review. Journal of Rock Mechanics and Geotechnical Engineering, 6(4), 287–300.

Hoek, E., & Brown, E.T. (2019). The Hoek–Brown failure criterion and GSI–2018 edition. Journal of Rock Mechanics and Geotechnical Engineering, 11(3), 445-463.

Hofmann, G. (2012). Correlating modelled elastic energy release with recorded seismicity in a deep tabular mine. Southern Hemisphere International Rock Mechanics Symposium, 2, 407-423.

Hofmann, G., Sewjee, R., & Van Aswegen, G. (2001). First steps in the integration of numerical modelling and seismic monitoring. Dynamic rock mass response to mining, 5.

Hofmann, G., Ogasawara, H., Katsura, T., & Roberts, D. (2012). An attempt to constrain the stress and strength of a dyke that accommodated a ML 2.1 seismic event. South. Hemisph. Int. Rock Mech. Symp, 1–15.

Hofmann, G., Murphy, S., Scheepers, L., & van Aswegen, G. (2013a). Surface stress modelling of some shear slip seismic events that occurred in Anglogold Ashanti's tabular mines. Rockbursts and Seismicity in Mines,8, 219-231.

Hofmann, G., Scheepers, L., & Ogasawara, H. (2013b). Loading conditions of geological faults in deep level tabular mines. In-Situ Rock Stress, 6, 560-580.

Horner, R., & Hasegawa, H. (1978). The seismotectonics of southern Saskatchewan. Canadian Journal of Earth Sciences, 15(8), 1341-1355.

Hudyma, M. (2004). Mining-Induced Seismicity in Underground, Mechanised, Hardrock Mines – Results of a World Wide Survey. Australian Centre for Geomechanics, 138 p.

Hudyma, M. (2008). Analysis and interpretation of clusters of seismic events in mines. (Doctoral dissertation). University of Western Australia (Australia).

Hudyma, M. (2010). Applied Mine Seismology Concepts and Techniques. Course Notes - available at researchgate.com.

Hudyma, M., Potvin, Y.H., Grant, D., Milne, D., Brummer, R.K., & Board, M.P. (1994). Geomechanics of sill pillar mining. North American Rock Mechanics Symposium, 1.

Hudyma, M., Heal, D., & Mikula, P. (2003). Seismic monitoring in mines—old technology, new applications. AGCM Conference, 1, pp. 209-226.

Hudyma, M., & Potvin, Y.H. (2010). An engineering approach to seismic risk management in hardrock mines. Rock mechanics and rock engineering, 43, 891-906.

Hudyma, M., Brown, L.G., Carusone, O., & Reimer, E. (2017). Seismic hazard in Canadian mines. Proceeding of the CIM AGM, Montreal, QC, Canada, 2.

Indraratna, B., Jayanathan, M., & Brown, T. (2008). Shear strength model for overconsolidated clay-infilled idealised rock joints. Géotechnique, 58(1), 55-65.

Inglis, C.E. (1913). Stresses in a plate due to the presence of cracks and sharp corners. Trans Inst Naval Archit, 55, 219-241.

Itasca (2021) DFN generated for the GH. Internal report.

Itasca (2023) DFN generation, analysis, and simplification. PFC user manual.

Jaeger, J.C. (1971). Friction of rocks and stability of rock slopes. Geotechnique, 21(2), 97-134.

Jaeger, J.C., Cook, N.W.G., & Zimmerman, R. (2009). Fundamentals of rock mechanics. John Wiley & Sons, 488 p.

Jager, A.J., & Ryder, J.A. (1999). A handbook on rock engineering practice for tabular hard rock mines. SIMRAC, Johannesburg, 371 p.

Jenkins, F.M., Williams, T.J., & Wideman, C.J. (1990). Rock burst mechanism studies at the Lucky Friday Mine. In US Symposium on Rock Mechanics (USRMS), 31. OnePetro.

Jordan, T.J. (2000). Unpublished presentation at ISS seminar. March 7th, Stellenbosch.

Jost, M.U., & Herrmann, R.B. (1989). A student's guide to and review of moment tensors. Seismological Research Letters, 60(2), 37-57.

Joughin, M.C. & Jager, A.J. (1983). Fracture of rock at stope faces in South African gold mines. In Rockbursts: Prediction & Control. London: Inst. of Min. and Metall., 53-66.

Kaiser, P.K., McCreath, D., & Tannant, D. (1996). Canadian rockburst research program 1990–1995, Vol. 1–6. CAMIRO Mining Division, Sudbury, ON, Canada.

Kaiser, P.K., & Cai, M. (2012). Design of rock support system under rockburst condition. Journal of Rock Mechanics and Geotechnical Engineering, 4(3), 215-227.

Kalenchuk, K., Hume, C., Morin, F., Bawden, W., Oke, J., & Palleske, C. (2017). The unanticipated performance of a weak massive rock mass at depth and the added value of observational engineering. Deep and High Stress Mining, 8, 801-812.

Kanamori, H., (2001). Energy budget of earthquakes and seismic efficiency. Earthquake Thermodynamics and Phase Transformations in the Earth's Interior, 76, 293-305.

Karekal, S., Rao, M., & Chinnappa, S. (2005). Mining-associated Seismicity in Kolar Gold Mines: Some Case Studies using Multi-fractals. Rockburst and Seismicity in mines (6), 635-640.

Kato, N., & Tullis, T.E. (2003). Numerical simulation of seismic cycles with a composite rate- and state-dependent friction law. Bulletin of the Seismological Society of America, 93(2), 841-853.

Kato, N., Lei, X. L., & Wen, X. (2007). A synthetic seismicity model for the Xianshine fault, Southwestern China: simulation using a rate- and state-dependent friction law. Geophys. J. Int., 169 286-300.

Kgarume, T.E., Spottiswoode, S.M., & Durrheim, R.J. (2009). Statistical Properties of Mine Tremor Aftershocks. Pure and Applied Geophysics, 167(1-2), 107-117.

Kijko, A., Drzezla, B., & T., S. (1987). Bimodal character of distribution of extreme seismic events in Polish mines. Acta Geophysica Pol., 35 157.

Kim, Y.S., Peacock, D.C.P., & Sanderson, D.J. (2004). Fault damage zones. Journal of Structural Geology, 26(3), 503-517.

Kisslinger, C. (1976). A review of theories of mechanisms of induced seismicity. Engineering Geology, 10(2-4), 85-98.

Knoll, P., & Kuhnt, W. (1990). Seismological and technical investigations of the mechanics of rock bursts. Rockbursts and Seismicity in Mines pp. 129–138.

Krishnamurthy, R., & Shringarputale, S. (1990). Rockburst hazards in Kolar gold fields. Rockburst and Seismicity in Mines, (2), 411-419.

Ladanyi, B., & Archambault, G. (1970). Simulation of shear behavior of a jointed rock mass. US Symposium on Rock Mechanics (USRMS), 11.

Ladanyi, B., & Archambault, G. (1977). Shear strength and deformability of filled indented joints. Int. Symposium on the Geotechnics of Structurally Complex Formations, 1, 317-326.

Lawrence, D. (1984). Seismicity in the Orange Free State gold mining district. Rockbursts and Seismicity in Mines, (6), 121-130.

Lee, S.W., Hong, E.S., Bae, S.I., & Lee, I.M. (2006). Modelling of rock joint shear strength using surface roughness parameter, Rs. Tunnelling and Underground Space Technology, 21(3-4).

Legge, N., & Spottiswoode, S.M. (1987). Fracturing and microseismicity ahead of a deep gold mine stope in the pre-remnant and remnant stages of mining. ISRM Congress, 6.

Lemos, J.V. (1987). A distinct element model for dynamic analysis of jointed rock with application to dam foundations and fault motion. (Doctoral dissertation) University of Minnesota (USA).

Lenhardt, W., & Hagan, T. (1989). Observations and possible mechanisms of pillar-associated seismicity at great depth. Technical challenges in deep level mining, 1183-1194.

Leslie, I., & Vezina, F. (2001). Seismic data analysis in underground mining operations using ESG's Hyperion systems. Quebec Mining Association Ground Control Colloque, 16.

Linkov, A.M. (1992). Dynamic phenomena in mines and the problem of stability. MTS System Corporation.

Linkov, A.M. (2013). Keynote lecture: Numerical modelling of seismicity: Theory and applications. Rockbursts and Seismicity in Mines, 8, 197-218.

Linkov, A.M., Rybarska-Rusinek, L., & Zoubkov, V.V. (2016). Reasonable sets of input parameters and output distributions for simulation of seismicity. International Journal of Rock Mechanics and Mining Sciences, 84, 87-94.

Lockner, D.A. (1995). Rock failure. Rock physics & phase relations: a handbook of physical constants, 127-147.

Lockner, D.A., & Beeler, N.M. (2002). Rock failure and earthquakes. International Geophysics Series, 81(A), 505-538.

Lourence, P.B., Jung, S.J., & Sprenke, K.F. (1993). Source mechanisms at the Lucky Friday mine: initial results from the North Idaho seismic network. Rockbursts and seismicity mines, 3, 217-222.

Lynch, R.A., Wuite, R., Smith, B.S., & Cichowicz, A. (2005). Micro-seismic monitoring of open pit slopes. Rockbursts and Seismicity in Mines, 6, 581-592.

Madariaga, R. (1976). Dynamics of an expanding circular fault. Bulletin of the Seismological Society of America, 66(3), 639-666.

Malan, D.F. (2011). Recent developments in the monitoring of excavation stability in South African mines. In ISRM Congress.

Malan, D.F., & Napier, J.A.L. (2021). A review of the role of underground measurements in the historical development of rock engineering in South Africa. Journal of the Southern African Institute of Mining and Metallurgy, 121(5), 201-216.

Malovichko, D.A. (2013). Improvement of numerical stress models using the source mechanisms of seismic events. Rockbursts and Seismicity in Mines, 8, 233-247.

Malovichko, D.A. (2017). Assessment and testing of seismic hazard for planned mining sequences. Conference on Deep and High Stress Mining, 8, 61-77.

Malovichko, D.A., & Basson, G. (2014). Simulation of mining induced seismicity using Salamon-Linkov method. Deep and High Stress Mining (ACG), 7, 667-680.

Martin, C., & Simmons, G. (1992). The Underground Research Laboratory: an opportunity for basic rock mechanics. ISRM News Journal, 1(1), 4-12.

Martin, C., & Christiansson, R. (2009). Estimating the potential for spalling around a deep nuclear waste repository in crystalline rock. International Journal of Rock Mechanics and Mining Sciences, 46(2), 219-228.

Mauk, J.L. (2002). Stratigraphy of the Proterozoic Revett Formation, Coeur d'Alene District, Idaho. US Department of the Interior, US Geological Survey, 143p.

McGarr, A. (1971). Violent deformation of rock near deep-level tabular excavations-seismic events. Bull. Seism. Soc. Am. 61, 1453-1466.

McGarr, A. (1981). Analysis of peak ground motion in terms of a model of inhomogeneous faulting. Journal of Geophysical Research: Solid Earth, 86(B5), 3901-3912.

McGarr, A. (1984). Some applications of seismic source mechanism studies to assessing underground hazard. Rockbursts and Seismicity in Mines, 1, 199-208.

McGarr, A. (1994). Some comparisons between mining-induced and laboratory earthquakes. Pure and Applied Geophysics, 142(3-4), 467-489.

McGarr, A. (1997). A mechanism for high wall-rock velocities in rockbursts. Pure and Applied Geophysics, 150(3-4), 381-391.

McGarr, A., Spottiswoode, S.M., & Gay, N. C. (1975). Relationship of mine tremors to induced stresses and to rock properties in the focal region. Bulletin of the Seismological Society of America, 65(4), 981-993.

McGarr, A., Spottiswoode, S.M., Gay, N., & Ortlepp, W. (1979). Observations relevant to seismic driving stress, stress drop, and efficiency. Journal of Geophysical Research: Solid Earth, 84(B5), 2251-2261.

McGarr, A., Simpson, D., Seeber, L., & Lee, W. (2002). Case histories of induced and triggered seismicity. International Geophysics Series, 81(A), 647-664.

McMahon, T. (1988). Rock burst research and the coeur d'alene district (Vol. 9186). United Sates Bureau of Mines, 45 p.

Mendecki, A.J. (1993). Keynote address: Real time quantitative seismology in mines. Rockbursts and Seismicity in Mines, Balkema, Rotterdam 287-295.

Mendecki, A.J. (1997). Seismic monitoring in mines. Springer Science & Business Media.

Mendecki, A.J. (2013). Mine seismology: glossary of selected terms. Rockburst and Seismicity in Mines Symposium, 8, 1-29.

Milev, A.M., & Spottiswoode, S.M. (1997). Integrated seismicity around deep-level stopes in South Africa. International Journal of Rock Mechanics and Mining Sciences, 34(199), 3-4.

Miller, E. (1967). Notes on rock mechanics research in the K.G.F. KFG Min. Metall. Soc. Bull, 95 23-83.

Mining-technology (2019) The top ten deepest mines in the world. Available at: https://www.mining-technology.com/features/feature-top-ten-deepest-mines-world-south-africa/ (Accessed: 11 June 2022).

Minney, D., Kotze, G., & van Aswegen, G. (1997). Seismic monitoring of the caving process above a retreating longwall at New Denmark Colliery, South Africa. Rockbursts and Seismicity in Mines, 4, 125-130.

Mitri, H.S., Tang, B. & Simon, R. (1999). FE modelling of mining-induced energy release and storage rates. Journal of the Southern African Institute of Mining and Metallurgy, 99(2), 103-110.

Mogi, K. (1962). Magnitude-frequency relation for elastic shock accompanying fractures of various materials and some related problems in earthquakes. Bulletin of the Earthquake Research Institute, 40, 831–853.

Moore, D.E., Summers, R., & Byerlee, J.D. (1989). Sliding behavior and deformation textures of heated illite gouge. Journal of Structural Geology, 11(3), 329-342.

Morkel, I.G., Wesseloo, J., & Potvin, Y.H. (2019). The validity of Es/Ep as a source parameter in mining seismology. In Deep Mining 2019, 9, 385-398.

Morissette, P.N.R. (2015). A ground support design strategy for deep underground mines subjected to dynamic-loading conditions. (Doctoral dissertation) University of Toronto (Canada).

Morissette, P.N.R., Hadjigeorgiou, J., Punkkinen, A., Chinnasane, D., & Sampson-Forsythe, A. (2017). The influence of mining sequence and ground support practice on the frequency and severity of rockbursts in seismically active mines of the Sudbury Basin. Journal of the Southern African Institute of Mining and Metallurgy, 117(1), 47-58.

Mungur, G.D., (2005). An evaluation of the seismic hazard prior to the extraction of a shaft pillar at Kloof Gold Mine, controlling seismic risk. Rockburst and seismicity in mines, 6, 453–460.

Murthy, R., & Gupta, P. (1983). Rock mechanics studies on the problem of ground control and rockbursts in the Kolar Gold Fields. Paper presented at the Symposium Papers, Rockbursts: Prediction and Control, Institute of Mining and Metallurgy, London (pp. 67-80).

Müller, W. (1991). Numerical simulation of rock bursts. Mining science and technology, 12(1), pp. 27-42.

Napier, J.A.L. (1987). The application of excess shear stress to the design of mine layouts. Journal of the Southern African Institute of Mining and Metallurgy, 87(12), 397-405.

Nordström, E., Dineva, S., & Nordlund, E. (2020). Back analysis of short-term seismic hazard indicators of larger seismic events in deep underground mines (LKAB, Kiirunavaara mine, Sweden). Pure and Applied Geophysics, 177, 763-785.

Newland, P., & Allely, B. (1957). Volume changes in drained triaxial tests on granular materials. Geotechnique, 7(1), 17-34.

Ng, L. K., Swan, G., & Board, M.P. (1993). The application of an energy approach in fault models for support design. Rockbursts and Seismicity in Mines, 3, 387-391.

Obreimoff, J. W. (1930). The splitting strength of mica. Proc. Roy. Soc. London, A, 127(805), 290-297.

Ohnaka, M. (1993). Critical size of the nucleation zone of earthquake rupture inferred from immediate foreshock activity. Journal of Physics of the Earth, 41(1), 45-56.

Ohnaka, M. (2003). A constitutive scaling law and a unified comprehension for frictional slip failure, shear fracture of intact rock, and earthquake rupture. Journal of Geophysical Research: Solid Earth, 108(B2).

Ohnaka, M., & Yamashita, T. (1989). A cohesive zone model for dynamic shear faulting based on experimentally inferred constitutive relation and strong motion source parameters. Journal of Geophysical Research: Solid Earth, 94(B4), 4089-4104.

Okubo, P.G. (1989). Dynamic rupture modeling with laboratory-derived constitutive relations. Journal of Geophysical Research: Solid Earth, 94(B9), 12321-12335.

Orrego, C., Cuello, D., & Rojas, E. (2013). Determination of induced stress condition inside Pilar Norte sector. Mining Technology, 120(1), 45-52.

Ollila, B. (2021). Time distance analysis of mine scale event. (Master thesis). Laurentian University of Sudbury, Canada.

Omori, F. (1894). On the Aftershocks of earthquakes. J. Coll. Sci. Imp. U. Tokyo. 7, 111–200.

Ortlepp, W.D. (1984). Rockbursts in South African gold mines: A phenomenological view. Rockbursts and Seismicity in Mines, 1, 165–178.

Ortlepp, W.D. (1992). The design of support for the containment of rockburst damage in tunnels-an engineering approach. Rock support in mining and underground construction, 593-609.

Ortlepp, W.D. (1993). High ground displacement velocities associated with rockburst damage. Rockbursts and seismicity in mines, 93, 101-106.

Ortlepp, W.D. (1997). Rock fracture and rockbursts: an illustrative study. South African Institute of Mining & Metallurgy, 98 p.

Ortlepp, W. D. (2000). Observation of mining-induced faults in an intact rock mass at depth. International Journal of Rock Mechanics and Mining Sciences, 37(1-2), 423-436.

Ortlepp, W.D. (2001). The behaviour of tunnels at great depth under large static and dynamic pressures. Tunnelling and Underground Space Technology, 16(1), 41–48.

Ortlepp, W.D. (2005). RaSiM comes of age—a review of the contribution to the understanding and control of mine rockbursts. Rockburst and Seismicity in Mines 6, 3–20.

Ortlepp, W.D., & Cook, N.G.W. (1964). The measurement and analysis of the deformation around deep, hard-rock excavations. Strata Control and Rock Mechanics 4(1).

Ortlepp, W.D., & Nicoll, A. (1964). The elastic analysis of observed strata movement by means of an electrical analogue. Journal of the Southern African Institute of Mining and Metallurgy, 65(4), 214-235.

Ortlepp, W.D., Van Aswegen, G., & Durrheim, R. J. (2001). The mechanism of a rock outburst in a quartzite tunnel in a deep gold mine. Rockbursts and Seismicity in Mines, 5, 53-58.

Papaliangas, T., Hencher, S., Lumsden, A., & Manolopoulou, S. (1993). The effect of frictional fill thickness on the shear strength of rock discontinuities. International journal of rock mechanics and mining sciences & geomechanics abstracts, 30, 81-91.

Paterson, M.S., & Wong, T.F. (2005). Experimental rock deformation-the brittle field. Springer, 347.

Patton, F.D. (1966). Multiple modes of shear failure in rock. ISRM Congress, 1.

Potvin, Y.H. (2009). Strategies and tactics to control seismic risks in mines. Journal of the Southern African Institute of Mining and Metallurgy, 109(3), 177-186.

Potvin, Y.H., & Wesseloo, J. (2013). Keynote Lecture: Improving seismic risk management in hardrock mines. Rockbursts and Seismicity in Mines, 8.

Power, W.L., Tullis, T. E., Brown, S. R., Boitnott, G. N., & Scholz, C. H. (1987). Roughness of natural fault surfaces. Geophysical Research Letters, 14(1), 29-32.

Priest, S.D. (1993). Discontinuity analysis for rock engineering. Springer Science & Business Media.

Priest, S.D., & Hudson, J.A. (1981). Estimation of discontinuity spacing and trace length using scanline surveys. In International Journal of Rock Mechanics and Mining Sciences & Geomechanics Abstracts, 18(3), 183-197.

Rabinowicz, E. (1951). The nature of the static and kinetic coefficients of friction. Journal of applied physics, 22(11), 1373-1379.

Rabinowicz, E. (1958). The intrinsic variables affecting the stick-slip process. Proceedings of the Physical Society, 71(4), 668.

Raffaldi, M.J., Seymour, J.B., Richardson, J., Zahl, E.G., & Board, M.P. (2019). Cemented paste backfill geomechanics at a narrow-vein underhand cut-and-fill mine. Rock mechanics and rock engineering, 52, 4925-4940.

RASIM (2022). Rockbursts and Seismicity in Mines–10. Conf. proceedings. Tucson, Arizona.

Rice, J. (1984). Shear instability in relation to the constitutive description of fault slip. Rockbursts and Seismicity in Mines, 1.

Richardson, E., & Jordan, T.H. (2002). Seismicity in deep gold mines of South Africa: Implications for tectonic earthquakes. Bulletin of the Seismological Society of America, 92(5), 1766-1782.

Ruina, A. (1983). Slip instability and state variable friction laws. Journal of Geophysical Research: Solid Earth, 88(B12), 10359-10370.

Ryder, J.A. (1987). Excess shear stress (ESS): An engineering criterion for assessing unstable slip and associated rockburst hazards. In 6th ISRM Congress, 1211–1215.

Ryder, J.A. (1988). Excess shear stress in the assessment of geologically hazardous situations. Journal of the Southern African Institute of Mining and Metallurgy, 88(1), 27-39.

Ryder, J.A., & Officer, N.C. (1964). An elastic analysis of strata movement observed in the vicinity of inclined excavations. Journal of the Southern African Institute of Mining and Metallurgy, 64(6), 219-244.

Ryder, J.A., & Napier, J. (1985). Error analysis and design of a large-scale tabular mining stress analyzer. Numerical Methods in Geomechanics, 5, 1549-1555.

Ryder, J.A., & Jager, A.J. (2002). A textbook on Rock Mechanics for tabular hard rock mines. SIMRAC, Johannesburg.

Saeb, S. (1990). A variance on the Ladanyi and Archambault's shear strength criterion. Rock joints, 701 705.

Sagy, A., Brodsky, E.E., & Axen, G.J. (2007). Evolution of fault-surface roughness with slip. Geology, 35(3), 283-286.

Sainoki, A. (2014). Dynamic behaviour of mining-induced fault slip. (Doctoral dissertation) McGill University (Canada).

Sainoki, A., & Mitri, H.S. (2017). Influence of mining activities on the reactivation of a footwall fault. Arabian Journal of Geosciences, 10, 1-15.

Salamon, M.D.G. (1963). Elastic analysis of displacements and stresses induced by the mining of seam or reef deposits—Part I. Journal of the Southern African Institute of Mining and Metallurgy, 64(4), 128-149.

Salamon, M.D.G. (1964a). Elastic analysis of displacements and stresses induced by the mining of seam or reef deposits—Part II: Practical methods of determining displacement, strain and stress components from a given mining geometry. Journal of the Southern African Institute of Mining and Metallurgy, 64(6), 197-218.

Salamon, M.D.G. (1964b). Elastic analysis of displacements and stresses induced by mining of seam or reef deposits—Part III: An application of the elastic theory: protection of surface installations by underground pillars. Journal of the Southern African Institute of Mining and Metallurgy, 64(10), 468-500.

Salamon, M.D.G. (1964c). Elastic analysis of displacements and stresses induced by mining of seam or reef deposits—Part IV: Inclined reef. Journal of the Southern African Institute of Mining and Metallurgy, 64(10), 319-338.

Salamon, M.D.G. (1968). Two-dimensional treatment of problems arising from mining tabular deposits in isotropic or transversely isotropic ground. International Journal of Rock Mechanics and Mining Sciences, 5(2), 159-185.

Salamon, M.D.G. (1974). Rock mechanics of underground excavations. Proc. 3rd ISRM Congress, 951-1099.

Salamon, M.D.G. (1983). Rockburst hazard and the fight for its alleviation in South African gold mines. Rockbursts, Prediction and Control (20), 11–52.

Salamon, M.D.G. (1984). Energy considerations in rock mechanics: fundamental results. Journal of the Southern African Institute of Mining and Metallurgy, 84(8), 233–246.

Salamon, M.D.G. (1993). Keynote address: Some applications of geomechanical modelling in rockburst and related research. Rockbursts and Seismicity in Mines, 3, 297-309.

Scheepers, L., Hofmann, G., Morkel, I., & Ashanti, A.G. (2012). The study of seismic response to production for a grid mining layout. Southern Hemisphere International Rock Mechanics Symposium, 2, 387–406.

Scheepers, L. (2022). Rockburst in South African Deep Level Gold Mining: What Do We Know? Rockbursts and Seismicity in Mines, 10, 13p.

Schmidt, E.S. (2018). Experimental and numerical investigation of hydraulic stimulation as a risk mitigation technique for fault slip rockburst hazards in deep underground mining. (Master thesis) University of British Columbia (Canada).

Scholz, C.H. (1968). The frequency-magnitude relation of microfracturing in rock and its relation to earthquakes. Bulletin of the Seismological Society of America, 58, 399–415.

Scholz, C.H. (1998). Earthquakes and friction laws. Nature, 391(6662), 37.

Scholz, C.H. (2002). The mechanics of earthquakes and faulting. Cambridge university press. Second edition.

Scholz, C.H. (2019). The mechanics of earthquakes and faulting. Cambridge university press. Third edition.

Scholz, C.H., Molnar, P., & Johnson, T. (1972). Detailed studies of frictional sliding of granite and implications for the earthquake mechanism. Journal of geophysical research, 77(32), 6392-6406.

Scholz, C.H., & Aviles, C.A. (1986). The fractal geometry of faults and faulting. Earthquake source mechanics, 37, 147-155.

Sellers, E., & Coetzer, S. (2003). Probabilistic design methodology for dealing with insitu stress variation. International Symposium on Rock Stress, 3(535), 542.

Seymour, J.B. (2023) Personal communication.

Seymour, J.B., Benton, D.J., Raffaldi, M., Johnson, J., Martin, L., Boltz, S., & Richardson, J. (2016). Improving ground control safety in deep vein mines. Mine Safety Science and Engineering, 3, 71-77.

Seymour, J.B., Raffaldi, M.J., Abraham, H., Johnson, J.C., & Zahl, E.G. (2017). Monitoring the in situ performance of cemented paste backfill at the Lucky Friday Mine. In Proceedings of Minefill, 19-22.

Sibson, R.H. (1986). Brecciation processes in fault zones: inferences from earthquake rupturing. Pure and Applied Geophysics, 124(1-2), 159-175.

Simon, R. (1999). Analysis of fault-slip mechanisms in hard rock mining. (Doctoral dissertation) McGill University (Canada).

Simpson, D. (1986). Triggered earthquakes. Annual Review of Earth and Planetary Sciences, 14(1), 21-42.

Simser, B., Deredin, R., Jalbout, A., & Butler, T. (2015). Use of microseismic monitoring data as an aid to rock mechanics decision making and mine design verification. In US Rock Mechanics/Geomechanics Symposium (pp. ARMA 15-374).

Smith (2021) Results for digitized in-stope discs, Gold-Hunter mine. Internal report

Spottiswoode, S.M. (1980). Source mechanism studies on Witwatersrand seismic events. (Doctoral dissertation) University of the Witwatersrand (South Africa).

Spottiswoode, S.M. (1984). Source Mechanisms of Mine Tremors at Blyvooruitzicht Gold Mine. Rockbursts and Seismicity in Mines, 6, 29-37.

Spottiswoode, S.M. (1988). Total seismicity, and the application of ESS analysis to mine layouts. Journal of the Southern African Institute of Mining and Metallurgy, 88(4), 109-116.

Spottiswoode, S.M. (1990). Volume excess shear stress and cumulative seismic moments. Rockbursts and Seismicity in Mines, 2, 39–43.

Spottiswoode, S.M. (1997). Energy release rate with limits to on-reef stress. SARES: 1st Southern African Rock Engineering Symposium, 252-257.

Spottiswoode, S.M. (2001). Keynote address: synthetic seismicity mimics observed seismicity in deep tabular mines. Rockbursts and Seismicity in Mines, 5, 371-377.

Spottiswoode, S.M. (2010). Mine seismicity: prediction or forecasting? Journal of the Southern African Institute of Mining and Metallurgy, 110(1), 11-20.

Spottiswoode, S.M., & McGarr, A. (1975). Source parameters of tremors in a deep-level gold mine. Bulletin of the seismological society of America, 65(1), 93-112.

Spottiswoode, S.M., Napier, J., Milev, A., & Vieira, F. (2000). Relationship between ERR and seismic energy release for different geotechnical areas. CSIR Mining Technology, 49 p.

Spottiswoode, S.M., & Milev, A.M. (2002). Methodology and computer program for applying improved, inelastic ERR for the design of mine layouts on planar reefs.

Spottiswoode, S.M., Linzer, L.M., & Majiet, S. (2008). Energy and stiffness of mine models and seismicity. SHIRMS, ACG, 693–707.

Spottiswoode, S.M., & Drummond, M. (2014). Pillar behaviour and seismicity in platinum mines. Journal of the Southern African Institute of Mining and Metallurgy, 114(10), 801-809.

Stacey, T. (2012). A philosophical view on the testing of rock support for rockburst conditions. Journal of the Southern African Institute of Mining and Metallurgy, 112(8), 01-08.

Starfield, A., & Fairhurst, C. (1968). How high-speed computers advance design of practical mine pillar systems. Eng. Min. J, 169(5), 78-84.

Stein, S., & Wysession, M. (2003). An Introduction to Seismology, Earthquakes. Earth Structure.

Stiller, H., Hurtig, E., Grosser, H., & Knoll, P. (1983). On the nature of mining tremors. Earthquake prediction research, 2(1), 57-67.

Sturgis, G.A., Berberick, D.R., Board, M.P., Strickland, W.H., & Swanson, M.T. (2017). Elliptical shaft excavation and furnishing in response to depth induced ground pressure. In Deep Mining (ACG), 8, 883-897.

Subbaramu, K.R., Rao, B.S.S., Krishnamurthy, R., & Srinivasan, C. (1985). Seismic investigation of rockburst in the Kolar Gold Fields. In Proc. 4th Conf. on AE/MS Activity in Geological structures and materials, Pennsylvania.

Swanson, P.L., & Sines, C.D. (1992). Characteristics of Mining-Induced Seismicity and Rock Bursting in a Deep Hard-Rock Mine. United States Bureau of Mines, 12 p.

Tannant, D., Brummer, R.K., & Yi, X. (1995). Rockbolt behaviour under dynamic loading: field tests and modelling. International journal of rock mechanics and mining sciences & geomechanics abstracts, 32, 537-550.

Timoshenko, S. P. and Goodier, J. N. (1970) Theory of Elasticity, 3rd edn. Wiley: New York.

Tinti, E., Cocco, M., Fukuyama, E., & Piatanesi, A. (2009). Dependence of slip weakening distance (D c) on final slip during dynamic rupture of earthquakes. Geophysical Journal International, 177(3), 1205-1220.

Trifu, C.I., & Urbancic, T.I. (1996). Fracture coalescence as a mechanism for earthquakes: observations based on mining induced microseismicity. Tectonophysics, 261(1-3), 193-207.

Trifu, C.I., & Shumila, V. (2002). Reliability of seismic moment tensor inversions for induced microseismicity at Kidd Mine, Ontario. The Mechanism of Induced Seismicity, 145-164.

Troncoso, J., Potvin, Y.H., & Wesseloo, J. (2012). Application of the limit equilibrium strength to the seismic assessment of shear related seismicity. In Deep Mining 2012 (ACG), 6, 389-400.

Turcotte, P. (2014) Personal communication.

UDMN (2023) The ultra deep mining network. Available at: https://www.cemi.ca/udmn/

Urbancic, T.I. (1991). Source studies of mining-induced microseismicity at Strathcona Mine, Sudbury, Canada: a spatial and temporal analysis. (Doctoral dissertation) Queen's University (Canada).

Urbancic, T.I., Young, R.P., Bird, S., & Bawden, W. (1992). Microseismic source parameters and their use in characterizing rock mass behaviour: considerations from Strathcona mine. CIM: rock mechanics and strata control sessions, 94, 26-30.

Urbancic, T., & Young, R. (1993). Space-time variations in source parameters of mining-induced seismic events with M< 0. Bulletin of the Seismological Society of America, 83(2), 378-397.

van Aswegen, G. (2005). Routine seismic hazard assessment in some South African mines. Rockburst and seismicity in mines, 6, 437-444.

van Aswegen, G., & Butler, A. (1993). Applications of quantitative seismology in South African gold mines. Rockbursts and Seismicity in Mines, 3, 261-266.

Vallejos Massa, J., & McKinnon, S.D. (2011). Correlations between mining and seismicity forre-entry protocol development.

Vogt, D. (2011). A renaissance for mining research in South Africa? Strategic versus tactical approaches in Mining, ACG, Y. Potvin (ed), pp. 231–246.

Wallace, R.E., & Morris, H.T. (1986). Characteristics of faults and shear zones in deep mines. Pure and Applied Geophysics, 124(1-2), 107-125.

Wawersik, W., & Fairhurst, C. (1970). A study of brittle rock fracture in laboratory compression experiments. International Journal of Rock Mechanics and Mining Sciences & Geomechanics Abstracts, 7, 561-575.

Wesseloo, J. (2014). Evaluation of the spatial variation of b-value. Journal of the Southern African Institute of Mining and Metallurgy, 114(10), 823-828.

Wesseloo, J. (2018). The spatial assessment of the current seismic hazard state for hard rock underground mines. Rock Mechanics and Rock Engineering, 51(6), 1839-1862.

White, B.G., & Whyatt, J.K. (1999). Role of fault slip on mechanisms of rock burst damage, Lucky Friday Mine, Idaho, USA.

White, B.G., Williams, T.J., & Whyatt, J.K. (2002). Mechanics of a large, strain-type rock burst and design for prevention.

Whyatt, J.K. (2001). Influence of geologic structures on stress variation and the potential for rockbursting in mines with particular reference to the Lucky Friday Mine, Idaho. (Doctoral dissertation) University of Minnesota (USA).

Whyatt, J.K., Williams, T.J., & Board, M.P. (1992). Rock mechanics investigations at the Lucky Friday Mine (in three parts) 2, Evaluation of underhand backfill practice for rockburst control. United States Bureau of Mines, 10p.

Whyatt, J.K., Williams, T.J., & Blake, W. (1995). In situ stress at the Lucky Friday Mine (in four parts) 4, Characterization of mine in situ stress field. United States Bureau of Mines, 27p.

Whyatt, J.K., Williams, T.J., Blake, W., Sprenke, K., & Wideman, C. (1996). Mining-induced seismicity at the Lucky Friday Mine: Seismic events of magnitude > 2.5, 1989–1994 (No. UCRL-CR-125538). Lawrence Livermore National Lab., 165p.

Whyatt, J.K., & White, B.G. (1998). Rock Bursting and Seismicity During Ramp Development Lucky Friday Mine, Mullan Idaho. US National Institute for Occupational Safety and Health.

Whyatt, J.K., Blake, W., Williams, T., & White, B.G. (2002). Sixty (60) years of experience with rock bursts in the Coeur d'Alene Mining District. Soc. of Min. Eng.

Wiles, T.D. (1998). Correlation between energy release rate and observed bursting conditions at Creighton Mine. Mt. Eliza: Mine Modelling Pty.

Wiles, T.D. (2005). Rockburst prediction using numerical modelling: Realistic limits for failure prediction accuracy. Rockbursts and Seismicity in Mines, 6, 57-63.

Wiles, T.D. (2014). Three ways to assess mining-induced fault instability using numerical modelling. South African Rock Engineering Symposium, 6.

Wiles, T.D. (2022). Mine Analysis Package in Three Dimensions, v.68. Mine Modelling Pty. Ltd. Australia.

Wiles, T.D., Lachenicht, R., & Van Aswegen, G. (2001). Integration of deterministic modelling with seismic monitoring for the assessment of rock mass response to mining: Part I theory. Rockburst and Seismicity in Mines, 5, 379-387.

Williams, T.J., Whyatt, J.K., & Poad, M.E. (1992). Rock mechanics investigations at the Lucky Friday Mine (in three parts): 1. Instrumentation of an experimental underhand longwall stope. United States Bureau of Mines, 26p.

Wilson, M., Foulger, G., Gluyas, J., Davies, R., & Julian, B. (2017). HiQuake: The Human-Induced Earthquake Database. Seismological Research Letters, 88(6), 1560-1565.

Woodward, K., Wesseloo, J., & Potvin, Y.H. (2017). The spatial and temporal assessment of clustered and time-dependent seismic responses to mining. In Deep Mining (ACG), 8, 157-171.

Wyllie, D.C. (2018). Rock slope engineering. 5th edition. CRC Press.

Wyss, M., Sammis, C. G., Nadeau, R.M., & Wiemer, S. (2004). Fractal dimension and b-value on creeping and locked patches of the San Andreas fault near Parkfield, California. Bulletin of the Seismological Society of America, 94(2), 410-421.

Yan, P., Lu, W., Chen, M., Shan, Z., Chen, X., & Zhou, Y. (2012). Energy release process of surrounding rocks of deep tunnels with two excavation methods. Journal of Rock Mechanics and Geotechnical Engineering, 4(2), 160-167.

Zhang, C., Feng, X., Zhou, H., Qiu, S., & Wu, W. (2011). A top pilot tunnel preconditioning method for the prevention of extremely intense rockbursts in deep tunnels excavated by TBMs. Rock Mechanics and Rock Engineering, 45(3), 289-309.

Zhao, Y., Yang, T., Zhang, P., Zhou, J., Yu, Q., & Deng, W. (2017). The analysis of rock damage process based on the microseismic monitoring and numerical simulations. Tunnelling and Underground Space Technology, 69, 1-17.

Zhou, J., Li, X., & Shi, X. (2012). Long-term prediction model of rockburst in underground openings using heuristic algorithms & support vector machines. Safety Science, 50(4), 629-644.

Zhou, J., Li, X., & Mitri, H.S. (2016). Classification of Rockburst in Underground Projects: Comparison of Ten Supervised Learning Methods. Journal of Computing in Civil Eng., 30(5).

Zhou, J., Chen, C., Du, K., Jahed Armaghani, D., & Li, C. (2020). A new hybrid model of information entropy and unascertained measurement with different membership functions for evaluating destressability in burst-prone underground mines. Engineering with Computers, 1-19.

Zoback, M.D., & Gorelick, S.M. (2012). Earthquake triggering and large-scale geologic storage of carbon dioxide. Proceedings of the National Academy of Sciences, 109(26), 10164-10168

APPENDIX A — ERR VERIFICATION FOR A HORIZONTAL REFF IN AN INFINITE ELASTIC MEDIUM

The verification example aims to establish confidence in the ERR for an advancing longwall as determined in MAP3D v68. The example involves calculating the stress and closures on a tabular reef in an infinite isotropic elastic medium subjected to hydrostatic stresses. The MAP3D model construct is shown in Figure A.1. The reef construct is defined by displacement discontinuity (DD) elements with the smallest width set to 3.125 m.

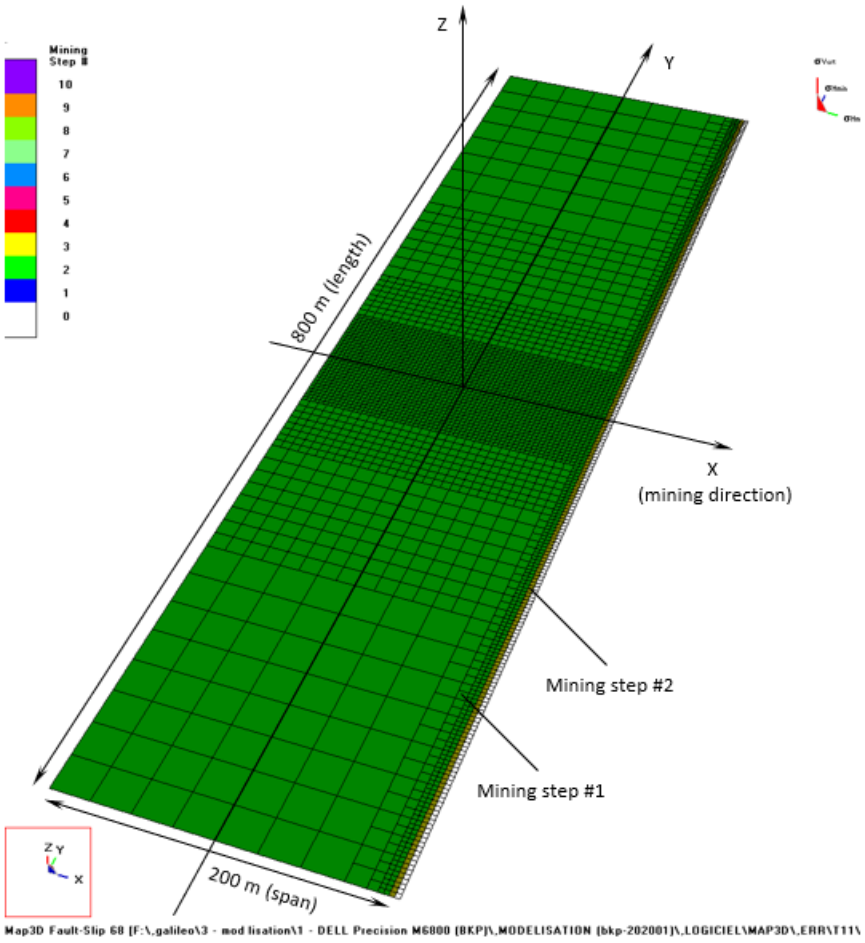


Figure A.1: Horizontal-reef construct built in MAP3D using DD elements, representing a parallel-sided longwall advancing in the x-axis direction

Two mining steps are simulated where the longwall is mined to an initial span of 200 m (mining step #1) and then advanced by 3.125 m on one side of the 800 m reef length (mining step #2). The reference frame (x-y-z) rests in the middle of the planar reef constructed at mining step #1.

The x-y plane coincides with the plane of the reef. The perpendicular stress and normal closures are investigated along the x-axis.

The model input parameters are listed in Table A.1. These values are typically assigned for quartzite rockmass in South African engineering textbooks (Budavari, 1983).

Table A.1: Model geometry, material properties and stresses, and MAP3D (mesh) control parameters

Model geometry	Material properties & stressfield	Control parameters
Half span (l) = 100 m	E = 60,000 MPa	Element length (AL) = 3.125
Length (L) = 800 m	$\upsilon = 0.25$	Element discretize (DON) = 1
Width (w) = 1 m	p_n = 100 MPa	Matrix Lumping (DOC) = 16
Advance (ψ) = 3.125 m		Element Lumping (DOE) = 8
		Grid Lumping (DOG) = 8

The analytical solution for vertical stress ahead of the tip of the reef may be determined from the equation (Salamon, 1968):

$$\sigma_n = \frac{p_n \cdot x}{\sqrt{x^2 - l^2}} \qquad A.1$$

The stress normal (σ_n) induced ahead of the reef calculated by MAP3D, for mining step #1, are compared to the analytical solution along the x-axis (Figure A.2).

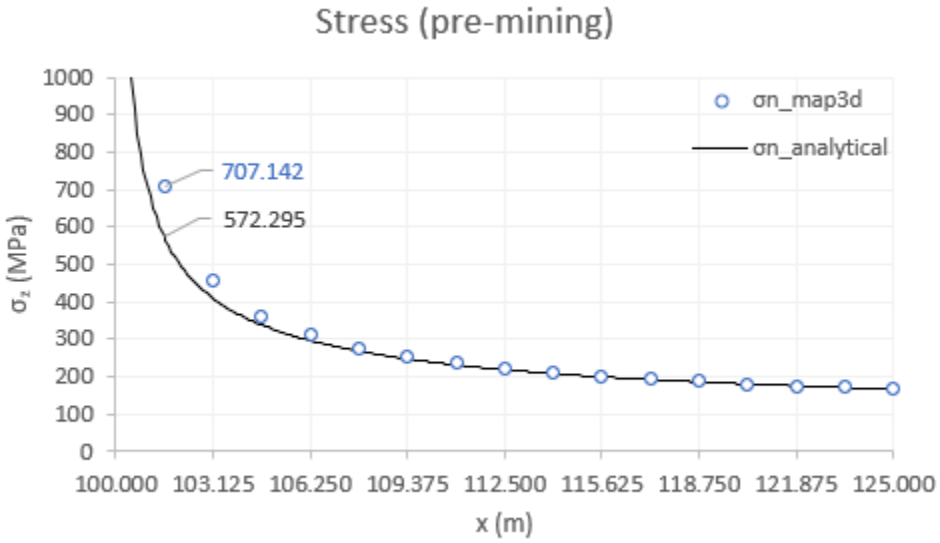


Figure A.2: Stress perpendicular to reef, comparing simulated vs analytical (in mining step#1)

The analytical solution for the distribution of closure on the reef may be given by the equation (Salamon, 1968):

$$\delta_n = \frac{4(1-\nu^2)}{E} \cdot p_n \cdot \sqrt{l^2 - x^2} \qquad A.2$$

The normal closure (δ_n) induced by extending the mining front calculated by MAP3D, for mining step #2, are compared to the analytical solution along the x-axis (Figure A.3).

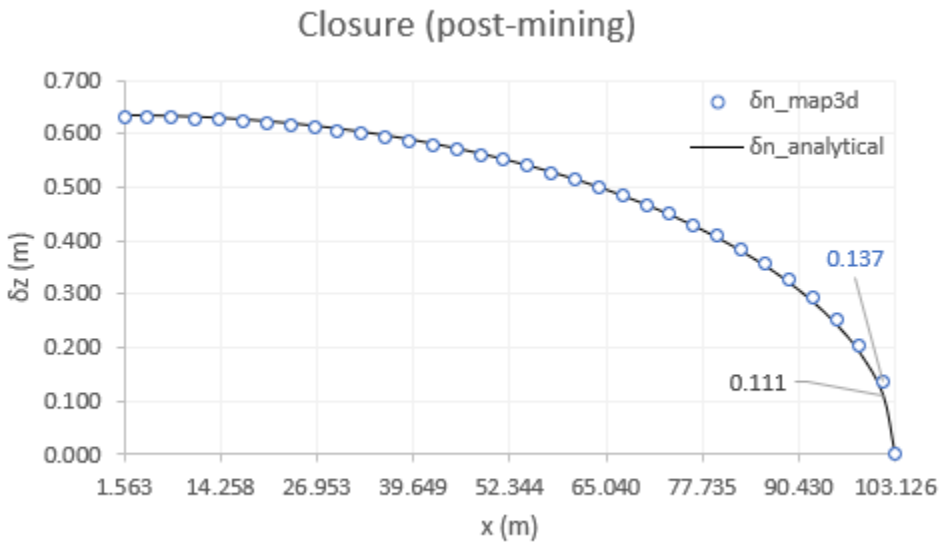


Figure A.3: Closure perpendicular to stope reef, comparing simulated vs analytical (mining step#2)

Tables A.3 and Table A.4 present the relative error percentages with respect of the analytical value. The numerical results are in good agreement (< 10%) with the equivalent analytical solution apart from the elements near the edge of the reef. It has been found that for BEM codes utilizing constant DD elements, both the stress and closure are consistently over-estimated (Ryder & Napier, 1985). However, as will be seen later, this has little impact on ERR calculations.

Table A.3: Stress results along the x-axis ahead of the leading front (mining step#1)

x (m)	σn_map3d	σn_analytical	error
100.000	-	-	-
101.562	707.142	572.295	+23.6%
103.125	455.327	409.315	+11.2%

Table A.3: Stress results along the x-axis ahead of the leading front (mining step#1) (cont'd)

x (m)	σn_map3d	σn_analytical	error
104.687	361.630	337.971	+7.0%
106.250	310.349	295.932	+4.9%
107.812	277.191	267.571	+3.6%
109.375	253.649	246.871	+2.7%
110.937	235.902	230.963	+2.1%
112.500	221.959	218.282	+1.7%
114.062	210.661	207.894	+1.3%
115.625	201.289	199.201	+1.0%
117.187	193.369	191.804	+0.8%
118.750	186.576	185.421	+0.6%
120.312	180.675	179.850	+0.5%
121.875	175.496	174.939	+0.3%
123.437	170.906	170.574	+0.2%
125.000	166.815	166.667	+0.1%

Table A.4: Normal closure determined along the x-axis from the mid-stope position after advancing the mining front by 3.125 m (mining step#2)

x(m)	δn_map3d	δn_analytical	error	comments
1.563	0.631	0.635	-0.7%	New mid-span position due to mining
26.563	0.611	0.615	-0.6%	~25% from mid-span
51.562	0.550	0.553	-0.4%	~50% from mid-span
76.562	0.430	0.428	+0.3%	~75% from mid-span
79.687	0.408	0.406	+0.5%	
82.812	0.384	0.381	+0.8%	
85.937	0.357	0.353	+1.2%	
89.062	0.328	0.322	+1.7%	
92.187	0.294	0.287	+2.5%	
95.312	0.254	0.244	+3.9%	
98.437	0.205	0.191	+7.3%	
101.563	0.137	0.111	+23.9%	~98% from mid-span
103.125	0.000	0.000	-	Edge of advanced reef (span=203.125 m)

The ERR_{BEM}, as calculated from BEM results, is given by (Ryder & Jager, 2000):

$$ERR_{bem} = \frac{1}{2} \cdot \sigma_n^{i-1} \cdot \delta_n^i \qquad A.3$$

*The subscript BEM (boundary element method) qualifies this parameter.

The ERR-c.s., as determined from the closed-form solution for induced stress and closure on a reef (Salamon, 1968), is given by:

$$ERR_{c.s.} = \frac{1}{2} \cdot \sigma_n \cdot \delta_n \qquad A.4$$

Substituting the analytical solution for normal stress and closure into the previous equation provides the following:

$$ERR_{c.s.} = \frac{2(1-v^2)}{E} \cdot {p_n}^2 \cdot l \qquad A.5$$

*The subscript C.S. (cross-section of reef) qualifies this formulation.

The ERR-i.p., as determined for the planar crack geometry, is given by (Budavari, 1983):

$$ERR_{i.p.} = \frac{\pi(1-v^2)}{E} \cdot {p_n}^2 \cdot l \qquad A.6$$

*The subscript I.P. (in plane of reef) qualifies this formulation.

Calculating the first two parameters, ERR-bem and ERR-c.s., assuming the values highlighted in Figure 1 and Figure 2, allows to compare to the ERR-i.p. solution. The ERR-bem calculated from MAP3D is in very close agreement (-2.5%) with the in-plane solution. The ERR-c.s. calculated from the cross section underestimates the energy release rate by -36.3% when compared to the in-plane solution. The lower Table A.5 show the summary of the results:

Table A.5: Energy Release Rates (MJ/m^2) per solution

ERR_bem	ERR_i.p.	error
48.6	49.9	-2.5%
ERR_cs	ERR_i.p.	error
31.7	49.9	-36.3%
ERR_cs_adjusted	ERR_i.p.	error
49.9	49.9	0.0%

Therefore, although BEM methods tend to overestimate (by ~20%) the normal stress and closure at the face of the reef, the energy release rate agrees with the in-plane solution very well (~2.5%). Caution should be used when estimating ERR from a cross-section as it has been illustrated here that the value is underestimated by ~36%, requiring a correction factor of π/2 to match the in-plane solution, see equation A.7.

$$ERR_{i.p.} = \frac{\pi}{2} \cdot ERR_{c.s.} \qquad A.7$$

REFERENCES

Budavari, S. (1983). Rock mechanics in mining practice.

Jager, A.J., & Ryder, J.A. (1999). A handbook on rock engineering practice for tabular hard rock mines. Safety in Mines Research Advisory Committee, Johannesburg, 46.

Salamon, M.D.G. (1968). Elastic moduli of a stratified rock mass. In International Journal of Rock Mechanics and Mining Sciences & Geomechanics Abstracts (Vol. 5, No. 6, pp. 519-527). Pergamon.

APPENDIX B — MAP3D V68 INPUT PARAMETERS

Table B.1: Pre-mining stress state

Pre-mining stress state	DD .inp file	FF .inp file
Horizontal Datum	+304.8	+304.8
$\Delta\sigma_{Hmax}$ variation [MPa/m]	-0.0440	-0.0440
$\Delta\sigma_{Hmin}$ variation [MPa/m]	-0.0350	-0.0350
$\Delta\sigma_{Vert}$ variation [MPa/m]	-0.0290	-0.0290
σ_{Hmax} trend [°]	-40	-40
σ_{Hmax} plunge [°]	0	0
σ_{Vert} trend [°]	0	0
σ_{Vert} plunge [°]	-90	-90

Table B.2: Control parameters

Control parameters	DD .inp file	FF .inp file
Maximum # of Time Steps (NLD)	10,000	10,000
Maximum # of Iterations (NIT)	10,000	10,000
Stress Tolerance (STOL)	0.1	0.1
Relaxation Parameter (RPAR)	1.2	1.2
Element Length (AL)	100	100
Grid Spacing (AG)	20	20
Grid Discretize (DOL)	2	2
Element Discretize (DON)	1	1
Matric Lumping (DOC)	32	4
Element Lumping (DOE)	8	8
Grid Lumping (DOG)	8	8
Aspect Ratio (DOR)	5	5

Table B.3: Model information

Model information	DD .inp file	FF .inp file
Number of Surfaces	39,294	163,378
Number of Coordinates	40,572	181,208
Number of Mining Steps	20+	6+

APPENDIX C — YOUNG'S MODULUS CALIBRATION

The rockmass elastic properties dictate the magnitude of closure observed in stope. For varying Young Modulus, the BEM (DD-element) model was used to simulate in-stope closures at the approximate location where in-field measurements have occurred (Seymour et al., 2017). Closure meter #4 (in 11S) and closure meter #5 (in 15S) were chosen. The Young Modulus was progressively reduced from 35.7 GPa, the upper laboratory scale value, to 18.9 GPa by 2.1 GPa increments. Each reduction in modulus required a model run where the simulated closures were extracted. The model assumes monthly mining steps (highest constructed resolution). Figure C.1 and Figure C.2 overlay the simulated normal closures for varying Moduli, atop the in-stope measurements in 11S and 15S, respectively. In both plots, the dashed lines represent measured displacements, while the continuous lines represent simulated displacements per Modulus.

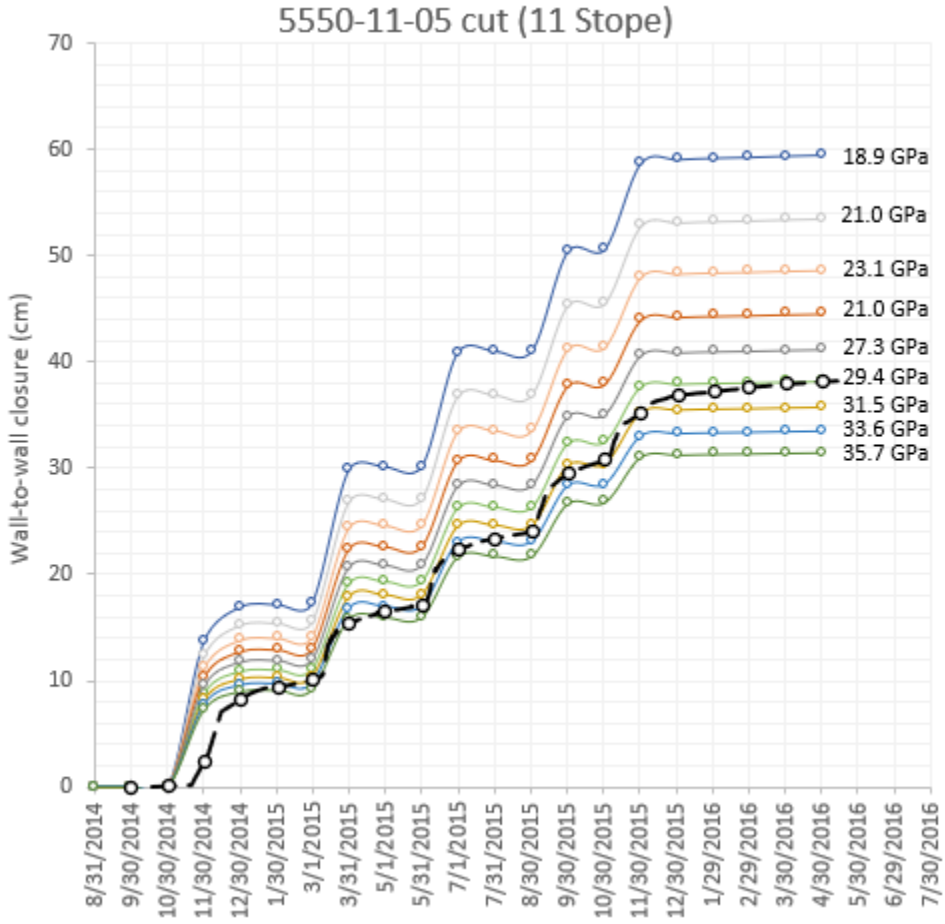


Figure C.1: Simulated vs measured (CM#4) in-stope closure in 11 Stope

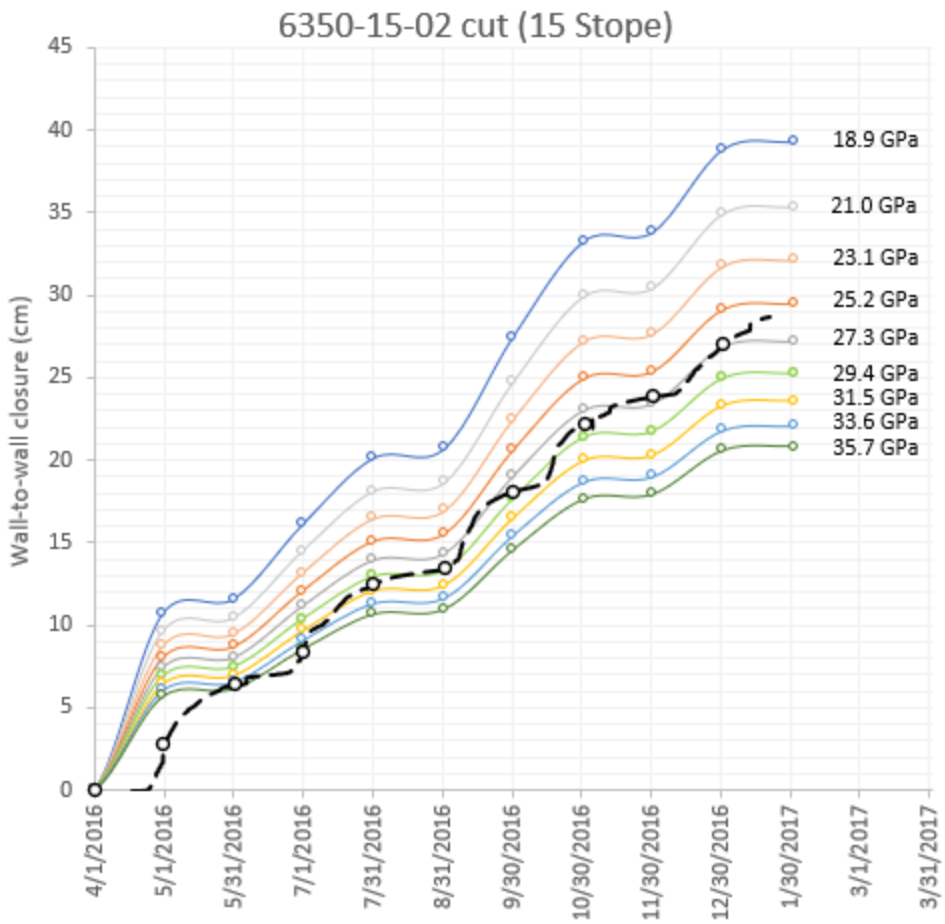


Figure C.2: Simulated vs measured (CM#5) in-stope closure in 15 Stope

The Root Mean Square Error (RMSE) was used for the analysis, where it served as the standard deviation of the difference between simulated and measured closures. For our case, the RMSE is expressed as follows:

$$RMSE = \sqrt{\frac{\sum_{i=1}^{n}(\delta n_i - \hat{\delta} n_i)^2}{n}} \qquad B.1$$

where: n = number of data points

δn_i = the i-th simulated normal displacement

$\hat{\delta} n_i$ = the i-th measurement normal displacement

The RMSE value was determined for each Modulus, per stope (see Table B.1 & Table B.2).

Table C.1: RMSE analysis for 11 Stope

CM#4	18.9 GPa	21.0 GPa	23.1 GPa	25.2 GPa	27.3 GPa	29.4 GPa	31.5 GPa	33.6 GPa	35.7 GPa
Measured (cm)	Simulated (cm)								
0.00	0.00	0.00	0.00	0.00	0.00	0.00	0.00	0.00	0.00
0.07	0.00	0.00	0.00	0.00	0.00	0.00	0.00	0.00	0.00
2.38	13.69	12.32	11.20	10.27	9.48	8.80	8.21	7.70	7.25
8.26	16.95	15.26	13.87	12.71	11.74	10.90	10.17	9.54	8.97
9.37	17.16	15.44	14.04	12.87	11.88	11.03	10.29	9.65	9.08
10.01	17.20	15.48	14.08	12.90	11.91	11.06	10.32	9.68	9.11
15.38	29.83	26.84	24.40	22.37	20.65	19.17	17.90	16.78	15.79
16.47	30.11	27.10	24.64	22.58	20.85	19.36	18.07	16.94	15.94
17.14	30.16	27.14	24.67	22.62	20.88	19.39	18.09	16.96	15.96
22.31	40.86	36.77	33.43	30.65	28.29	26.27	24.52	22.98	21.63
23.38	40.98	36.88	33.53	30.74	28.37	26.35	24.59	23.05	21.70
24.11	41.01	36.91	33.55	30.76	28.39	26.36	24.61	23.07	21.71
29.41	50.36	45.32	41.20	37.77	34.86	32.37	30.21	28.33	26.66
30.81	50.58	45.52	41.38	37.93	35.02	32.51	30.35	28.45	26.78
35.20	58.63	52.77	47.97	43.97	40.59	37.69	35.18	32.98	31.04
36.86	59.00	53.10	48.27	44.25	40.84	37.93	35.40	33.19	31.23
37.20	59.14	53.22	48.38	44.35	40.94	38.01	35.48	33.26	31.31
37.60	59.21	53.29	48.45	44.41	40.99	38.06	35.53	33.31	31.35
37.93	59.33	53.40	48.54	44.50	41.07	38.14	35.60	33.37	31.41
38.14	59.41	53.47	48.61	44.56	41.13	38.19	35.65	33.42	31.45
RMSE =	**16.65**	**12.52**	**9.16**	**6.41**	**4.18**	**2.54**	**1.96**	**2.61**	**3.67**

Table C.2: RMSE analysis for 15 Stope

CM#5	18.9 GPa	21.0 GPa	23.1 GPa	25.2 GPa	27.3 GPa	29.4 GPa	31.5 GPa	33.6 GPa	35.7 GPa
Measured (cm)	Simulated (cm)								
0.00	0.00	0.00	0.00	0.00	0.00	0.00	0.00	0.00	0.00
2.75	10.68	9.61	8.74	8.01	7.40	6.87	6.41	6.01	5.66
6.39	11.57	10.41	9.47	8.68	8.01	7.44	6.94	6.51	6.13
8.38	16.07	14.46	13.15	12.05	11.12	10.33	9.64	9.04	8.51
12.49	20.10	18.09	16.45	15.08	13.92	12.92	12.06	11.31	10.64
13.41	20.68	18.61	16.92	15.51	14.32	13.30	12.41	11.63	10.95
18.09	27.45	24.71	22.46	20.59	19.01	17.65	16.47	15.44	14.53
22.21	33.25	29.93	27.20	24.94	23.02	21.37	19.95	18.70	17.60
23.83	33.80	30.42	27.65	25.35	23.40	21.73	20.28	19.01	17.89
27.03	38.84	34.96	31.78	29.13	26.89	24.97	23.31	21.85	20.56
RMSE =	**8.42**	**6.07**	**4.21**	**2.79**	**1.91**	**1.78**	**2.25**	**2.92**	**3.59**

The RMSE per Modulus within each stope was plotted in Figure C.3. For 11 Stope, the best fit between simulated and measured closures was observed for 31.5 Gpa (at RMSE = 1.96), while 15 Stope showed the best fit at 27.3 Gpa (with RMSE = 1.78 cm). The arithmetic RMSE averages for both stopes are presented in the table below.

Table C.3: Average RMSE per Young Modulus

	18.9 GPa	21.0 GPa	23.1 GPa	25.2 GPa	27.3 GPa	29.4 GPa	31.5 GPa	33.6 GPa	35.7 GPa
RMSE	12.53	9.29	6.68	4.60	3.04	2.16	2.11	2.76	3.63

A single Young Modulus was attributed to the GH rockmass since both stopes were developed in the same (rock-unit) formation. Hence, the rockmass was assigned to an Elastic Modulus of 29.4 GPa, representing an average RMSE of 2.16 cm.

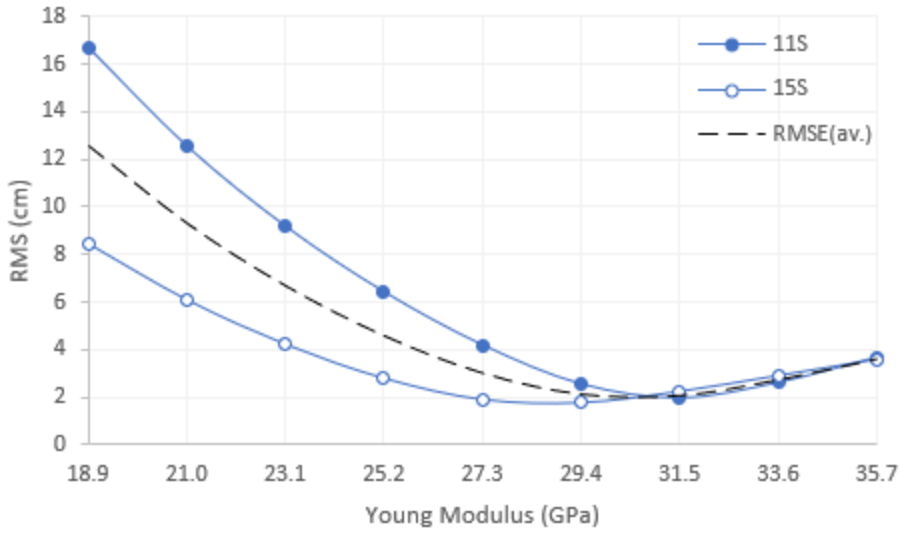


Figure C.3: RMSE per Young Moduli

REFERENCE

Seymour, J. B., Raffaldi, M. J., Abraham, H., Johnson, J. C., & Zahl, E. G. (2017, February). Monitoring the in situ performance of cemented paste backfill at the Lucky Friday mine. In Proceedings of Minefill (pp. 19–22).